THEORETICAL ASPECTS OF SPIN DYNAMICS AND SPIN TRANSPORT IN LOW-CONDUCTING AND INSULATING MATERIALS

by

Yue Zhang

A dissertation submitted to the faculty of
The University of Utah
in partial fulfillment of the requirements for the degree of

Doctor of Philosophy

in

Physics

Department of Physics and Astronomy

The University of Utah

May 2017

The University of Utah Graduate School

STATEMENT OF DISSERTATION APPROVAL

The dissertation of **Yue Zhang**

has been approved by the following supervisory committee members:

Mikhail Raikh	, Chair	**Nov 18 2016**
		Date Approved
Sarah Li	, Member	**Nov 18 2016**
		Date Approved
Dmytro Pesin	, Member	**Nov 18 2016**
		Date Approved
Brian Saam	, Member	**Nov 18 2016**
		Date Approved
Ashutosh Tiwari	, Member	**Nov 18 2016**
		Date Approved

and by **Benjamin Bromley**, Chair/Dean of the Department/College/School of **Physics and Astronomy**

and by David B. Kieda, Dean of The Graduate School.

ABSTRACT

The main physical reason why spintronics is promising for applications is that the lifetime of a carrier spin is much longer than the energy relaxation time. In other words, while orbital motion of a carrier at high temperature is completely incoherent, the carrier spin still "remembers" its initial direction. Due to this long lifetime, the response of the spin polarization to external fields, namely, dc-field, ac-drive, and random hyperfine field, can be studied experimentally even at room temperature. Theoretically, the spin dynamics in external fields is quite nontrivial. We studied the following delicate manifestations of this dynamics, all related to experiments:

(i) Evolution of the spin noise spectrum with ac drive.

(ii) Spin-dependent resonant tunneling between normal and ferromagnetic electrodes.

(iii) Spin pumping from a ferromagnet into a hopping insulator.

(iv) The shape of the Hanle curves in transition metal dichalcogenides, possessing strong built-in spin-orbit fields.

(v) Hyperfine-field induced spin dephasing for localized carriers with heavy-tailed Levy distribution of hopping times.

Another peculiar aspect of the spin degree of freedom is that spin-orbit coupling can affect the motion of the spin fluxes (spin Hall effect) or even create spin-polarized edge states (quantum spin Hall effect). Both phenomena were observed experimentally. We studied the following aspects of these phenomena:

(i) Effective spin Hall properties of a medium with strongly inhomogeneous spin-orbit coupling.

(ii) Quantum spin Hall effect in the presence of magnetic dopants which eliminate one of the two counter-propagating edge states (quantum anomalous Hall effect).

CONTENTS

ACKNOWLEDGEMENTS

This thesis would not be possible without the support of many people. Firstly, I would like to thank my advisor, Dr. Mikhail Raikh, without whose tireless efforts and sage advice on all matters the present work would not exist. Secondly, I would like to acknowledge the MRSEC, who through the grant MRSEC DMR-1121252 funded the research. I would also like to thank all of the members of my supervisory committee for fruitful discussions about different research topics, for the time invested into committee meetings, as well as studying my thesis.

CHAPTER 1

INTRODUCTION

The present thesis reports on theoretical studies of various aspects of spin dynamics and spin transport in low-conducting and and insulating materials. It consists of nine chapters. Each of the chapters is experimentally motivated. Experimental motivations are briefly outlined below.

1.1 Part I: Spin dynamics

The motivation for Chapter 2 was the recent report [1] on the observation and detailed study of the spin noise in the system of self-assembled GaAs quantum dots. The origin of spin noise are the equilibrium fluctuations of the local spin density as a result of random motion of spins. The characteristic time of this motion is the spin relaxation time, τ_s. Fluctuations of spin density give rise to the fluctuating nondiagonal term in the dielectric tersor, this non-diagonal term will, in turn, cause random Faraday rotations of the polarization of light incident on the sample. The spin-noise spectrum was measured in Ref. [1] and in subsequent publications using the Faraday-rotation technique. This spectrum reflects the dynamics of the carrier spins confined in the dots. These dynamics are, naturally, sensitive to the magnetic field acting in the spin. In the absence of external field, the carrier spin precesses in the field created by neighboring nuclei, as illustrated in Fig. 1.1. In the presence of an external magnetic field, the spectrum acquires a new peak at around the Larmour frequency; see Figure 1.2. It is seen that the spectrum is quite broad. The origin of the broadening is the distribution of the hyperfine fields over the dots. At the core of the research reported in Chapter 2 is the suggestion that a deeper insight into the actual spin dynamics can be obtained if, in addition to the external magnetic field, an external ac drive is applied. Obviously, this drive has a dramatic effect on the spin dynamics when its frequency, Ω_{dr}, is close to the Larmour frequency. We demonstrate that the effect of the drive on the spin-noise spectrum is more delicate, namely, that the additional peaks in the spectrum, caused by the drive, remain sharp even when ω_{dr} is much smaller than the typical hyperfine field. The reason is that the drive affects only the spins for which the

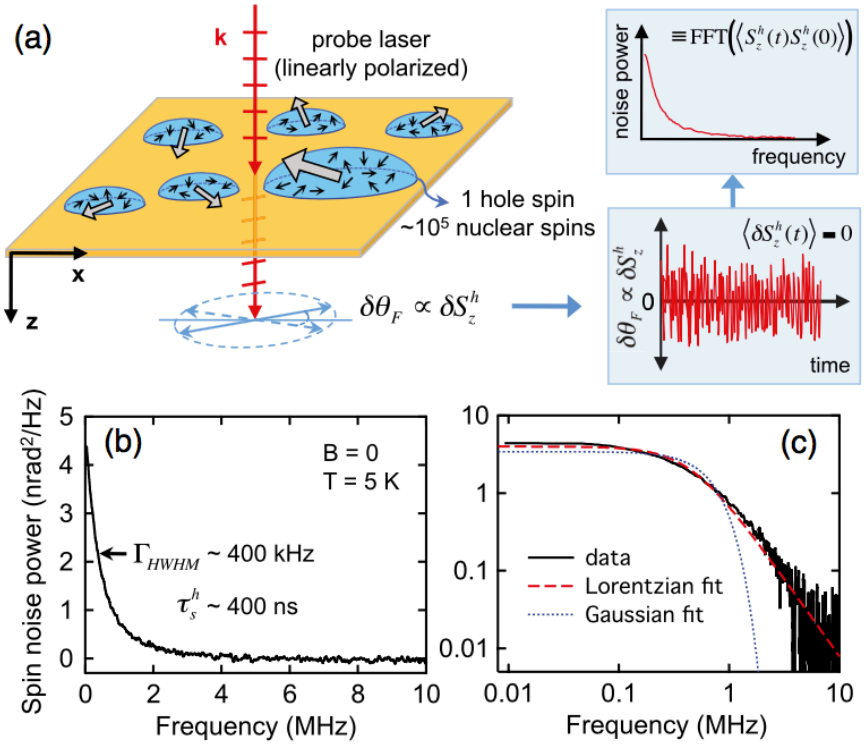

Figure 1.1: (color online). Experiment of spin noise. (a) Experimental schematic: The random spin fluctuations $\delta S_z^h(t)$ of resident holes in (In,Ga)As/GaAs QDs impart Faraday rotation fluctuations $\delta\theta_F(t)$ on a linearly polarized probe laser. The power spectral density of this "spin noise" is measured with a balanced photodiode bridge and digital spectrum analyzer. (b) Typical spin noise power spectrum of the resident holes at low temperature (5 K) and zero applied magnetic field ($B = 0$). The 400 kHz half-width of the spin noise indicates a long 400 ns correlation time half-width of the hole spins. (c) The same spectrum on a log-log scale. The noise line shape closely follows a Lorentzian, indicating exponentially decaying hole spin correlations at $B = 0$, in contrast with recent theories (adapted from Ref. [1]).

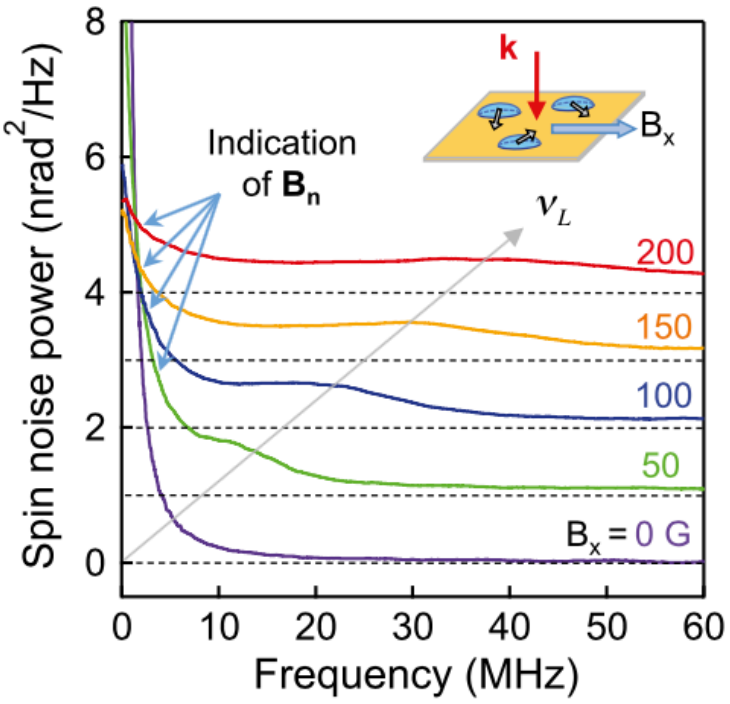

Figure 1.2: (color online). Hole spin noise in purely transverse applied magnetic fields (B_x). In addition to the expected shift of the hole spin noise to the hole Larmor frequency ($\nu = g_\perp^h \mu_B B_x/h$, with $g_\perp^h \sim 0.15$), there remains a finite noise component at zero frequency. This reveals the presence of the longitudinal (**z**) components of the nuclear Overhauser magnetic field, $\mathbf{B_n}$. Longitudinal fields, real or effective, necessarily result in spin noise at zero frequency. The integrated noise power remains constant (adapted from Ref. [1]).

local Larmour frequency is close to the drive frequency. The shape of the low-frequency "Rabi"-peak in $\langle \delta s_\omega^2 \rangle$ is universal with both, the position and the width, being of the order of ω_{dr}. When the drive amplitude exceeds the width of the hyperfine field distribution, the noise spectrum transforms into a set of sharp peaks centered at harmonics of the drive frequency.

For a carrier localized in a dot, the hyperfine field can be considered as static. This is because the Larmour frequency for a nucleus is much smaller than for an electron or for a hole. In Chapter 3 we study the spin dynamics of a carrier in hyperfine field changing rapidly with time. This situation is pertinent, e.g., to organic spin valves [2], see Fig. 1.3, where the carriers move between two magnetized electrodes by hopping over sites. Hyperfine fields on the sites are random and uncorrelated. Thus, in the course of motion, the carrier spin"sees" the rapidly changing magnetic field. This leads to randomizing of the initial spin direction, i.e., to spin relaxation. The rate of this relaxation is expressed via the r.m.s. field and the residence time on the site by the celebrated Dyakonov-Perel expression [3] . The Dyakonov-Perel mechanism of spin relaxation is fully analogous to the more general mechanism of the spectral narrowing [4]. However, this expression implies that all the residence times are of the same order. For hops over the localized states the residence times are very widely spread. In Chapter 3 we generalize the theory of the spin relaxation to account for this wide spread. Namely, we consider the situation when, due to disorder in the site positions and energies, the on-site residence times, τ, are spread according to the Lévy distribution. The power-law tail $\propto \tau^{-1-\alpha}$ in the distribution of τ does not affect the conventional spectral narrowing for $\alpha > 2$, but leads to a dramatic acceleration of the free induction decay in the domain $2 > \alpha > 1$. The next abrupt acceleration of the decay takes place as α becomes smaller than 1. In the latter domain the decay does not follow a simple-exponent law. To capture the behavior of the average spin in this domain, we solve the evolution equation for the average spin using the approach different from the conventional approach based on the Laplace transform. Unlike the free induction decay, the tail in the distribution of the residence times leads to the slow decay of the spin echo. The echo is dominated by realizations of the carrier motion for which the number of sites visited by the carrier is minimal.

1.2 Part II: Spin transport

The experimental motivation for Chapter 4 was experimental demonstration of spin pumping from a microwave-driven ferromagnet into an organic semiconductor in Ref. [5];

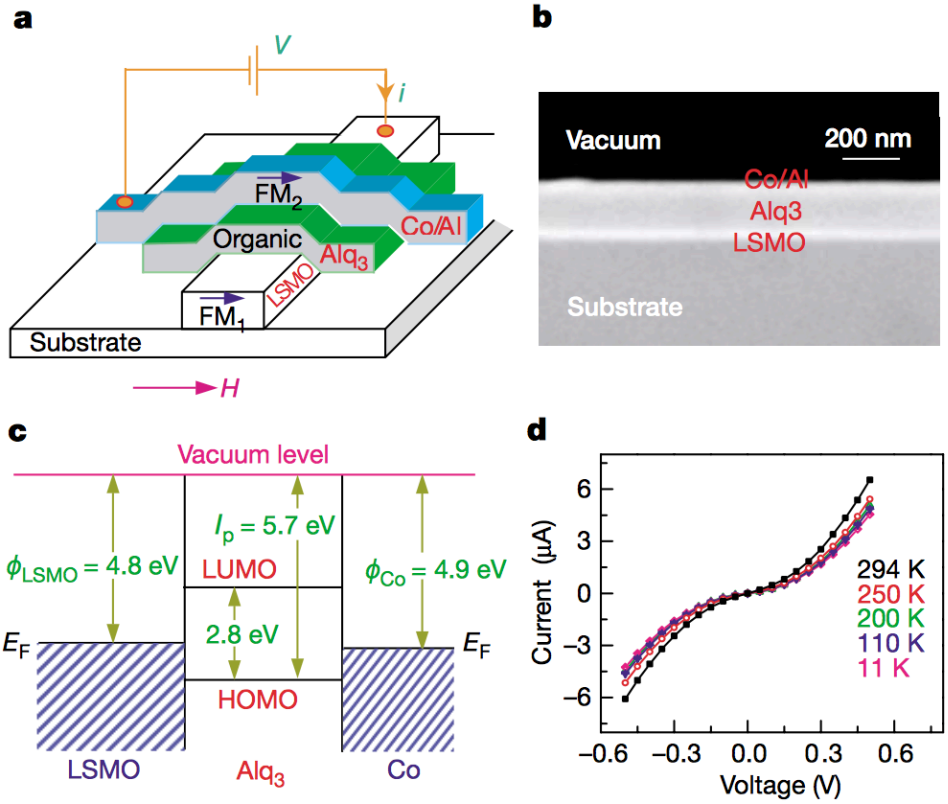

Figure 1.3: The structure and transport properties of the fabricated organic spin-valve devices. **a**, Schematic representation of a typical device that consists of two FM electrodes (FM_1 and FM_2) and an OSE spacer. Spin-polarized electrical current I flows from FM_1 (LSMO), through the OSE spacer (Alq_3), to FM_2 (Co) when a positive bias V is applied. An in-plane magnetic field, H, is swept to switch the magnetization directions of the two FM electrodes separately. **b**, Scanning electron micrograph of a functional organic spin-valve consisting of a 60-monolayer-thick LSMO film, a 160-nm-thick Alq_3 spacer, a 3.5-nm-thick Co electrode and a 35-nm-thick Al electrode. **c**, Schematic band diagram of the OSE device in the rigid band approximation showing the Fermi levels and the work functions of the two FM electrodes, LSMO and Co, respectively, and the HOMO–LUMO levels of Alq_3. **d**, $I - V$ response of the organic spin-valve device with $d = 200$ nm at several temperatures (adapted from Ref. [2]).

see Fig. 1.4. In all previous spin-pumping experiments the spin current was injected into nonmagnetic metallic materials with *free* electrons. By contrast, in organic semiconductors the carriers are localized on the sites, and the transport of charge is due to hopping. The objective of the research was to identify the mechanism of generation and propagation of spin current in a hopping insulator. We found that, unlike metals, the spin polarization at the boundary with a ferromagnet is created as a result of magnon absorption within pairs of localized states and it spreads following the current-currying resistor network (although the charge current is absent). We consider a classic resonant mechanism of the ac absorption in insulators and adapt it to the absorption of magnons. A strong enhancement of pumping efficiency is predicted when the Zeeman splitting of the localized states in an external magnetic field is equal to the frequency of ferromagnetic resonance. Under this condition the absorption of a magnon takes place within *individual* sites.

Chapter 5 was also motivated by Ref. [5] by the Cambridge group and subsequent papers [6, 7] by the Utah group. It turns out that spin current can be not only pumped into an organic semiconductor, but it induces the voltage difference between the sample edges across the spin current, the so-called Inverse Spin Hall Effect (ISHE); see Fig. 1.4. There experimental results pose two puzzles. Firstly, the spin-orbit coupling responsible for ISHE is known to be very weak in organic materials. Secondly, the ISHE is the result of spin-dependent scattering of *free* carriers, while in organic materials with localized carriers the momentum is not a good quantum number.

With regard to the first puzzle, it was demonstrated in Ref. [6] that the spin-orbit coupling is introduced into organic material by implanting Pt atoms into the carbon chains. The optical manifestation of such an implantation is illustrated in Fig. 1.5. Concerning the second puzzle, we have resorted to a cartoon-like model, and assumed that Pt atoms form granules. Then the polymer with Pt is modeled by a normal layer without spin-orbit coupling and the granules with strong spin-orbit coupling dissolved in it. We have studied the effective spin Hall properties of such a composite. In particular, we calculated the effective spin Hall angle and the effective spin diffusion length. Our main qualitative finding is that, when the bare spin diffusion length is much smaller than the radius of the grain, the *effective* spin diffusion length is strongly enhanced, well beyond the "geometrical" factor. The physical origin of this additional enhancement is that, with a small diffusion length, the spin current mostly flows *around the grain* without suffering much loss. We also demonstrate that the voltage created by a spin current is sensitive to a very weak magnetic field directed along the spin current, and even reverses sign in a certain domain of fields. The origin of

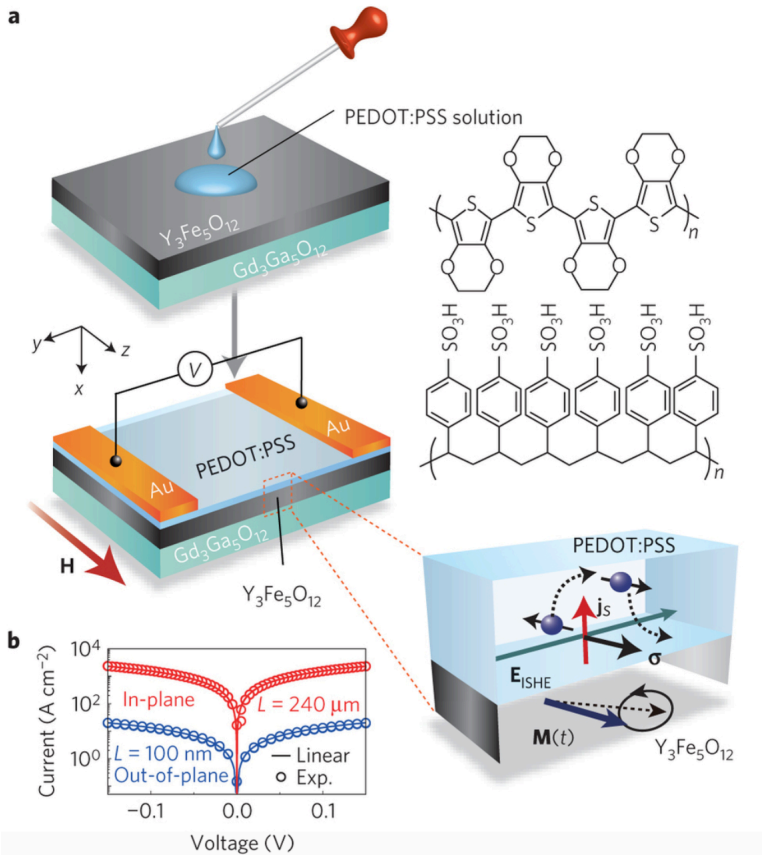

Figure 1.4: Spin–charge conversion in organic material. **a**, Schematic illustrations of the PEDOT:PSS/$Y_3Fe_5O_12$ film. The PEDOT:PSS film was spin-coated onto a $Y_3Fe_5O_12$ film. **H** and **M**(t) denote the external magnetic field and dynamical magnetization, respectively. $\mathbf{E}_{ISHE}$, $\mathbf{j}_s$ and σ denote the electric field due to the spin–charge conversion, the flow direction of the spin current, and the spin-polarization vector of the spin current, respectively. **b**, Current–voltage characteristics for the PEDOT:PSS film, where the blue and red circles are the experimental data measured along the x and y directions, respectively. L is the distance between the voltage probes (adapted from Ref. [5]).

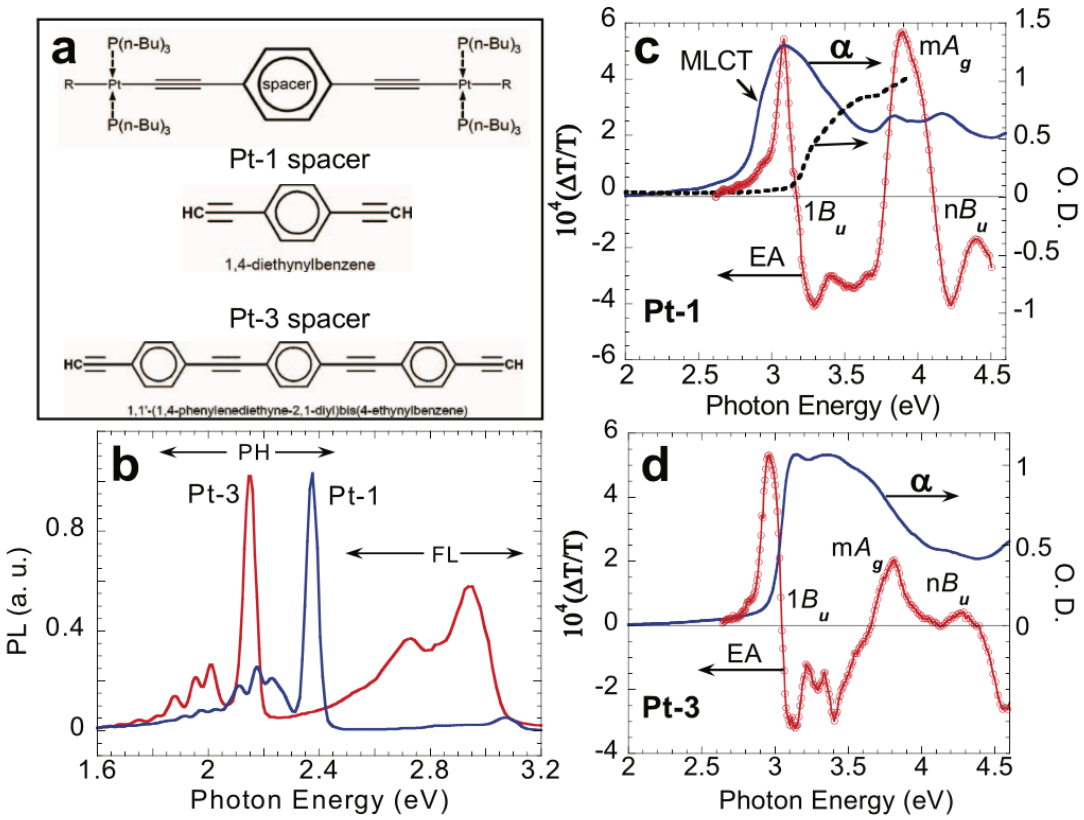

Figure 1.5: Linear and NLO measurements of the Pt-polymers. (a), Chemical structures of the two Pt-polymers, where the "spacer" in Pt-1 has a single phenyl ring, whereas that of Pt-3 has three phenyl rings. (b), Normalized photoluminescence emission spectrum of Pt-1 (blue) and Pt-3 (red) films. FL (PH) stands for fluorescence (phosphorescence) emission. (c) and (d), Electroabsorption (EA) spectra of Pt-1 (c) and Pt-3 (d) films, compared to their respective absorption (a) spectrum. The absorption of a non-Pt polymer film is also shown (broken line) in (c). The three excited "essential states" $1B_u$, mA_g, and nB_u, as well as the novel state, Metal-to-Ligand Charge Transfer (MLCT) are assigned (adapted from Ref. [6]).

this sensitivity is that the spin precession, caused by the magnetic field, takes place outside the grains where SO is absent.

The experimental motivation for Chapter 6 was the phenomenon of three-terminal spin transport reported by many groups. The experimental setup is illustrated in Fig. 1.6. Unlike the conventional four-terminal spin-transport experiments, where the injector and detector circuits are separated in space, in three-terminal setup they are combined. Then the question arises: what physical process is responsible for the generation of the three-terminal Hanle voltage V upon passage of the current I, Fig. 1.6. There are experimental indications that V does *not* reflect the conventional spin diffusion as in four-terminal setup: the width of $V(B)$ curve, where B is the external field, was the same for very different materials and this width did not depend on tempertature. This led the authors of Ref. [8] to the idea that the three-terminal spin transport is based on the resonant tunneling of electrons between ferromagnetic and normal electrodes via an impurity. The sensitivity of current to a weak external magnetic field stems from a spin blockade, which, in turn, is enabled by strong on-site repulsion. In Chapter 6 we demonstrate that this sensitivity exists even in the absence of repulsion when a single-particle description applies. Within this description, we calculate exactly the resonant-tunneling current between the electrodes. The mechanism of magnetoresistance, completely different from spin blocking, has its origin in the interference of virtual tunneling amplitudes. Spin imbalance in a ferromagnetic electrode is responsible for this interference and the resulting coupling of the Zeeman levels. This coupling also affects the current in the correlated regime.

The motivation for the research reported in Chapter 7 was a recent discovery of new materials: transition metal dichalcogenides (TMDs). A most prominent example of TMD is MoS_2. With regard to atomic structure, these materials are similar to graphene and appear in the form of one or several monolayers. However, the electron spectrum in these materials is dramatically different from graphene. The most important difference is that, unlike graphene, TMDs possess a sizable bandgap, which makes them attractive for the practical applications. The other prominent difference is that K and K' valleys in the spectrum are not identical. This inequivalence gives rise to the splitting of the spectrum. The splitting manifests itself in the presence of two exciton peaks in the optical absorption and the Kerr rotation spectra; see Fig. 1.7. In general, the bulk of experimental studies of TMDs is carried out by optical means. Ultimately, in Chapter 7 we studied how the peculiar electron spectrum of TMDs manifests itself in the spin transport. This spin transport appears to be very different from the conventional spin transport in semiconductors for the following

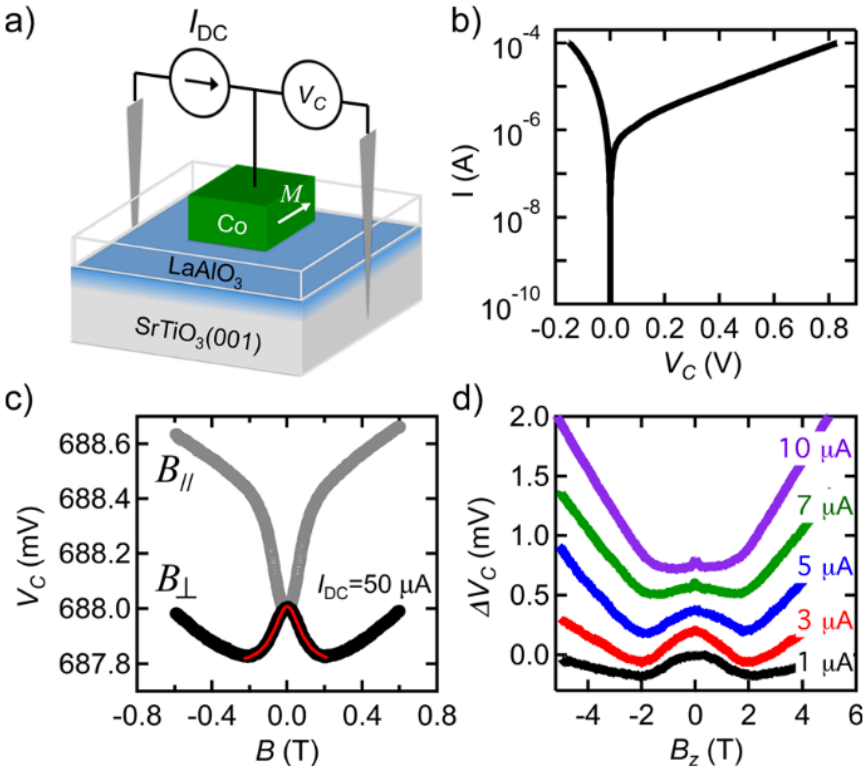

Figure 1.6: Three-terminal Hanle experiment. (a) Schematic of a $Co/LaAlO_3/SrTiO_3$ junction in a three-terminal geometry. (b) Three-terminal $I-V$ curve measured at $T = 10$ K. (c) Field dependence of the contact voltage, V_C, due to the application of an out-of-plane ($B_\perp$) applied field (black) at $T = 10$ K. Red line is a Lorentzian fit. The corresponding field dependence of V_C observed when the magnetic field is applied in-plane (grey), parallel to the magnetization of the Co electrode ($B_{//}$). (d) Relative change, $\Delta V_C = V_C(B_z) - V_C(0)$, for $Co/LaAlO_3/SrTiO_3$ as a function of B_z between ± 5 T measured for several bias states at $T = 10$ K. Measured at $I_{DC} = 1\mu A$ (black, $V_C(0) = 67$ mV), $3\mu A$ (red, $V_C(0) = 192$ mV), $5\mu A$ (blue, $V_C(0) = 274$ mV), $7\mu A$ (green, $V_C(0) = 334$ mV), and $10\mu A$ (purple, $V_C(0) = 400$ mV) (adapted from Ref. [9]).

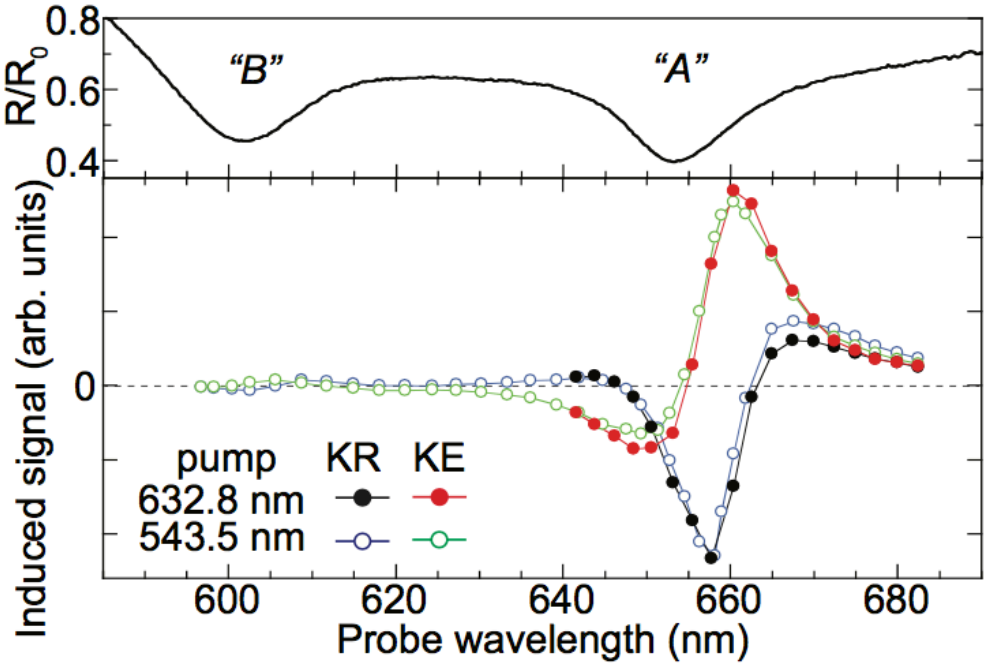

Figure 1.7: Spectral dependence of the optically induced Kerr rotation/ellipticity signals in monolayer MoS_2. The upper (black) trace shows the normalized reflectance spectrum R/R_0 from a MoS_2 crystal at 5 K. "A" and "B" exciton features are clear. The lower traces show the optically induced KR and KE signals as a function of the probe laser wavelength at $B_y = 0$. A strong resonance at the "A" exciton is observed. Results using two different pump laser wavelengths are shown (632.8 nm and 543.5 nm) (adapted from Ref. [10]).

reason.

Valley asymmetry of the spectrum in TMDs originates from the spin-orbit coupling. Presence of spin-orbit fields of opposite signs for electrons in K and K' valleys in combination with possibility of intervalley scattering result in a nontrivial spin dynamics. This dynamics is reflected in the dependence of nonlocal resistance on external magnetic field (the Hanle curve). We calculate theoretically the Hanle shape in TMDs. It appears that, unlike conventional materials without valley asymmetry, the Hanle shape in TMDs is different for normal and parallel orientations of the external field. For normal orientation, it has two peaks for slow intervalley scattering, while, for fast intervalley scattering the shape is usual. For parallel orientation, the Hanle curve exhibits a cusp at zero field. This cusp is a signature of a slow-decaying valley-asymmetric mode of the spin dynamics.

1.3 Part III: Quantum anomalous Hall effect

The last part of the thesis, Chapters 8 and 9, does not deal with spin physics, but rather with *pseudospin* physics, although the spin degree of freedom plays an important role in revealing this physics. Topological insulators, like Bi_2Te_3, discovered experimentally approximately a decade ago represent semiconductors with spin-degenerate Dirac spectrum. This Dirac spectrum emerges from a Hamiltonian $\hat{h}(\mathbf{k}) = A(k_x\sigma_x + k_y\sigma_y) + M\sigma_z$, where M denotes the gap, while σ_x, σ_y, σ_z are the Pauli matrices acting in the pseudospin (electron-heavy hole) subspace. The exciting property of the topological insulators is that their boundaries can support chiral edge modes. The states with spin $\uparrow$ propagate in one direction, while the states with spin $\downarrow$ propagate in the opposite direction. Each of the edge modes is similar to the edge state in the quantum Hall effect. However, the fact that they exist in pairs complicates the experimental observation of the Hall quantization. Very recently this complication has been overcome experimentally by doping the topological insulators with magnetic atoms Cr or V. At large enough concentration of the dopants they align their spin, lifting the degeneracy of the edge modes. Another important consequence of magnetic doping is that, at proper concentration of the dopants, the gap for one of the spin projections can be very small and even pass through zero. This passage through zero leads to the disappearance of the edge mode, which is closely analogous to the quantum Hall transition. With only one edge mode at the Fermi level, the quantization of the components of the resistivity tensor was readily observed, see Fig. 1.8, upon applying a small magnetic field which controls the degree of the spin alignment of the dopants. Resistance jumps accompanying the ferromagnetic transition in the system of dopants go

under the name quantum anomalous Hall (QAH) effect. Most recent experiments revealed that the quantized anomalous Hall resistance reflects the complex dynamics of the spins of the dopants, exhibiting jumps whenever the domains reorient; see Fig. 1.9.

The focus of the research in Chapter 8 was the effect of the confinement on the edge modes. It is shown that, unlike the conventional quantum Hall effect where all edge states are chiral, in QAH effect, the soft boundary leads to nonchiral edge modes which are present on both sides of the ferromagnetic transition. Wave functions of nonchiral modes are different above and below the transition: on the "topological" side, where the chiral edge mode is supported, nonchiral modes are much less localized than on the "trivial" side. Thus, the disorder-induced scattering into these states extends the localization length of the chiral edge mode. The prime experimental manifestation of nonchiral modes is that, by contributing to longitudinal resistance, they smear the resistance quantization at QAH transition.

The research reported in Chapter 9 is focused on the specifics of QAH effect in realistic samples, where portion x of magnetic dopants fluctuates in space. These fluctuations smear the QAH transition by creating the in-gap states. Specifically, we find the density of in-gap states, $N(E)$, emerging as a result of statistic fluctuations of the composition, x, in the vicinity of the transition point, where the *average* gap, $\overline{E}_g$, passes through zero. Local gap follows the fluctuations of x. Using the instanton approach, we show that, near the gap edges, the tails are exponential, $\ln N(E) \propto -\left(\overline{E}_g - |E|\right)$, and the tail states are due to small gap reduction. Our main finding is that, even when the smearing magnitude exceeds the gap-width, there exists are semihard gap around zero energy, where $\ln N(E) \propto -\frac{\overline{E}_g}{|E|} \ln\left(\frac{\overline{E}_g}{|E|}\right)$. The states responsible for $N(E)$ originate from local gap reversals within narrow rings. The consequence of semihard gap is the Arrhenius, rather than variable-range hopping, temperature dependence of the diagonal conductivity at low temperatures.

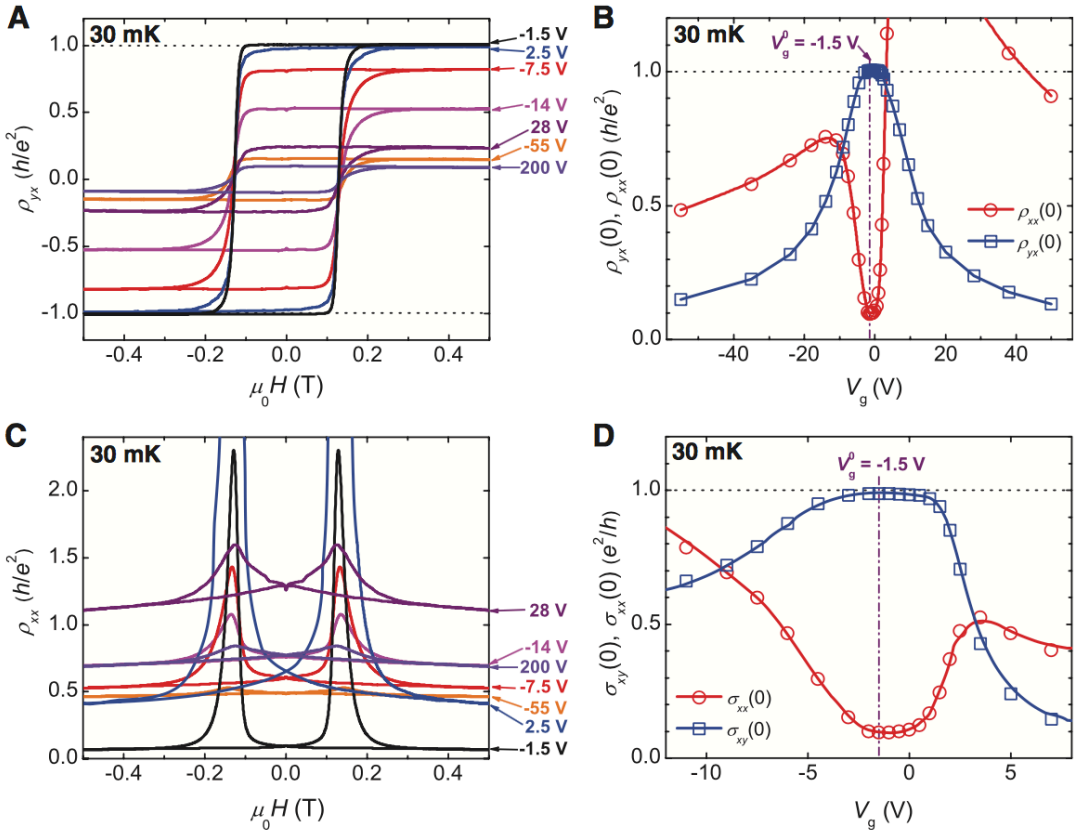

Figure 1.8: The QAH effect measured at 30 mK. (**A**) Magnetic field dependence of ρ_{yx} at different $V_g s$. (**B**) Dependence of $\rho_{yx}(0)$ (empty blue squares) and $\rho_{xx}(0)$ (empty red circles) on V_g. (**C**) Magnetic field dependence of ρ_{xx} at different $V_g s$. (**D**) Dependence of $\sigma_{xy}(0)$ (empty blue squares) and $\sigma_{xx}(0)$ (empty red circles) on V_g. The vertical purple dashed-dotted lines in (B) and (D) indicate the V_g for V_g^0. A complete set of the data is shown in fig. S3 (adapted from Ref. [11]).

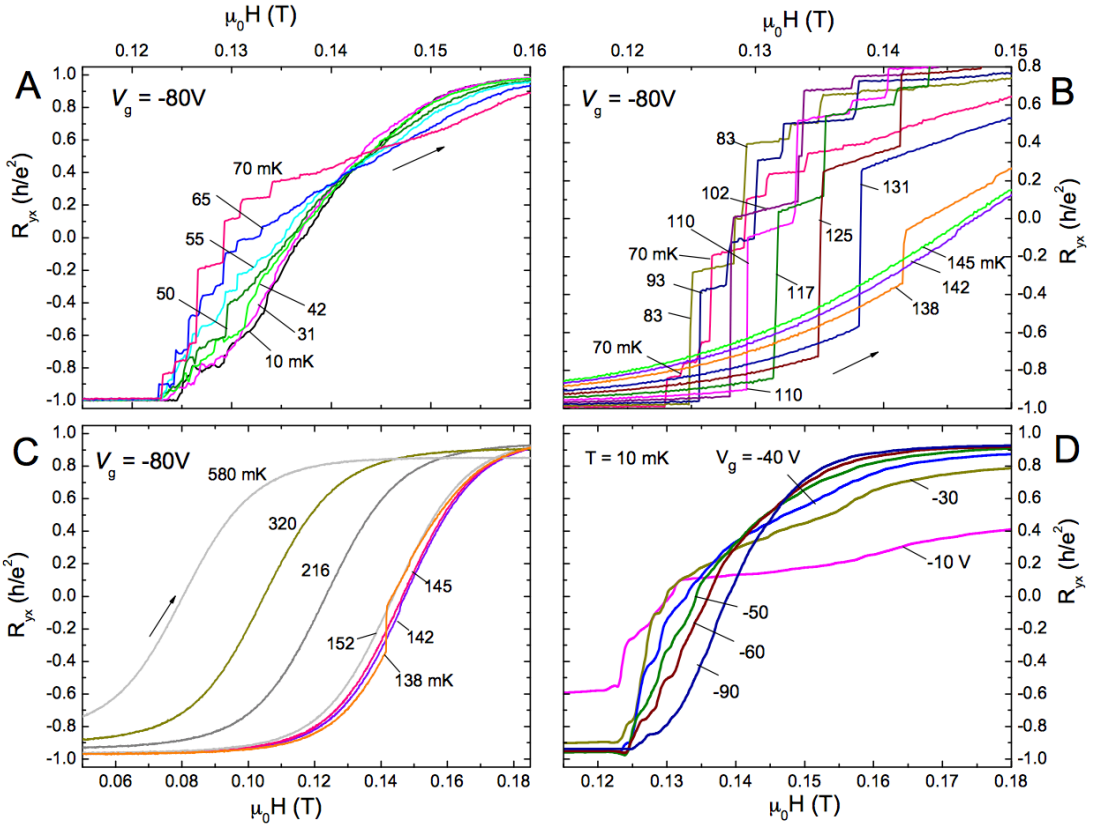

Figure 1.9: Jumps in R_{yx} at the transition between Chern states. Panel (A) shows traces of R_{yx} at selected T ($10 \rightarrow 70$ mK) as H is slowly swept (10 mT/min) past H_c as indicated by the arrows. The transition between Chern states $C = \pm 1$ is nominally smooth below 40 mK. Starting near T_1 65 mK, small vertical jumps appear near the start of the transition. Panel (B) shows R_{yx} vs. H in the important interval 70 mK$\leq T \leq$ 145 mK in which large jumps are clustered. Starting at 83 mK, the system "escapes" the $C = -1$ state by a very large initial jump, followed by a cascade of smaller ones. Focussing on the initial jump, we see that field $H_J(T)$ that triggers the jump (kink feature) increases steadily as T rises to 142 mK. Above 131 mK, the jump magnitude ΔR_{yx} sharply decreases, becoming unresolved above T_2 145 mK. Panel (C) shows that, from T_2 to 580 mK, R_{yx} changes smoothly over the (now broadened) transition. Panel (D) shows how the R_{yx} curves change with V_g at 10 mK. At optimal gating ($V_g = -90$ V), the transition is smooth, but as V_g is increased to -10 V, the jumps reappear, implying that a small amount of dissipation is necessary to seed the jump at the lowest T. The experimental time constants are 1s in all panels except D, where it is 5 s (see Supplement). (adapted from Ref. [12]).

1.4 References

[1] Y. Li, N. Sinitsyn, D. L. Smith, D. Reuter, A. D. Wieck, D. R. Yakovlev, M. Bayer, and S. A. Crooker, Phys. Rev. Lett. **108**, 186603 (2012).

[2] Z. H. Xiong, D. Wu, Z. V. Vardeny, and J. Shi, Nature (London) **427**, 821 (2004).

[3] M. I. Dyakonov and V. I. Perel, Sov. Phys. Solid State **13**, 3023 (1971).

[4] P. W. Anderson and P. R. Weiss, Rev. Mod. Phys. **25**, 269 (1953).

[5] K. Ando, S. Watanabe, S. Mooser, E. Saitoh, and H. Sirringhaus, Nat. Mater. **12**, 622 (2013).

[6] C.-X. Sheng, S. Singh, A. Gambetta, T. Drori, M. Tong, S. Tretiak, and Z. V. Vardeny, Sci. Rep. **3**, 2653 (2013).

[7] D. Sun, K. J. v. Schooten, M. Kavand, H. Malissa, C. Zhang, M. Groesbeck, C. Boehme, and Z. V. Vardeny, Nat. Mater. **15**, 863 (2016).

[8] Y. Song and H. Dery, Phys. Rev. Lett. **113**, 047205 (2014)

[9] A. G. Swartz, S. Harashima, Y. Xie, D. Lu, B. Kim, C. Bell, Y. Hikita, and H. Y. Hwang, Appl. Phys. Lett. **105**, 032406 (2014)

[10] L. Yang, N. A. Sinitsyn, W. Chen, J. Yuan, J. Zhang, J. Lou, and S. A. Crooker, Nat. Phys. **11**, 830 (2015).

[11] C.-Z. Chang, J. Zhang, X. Feng, J. Shen, Z. Zhang, M. Guo, K. Li, Y. Ou, P. Wei, L.-L. Wang, Z.-Q. Ji, Y. Feng, S. Ji, X. Chen, J. Jia, X. Dai, Z. Fang, S.-C. Zhang, K. He, Y. Wang, L. Lu, X.-C. Ma, and Q.-K. Xue, Science **340**, 167 (2013).

[12] M. Liu, W. Wang, A. R. Richardella, A. Kandala, J. Li, A. Yazdani, N. Samarth, and N. P. Ong, arXiv:1603.02311.

PART I

SPIN DYNAMICS

CHAPTER 2

EVOLUTION OF THE INHOMOGENEOUSLY BROADENED SPIN NOISE SPECTRUM WITH AC DRIVE

2.1 Introduction

Common experimental techniques for the study of spin dynamics in semiconductors include the polarization of luminescence upon optical spin orientation [1] and the time-resolved Faraday rotation [2].

Within the first technique, developed more than four decades ago, a semiconductor is excited with a circular-polarized light, and the degree of circular polarization, $\mathcal{P}$ of luminescence is measured as a function of external magnetic field, Ω. This decay is described by a Lorentzian: $\mathcal{P}(\Omega) = \mathcal{P}(0)/(1+\Omega^2 T_2^2)$, where T_2 is the spin lifetime. Thus, the analysis of $\mathcal{P}(\Omega)$ dependence allows one to infer the value of T_2. Strong temperature dependence of T_2 observed was accounted for within the Dyakonov-Perel mechanism of spin relaxation [3].

The second technique was developed two decades later. It also involves a pulsed excitation, but the quantity measured is the Faraday rotation of the probe pulse as a function of delay, Δt, between the pump and the probe pulses. To the first approximation, this rotation is proportional to $\cos(\Omega\Delta t)\exp[-\Delta t/T_2]$, where the oscillations originate from the Larmour precession of electrons in course of their equilibration. Experimental results [2] shown in Figure 2.1 reveal the following peculiar features of the spin dynamics: (i) the frequency Ω depends strongly on the electron energy; (ii) the lifetime T_2 is a strong and nonmonotonic function of doping.

Recently, a third technique, spin noise spectroscopy, had been applied to bulk semiconductors [4-6] and various semiconductor structures [7-10], see the reviews [11] and [12] for comprehensive literature. Within the spin-noise technique, the dynamics of spins manifests itself via random modulation of the refraction indices for the left- and right-polarized light. This modulation results in a random rotation angle of the plane of polarization of the transmitted light. Power Fourier spectrum of these random rotations is proportional to the

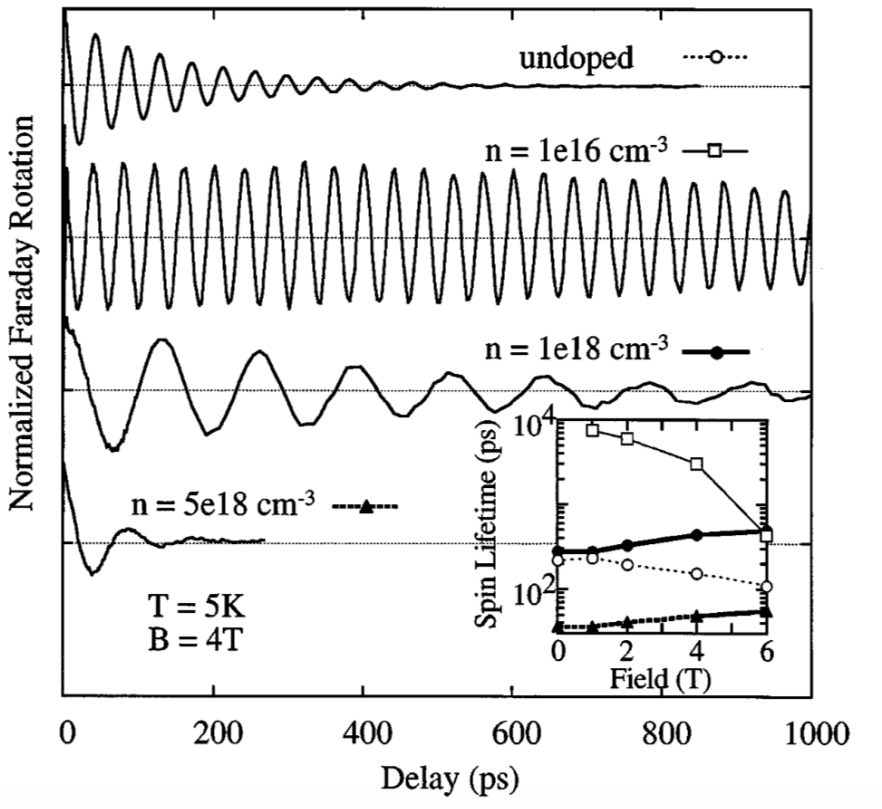

Figure 2.1: TRFR for undoped and n-type GaAs at B= 4T. Data are normalized just after zero pump-probe delay. Plots are offset for clarity, with zeros marked by dotted lines. The inset shows T_2^* vs field. Data are taken at $T = 5$K with $N_{ex} = 2 \times 10^{14}, 1.4 \times 10^{14}$, and 3×10^{14}cm^{-3} for $n = 0, 10^{16}, 10^{18}, and\ 5 \times 10^{18}$, respectively (adapted from Ref. [2]).

spectrum, δs_ω^2, of the spin fluctuations. A setup for a typical spin-noise experiment is shown in Figure 2.2. If the spin dynamics of electrons contains a frequency, Ω, the spectrum is peaked at this frequency. In the experiment, this peak is resolved by averaging δs_ω^2 over a long time interval, as illustrated in Figure 2.2. Application of spin-noise technique to an ensemble of self-assembled quantum dots allowed us to resolve such delicate characteristics of the spin dynamics as anisotropy of g-factor; see Figure 2.3.

Originally, the spin-noise measurements were conducted on atomic vapors [13, 14]. With regard to spin-noise, the principal difference between the vapors and semiconductors is that all spin-related frequencies in vapor are the same, while, in semiconductors, these frequencies are strongly different for different electrons. This is because, without external magnetic field, each electron spin precesses around its individual hyperfine field created by nuclei which are located within the extent of the electron wave function [15, 16]. Importantly, the observation of spin noise for localized electrons and holes, see, e.g., Refs. [6], [8]-[10], was possible even despite the strong inhomogeneous broadening. When the applied magnetic field is much smaller than the typical hyperfine field, the spin noise spectrum reflects the distribution of the hyperfine fields [17-20]. More precisely, the spectrum has the form [17]

$$\langle \delta s_\omega^2 \rangle = \frac{\pi}{6} \left\{ \Delta(\omega) + \int_0^\infty d\Omega_N F(\Omega_N) \Big[\Delta(\omega - \Omega_N) + \Delta(\omega + \Omega_N) \Big] \right\}, \tag{2.1}$$

where

$$\Delta(\omega) = \frac{\tau_s}{\pi(1 + \omega^2 \tau_s^2)} \tag{2.2}$$

is a Lorentzian and τ_s is the electron spin-relaxation time. The second term in Eq. (2.1) represents the average over the hyperfine fields, Ω_N, distributed as[21]

$$F(\Omega_N) = \frac{4}{\sqrt{\pi}\delta_e^3} \Omega_N^2 \exp\Big[-\frac{\Omega_N^2}{\delta_e^2} \Big]. \tag{2.3}$$

When the width, δ_e, of the distribution exceeds τ_s^{-1}, the second term becomes $\frac{\pi}{6}\left[F(\omega) + F(-\omega)\right]$, i.e., the shape of the noise spectrum reproduces the distribution of Ω_N. The first term in Eq. (2.1) represents a peak centered at $\omega = 0$. It originates from the fact that the spin component parallel to the hyperfine field does not precess.

Very recently [22], in the spin-noise experiment on a vapor of ^{41}K alkali atoms, it was found that the ac drive splits the noise spectrum into a Mollow triplet. This splitting can be interpreted as a result of modified spin dynamics in the presence of drive. In fact, such evolution of the noise spectrum is in accord with the theoretical study of Ref. [23] where the noise of a driven two-level system was considered. It was demonstrated[23] that

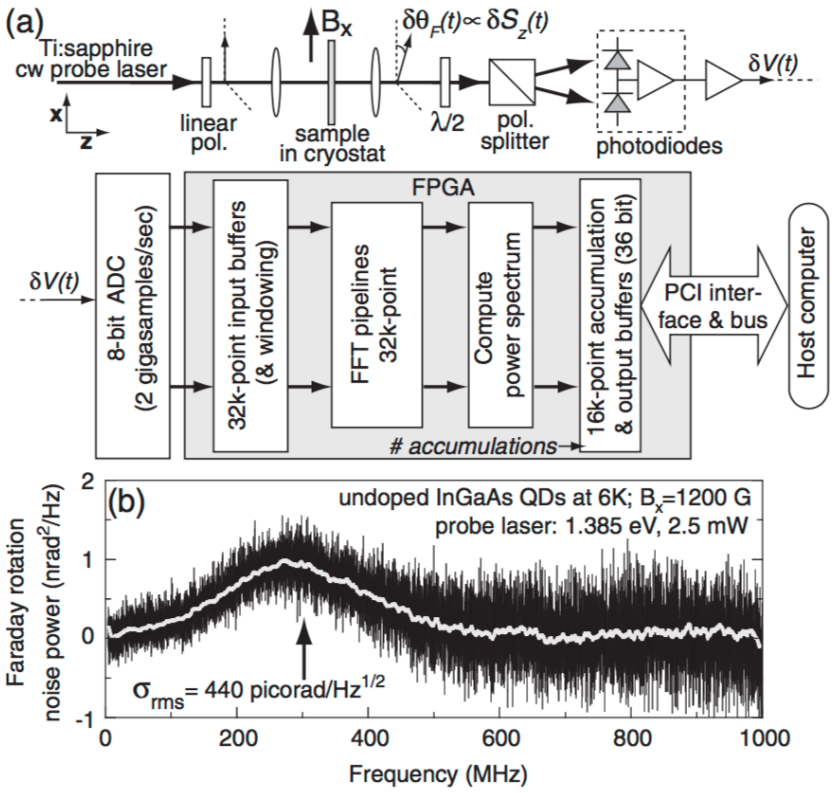

Figure 2.2: Experiment of spin noise. (a) Experimental schematic. Spin fluctuations $\delta S_z(t)$ impart Faraday rotation fluctuations $\delta\theta_F(t)$ on the probe laser. $\delta V(t)$ is digitized at $2GS/s$, and its power spectrum from $0-1$GHz is computed and averaged continuously on a FPGA. (b) A raw noise power spectrum showing hole spin noise in (In,Ga)As QDs after 600s averaging. The rms noise floor at 300MHz is 440 picorad/$\sqrt{Hz}$, which can be further reduced by smoothing (grey line) (adapted from Ref. [7]).

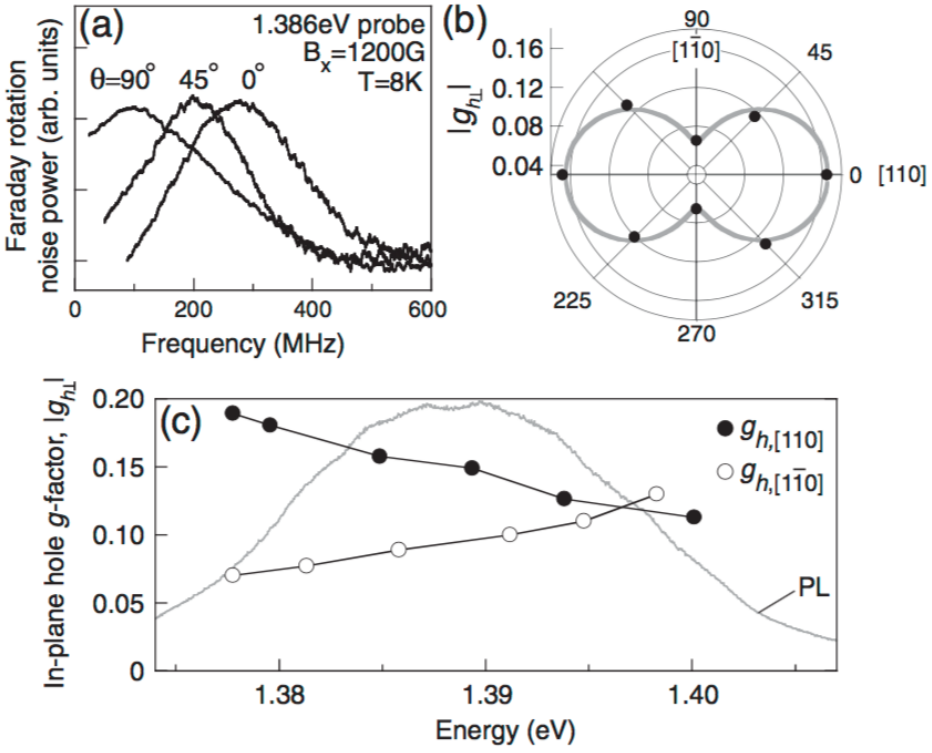

Figure 2.3: Measuring spin noise using Faraday rotation. (a) Hole spin noise with [110] axis rotated 0° , 45° , and 90° from B_x. (b) In-plane anisotropy of $g_{h\perp}$ at 1.386eV. (c) Energy-dependent anisotropy of $g_{h\perp}$ (adapted from Ref. [7]).

the drive-induced additional harmonics in the dynamics of the two-level system manifest themselves as additional peaks in the noise spectrum.

With regard to semiconductors, there is a question: what happens to the spin noise spectrum in the presence of drive when the local hyperfine fields are widely distributed? Since the positions of the drive-related peaks depend on the local value of Ω_N, it might be expected that they average out. Below we demonstrate that this is not the case. It appears that the drive-related peaks remain sharp after averaging. The reason is that the major contribution to the averaged peaks comes from the realizations of the hyperfine field for which Ω_N is close to the drive frequency, Ω_{dr}. More precisely, the domain of Ω_N contributing to $\langle \delta s_\omega^2 \rangle$ is $|\Omega_N - \Omega_{dr}| \sim \omega_{dr}$, where ω_{dr} is the drive amplitude.

If the frequency Ω_{dr} exceeds δ_e there are no realizations of the hyperfine field in resonance with drive. In this case the drive has a strong effect on the noise spectrum when the amplitude ω_{dr} becomes comparable to Ω_{dr}. We will see that $\langle \delta s_\omega^2 \rangle$ transforms into a sequence of peaks at $\omega_n = n\Omega_{dr}$. The magnitudes of the peaks behave essentially as $J_n^2(\omega_{dr}/\Omega_{dr})$, where $J_n(x)$ is the Bessel function of the order n.

2.2 General expression for the noise spectrum with drive

In the absence of spin relaxation and drive, the spin dynamics is governed by the equation $\frac{d\mathbf{S}}{dt} = \mathbf{\Omega}_N \times \mathbf{S}$, which yields three modes:

$$\begin{pmatrix} S_+ \\ S_z \\ S_- \end{pmatrix} = A_+ \begin{pmatrix} e^{i\Omega_N t} \\ 0 \\ 0 \end{pmatrix} + A_z \begin{pmatrix} 0 \\ 1 \\ 0 \end{pmatrix} + A_- \begin{pmatrix} 0 \\ 0 \\ e^{-i\Omega_N t} \end{pmatrix}, \tag{2.4}$$

where $S_\pm = \frac{1}{\sqrt{2}}(S_x \pm iS_y)$. Here we assumed that the field $\mathbf{\Omega}_N$ is directed along the z-axis. Spin relaxation is incorporated into the right-hand side of the equation of motion via a term, $-\frac{\mathbf{S}}{\tau_s}$. As a result, the constants $A_\pm$ and A_z in Eq. (2.4) evolve with time simply as $\frac{dA_\pm}{dt} + \frac{A_\pm}{\tau_s} = 0$ and $\frac{dA_z}{dt} + \frac{A_z}{\tau_s} = 0$. The fact that the coefficients $A_\pm$ and A_z decay as a simple exponent is sufficient [17-20] to present the noise spectrum as

$$\delta s_{z\omega}^2 = \frac{\pi}{2}\Delta(\omega) \tag{2.5}$$

$$\delta s_{x\omega}^2 = \delta s_{y\omega}^2 = \frac{\pi}{4}\Big[\Delta(\omega - \Omega_N) + \Delta(\omega + \Omega_N)\Big]. \tag{2.6}$$

In the presence of the ac drive the equation describing the spin dynamics assumes the form

$$\frac{d\mathbf{S}}{dt} = \Big[\mathbf{\Omega}_N + 2\boldsymbol{\omega}_{dr}\cos\ (\Omega_{dr}t)\Big] \times \mathbf{S}, \tag{2.7}$$

where $2\boldsymbol{\omega}_{dr}$ and Ω_{dr} are the drive amplitude and frequency, respectively. We will still assume that the hyperfine field is directed along the z-axis. Then the component of drive, responsible for the spin precession, is $2\omega_{\perp dr}$, which is the projection of the driving field on the x-y plane. If the drive amplitude is much smaller than Ω_N, the rotating wave approximation applies. Then the solution of Eq. (2.7) is well known since the classical paper [24]. We will cast this solution in the form, which, in the limit $\omega_{dr} \to 0$, reduces to Eq. (2.4). Namely:

$$\begin{pmatrix} S_+ \\ S_z \\ S_- \end{pmatrix} = A_+ \begin{pmatrix} \alpha_+ e^{i(\Omega_{dr}-\omega_R^N)t} \\ \alpha_z e^{-i\omega_R^N t} \\ \alpha_- e^{-i(\Omega_{dr}+\omega_R^N)t} \end{pmatrix} + A_z \begin{pmatrix} \beta_+ e^{i\Omega_{dr}t} \\ \beta_z \\ \beta_- e^{-i\Omega_{dr}t} \end{pmatrix} + A_- \begin{pmatrix} \gamma_+ e^{i(\Omega_{dr}+\omega_R^N)t} \\ \gamma_z e^{i\omega_R^N t} \\ \gamma_- e^{-i(\Omega_{dr}-\omega_R^N)t} \end{pmatrix}, \tag{2.8}$$

where ω_R^N is the frequency of the Rabi oscillations defined as

$$\omega_R^N = \left[\omega_{\perp dr}^2 + (\Omega_{dr} - \Omega_N)^2\right]^{1/2}. \tag{2.9}$$

The relation between the coefficients for each mode of precession, say, between α_+, α_z, and α_-, follows from Eq. (2.7)

$$\alpha_+ = -\frac{\omega_{\perp dr}^2}{2\omega_R^N(\Omega_{dr} - \Omega_N - \omega_R^N)} \tag{2.10}$$

$$\alpha_z = \frac{\omega_{\perp dr}}{\sqrt{2}\omega_R^N} \tag{2.11}$$

$$\alpha_- = -\frac{\omega_{\perp dr}^2}{2\omega_R^N(\Omega_{dr} - \Omega_N + \omega_R^N)}. \tag{2.12}$$

The magnitudes of α_+, α_z, α_- are chosen in such a way that the corresponding eigenvector in Eq. (2.8) is normalized. It is easy to see that, as the drive decreases, α_+ approaches one, while α_z and α_- vanish. This applies for $\Omega_{dr} > \Omega_N$. For the opposite relation, α_+ vanishes upon decreasing drive, while α_- approaches one. In a similar way, for the remaining two eigenvectors we have

$$\beta_+ = \beta_- = \alpha_z \tag{2.13}$$

$$\beta_z = \frac{\Omega_{dr} - \Omega_N}{\omega_R^N} \tag{2.14}$$

$$\gamma_+ = \alpha_-, \quad \gamma_- = \alpha_+, \quad \gamma_z = \alpha_z. \tag{2.15}$$

In the presence of spin relaxation the coefficients $A_\pm$ and A_z in Eq. (2.8) satisfy the same equation as in the absence of drive. This allows us to establish the form of the noise spectrum, $\delta s_\omega^2 = \frac{1}{3}(\delta s_{\omega z}^2 + \delta s_{\omega +}^2 + \delta s_{\omega -}^2)$, of the driven system in the same way as Eq. (2.5) followed from Eq. (2.4). One has

$$\delta s_\omega^2 = \frac{\pi}{6}\Big\{\beta_z^2\Delta(\omega) + \gamma_z^2\Delta(\omega - \omega_R^N) + \alpha_z^2\Delta(\omega + \omega_R^N)$$

$$+\beta_+^2\Delta(\omega-\Omega_{dr})+\beta_-^2\Delta(\omega+\Omega_{dr})+$$
$$\gamma_+^2\Delta(\omega-\Omega_{dr}-\omega_R^N)+\alpha_-^2\Delta(\omega+\Omega_{dr}+\omega_R^N)+$$
$$\alpha_+^2\Delta(\omega-\Omega_{dr}+\omega_R^N)+\gamma_-^2\Delta(\omega+\Omega_{dr}-\omega_R^N)\Big\}. \quad (2.16)$$

It is a direct consequence of normalization of the eigenvectors in Eq. (2.8) that the area $\int d\omega\delta s_\omega^2$ does not depend on the drive. Four groups of terms corresponding to the four lines in Eq. (2.16) can be interpreted as follows. The low-frequency peak $\propto\Delta(\omega)$ in the presence of drive develops two satellites at $\omega=\pm\omega_{dr}$. From the relation $\beta_z^2+\gamma_z^2+\alpha_z^2=1$, which can be easily checked using Eqs. (2.10), (2.13), it follows that the noise power gets redistributed between the three peaks. The peak which, in the absence of drive, was located at $\omega=\Omega_N$ shifts to the position $\omega=\Omega_{dr}-\omega_R^N$. It also follows from Eq. (2.16) that this peak develops two satellites at higher frequencies $\omega=\Omega_{dr}$ and at $\omega=\Omega_{dr}+\omega_R^N$ with magnitudes β_+^2 and γ_+^2, respectively. Again, the net noise power in these three peaks does not depend on drive.

Suppose that the drive is weak, $\omega_{\perp dr}\ll\Omega_N$. For a typical realization of the hyperfine field the difference $\Omega_N-\Omega_{dr}$ is much bigger than $\omega_{\perp dr}$. Then the relative magnitude of the satellites of the zero-frequency peak is equal to $\omega_{\perp dr}^2/2(\Omega_N-\Omega_{dr})^2$. With regard to the peak at $\omega=\Omega_N$, its shift due to drive is small, namely, $\omega_{\perp dr}^2/2(\Omega_N-\Omega_{dr})$. The magnitudes of these satellites evolve differently with drive: while the satellite at $\omega=\Omega_{dr}$ grows as $\omega_{\perp dr}^2/2(\Omega_N-\Omega_{dr})^2$, the satellite at $\omega=\Omega_{dr}+\omega_R^N\approx 2\Omega_{dr}-\Omega_N$ has a much smaller relative magnitude $\sim\omega_{\perp dr}^4/16(\Omega_N-\Omega_{dr})^4$. A generic noise spectrum is illustrated in Fig. 2.4. Overall, the effect of drive on the noise spectrum for a *typical* Ω_N is weak. In addition, the positions of all satellites, except the peak at $\omega=\Omega_{dr}$, depend on Ω_N, i.e., these positions are random. It is not clear whether these satellites manifest themselves in the *ensemble-averaged* noise spectrum. As we will see in the next Section, the averaging preserves the drive-induced peaks in the noise spectrum. The reason is that the realizations of Ω_N, which survive the averaging, are the those in "resonance" with drive. For such realizations, with $|\Omega_N-\Omega_{dr}|\sim\omega_{\perp dr}$, the magnitudes of the satellites are anomalously big. This compensates for the small statistical weight of the resonant configurations.

2.3 Ensemble averaging

We will perform the averaging over hyperfine fields in two steps. Firstly, we will average over the magnitudes, Ω_N, with distribution function $F(\Omega_N)$. Then as a second step, we will average over directions of $\mathbf{\Omega}_N$ with respect to the driving field, $\boldsymbol{\omega}_{dr}$.

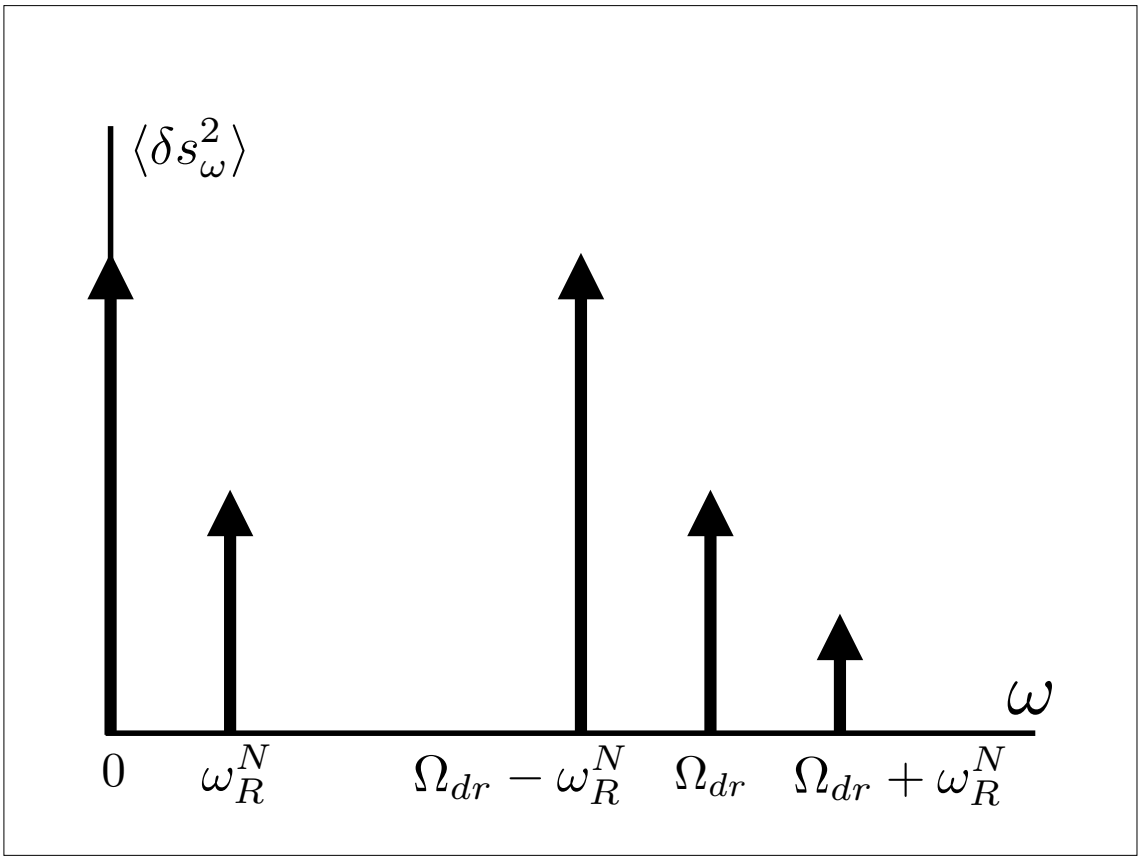

Figure 2.4: An illustration of the noise spectrum for a typical realization of the hyperfine field in the presence of the ac drive. Due to drive, a zero-frequency peak develops a satellite at $\omega = \omega_R^N$, Eq. (2.9). The peak which, in the absence of drive, was located at $\omega = \Omega_N$ shifts to $\omega = \Omega_{dr} - \omega_R^N$ and develops two satellites at driving frequency and at $\omega = \Omega_{dr} + \omega_R^N$. The magnitudes of the satellites scale with the drive amplitude as ω_{dr}^2 and ω_{dr}^4, respectively. Both satellites are located to the right from the main peak, which corresponds to driving frequency exceeding Ω_N.

2.3.1 Averaging over the magnitudes of hyperfine fields

Averaging of the first term in Eq. (2.16) is straightforward, since $\Delta(\omega)$ does not depend on Ω_N. Using the definition Eq. (2.13), we have

$$\frac{\pi}{6}\langle\beta_z^2\rangle\Delta(\omega) = \frac{\pi}{6}\Big[1 - \int_0^\infty d\Omega_N \frac{\omega_{\perp dr}^2 F(\Omega_N)}{(\Omega_N - \Omega_{dr})^2 + \omega_{\perp dr}^2}\Big]\Delta(\omega). \tag{2.17}$$

Taking into account that the typical difference $(\Omega_N - \Omega_{dr}) \sim \delta_e$ is much bigger than the drive amplitude, $\omega_{\perp dr}$, we get

$$\frac{\pi}{6}\Big[1 - \pi\omega_{\perp dr}F(\Omega_{dr})\Big]\Delta(\omega). \tag{2.18}$$

Thus, the reduction of the magnitude of the zero-frequency peak due to drive is *linear* in drive amplitude and comes from the "resonant" realizations of the hyperfine fields for which $\Omega_N \approx \Omega_{dr}$.

It is less trivial to realize that the peaks at $\omega = \pm\omega_R^N$ described by the second and third terms in Eq. (2.16) remain sharp upon averaging even though their positions depend on Ω_N. The expression for the average of the second term reads

$$\frac{\pi}{6}\langle\gamma_z^2\Delta(\omega - \omega_R^N)\rangle = \frac{\pi}{12}\omega_{\perp dr}^2 \int_0^\infty d\Omega_N \frac{\Delta(\omega - \omega_R^N)F(\Omega_N)}{(\omega_R^N)^2}. \tag{2.19}$$

At this point we make use of the fact that the width of the Lorentzian, $\Delta(\omega - \omega_R^N)$, is much smaller than the width of the distribution function. Firstly, this allows to set $\omega_R^N = \omega$ in the denominator. Secondly, the values Ω_N that contribute to the integral are close to

$$\Omega_N = \Omega_{dr} \pm \sqrt{\omega^2 - \omega_{\perp dr}^2}. \tag{2.20}$$

Upon switching to the integration over ω_R^N and taking into account that

$$\frac{d\omega_R^N}{d\Omega_N} = \frac{\sqrt{(\omega_R^N)^2 - \omega_{\perp dr}^2}}{\omega_R^N} = \frac{\sqrt{\omega^2 - \omega_{\perp dr}^2}}{\omega}, \tag{2.21}$$

we find

$$\frac{\pi}{6}\langle\gamma_z^2\Delta(\omega - \omega_R^N)\rangle = \frac{\pi}{12}\frac{\omega_{\perp dr}^2}{\omega\sqrt{\omega^2 - \omega_{\perp dr}^2}} \times \Big[F\Big(\Omega_{dr} - \sqrt{\omega^2 - \omega_{\perp dr}^2}\Big) + F\Big(\Omega_{dr} + \sqrt{\omega^2 - \omega_{\perp dr}^2}\Big)\Big]. \tag{2.22}$$

Since the driving frequency is much bigger than the driving amplitude, both arguments in the distribution function can be replaced by Ω_N. With regard to the frequency dependence, Eq. (2.22) exhibits an integrable divergence near $\omega \approx \omega_{\perp dr}$. Most importantly, the averaged

peak falls off rapidly with ω as the difference $\omega-\omega_{\perp dr}$ increases. From the area conservation, it follows from Eq. (2.18) that the area under the peak Eq. (2.22) should be equal to $\frac{\pi^2}{12}\omega_{\perp dr}F(\Omega_{dr})$. On the other hand, from Eq. (2.22) we see that this area comes from the domain $(\omega-\omega_{\perp dr})\sim\omega_{\perp dr}\ll\delta_e$, i.e., the area conservation is ensured *locally*. This supports our statement that the averaged peak remains narrow.

Two terms on the second line of Eq. (2.16) describe the peaks at $\omega=\pm\Omega_{dr}$. Similar to the $\Delta(\omega)$ peak, their shape is not affected by the ensemble averaging. Averaging of the magnitude is completely analogous to that for $\Delta(\omega)$ peak since $\beta_z^2+2\alpha_z^2=1$. Thus, the contribution of these peaks to the noise spectrum is given by

$$\frac{\pi^2}{12}\omega_{\perp dr}F(\Omega_{dr})\Delta(\omega\pm\Omega_{dr}), \tag{2.23}$$

and grows linearly with the drive amplitude.

The last two lines in Eq. (2.16) describe the peaks in the noise spectrum at frequencies $\omega=\pm\Omega_{dr}\pm\omega_R^N$. Firstly, we note that the magnitudes of all four peaks are equal to each other. This follows from the fact that these magnitudes, $\gamma_\pm^2$ and $\alpha_\pm^2$, are determined by the values of Ω_N for which the arguments of the corresponding Lorentzians are zero. Now the equality of all peak magnitudes follows from the relation

$$\gamma_+|_{\Omega_N=\omega-\omega_R^N}=\alpha_+|_{\Omega_N=\omega+\omega_R^N}\,, \tag{2.24}$$

which is easy to check using Eqs. (2.10) and (2.13). Focusing on positive ω, the averaging over Ω_N is easy to perform by replacing Lorentzians by corresponding δ-functions and using the following identities

$$\delta\Big(\omega-\Omega_{dr}-\omega_R^N\Big)+\delta\Big(\omega-\Omega_{dr}+\omega_R^N\Big)=2\omega_R^N\delta\Big((\omega-\Omega_{dr})^2-(\omega_R^N)^2\Big)=\frac{\omega_R^N}{\sqrt{(\omega-\Omega_{dr})^2-\omega_{\perp dr}^2}}$$
$$\times\Big[\delta\Big(\sqrt{(\omega-\Omega_{dr})^2-\omega_{\perp dr}^2}-(\Omega_{dr}-\Omega_N)\Big)+\delta\Big(\sqrt{(\omega-\Omega_{dr})^2-\omega_{\perp dr}^2}+(\Omega_{dr}-\Omega_N)\Big)\Big]. \tag{2.25}$$

Upon averaging, the last two δ-functions pick the distribution $F(\Omega_N)$ at the values $\Omega_N=\Omega_{dr}\pm\sqrt{(\omega-\Omega_{dr})^2+\omega_{\perp dr}^2}$. The resulting average shape of the two peaks at $\omega=\Omega_{dr}\pm\omega_R^N$ reads

$$\frac{\pi\omega_{\perp dr}^4}{24|\omega-\Omega_{dr}|\sqrt{(\omega-\Omega_{dr})^2-\omega_{\perp dr}^2}}$$
$$\times\left[\frac{F\Big(\Omega_{dr}-\sqrt{(\omega-\Omega_{dr})^2-\omega_{\perp dr}^2}\Big)}{(\omega-\Omega_{dr}+\sqrt{(\omega-\Omega_{dr})^2-\omega_{\perp dr}^2})^2}+\frac{F\Big(\Omega_{dr}+\sqrt{(\omega-\Omega_{dr})^2-\omega_{\perp dr}^2}\Big)}{(\omega-\Omega_{dr}-\sqrt{(\omega-\Omega_{dr})^2-\omega_{\perp dr}^2})^2}\right]. \tag{2.26}$$

Note now, that in the limit $\omega_{\perp dr} \to 0$ the above expression reproduces the second term in Eq. (2.1), i.e., the background noise spectrum in the absence of drive. Formally this follows from the fact that either the first denominators in Eq. (2.26) (for $\omega < \Omega_{dr}$) or the second denominator (for $\omega > \Omega_{dr}$) becomes small, $\propto \omega_{\perp dr}^4$. In order to isolate the drive-related peaks from Eq. (2.26) one has to subtract

$$\frac{\pi}{6} F\Big(\Omega_{dr} + \frac{\omega - \Omega_{dr}}{|\omega - \Omega_{dr}|}\sqrt{(\omega - \Omega_{dr})^2 - \omega_{\perp dr}^2}\Big) \tag{2.27}$$

from Eq. (2.26). This subtracted term is a smooth function of ω. On the other hand, after the subtraction, Eq. (2.26) would describe two narrow peaks at $\omega + \Omega_{dr} \pm \omega_{\perp dr}$. This again allows us to set $\Omega_N = \Omega_{dr}$ in the argument of distribution function. It is convenient to cast the final result in the form

$$\frac{\pi}{12}\Big[\frac{|\omega - \Omega_{dr}|}{\sqrt{(\omega - \Omega_{dr})^2 - \omega_{\perp dr}^2}} + \frac{\sqrt{(\omega - \Omega_{dr})^2 - \omega_{\perp dr}^2}}{|\omega - \Omega_{dr}|} - 2\Big] F(\Omega_{dr}). \tag{2.28}$$

It is worth noting that the peaks described by Eq. (2.26), having the same width $\sim \omega_{\perp dr}$, are "shaper" than the peak Eq. (2.22) at the Rabi frequency. They decay as $\omega_{\perp dr}^4/(\omega - \Omega_{dr})^4$, while the peak at the Rabi frequency decays as $\omega_{\perp dr}^2/\omega^2$.

2.3.2 Averaging over orientations of hyperfine fields

The shape of the peaks in the noise spectrum derived above depends on $\omega_{\perp dr}$, the projection of the driving field on the plane normal to the local hyperfine field. If the angle between $\mathbf{\Omega}_N$ and $\boldsymbol{\omega}_{dr}$ is θ, then $\omega_{\perp dr} = \omega_{dr} \sin\theta$. To find the ensemble-averaged shape of the noise spectrum with drive one has to average over θ all four contributions Eqs. (2.18), (2.22),(2.23), and (2.28) as $\frac{1}{2}\int_0^\pi d\theta \sin\theta$ (.....).

Averaging of Eqs. (2.18), (2.23) simply reduces to the replacement of $\omega_{\perp dr}$ by $\frac{\pi}{4}\omega_{dr}$ without affecting the Lorentzian shapes of the narrow peaks. The prime effect of averaging of Eqs. (2.22) and (2.28) is the rounding of $1/\sqrt{\omega - \omega_{\perp dr}}$ and $1/\sqrt{\omega - \Omega_{dr} \pm \omega_{\perp dr}}$ anomalies. These anomalies do not disappear completely but become logarithmical. Both averages can be evaluated analytically. The averaging of Eq. (2.22) yields

$$\frac{\pi}{6} F(\Omega_{dr})\; G\Big(\frac{\omega}{\omega_{dr}}\Big), \tag{2.29}$$

where the dimensionless function $G(z)$ describing the averaged shape is given by

$$G(z) = \frac{1}{2}\int_0^\pi d\theta\; \frac{\sin^3\theta}{z\sqrt{z^2 - \sin^2\theta}} = \begin{cases} \frac{z^2+1}{2z}\ln\frac{z+1}{\sqrt{1-z^2}} - \frac{1}{2}, & z < 1, \\ \frac{z^2+1}{4z}\ln\frac{z+1}{z-1} - \frac{1}{2}, & z > 1. \end{cases} \tag{2.30}$$

The divergence near $z = 1$ should be cut off at $(1 - z) \sim 1/\omega_{dr}\tau_s$. The large-$z$ behavior of Eq. (2.30) is $G(z) \approx 2/3z^2$.

The result of averaging of Eq. (2.28) can be presented in the form similar to Eq. (2.30)

$$\frac{\pi}{12}F(\Omega_{dr})H\Big(\frac{|\omega-\Omega_{dr}|}{\omega_{dr}}\Big), \tag{2.31}$$

where the function $H(z)$ is defined as

$$H(z)=\frac{1}{2}\int\limits_0^\pi d\theta\ \frac{2z\sin\theta-\sin^3\theta}{\sqrt{z^2-\sin^2\theta}}-2. \tag{2.32}$$

Similarly to Eq. (2.30), the integral can be evaluated analytically, yielding

$$H(z)=\begin{cases}\frac{3z^2-1}{2z}\ln\frac{z+1}{\sqrt{1-z^2}}-\frac{3}{2}, & z<1,\\ \frac{3z^2-1}{4z}\ln\frac{z+1}{z-1}-\frac{3}{2}, & z>1.\end{cases} \tag{2.33}$$

The large-z behavior of the combination in the square brackets is $\propto 1/z^4$. Dimensionless functions $G(z)$ and $H(z)$ are plotted in Fig. 2.5.

Combining all the above, the final result for the ensemble-averaged noise spectrum of the driven system can be cast in the form

$$\begin{aligned}\langle\delta s_\omega^2\rangle =&\frac{\pi}{6}\Big[1-\frac{\pi^2\omega_{dr}}{4}F(\Omega_{dr})\Big]\Delta(\omega)+\frac{\pi}{6}F(\omega)\\ &+\frac{\pi}{6}F(\Omega_{dr})\Bigg\{G\Big(\pm\frac{\omega}{\omega_{dr}}\Big)+\frac{\pi^2}{8}\omega_{dr}\Delta(\omega\pm\Omega_{dr})+\frac{1}{2}H\Big(\frac{|\omega\pm\Omega_{dr}|}{\omega_{dr}}\Big)\Bigg\}.\end{aligned} \tag{2.34}$$

It is natural that the drive-related contributions are proportional to the density, $F(\Omega_{dr})$, of the resonant realizations of hyperfine fields. The net effect of drive on the noise spectrum is maximal if Ω_{dr} is chosen near the maximum of the distribution $F(\Omega_N)$. Then, at frequencies $\omega\sim\omega_{dr}$, the background noise is determined by $F(\omega)\propto\omega^2$ and is much *weaker* than the low-frequency peak due to drive. The area under all three peaks in the second line of Eq. (2.34) is $\sim\omega_{dr}$. In this regard, the weakness of drive means that the portion of the noise spectrum affected by drive is relatively small. However, within this portion, the spectrum is fully dominated by drive, since, for the resonant realizations, the drive changes the spin dynamics completely. Formally, it is the consequence of Eq. (2.9) that for $(\Omega_N-\Omega_{dr})\lesssim\omega_{dr}$ all the frequencies ω_R^N are close to ω_{dr}. The evolution of the noise spectrum with drive amplitude is illustrated in Fig. 2.6.

2.4 Fast drive

If the drive frequency is much bigger than the width of distribution of the hyperfine fields, there are no realizations of $\mathbf{\Omega}_N$ which are in resonance with drive. For all realizations, the spin dynamics will be affected by drive when the amplitude, ω_{dr}, becomes comparable

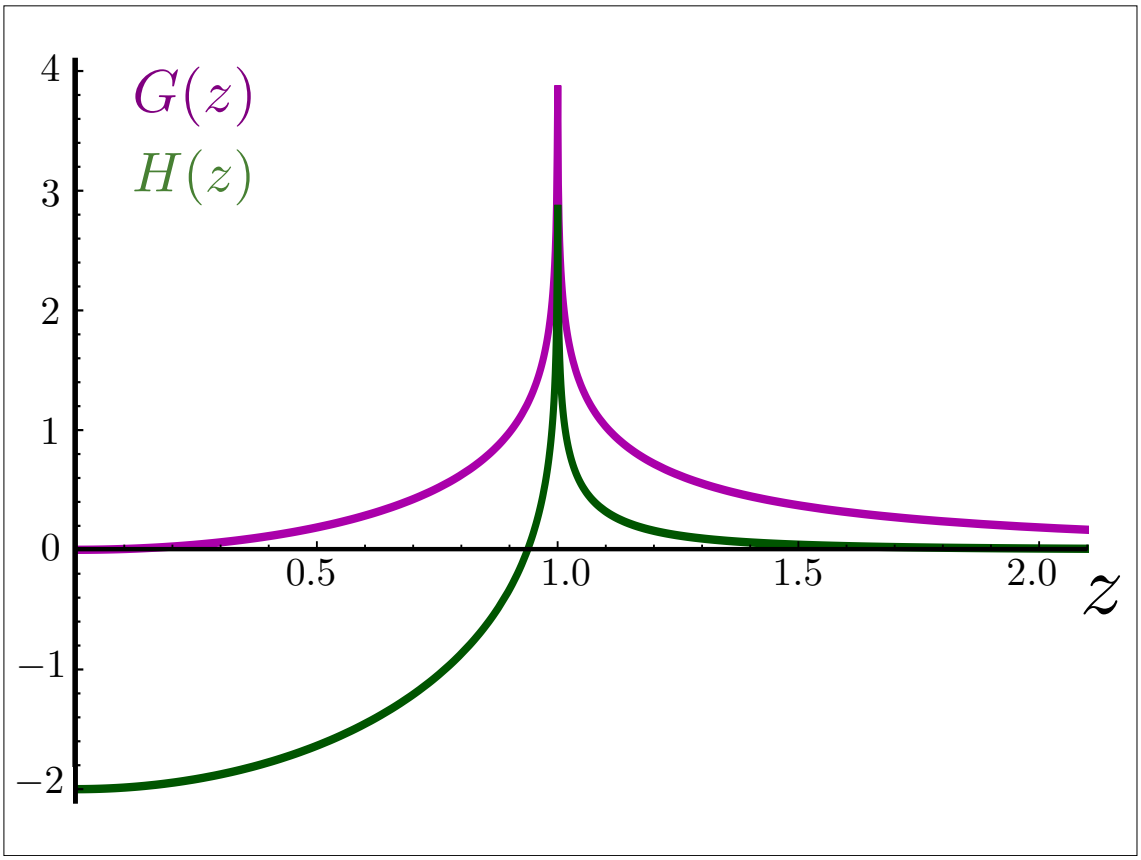

Figure 2.5: (color online). Dimensionless functions $G(z)$ (purple) and $H(z)$ (green) describing the shapes of the peaks at Rabi frequency and at driving frequency in the averaged noise spectrum are plotted from Eqs. (2.30) and (2.33), respectively.

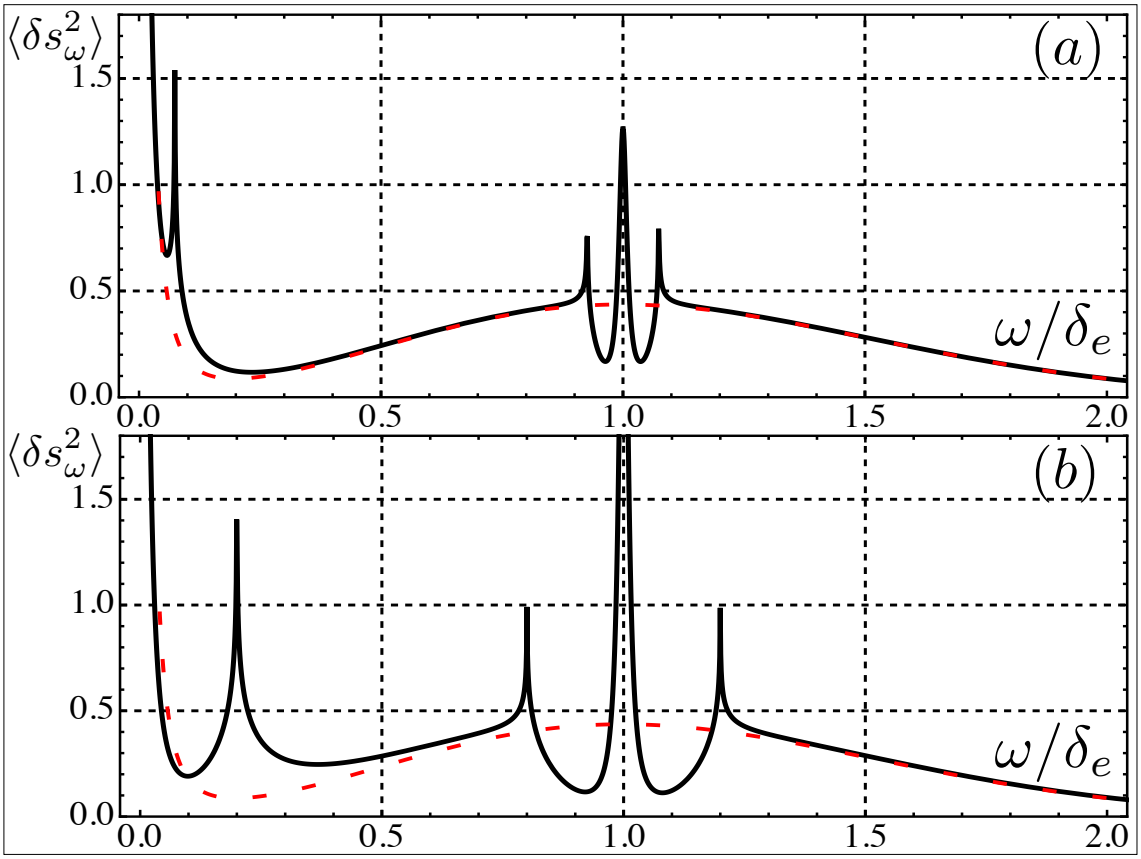

Figure 2.6: (color online). Averaged noise spectra are plotted from Eq. (2.34) for driving frequency, Ω_{dr}, corresponding to the maximum of the hyperfine field distribution and two amplitudes of the drive: $2\omega_{dr} = 0.15\delta_e$ (a) and $2\omega_{dr} = 0.4\delta_e$ (b). Even for weak drive the drive-induced satellites in the averaged spectra are well-pronounced. The width of the central peak at $\omega = \Omega_{dr}$ is $\tau_s^{-1} = 10^{-2}\delta_e$. The spectra in the absence of drive, illustrating the conservation of the net noise power, are shown with red lines.

to Ω_{dr}. Suppose that $\boldsymbol{\omega}_{dr}$ is directed along x, while the projections of $\boldsymbol{\Omega}_N$ are equal to Ω_N^x, Ω_N^y, and Ω_N^z. Without drive, the two frequencies of the spin dynamics are $\omega = 0$ and $\omega = \Omega_N = \left[(\Omega_N^x)^2 + (\Omega_N^y)^2 + (\Omega_N^z)^2\right]^{1/2}$. The prime effect of a fast drive is that the frequency Ω_N transforms into

$$\lambda_N = \left[(\Omega_N^x)^2 + \left\{(\Omega_N^y)^2 + (\Omega_N^z)^2\right\} J_0^2\Big(\frac{\omega_{dr}}{\Omega_{dr}}\Big)\right]^{1/2}, \tag{2.35}$$

where $J_0(x)$ is the zero-order Bessel function. Besides, both frequencies $\omega = 0$ and $\omega = \lambda_N$ acquire satellites at $\omega = n\Omega_{dr}$ and $\omega = \lambda_N + n\Omega_{dr}$. The derivation of Eq. (2.35) is given in the Appendix. According to Eq. (2.35), as the drive amplitude increases, $J_0\Big(\frac{\omega_{dr}}{\Omega_{dr}}\Big)$ falls off, so that the spin precesses only in the y-z plane.

The derivation of the noise spectrum in the case of a fast drive is in line with procedure employed in Sect II. In the Appendix, along with deriving Eq. (2.35), we find the solutions of the equations of motion of a driven spin corresponding to the frequencies $\omega = 0$ and $\omega = \lambda_N$ and present these solutions in the form of combination of the normalized eigenvectors similar to Eq. (2.8)

$$\begin{pmatrix} S_+ \\ S_x \\ S_- \end{pmatrix} = B_+ \begin{pmatrix} \mu_+ e^{i\lambda_N t + i\Phi(t)} \\ \mu_x e^{i\lambda_N t} \\ \mu_- e^{i\lambda_N t - i\Phi(t)} \end{pmatrix} + B_x \begin{pmatrix} \eta_+ e^{i\Phi(t)} \\ \eta_x \\ \eta_- e^{-i\Phi(t)} \end{pmatrix} + B_- \begin{pmatrix} \nu_+ e^{-i\lambda_N t + i\Phi(t)} \\ \nu_x e^{-i\lambda_N t} \\ \nu_- e^{-i\lambda_N t - i\Phi(t)} \end{pmatrix}, \tag{2.36}$$

where $S_\pm = \frac{1}{\sqrt{2}}(S_y \pm iS_z)$, the oscillating phase $\Phi(t)$ is defined as

$$\Phi(t) = \omega_{dr} \int_0^t dt' \cos(\Omega_{dr} t') = \frac{\omega_{dr}}{\Omega_{dr}} \sin(\Omega_{dr} t), \tag{2.37}$$

and the components of the eigenvectors are related as follows

$$\eta_x = \frac{\Omega_N^x}{\lambda_N}, \tag{2.38}$$

$$\mu_x = \nu_x = -i\eta_+ = i\eta_- = -\frac{\left[(\Omega_N^y)^2 + (\Omega_N^z)^2\right]^{\frac{1}{2}}}{\sqrt{2}\lambda_N} J_0\Big(\frac{\omega_{dr}}{\Omega_{dr}}\Big), \tag{2.39}$$

$$\mu_+ = -\nu_- = \frac{i}{2} \frac{\left[(\Omega_N^y)^2 + (\Omega_N^z)^2\right]}{\lambda_N(\lambda_N - \Omega_N^x)} J_0^2\Big(\frac{\omega_{dr}}{\Omega_{dr}}\Big), \tag{2.40}$$

$$\mu_- = -\nu_+ = \frac{i}{2} \frac{\left[(\Omega_N^y)^2 + (\Omega_N^z)^2\right]}{\lambda_N(\lambda_N + \Omega_N^x)} J_0^2\Big(\frac{\omega_{dr}}{\Omega_{dr}}\Big). \tag{2.41}$$

The components S_x of the eigenvectors are simple exponents. Then the contribution $\delta s_{x\omega}^2$ to the noise spectrum follows directly from Eq. (2.36)

$$\delta s_{x\omega}^2 = \frac{\pi}{2}\Big[|\eta_x|^2 \Delta(\omega) + |\mu_x|^2 \Delta(\omega - \lambda_N) + |\nu_x|^2 \Delta(\omega + \lambda_N)\Big]. \tag{2.42}$$

Concerning the contributions $\delta s^2_{y\omega}$ and $\delta s^2_{z\omega}$, they originate from the S_+ and S_- components of the eigenvectors, which are not simple exponents. This gives rise to the satellites spaced by $n\Omega_{dr}$ in the noise spectrum. Relative magnitudes of the satellites are found from the Fourier expansion

$$\exp(i\Phi(t)) = \sum_n J_n\Big(\frac{\omega_{dr}}{\Omega_{dr}}\Big)\exp(in\Omega_{dr}t). \tag{2.43}$$

Since $\delta s^2_{y\omega}$ and $\delta s^2_{z\omega}$ give equal contributions to the ensemble-averaged spectrum, it is convenient to average the combination $\delta s^2_{y\omega} + \delta s^2_{z\omega}$. For this combination the result for a given hyperfine field assumes a compact form

$$\begin{aligned}\delta s^2_{y\omega} + \delta s^2_{z\omega} =& \frac{\pi}{2}\Big[(|\eta_+|^2 + |\eta_-|^2)\sum_n J_n^2\Big(\frac{\omega_{dr}}{\Omega_{dr}}\Big)\Delta(\omega - n\Omega_{dr}) \\ &+ (|\mu_+|^2 + |\mu_-|^2)\sum_n J_n^2\Big(\frac{\omega_{dr}}{\Omega_{dr}}\Big)\Delta(\omega - \lambda_N - n\Omega_{dr}) \\ &+ (|\nu_+|^2 + |\nu_-|)^2\sum_n J_n^2\Big(\frac{\omega_{dr}}{\Omega_{dr}}\Big)\Delta(\omega + \lambda_N + n\Omega_{dr})\Big].\end{aligned} \tag{2.44}$$

From Eqs. (2.42) and (2.44) we can trace the evolution of the averaged noise spectrum upon increasing the drive amplitude. Firstly, in the weak-drive limit, $\omega_{dr} \ll \Omega_{dr}$, when the magnitudes of the satellites are negligible, averaging of Eqs. (2.42), (2.44) reproduces the result Eq. (2.1). Indeed, when $J_0\Big(\frac{\omega_{dr}}{\Omega_{dr}}\Big) \approx 1$, the frequency λ_N returns to Ω_N. The magnitudes, $|\eta_x|^2$ and $(|\eta_+|^2 + |\eta_-|^2)$, of a zero-frequency peaks in Eqs. (2.42) and (2.44) become $(\Omega^x_N)^2/\Omega^2_N$ and $[(\Omega^y_N)^2 + (\Omega^z_N)^2]/\Omega^2_N$, as in the absence of drive. Similarly, the fact that the magnitude of $\omega = \lambda_N$ peak assumes its zero-drive value follows from general relation $|\mu_x|^2 + |\mu_+|^2 + |\mu_-|^2 = 1$.

As the drive amplitude increases, the magnitude of a $\omega = 0$ peak first decreases but eventually returns to its zero-drive value. Indeed, in the limit $J_0\Big(\frac{\omega_{dr}}{\Omega_{dr}}\Big) \to 0$, we have $|\eta_x|^2 \approx 1$, while η_+ and η_- vanish. This suggests that the $\omega = n\Omega_{dr}$ satellites of a zero-frequency peak develop at $\omega_{dr} \sim \Omega_{dr}$, but disappear in the strong-drive limit. By contrast, the satellites at $\omega = \pm\lambda_N + n\Omega_{dr}$ persist in the strong-drive limit. In this limit μ_x vanished, and thus we have $|\mu_+|^2 + |\mu_-|^2 \approx 1$. This suggests that all the noise power in $\omega = \lambda_N$ peak at zero drive gets redistributed between the satellites at strong drive. Also, in the limit of strong drive, we have $\lambda_N \approx |\Omega^x_N|$, so that Eq. (2.44) assumes the form

$$\delta s^2_{y\omega} + \delta s^2_{z\omega} = \frac{1}{2}\sum_{n\neq 0} J_n^2\Big(\frac{\omega_{dr}}{\Omega_{dr}}\Big)\frac{\tau_s}{1 + (\omega + \Omega^x_N + n\Omega_{dr})^2\tau_s^2}. \tag{2.45}$$

At zero drive the ensemble averaging over Ω_N resulted in the noise spectrum given by $F(\omega)$, Eq. (2.3). By contrast, from Eq. (2.45) we see that, for a strong drive, the ensemble

averaging of each term yields the distribution function of Ω_N^x, i.e., the shapes of the satellites are gaussian. The overall noise spectrum in the presence of a fast drive is illustrated in Figs. 2.7, 2.8.

2.5 Discussion

Our main result is Eq. (2.34) for the averaged noise spectrum. This result was obtained within the rotating wave approximation and applies for large enough drive amplitudes $\omega_{dr}\tau_s \gg 1$. Fig. 2.6 illustrates the evolution of the spectrum with ω_{dr}. As ω_{dr} increases, the magnitude of a central peak at $\omega = \Omega_{dr}$ grows linearly with drive, while the satellites at $|\omega \pm \Omega_{dr}| = \omega_{dr}$ broaden linearly with drive. Central peak and satellites merge at weak drive $\omega_{dr}\tau_s \sim 1$. For smaller ω_{dr} the effect of drive on the spin dynamics is weak even for "resonant" hyperfine field configurations and can be treated perturbatively. The effect of drive amounts to replacement ω_{dr} by $\omega_{dr}^2\tau_s$ in the amplitude of the cental peak. The relative correction to the background value of $\langle \delta s_\omega^2 \rangle$ due to drive is $\omega_{dr}^2\tau_s^2 \ll 1$. Despite being small, the effect of drive can be distinguished in the derivative with respect to ω. Indeed, the derivative of the background can be estimated as $\frac{1}{\delta_e}F(\Omega_{dr})$, while the estimate for the derivative of the central peak is $\omega_{dr}^2\tau_s^3 F(\Omega_{dr})$. Thus the drive dominates the derivative in the domain

$$\omega_{dr}\tau_s \gg \frac{1}{(\delta_e\tau_s)^{1/2}}. \tag{2.46}$$

Large typical value of the hyperfine field, $\delta_e \gg \tau_s^{-1}$, which is presumed, allows us to distinguish the effect of drive even when it is weak.

As in Refs. [17-20], we assumed that spin-relaxation time, τ_s, resulting from random short-time correlated fields different from hyperfine field, is the same for all elements of the ensemble. The ac-driven system is stationary but not equilibrium. Still we calculated the noise spectrum from eigenmodes. Justification for doing this is that the temperature is much higher than all the frequencies involved. Under this condition, all the eigenmodes are equally represented in the spin dynamics [19].

In a recent paper [25] a direct measurement of the spin-relaxation rate, τ_s^{-1}, was reported. Such a measurement became possible due to implementing of the spin noise correlation techniques, which involves two laser beams and allows one to probe only specific configurations of the hyperfine field. In this regard, the effect of the ac drive is prominent because it also results from specific "resonant" configurations.

In experiments on different semiconductor structures [5, 6, 8, 9] the measured width of the noise spectra ranged from $\sim$ 2MHz to $\sim$ 50MHz. Application of the ac drive with

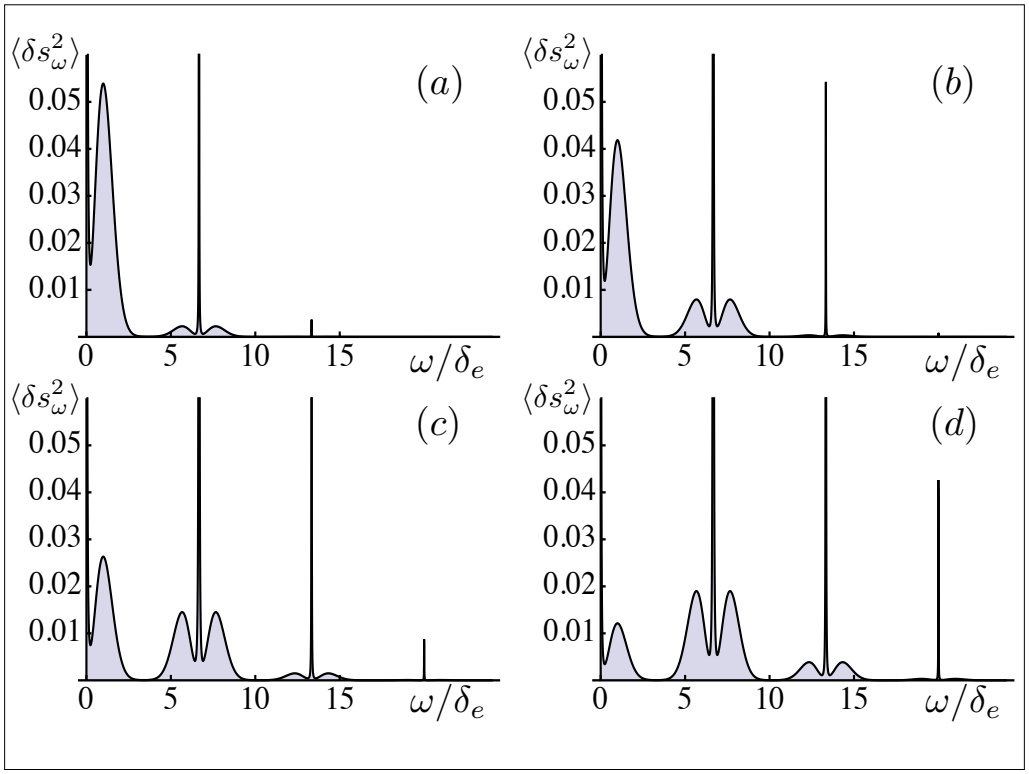

Figure 2.7: (color online). Evolution of the averaged noise spectra in the case of a fast drive, $\Omega_{dr} = 6.7\delta_e$, with drive amplitude, ω_{dr}. The values of the amplitudes are $\omega_{dr} = 0.4\Omega_{dr}$(a), $\omega_{dr} = 0.8\Omega_{dr}$ (b), $\omega_{dr} = 1.2\Omega_{dr}$ (c), and $\omega_{dr} = 1.6\Omega_{dr}$(d). Narrow peaks have the width $\tau_s^{-1} = 0.0067\delta_e$. Satellites of the zero-frequency peak at $\omega = n\Omega_{dr}$ gradually develop upon increasing ω_{dr}. Since the value $J_0\left(\frac{\omega_{dr}}{\Omega_{dr}}\right)$ is close to 1 for all ω_{dr} the low-frequency parts of the spectra have the same shape as in the absence of drive.

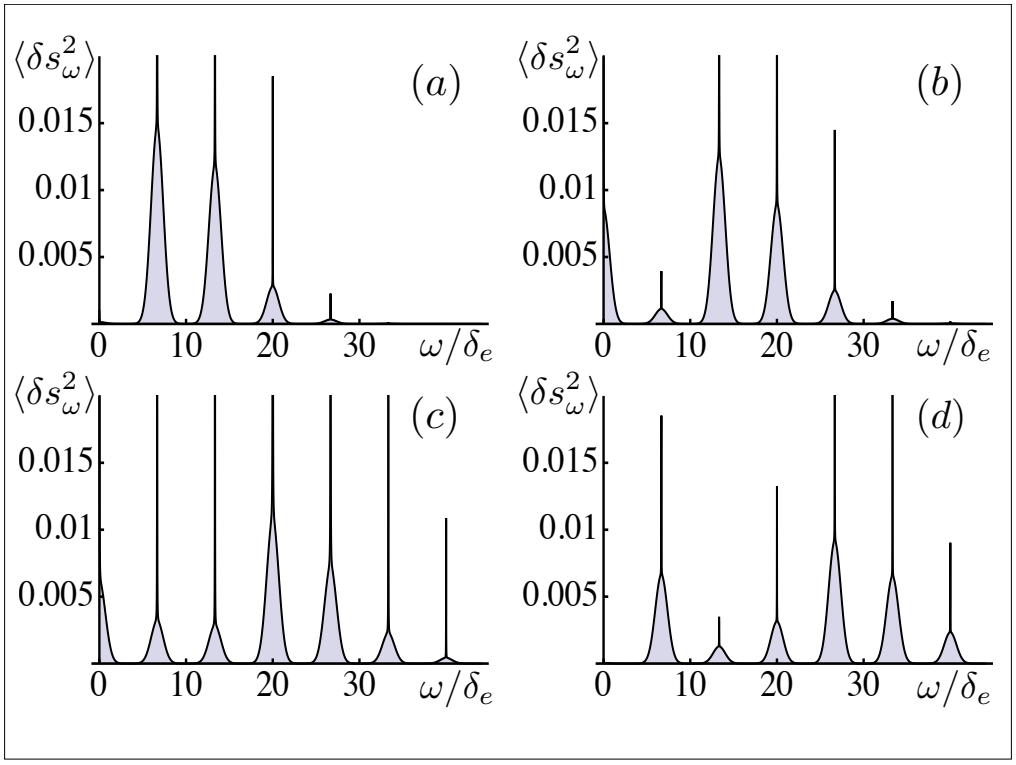

Figure 2.8: (color online). Same as Fig. 2.7 for stronger drive amplitudes $\omega_{dr} = 2.5\Omega_{dr}$(a), $\omega_{dr} = 3.5\Omega_{dr}$ (b), $\omega_{dr} = 4.5\Omega_{dr}$ (c), and $\omega_{dr} = 5.6\Omega_{dr}$(d). The peaks at $\omega = n\Omega_{dr}$ have gaussian shape. Their amplitudes evolve with drive in *oscillating* fashion.

comparable frequency does not constitute a problem, see, e.g., Ref. [26]. It will require adding a coil to the conventional setup [5, 6, 8, 9].

Due to isotropy of the hyperfine fields the noise spectrum calculated above does not depend on the direction of the ac magnetic field. This is the case when the electron g-factor is isotropic. In an experiment [8] it was established that the g-factor is strongly anisotropic[28]. This conclusion was drawn from the analysis of the shift of the noise spectrum maximum with the external magnetic field. With anisotropic g-factor, drive-induced features of the noise spectrum will depend on the direction of ω_{dr}. While the position of a peak at $\omega = \Omega_{dr}$ is insensitive to the anisotropy, the separation of the satellites will be bigger for the drive polarization along the bigger g-value.

2.6 Appendix

Without loss of generality we can set $\Omega_N^y = 0$. We start from the equations of motion for the spin projections

$$\frac{\partial S_x}{\partial t} = -\Omega_N^z S_y, \tag{2.47}$$

$$\frac{\partial S_y}{\partial t} = -(\omega_{dr}\cos\Omega_{dr}t + \Omega_N^x)S_z + \Omega_N^z S_x, \tag{2.48}$$

$$\frac{\partial S_z}{\partial t} = (\omega_{dr}\cos\Omega_{dr}t + \Omega_N^x)S_y. \tag{2.49}$$

To take advantage of the fact that the drive is fast it is convenient [27] to switch to the new variables

$$S_{x'} = S_x, \tag{2.50}$$

$$S_{y'} = S_y\cos\big(\Phi(t) + \Omega_N^x t\big) + S_z\sin\big(\Phi(t) + \Omega_N^x t\big), \tag{2.51}$$

$$S_{z'} = -S_y\sin\big(\Phi(t) + \Omega_N^x t\big) + S_z\cos\big(\Phi(t) + \Omega_N^x t\big), \tag{2.52}$$

where the phase $\Phi(t)$ is defined by Eq. (2.37). The physical meaning of the above transformation is moving into the rotating frame in which the ac field is canceled. The equations of motion for the new variables read

$$\begin{aligned}
\frac{\partial S_{x'}}{\partial t} &= \Omega_N^z S_z\sin\big(\Phi(t) + \Omega_N^x t\big) - \Omega_N^z S_y\cos\big(\Phi(t) + \Omega_N^x t\big),\\
\frac{\partial S_{y'}}{\partial t} &= \Omega_N^z S_x\cos\big(\Phi(t) + \Omega_N^x t\big),\\
\frac{\partial S_{z'}}{\partial t} &= -\Omega_N^z S_{x'}\sin\big(\Phi(t) + \Omega_N^x t\big).
\end{aligned} \tag{2.53}$$

As a next step, we average Eqs. (2.53) over the time interval $\left(-\frac{\pi}{\Omega_{dr}}, \frac{\pi}{\Omega_{dr}}\right)$. The justification for this step is that, since $\Omega_{dr} \gg \Omega_N$, the spin projections do not change significantly during this interval. Thus one can average only $\cos\big(\Phi(t) + \Omega_N^x t\big)$ and $\sin\big(\Phi(t) + \Omega_N^x t\big)$

$$\langle \cos\big(\Phi(t) + \Omega_N^x t\big)\rangle = J_0\Big(\frac{\omega_{dr}}{\Omega_{dr}}\Big)\cos\Omega_N^x t, \tag{2.54}$$

$$\langle \sin\big(\Phi(t) + \Omega_N^x t\big)\rangle = J_0\Big(\frac{\omega_{dr}}{\Omega_{dr}}\Big)\sin\Omega_N^x t. \tag{2.55}$$

It is also convenient to switch in the averaged equations to $S_{+'} = \frac{1}{\sqrt{2}}(S_{y'} + S_{z'})$ and $S_{-'} = \frac{1}{\sqrt{2}}(S_{y'} - S_{z'})$. Then we get

$$\begin{aligned}
\frac{\partial S_{x'}}{\partial t} &= -\frac{1}{\sqrt{2}}\Omega_N^z J_0\Big(\frac{\omega_{dr}}{\Omega_{dr}}\Big)\Big[S_{+'}e^{i\Omega_N^x t} + S_{-'}e^{-i\Omega_N^x t}\Big],\\
\frac{\partial S_{+'}}{\partial t} &= \frac{1}{\sqrt{2}}\Omega_N^z J_0\Big(\frac{\omega_{dr}}{\Omega_{dr}}\Big)S_{x'}e^{-i\Omega_N^x t},\\
\frac{\partial S_{-'}}{\partial t} &= \frac{1}{\sqrt{2}}\Omega_N^z J_0\Big(\frac{\omega_{dr}}{\Omega_{dr}}\Big)S_{x'}e^{i\Omega_N^x t}.
\end{aligned} \tag{2.56}$$

We see that the dynamics after averaging is slow, which justifies the averaging performed, see Ref. [27] for rigorous justification. One can also see that Eq. (2.56) have the form of equations of motion in a constant magnetic field with x- and z-components being Ω_N^x and $\Omega_N^z J_0\Big(\frac{\omega_{dr}}{\Omega_{dr}}\Big)$, respectively. Finite Ω_N^y is naturally included as a y-component. This immediately leads us to Eq. (2.35) of the main text. Three eigenvectors correspond to rotations with frequencies $\omega = \lambda_N$, $\omega = 0$, and $\omega = -\lambda_N$. To return to the lab frame one has to multiply $S_{+'}$ by $\exp\left(i\Phi(t) + i\Omega_N^x t\right)$ and $S_{-'}$ by $\exp\left(-i\Phi(t) - i\Omega_N^x t\right)$. This does not change the relation between the components of the eigenvectors which have the form Eq. (2.36).

2.7 References

[1] M. I. Dyakonov and V. I. Perel, in *Optical Orientation*, edited by F. Meier and B. Zakharchenya North-Holland, Amsterdam, 1984, pp. 1171.

[2] J. M. Kikkawa and D. D. Awschalom, Phys. Rev. Lett. **80** 4313, (1998).

[3] M. I. Dyakonov and V. I. Perel, Sov. Phys. Solid State **13**, 3023 (1971).

[4] M. Oestreich, M. Romer, R. G. Haug, and D. Hagele, Pys. Rev. Lett. **95**, 216603 (2005).

[5] S. A. Crooker, L. Cheng, and L. D. Smith, Phys. Rev. B **79**, 035208 (2009).

[6] H. Horn, A. Balocchi, X. Marie, A. Bakin, A. Waag, M. Oestreich, and J. Hubner, Phys. Rev. B **87**, 045312 (2013).

[7] G. M. Müller, M. Römer, D. Schuh, W. Wegscheider, J. Hübner, and M. Oestreich, Phys. Rev. Lett. **101**, 206601 (2008).

[8] S. A. Crooker, J. Brandt, C. Sandfort, A. Greilich, D. R. Yakovlev, D. Reuter, A. D. Wieck, and M. Bayer, Phys. Rev. Lett. **104**, 036601 (2010).

[9] Y. Li, N. Sinitsyn, D. L. Smith, D. Reuter, A. D. Wieck, D. R. Yakovlev, M. Bayer, and S. A. Crooker, Phys. Rev. Lett. **108**, 186603 (2012).

[10] V. S. Zapasskii, A. Greilich, S. A. Crooker, Y. Li, G. G. Kozlov, D. R. Yakovlev, D. Reuter, A. D. Wieck, and M. Bayer, Phys. Rev. Lett. **110**, 176601 (2013).

[11] G. M. Müller, M. Oestreich, M. Römer, and J. Hübner, Physica E **43**, 569 (2010).

[12] J. Hübner, F. Berski, R. Dahbashi, and M. Oestreich Phys. Stat. Solidi B **251** 1824 (2014).

[13] E. Aleksandrov and V. Zapasskii, Sov. Phys. JETP **54**, 64 (1981) [Zh. Exp. Teor. Fiz. **81**, 132 (1981)].

[14] S. A. Crooker, D. G. Rickel, A. V. Balatsky, and D. L. Smith, Nature (London) **431**, 49 (2004).

[15] I. A. Merkulov, A. L. Efros, and M. Rosen, Phys. Rev. B **65**, 205309 (2002).

[16] A. V. Khaetskii, D. Loss, and L. Glazman, Phys. Rev. Lett. **88**, 186802 (2002).

[17] M. M. Glazov and E. L. Ivchenko, Phys. Rev. B **86**, 115308 (2012).

[18] J. Hackmann, D. S. Smirnov, M. M. Glazov, and F. B. Anders, Phys. Stat. Solidi **251**, 1270 (2014).

[19] D. S. Smirnov, M. M. Glazov, and E. L. Ivchenko, Phys. Solid State **56**, 254 (2014).

[20] D. S. Smirnov, arXiv:1412.0534.

[21] K. Schulten and P. G. Wolynes, J. Chem. Phys. **68**, 3292 (1978).

[22] P. Glasenapp, N. A. Sinitsyn, L. Yang, D. G. Rickel, D. Roy, A. Greilich, M. Bayer, and S. A. Crooker Phys. Rev. Lett. **113**, 156601 (2014).

[23] H. Brox, J. Bergli, and Y. M. Galperin, Phys. Rev. B **84**, 245416 (2011).

[24] I. I. Rabi, Phys. Rev. **51**, 652 (1937).

[25] L. Yang, P. Glasenapp, A. Greilich, D. R. Yakovlev, M. Bayer, and S. A. Crooker, Nat. Commun. **5**, 4949 (2014).

[26] D. R. McCamey, K. J. van Schooten, W. J. Baker, S.-Y. Lee, S.-Y. Paik, J. M. Lupton, and C. Boehme, Phys. Rev. Lett. **104**, 017601 (2010).

[27] R. Glenn, M. E. Limes, B. Pankovich, B. Saam, and M. E. Raikh, Phys. Rev. B **87**, 155128 (2013).

[28] In fact, the g-factors in the quantum dots in experiments Refs. [9], [10] are strongly dispersed. We are grateful to Y. Li for this remark.

CHAPTER 3

SPECTRAL NARROWING AND SPIN ECHO FOR LOCALIZED CARRIERS WITH HEAVY-TAILED LÉVY DISTRIBUTION OF HOPPING TIMES

3.1 Introduction

A concept of the spectral narrowing of the magnetic resonance lineshape was quantified more than sixty years ago in a seminal paper [1].

In application to free induction decay (FID), this concept can be recapped as follows. In the presence of the time-dependent random magnetic field, $b(t)$, the decay of the FID signal is determined by the average $\left\langle \exp\left[i\int\limits_0^t dt' b(t')\right]\right\rangle$. The character of the decay depends on the relation between the typical magnitude, b_0, of $b(t)$ and the correlation time, τ. For long correlation time $b_0\tau \gg 1$, the decay is gaussian, $\propto \exp(-b_0^2 t^2)$, reflecting the gaussian distribution of the magnitudes of $b(t)$. In the opposite limit, $b_0\tau \ll 1$, the integrand rapidly changes sign, which is the origin of the spectral narrowing. If the time intervals between the subsequent sign changes are δt_1, δt_2, δt_3, and so on, then the average, $\left\langle \exp\left[i\int\limits_0^t dt' b(t')\right]\right\rangle$, over the field realizations can be rewritten as $\exp\left[-b_0^2\sum\limits_{i=1}^{n}(\delta t_i)^2\right]$. On the other hand, the number of the sign changes, n, is determined by the condition $\sum\limits_{i=1}^{n}\delta t_i = t$. This leads to a simple exponential behavior, $\exp(-t/\tau_s)$, of the FID signal, where

$$\frac{1}{\tau_s} = b_0^2\frac{\overline{(\delta t)^2}}{\overline{\delta t}}. \tag{3.1}$$

The two regimes of the FID translate into distinctive resonance lineshapes. For Gaussian decay the form of the line is a Gaussian, while for exponential decay this form is Lorentzian, and thus falls off much slower with detuning; see Figure 3.1.

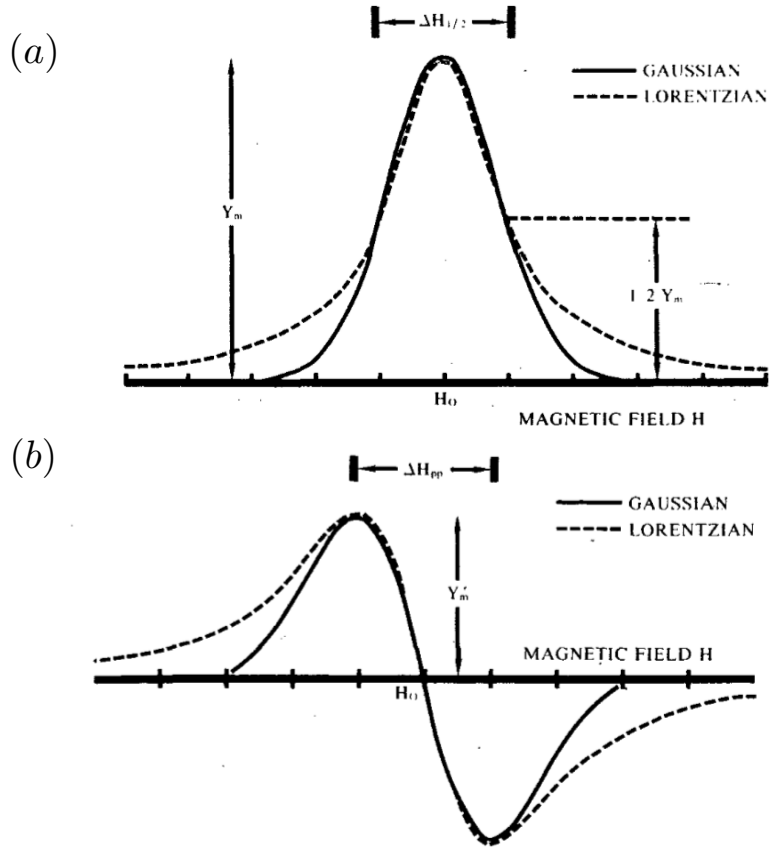

Figure 3.1: Spectral narrowing. (a) Comparison of Gaussian and Lorentzian absorption lineshapes. (b) Comparison of Gaussian and Lorentzian first-derivative absorption lineshapes (adapted from Ref. [19]).

If the random field is characterized by a *single* correlation time, τ_0, then the intervals δt_i obey the Poisson distribution

$$p_0(\delta t, \tau_0) = \frac{1}{\tau_0} \exp\big[-\delta t/\tau_0\big]. \tag{3.2}$$

Averaging with this distribution in Eq. (3.1) yields a well-known result, $\tau_s = 1/2b_0^2\tau_0$, for the decay rate. In the field of semiconductors this result is also known as the Dyakonov-Perel spin relaxation time [2].

A nontrivial situation emerges when the correlation times, τ, are broadly distributed. Then Eq. (3.1) takes the form

$$\frac{1}{\tau_s} = 2b_0^2 \frac{\langle \tau^2 \rangle}{\langle \tau \rangle}, \tag{3.3}$$

where the averaging is performed over the distribution, $F(\tau)$, of the correlation times. Such a situation is generic, e.g., for the dispersive transport in disordered semiconductors [3-9]. Broad distribution of the τ-values stems from the spread in the activation energies. Another example is a system with hopping transport, where the broad distribution of τ is the result of the spread in the hopping distances. In both cases $F(\tau)$ has a power-law tail: $F(\tau) \propto \tau^{-1-\alpha}$. Such a distribution, also known as the Lévy distribution, is normalizable for positive α. However, for $\alpha < 2$ the average $\langle \tau^2 \rangle$ diverges. Formally, this implies that τ_s turns to zero. On the physical level, this means that, on certain occasions, the spin spends enough time in some given field to exercise a full rotation; see Fig. 3.2. Although the portion of these occasions is small $\sim (b_0\tau_0)^\alpha$, they change the average spin dynamics dramatically. Theoretical study of this dynamics is the subject of the present paper. We find that, for $\alpha < 2$, the FID retains the form of a simple exponent, but the rate, τ_s^{-1}, shortens and becomes a strong function of the tail parameter, α. Our results can be summarized as

$$\frac{1}{\tau_s} = \begin{cases} D_1(\alpha)\ b_0^2\tau_0, & \alpha > 2 \\ D_2(\alpha)\ b_0^\alpha \tau_0^{\alpha-1}, & 2 > \alpha > 1 \\ D_3(\alpha)\ b_0, & 1 > \alpha > 0, \end{cases} \tag{3.4}$$

where $D_1(\alpha)$, $D_2(\alpha)$, and $D_3(\alpha)$ are the dimensionless functions of the tail parameter. Change of the behavior of τ_s at $\alpha = 2$ is due to the formal divergence of $\langle \tau^2 \rangle$, while the change at $\alpha = 1$ is due to the formal divergence of $\langle \tau \rangle$, which enters into the denominator of Eq. (3.3). We also find that the crossovers at $\alpha = 2$ and $\alpha = 1$ take place within narrow intervals: $|\alpha - 2| \sim 1/|\ln b_0\tau_0|$ and $|\alpha - 1| \sim 1/|\ln b_0\tau_0|$.

Another phenomenon which is strongly affected in the presence of multiple waiting time is spin echo [10]. The effect of the tail in $F(\tau)$ on the echo is opposite to the effect of $F(\tau)$

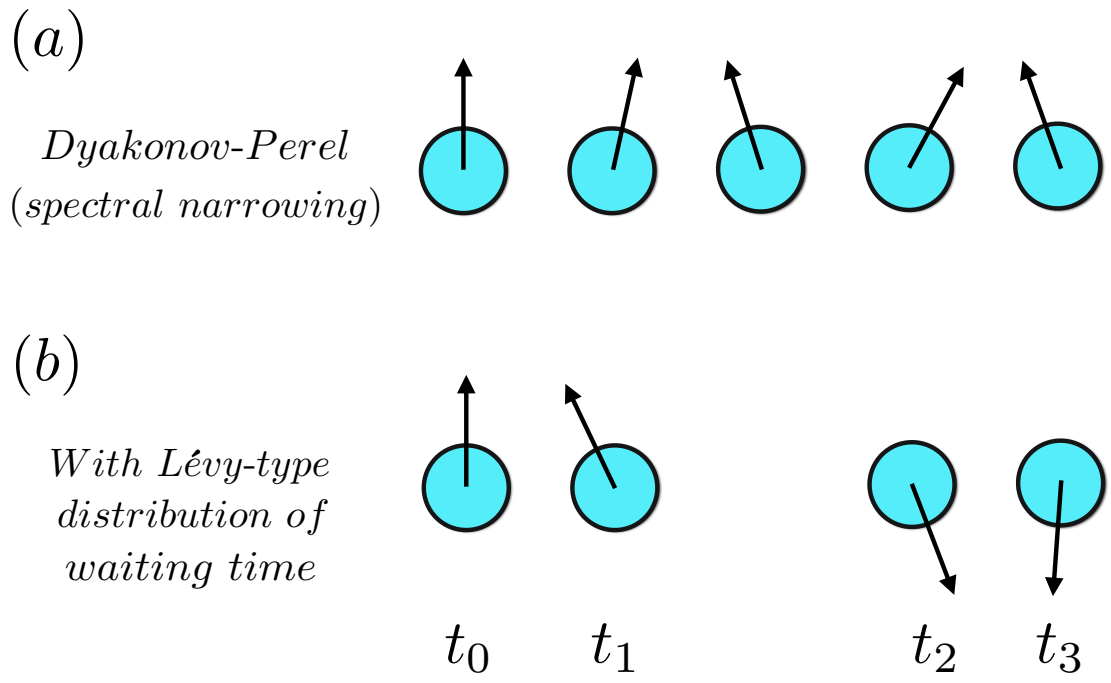

Figure 3.2: (color online). The contrast between (a) Dyakonov-Perel spin relaxation with a single correlation time and (b) spin relaxation with broad distribution of the waiting times is illustrated schematically. Allowance for anomalously long waiting times accelerates the relaxation.

on the spin relaxation rate. The echo decays *slower* due to this tail. The average echo signal is determined by the realizations with longest waiting times.

The paper is organized as follows. In Sect. 2 we derive a closed equation for the FID averaged over the realizations of random fields. Asymptotic (in parameter $b_0\tau_0 \ll 1$) solution of this equation is found in Sect. 3, where we derive the result Eq. (3.4) and also find the crossover behaviors near $\alpha = 2$ and $\alpha = 1$. In Sect. 4 we analyze the decay of the average echo signal. Concluding remarks are presented in Sect. 5.

3.2 Basic equation for average FID with multiple relaxation times

As it was mentioned in the Introduction, the physical picture which we have in mind is the carrier motion between the sites either by hopping or by trapping-detrapping process [3-9]. The time-dependent magnetic field of a hyperfine origin [11], acting on the carrier spin, represents a sequence of steps $\boldsymbol{b}(t) = \sum_i \boldsymbol{b}_i \left[\Theta(t_{i+1} - t) - \Theta(t - t_i)\right]$, where $\Theta(x)$ is the step-function and the step durations, $(t_{i+1} - t_i)$, are distributed according to the Poisson distribution Eq. (3.2), in which τ_0 is distributed according to $F(\tau)$. Since the sites are separated in space, random fields, $\boldsymbol{b}_i$, at different sites are *completely uncorrelated*, as it is illustrated in Fig. 3.3, left panel. We also assume that the motion is three-dimensional, so that the effect of occasional returns to the same site are negligible [12-14].

Suppose that at time moment $t = 0$ a carrier occupies the site $i = 0$, and its spin is directed along the z-axis. After time t the carrier can either remain on the site $i = 0$ or hop on the neighboring site $i = 1$. The probability to stay is $p_0(t, \tau^{(0)})$, defined by Eq. (3.2), where $\tau^{(0)}$ is a waiting time for the hop $0 \to 1$. We assume that the external magnetic field is directed along the x-axis, so that only the x-components of the fields $b^{(0)}$ and $b^{(1)}$ on the sites $i = 0$ and $i = 1$ are important. If the carrier stays on $i = 0$, then the z-projection of its spin after time t is equal to $\cos b^{(0)}t$. If the carrier hops after time $t_1 < t$, then this projection is equal to $\cos\left[b^{(0)}t_1 + b^{(1)}(t - t_1)\right]$. Taking into account that the moments t_1 are random, the value of $S_z(t)$ can be presented as a sum

$$\begin{aligned} S_z(t) =& p_0(t, \tau^{(0)}) \cos b^{(0)}t \\ &+ \int_0^t dt_1 \frac{d(1 - p_0(t_1, \tau^{(0)}))}{dt_1} \cos\left[b^{(0)}t_1 + b^{(1)}(t - t_1)\right]. \end{aligned} \tag{3.5}$$

The derivative in the integrand is the probability density of the hop. If there is a site $i = 2$ on which the carrier can hop from $i = 1$, the expression Eq. (3.5) gets modified. It acquires a third term describing the possibility of the hop $1 \to 2$, with corresponding waiting time

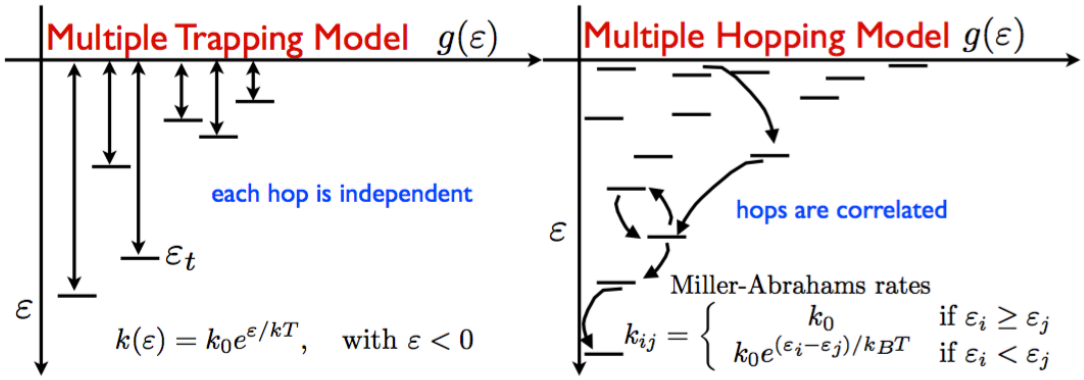

Figure 3.3: (color online). Depictions of multiple trapping (left) and hopping (right) models. Each hop in the multiple trapping model is independent of its previous hops. We call this uncorrelated hopping. By its very nature then, the local fields felt by the spin are also independent at each hop. The multiple hopping models include correlations. For instance, a carrier beginning high in energy (as shown) will tend to cascade downwards in energy when operating under the Miller-Abrahams hopping rates. Since sites are correlated, the local fields are also correlated, which can be important when a spin hops back and forth between a small number of sites (adapted from Ref. [8]).

$\tau^{(1)}$. If this hop takes place, S_z acquires the value $\cos\left[b^{(0)}t_1 + b^{(1)}t_2 + b^{(2)}(t - t_1 - t_2)\right]$, where t_2 is a random residence time on the site $i = 1$ and $b^{(2)}$ is the random field on the site $i = 2$.

For an infinite number of possible hops Eq. (3.5) transforms into an infinite series. Averaging each term over the gaussian distribution of magnetic fields and realizations of waiting times generates a series for average spin projection, $\overline{S}_z(t)$. It can be verified that $\overline{S}_z(t)$ satisfies the equation

$$\overline{S}_z(t) = \left\langle e^{-t/\tau} \right\rangle e^{-b_0^2 t^2} + \int_0^t dt_1 A(t_1) \overline{S}_z(t - t_1), \tag{3.6}$$

where the function $A(t)$ is defined as

$$A(t) = \left\langle \frac{1}{\tau} e^{-t/\tau} \right\rangle e^{-b_0^2 t^2}, \tag{3.7}$$

and $\langle .... \rangle$ stands for averaging over the broadly distributed waiting times. The above closed equation describes the averaged spin relaxation. In the next Section we solve it in different domains of the tail parameter α.

3.3 Solution of equation for $\overline{S}_z(t)$

For concreteness, we choose the distribution function of the waiting times in the form

$$F(\tau) = \frac{C_\alpha \tau_0^\alpha}{(\tau_0^2 + \tau^2)^{\frac{1+\alpha}{2}}}. \tag{3.8}$$

For $\tau \gg \tau_0$, we have $F(\tau) \propto \tau^{-1-\alpha}$, and the coefficient C_α which insures the normalization is given by

$$C_\alpha = \frac{2\Gamma(\frac{1+\alpha}{2})}{\pi^{1/2}\Gamma(\frac{\alpha}{2})}. \tag{3.9}$$

As we demonstrate in the Appendix, for the multiple trapping model [9] the form Eq. (3.8) describes accurately not only the tail but the entire body of the distribution. While the *typical* time, τ_0, is short, $\tau_0 \ll b_0^{-1}$, the distribution has a long tail $F(\tau) \propto \tau^{-1-\alpha}$.

We start the analysis of the basic equation Eq. (3.6) by noticing that at times $t \gg \tau_0$ the first term is small. Indeed, averaging with the help of Eq. (3.8) yields

$$\left\langle e^{-t/\tau} \right\rangle \sim \left(\frac{\tau_0}{t}\right)^\alpha. \tag{3.10}$$

A crucial step of the analysis is making use of the fact that spin relaxation takes place over a large number of hops. This allows one to expand $\overline{S}_z$ in the integrand

$$\overline{S}_z(t - t_1) \approx \overline{S}_z(t) - t_1 \frac{d\overline{S}_z}{dt}(t). \tag{3.11}$$

Upon this expansion, Eq. (3.6) can be easily solved, yielding

$$\overline{S}_z(t) = \exp\Big[-\int_0^t dt_1 \Phi(t_1)\Big], \tag{3.12}$$

where the function $\Phi(t)$ is defined as

$$\Phi(t) = \frac{1 - \int_0^t dt_2 A(t_2)}{\int_0^t dt_2 t_2 A(t_2)}. \tag{3.13}$$

For $\alpha > 1$ the characteristic time, τ_s, for the spin dynamics is much longer than b_0^{-1} (we will check this assumption later). On the other hand, even for wide distribution of the waiting times, the function $A(t)$ falls off dramatically for $t \gtrsim b_0^{-1}$. This allows one to extend the upper limits in the integrals in Eq. (3.13) to ∞. Then Eq. (3.12) reduces to a simple exponential decay

$$\overline{S}_z(t) = \exp\Big(-\frac{t}{\tau_s}\Big), \tag{3.14}$$

with the decay rate given by

$$\frac{1}{\tau_s} = \Phi(\infty) = \frac{\int_0^\infty dt \Big\langle \frac{1}{\tau} e^{-t/\tau} \Big\rangle \Big(1 - e^{-b_0^2 t^2}\Big)}{\int_0^\infty dt t \Big\langle \frac{1}{\tau} e^{-t/\tau} \Big\rangle e^{-b_0^2 t^2}}. \tag{3.15}$$

If the averages in the numerator and denominator decayed rapidly at $t \gtrsim \tau_0$, we would be allowed, by virtue of the condition $b_0 \tau_0 \ll 1$, to replace $\exp\big(-b_0^2 t^2\big)$ by 1 in the denominator and expand $\Big[1 - \exp\big(-b_0^2 t^2\big)\Big]$ in the numerator. In this way, we would retrieve the standard expression Eq. (3.3) for the Dyakonov-Perel relaxation time. Calculating $\langle \tau^2 \rangle$ and $\langle \tau \rangle$ with the help of the distribution Eq. (3.8), we find

$$\frac{1}{\tau_s} = \frac{\pi^{1/2}(\alpha - 1)\Gamma(\frac{\alpha-2}{2})}{2\Gamma(\frac{\alpha+1}{2})} b_0^2 \tau_0 \tag{3.16}$$

This expression is valid if $\langle \tau^2 \rangle$ is finite, which corresponds to $\alpha > 2$. The prefactor in this expression specifies the function $D_1(\alpha)$ in Eq. (3.4). The function $D_1(\alpha)$ falls off monotonically with α. At $\alpha \gg 1$ it behaves as $\left(\frac{2\pi}{\alpha}\right)^{1/2}$.

In the domain $1 < \alpha < 2$ the value of $\langle \tau^2 \rangle$ diverges while $\langle \tau \rangle$ remains finite. The latter still allows one to set $b_0 = 0$ in the denominator of Eq. (3.15), but the numerator cannot be expanded anymore. The explicit expression for the numerator in Eq. (3.15) reads

$$\int_0^\infty dt \Big\langle \frac{1}{\tau} e^{-t/\tau} \Big\rangle \Big(1 - e^{-b_0^2 t^2}\Big) = \int_0^\infty d\tau \int_0^\infty dt \frac{C_\alpha \tau_0^\alpha}{(\tau_0^2 + \tau^2)^{\frac{1+\alpha}{2}} \tau} e^{-t/\tau} \Big(1 - e^{-b_0^2 t^2}\Big) \tag{3.17}$$

Upon introducing the new variables $z = t/\tau$ and $w = b_0 z\tau$, the integral in the right-hand side takes the form

$$C_\alpha (b_0\tau_0)^\alpha \int_0^\infty dz\ z^\alpha e^{-z} \int_0^\infty dw \frac{1 - e^{-w^2}}{[(b_0\tau_0 z)^2 + w^2]^{\frac{\alpha+1}{2}}}. \tag{3.18}$$

Since the characteristic z in Eq. (3.18) is ~ 1, we can neglect $(b_0\tau_0 z)^2$ in the denominator, after which the double integral factorizes, yielding

$$C_\alpha (b_0\tau_0)^\alpha \Gamma(\alpha)\Gamma\Big(\frac{2-\alpha}{2}\Big). \tag{3.19}$$

Then the corresponding expression for the relaxation time in the domain $1 < \alpha < 2$ acquires the form

$$\frac{1}{\tau_s} = (\alpha - 1)\Gamma(\alpha)\Gamma\Big(\frac{2-\alpha}{2}\Big)\frac{(b_0\tau_0)^\alpha}{\tau_0}, \tag{3.20}$$

where the prefactor specifies the function $D_2(\alpha)$ in Eq. (3.4).

3.3.1 Vicinity of $\alpha = 2$

We see that at the demarkation value $\alpha = 2$ both functions $D_1(\alpha)$ and $D_2(\alpha)$ diverge, so that the expressions Eq. (3.16) and Eq. (3.20) yield $\tau_s \to 0$. This suggests that the crossover domain should be treated more carefully. Namely, we rewrite the integral over w in Eq. (3.18) as

$$\int_0^\infty dw \frac{1 - e^{-w^2}}{[(b_0\tau_0 z)^2 + w^2]^{\frac{\alpha+1}{2}}} = \frac{\Gamma(\frac{2-\alpha}{2})}{\alpha} + \int_0^\infty dw \Big[\frac{1}{[(b_0\tau_0 z)^2 + w^2]^{\frac{\alpha+1}{2}}} - \frac{1}{w^{\alpha+1}}\Big]\Big(1 - e^{-w^2}\Big). \tag{3.21}$$

The integral in the right-hand side converges at small $w \sim b_0\tau_0 z$, which allows one to expand $(1 - e^{-w^2})$. Upon introducing the variable $v = (\frac{w}{b_0\tau_0 z})^2$, this integral takes the form

$$\frac{(b_0\tau_0 z)^{2-\alpha}}{2} \int_0^\infty dv \Big[\frac{v^{1/2}}{(1+v)^{\frac{\alpha+1}{2}}} - \frac{1}{v^{\frac{\alpha}{2}}}\Big]. \tag{3.22}$$

Now we rewrite the integral $\int_0^\infty \frac{dv}{v^{\frac{\alpha}{2}}}$ as a sum of integrals from 0 to 1 and from 1 to ∞. The integral from 1 to ∞ is then combined with the first integral in Eq. (3.22) in which domain of integration is shifted by 1. This yields

$$\frac{(b_0\tau_0 z)^{2-\alpha}}{2}\Big[-\int\limits_0^1 dv\frac{1}{v^{\frac{\alpha}{2}}}+\int\limits_1^\infty dq\frac{(q+1)^{1/2}-q^{1/2}}{q^{\frac{\alpha+1}{2}}}\Big]. \tag{3.23}$$

Note that the second integral in the square brackets remains finite at $\alpha = 2$, while the first integral diverges. Keeping only the diverging part and combining it with $\frac{1}{\alpha}\Gamma\Big(\frac{2-\alpha}{2}\Big) \approx \frac{1}{2-\alpha}$, we establish the behavior of the spin relaxation rate Eq. (3.20) near $\alpha = 2$

$$\frac{1}{\tau_s} = 2b_0^2\tau_0|\ln b_0\tau_0|\Upsilon\Big((\alpha-2)|\ln b_0\tau_0|\Big). \tag{3.24}$$

where the crossover function $\Upsilon(z)$ is defined as

$$\Upsilon(z) = \frac{1-e^{-z}}{z}. \tag{3.25}$$

Thus the expressions Eq. (3.16) and Eq. (3.20) are valid outside the interval $|\alpha - 2| \sim |\ln b_0\tau_0|^{-1}$, which is parametrically narrow.

3.3.2 Vicinity of $\alpha = 1$

We see that Eq. (3.20) yields $\tau_s \to \infty$ as α approaches 1 from the above. This is the result of the divergence of $\langle\tau\rangle$ in this limit. To regularize the behavior of Eq. (3.20), we need to calculate the denominator in Eq. (3.15) more accurately. We start from the explicit form of this denominator

$$\int\limits_0^\infty dttA(t) = \int\limits_0^\infty d\tau\int\limits_0^\infty dt\frac{C_\alpha\tau_0^\alpha}{(\tau_0^2+\tau^2)^{\frac{1+\alpha}{2}}\tau}te^{-t/\tau}e^{-b_0^2t^2} \tag{3.26}$$

The same change of variables $z = t/\tau$ and $w = b_0 z\tau$, allows us to cast the integral in the form

$$C_\alpha\tau_0(b_0\tau_0)^{\alpha-1}\int\limits_0^\infty dz\ z^\alpha e^{-z}\int\limits_0^\infty dw\frac{we^{-w^2}}{[(b_0\tau_0 z)^2+w^2]^{\frac{\alpha+1}{2}}}. \tag{3.27}$$

Formally, the singular behavior of this integral at $\alpha = 1$ follows from the fact that at $\alpha = 1$ integration over w yields logarithm if we neglect a small parameter $(b_0\tau_0)^2$ in the denominator. To capture this behavior, we rewrite the integral over w using the integration by parts

$$\int\limits_0^\infty dw\frac{we^{-w^2}}{[(b_0\tau_0 z)^2+w^2]^{\frac{\alpha+1}{2}}} = \frac{1}{\alpha-1}\Big[(b_0\tau_0 z)^{1-\alpha}-\int\limits_0^\infty dw\frac{2we^{-w^2}}{[(b_0\tau_0 z)^2+w^2]^{\frac{\alpha-1}{2}}}\Big]. \tag{3.28}$$

Now we can safely neglect $(b_0\tau_0)^2$ in the denominator and perform the integration over z, which yields

$$\frac{C_\alpha \tau_0 (b_0\tau_0)^{\alpha-1}}{\alpha-1}\Big[\Gamma(2\alpha-1)(b_0\tau_0)^{1-\alpha} - \Gamma(\alpha)\Gamma(\frac{3-\alpha}{2})\Big]. \tag{3.29}$$

Finally, the behavior of τ_s in the vicinity of $\alpha = 1$ can be expressed in terms of the crossover function $\Upsilon(z)$ defined by Eq. (3.25)

$$\begin{aligned}\frac{1}{\tau_s} =& \frac{(\alpha-1)\Gamma(\alpha)\Gamma\left(\frac{2-\alpha}{2}\right)}{\Gamma(2\alpha-1) - \Gamma(\alpha)\Gamma(\frac{3-\alpha}{2})(b_0\tau_0)^{\alpha-1}} \frac{(b_0\tau_0)^\alpha}{\tau_0} \\ \approx& \frac{(\alpha-1)\pi^{1/2}}{1-(b_0\tau_0)^{\alpha-1}} \frac{(b_0\tau_0)^\alpha}{\tau_0} = \frac{\pi^{1/2} b_0}{|\ln b_0\tau_0|} \frac{1}{\Upsilon\Big((1-\alpha)|\ln b_0\tau_0|\Big)}.\end{aligned} \tag{3.30}$$

Unlike Eq. (3.24), the crossover function appears in the denominator. Directly at $\alpha = 1$ Eq. (3.30) yields

$$\frac{1}{\tau_s} = \pi^{1/2}\frac{b_0}{|\ln b_0\tau_0|}. \tag{3.31}$$

The fact that for all α greater than or equal to 1 the value τ_s^{-1} is smaller than b_0 justifies the ansatz: $\overline{S}_z(t-t_1) = \overline{S}_z(t) - t_1 d\overline{S}_z/dt$ and the extension of the upper limit in Eq. (3.13) to ∞.

3.3.3 $\alpha < 1$

For $\alpha < 1$ we cannot extend the limits of integration in Eq. (3.13) to infinity. Instead, we rewrite the expression Eq. (3.7) for $A(t)$ as follows

$$A(t) = \left\langle \frac{1}{\tau} e^{-t/\tau} \right\rangle \left(e^{-b_0^2 t^2} - 1 \right) + \left\langle \frac{1}{\tau} e^{-t/\tau} \right\rangle. \tag{3.32}$$

The integration over t in the second term can be carried out explicitly. Then Eq. (3.13) acquires the form

$$\Phi(t) = \frac{\left\langle e^{-t/\tau} \right\rangle + \int\limits_0^t dt_2 \left\langle \frac{1}{\tau} e^{-t_2/\tau} \right\rangle \left(1 - e^{-b_0^2 t_2^2}\right)}{\int\limits_0^t dt_2 t_2 \left\langle \frac{1}{\tau} e^{-t_2/\tau} \right\rangle e^{-b_0^2 t_2^2}}. \tag{3.33}$$

In calculating both averages we can use the power-law tail of the distribution Eq. (3.8)

$$\left\langle \frac{1}{\tau} e^{-t/\tau} \right\rangle \approx C_\alpha \frac{\tau_0^\alpha}{t^{\alpha+1}} \Gamma(\alpha+1), \quad \left\langle e^{-t/\tau} \right\rangle \approx C_\alpha \frac{\tau_0^\alpha}{t^\alpha} \Gamma(\alpha). \tag{3.34}$$

These expressions apply for $t \gg \tau_0$. Substituting them into Eq. (3.33) and then Eq. (3.34) into Eq. (3.12), we arrive at the final result for $\overline{S}_z(t)$

$$\overline{S}_z(t) = \exp\left[- \int\limits_{b_0\tau_0}^{b_0 t} dx \frac{\frac{1}{x^\alpha} + \alpha \int\limits_0^x dx_1 x_1^{-\alpha-1}(1 - e^{-x_1^2})}{\alpha \int\limits_0^x dx_1 x_1^{-\alpha} e^{-x_1^2}} \right]. \tag{3.35}$$

To analyze Eq. (3.35) in the domain $\tau_0 < t < b_0^{-1}$, we note that for small x the integrand in the exponent behaves as $\frac{1-\alpha}{\alpha x}$, which leads to the power-law decay of $\overline{S}_z(t)$

$$\overline{S}_z(t)\Big|_{t\ll b_0^{-1}} \approx \exp\Big[-\frac{1-\alpha}{\alpha}\ln(t/\tau_0)\Big] = \Big(\frac{\tau_0}{t}\Big)^{\frac{1-\alpha}{\alpha}}. \tag{3.36}$$

This behavior should be compared to the first term in Eq. (3.6), which we neglected. The power-law Eq. (3.36) dominates at $\alpha > 0.6$.

In the long-time limit $b_0 t \gg 1$ the integral in Eq. (3.35) is determined by large x. For large x the integrand saturates at the value $\frac{(1-\alpha)\Gamma(\frac{2-\alpha}{2})}{\alpha\Gamma(\frac{3-\alpha}{2})}$, so that the resulting expression for $\overline{S}_z(t)$ reads

$$\overline{S}_z(t)\Big|_{t\gg b_0^{-1}} \approx \Big(b_0\tau_0\Big)^{\frac{1-\alpha}{\alpha}} \exp\Big[-\frac{(1-\alpha)\Gamma(\frac{2-\alpha}{2})}{\alpha\Gamma(\frac{3-\alpha}{2})} b_0 t\Big]. \tag{3.37}$$

Since we neglected the first term in Eq. (3.6), the result Eq. (3.37) does not capture the initial stage of the decay, which is dominated by this first term. The decay in the entire time domain is described by Eq. (3.37) when α is so close to 1 that the prefactor in Eq. (3.37) is not small. Then Eq. (3.37) captures the spin decay, which is a simple exponent with

$$\frac{1}{\tau_s} \approx (1-\alpha)\pi^{1/2} b_0. \tag{3.38}$$

Comparing this to Eq. (3.4), we conclude that the function $D_3(\alpha)$ has the form $(1-\alpha)\pi^{1/2}$ near $\alpha = 1$. Note that this expression is consistent with Eq. (3.30) for $(\alpha-1) \gg |\ln(b_0\tau_0)|^{-1}$.

The overall behavior of the relaxation rate with α is illustrated in Fig. 3.4. In Fig. 3.5 we plot the time evolution of $\ln \overline{S}_z(t)$ using the general expression Eq. (3.35). We see that the smaller α is, the later the curves converge to the straight lines corresponding to a simple exponential behavior. The convergence is final only for biggest $\alpha = 0.9$. For smaller α-values the slopes keep increasing with time beyond the maximal $t = 1.5/b_0$ shown in the figure. The slopes saturate at the values predicted by Eq. (3.37) only at very large times.

3.4 Spin echo decay with a Lévy-type waiting times distribution

It is well known[10] that the motion narrowing strongly affects the decay of the spin echo, which is formally defined as $\overline{S}_E(T) = \big\langle \exp\Big[i\Big(\int\limits_0^{\frac{T}{2}} dtb(t) - \int\limits_{\frac{T}{2}}^{T} dtb(t)\Big)\Big]\big\rangle$. If the random magnetic field is characterized by a single correlation time τ, the decay of the spin echo would follow the FID signal, i.e., $\overline{S}_E(T) = \overline{S}(T)$. The situation is very different for the

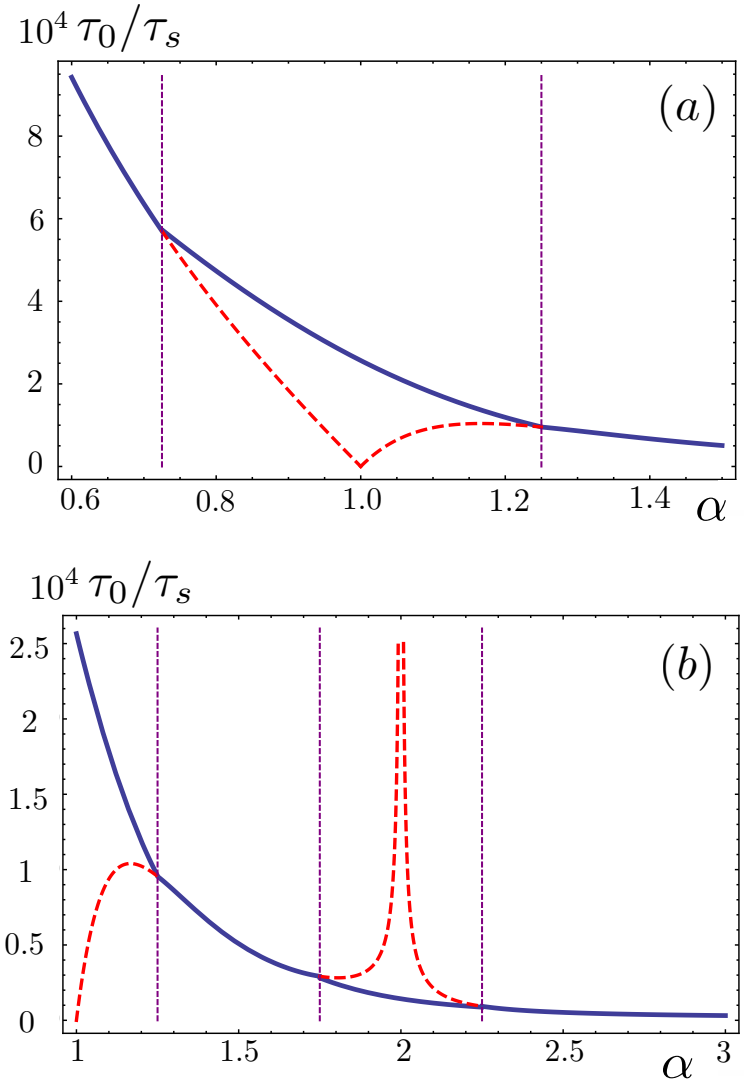

Figure 3.4: (color online). The relaxation rate depends on tail-parameter. (a) Acceleration of the relaxation rate with decreasing the tail-parameter, α, is illustrated in the domain $0.6 < \alpha < 1.5$. Dashed red curves are plotted from Eq. (3.38) (for $\alpha < 1$), and Eq. (3.20) (for $1 < \alpha < 1.5$). The curves exhibit a dip near $\alpha = 1$. They are connected by the crossover expression Eq. (3.30). (b) Domain $1 < \alpha < 3$. Dashed red curves are plotted from Eq. (3.20) (for $1 < \alpha < 2$), and from Eq. (3.16) (for $\alpha > 2$). The curves exhibit a divergence near $\alpha = 2$. They are connected by the crossover expression Eq. (3.24). All the curves are plotted for $b_0\tau_0 = 10^{-3}$.

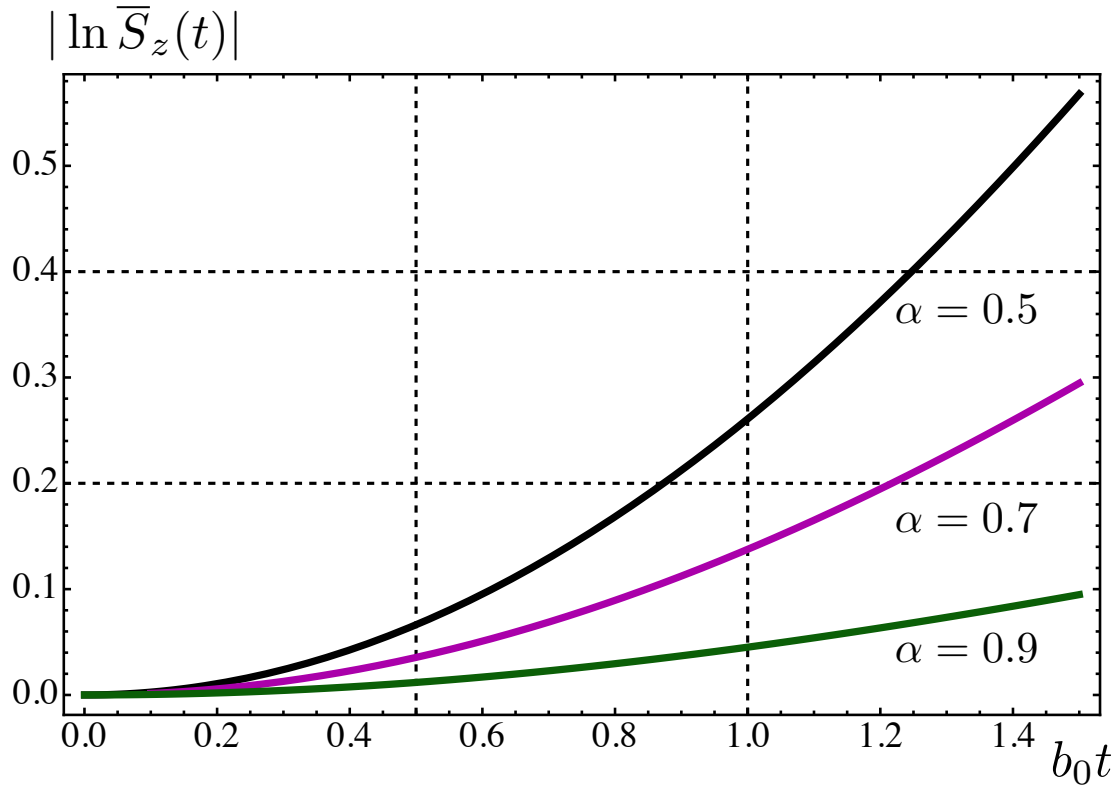

Figure 3.5: (color online). The time evolution of $|\ln \overline{S}_z(t)|$ is plotted from Eq. (3.35) for $b_0\tau_0 = 10^{-3}$ and the values of the tail-parameter: $\alpha = 0.9$ (green), $\alpha = 0.7$ (purple), and $\alpha = 0.5$ (black). The smaller α is, the later the curves converge to the straight lines. The convergence is final only for $\alpha = 0.9$. For smaller α the slopes keep increasing with time beyond the maximal $t = 1.5/b_0$ and saturate at the values predicted by Eq. (3.37) only at very large times. The domain where the first term in Eq. (3.6) dominates the decay corresponds to $b_0 t \lesssim 10^{-3}$, and is not represented in the figure.

broad distribution of τ. Indeed, the shortening of the FID time, τ_s, for distribution Eq. (3.8) with power-law tail was due to the possibility for a carrier to occasionally sit on a given site, i, during the time, τ_i, much longer than a typical time, τ_0. These sites give anomalously strong contribution, $\left\langle \exp\left[i\int\limits_{t_i}^{t_i+\tau_i} dt b_i(t)\right]\right\rangle$, to the decay. The same physics suggests that, for distribution of τ with power-law tail, the echo signal will decay *slowly* with T. This is because the contributions from anomalously long residence times are eliminated in the echo signal. To quantify this statement, consider a situation when a carrier populates a certain site, i, at time $T_1 < T/2$ and leaves it at time $T_2 > T/2$. Then the contribution from this site to the unaveraged echo signal is given by

$$\exp\left\{ib_i\left[\left(\frac{T}{2}-T_1\right)-\left(T_2-\frac{T}{2}\right)\right]\right\}=\exp\left[ib_i\Big(T-T_1-T_2\Big)\right]. \tag{3.39}$$

Assume now that the carrier makes many hops before arrival to the site i and many hops after departure from the site i. Then the probabilities to preserve spin during the time intervals $(0,T_1)$ and (T_2,T) are given by $\exp\left[-T_1/\tau_s\right]$ and $\exp\left[-(T-T_2)/\tau_s\right]$, respectively. As a result, the contribution to $\overline{S}_E(T)$ from this realization of the random fields reads

$$\int\limits_0^{\frac{T}{2}}\frac{dT_1e^{-\frac{T_1}{\tau_s}}}{\tau_s}\int\limits_{\frac{T}{2}}^{T}\frac{dT_2e^{-\frac{T-T_2}{\tau_s}}}{\tau_s}\Big\langle p_0(T_2-T_1,\tau)\Big\rangle e^{-b_0^2(T-T_1-T_2)^2}. \tag{3.40}$$

To analyze this expression, it is convenient to introduce a new variable, $T_3 = T - T_2$. Then it takes the form

$$\int\limits_0^{\frac{T}{2}}\frac{dT_1e^{-\frac{T_1}{\tau_s}}}{\tau_s}\int\limits_{0}^{\frac{T}{2}}\frac{dT_3e^{-\frac{T_3}{\tau_s}}}{\tau_s}\Big\langle p_0(T-T_3-T_1,\tau)\Big\rangle e^{-b_0^2(T_3-T_1)^2}. \tag{3.41}$$

The average in Eq. (3.41) is equal to $C_\alpha\Gamma(\alpha)\tau_0^\alpha/\big(T-T_3-T_1\big)^\alpha$, see Eq. (3.34).

The most sound consequence of Eq. (3.41) is that the echo signal survives at times much longer than τ_s. Indeed, characteristics T_1, T_3 in Eq. (3.41) are $\sim\tau_s$. For $T\gg\tau_s$ the upper limits in the integrals can be extended to infinity, while the average can be replaced by $C_\alpha\Gamma(\alpha)\tau_0^\alpha/T^\alpha$. Then we get

$$C_\alpha\Gamma(\alpha)\Big(\frac{\tau_0}{T}\Big)^\alpha\int\limits_0^\infty dx\ e^{-x}\int\limits_0^\infty dy\ e^{-y}\exp\Big[-b_0^2\tau_s^2(x-y)^2\Big], \tag{3.42}$$

where we have introduced the dimensionless variables $x = T_1/\tau_s$ and $y = T_3/\tau_s$. Within a numerical constant the double integral is equal to $\big(b_0\tau_s\big)^{-1}$. Thus, we conclude that the echo signal falls off as a power law:

$$\overline{S}_E(T) \sim \left(b_0\tau_s\right)^{-1}\left(\frac{\tau_0}{T}\right)^{\alpha}. \tag{3.43}$$

It is seen from Eq. (3.43) that $\overline{S}_E(T)$ contains a small parameter $\left(b_0\tau_s\right)^{-1}$. At this point, we note that due to a long tail in the waiting time distribution, there is a nonexponential probability that during time, T, the carrier does not hop at all. The contribution to echo signal from such realizations does not contain random magnetic field and falls with T in the same way as Eq. (3.43). Thus, the final result for the echo signal reads

$$\overline{S}_E(T) = \Big\langle p_0(T,\tau)\Big\rangle = C_\alpha\Gamma(\alpha)\Big(\frac{\tau_0}{T}\Big)^{\alpha}. \tag{3.44}$$

3.5 Concluding remarks

As a quantitative measure of acceleration of the relaxation rate, caused by the tail in the distribution, $F(\tau)$, one can consider a ratio of the times for the values of the tail-parameter $\alpha = 1$ and $\alpha = 2$. From Eqs. (3.24) and (3.31) one finds

$$\frac{\tau_s(\alpha=2)}{\tau_s(\alpha=1)} = \frac{\pi^{1/2}}{2b_0\tau_0|\ln(b_0\tau_0)|^2}. \tag{3.45}$$

Both values of τ_s are determined by the tail. Parametrical, in $b_0\tau_0 \ll 1$, difference between the two values is due to the fact that for $\alpha = 1$ the portion of sites on which the carrier spin exercises a full rotation is $\sim (b_0\tau_0)$ for $\alpha = 1$ and $\sim (b_0\tau_0)^2$ for $\alpha = 2$.

In replacing the expression Eq. (3.12) by $\exp(-t/\tau_s)$, we argued that this replacement is valid for $t \gtrsim b_0^{-1}$. This means that in Eq. (3.12) we chose the lower limit $t_1 \sim b_0^{-1}$. Uncertainty in this lower limit leads to uncertainty in the prefactor in Eq. (3.14) $\sim \exp\Big(1/b_0\tau_s\Big)$, which can be neglected since the product $b_0\tau_s$ is big. Yet another contribution to the prefactor comes from $\int\limits_{\tau_0}^{1/b_0} dt_1\Phi(t_1)$. To estimate this contribution, we note that for $t \lesssim b_0^{-1}$

$$\Phi(t)\Big|_{t<b_0^{-1}} \approx \frac{1-\int\limits_0^t dt_2\Big\langle \frac{1}{\tau}e^{-t_2/\tau}\Big\rangle}{\int\limits_0^t dt_2 t_2\Big\langle \frac{1}{\tau}e^{-t_2/\tau}\Big\rangle} = \frac{\Big\langle e^{-t/\tau}\Big\rangle}{\Big\langle \tau-(t+\tau)e^{-t/\tau}\Big\rangle}. \tag{3.46}$$

For $t \gtrsim \tau_0$ we can neglect the second term in the denominator and perform integration over time, yielding

$$\int\limits_0^t dt_1\Phi(t_1)\Big|_{t<b_0^{-1}} = \frac{\Big\langle \tau(1-e^{-t/\tau})\Big\rangle}{\langle\tau\rangle}. \tag{3.47}$$

Thus, the contribution to the prefactor from small times does not exceed 1. In fact, the contribution Eq. (3.47) comes from neglecting the first term, $\big\langle \exp(-\frac{t}{\tau}-b_0^2t^2)\big\rangle$, in the basic

equation Eq. (3.6). We effectively replaced the first by the initial condition: $\overline{S}_z(t \sim \tau_0) = 1$. More accurate calculation, based on the Laplace transform, suggests that for $\alpha > 1$ the true prefactor is 1.

Formal solution of Eq. (3.6) can be expressed in the form of the inverse Laplace transform, see, e.g., Ref. [15]

$$\overline{S}_z(t) = \frac{1}{2\pi i} \int\limits_{\gamma - i\infty}^{\gamma + i\infty} \frac{S_z^{(0)}(s)}{1 - K(s)} \tag{3.48}$$

where the functions $S_z^{(0)}(s)$ and $K(s)$ are defined as

$$S_z^{(0)}(s) = \int\limits_0^\infty dt \Big\langle e^{-t/\tau} \Big\rangle e^{-st - b_0^2 t^2}, \tag{3.49}$$

$$K(s) = \int\limits_0^\infty dt \Big\langle \frac{1}{\tau} e^{-t/\tau} \Big\rangle e^{-st - b_0^2 t^2}$$

The decay of $\overline{S}_z(t)$ is defined by the poles, $s = s_0$, for which $K(s_0) = 1$. For $\alpha > 1$, one can retain only the smallest s_0 and find it by expanding $K(s)$ at small s. This readily yields $s_0 = -\Phi(\infty) = -\tau_s^{-1}$, i.e., the same expression Eq. (3.15) for the decay rate as was found in Sect. II from the different approach. The justification for expanding $K(s)$ is that the exponent $\exp\big(-b_0^2 t^2\big)$ ensures the convergence of the integral Eq. (3.49) at $t \sim b_0^{-1}$ when $\exp\big(-s_0 t\big)$ is close to 1. Thus, for $\alpha > 1$, the results of the two approaches to solving Eq. (3.6) coincide. Moreover, the solution Eq. (3.48) takes into account the first term in Eq. (3.6), which we have neglected. The prefactor in front of $\exp\big(-t/\tau_s\big)$ calculated from Eq. (3.48) is given by

$$-\frac{S_z^{(0)}(s_0)}{K'(s_0)} \approx \frac{\int\limits_0^\infty dt \Big\langle e^{-t/\tau} \Big\rangle e^{-b_0^2 t^2}}{\int\limits_0^\infty dt\ t \Big\langle \frac{1}{\tau} e^{-t/\tau} \Big\rangle e^{-b_0^2 t^2}}. \tag{3.50}$$

It appears that we can neglect the exponent $\exp\big(-b_0^2 t^2\big)$ in the integrands in the numerator and the denominator. This is because both integrals converge for $\alpha > 1$ and are equal to $\langle \tau \rangle$, which is finite for $\alpha > 1$. Thus the true prefactor is equal to 1, as was mentioned above.

For $\alpha < 1$ the formal solution Eq. (3.48) becomes useless. This is because the pole s_0 cannot be found analytically, and, moreover, many poles (corresponding to $s \sim b_0$) contribute to $\overline{S}_z(t)$. This also follows from our solution Eq. (3.36) and from Fig. 3.5. It is seen that $\overline{S}_z(t)$ follows a simple exponential behavior only for large times, $b_0 t \gtrsim 1$.

In the paper [8] the effect of the power-law tail in $F(\tau)$ on the decay of $\overline{S}_z(t)$ was analyzed. The analysis relied on the solution of Eq. (3.6) in the form of Eq. (3.48). The

authors did not analyze the behavior of τ_s in different domains of the tail-parameter, α. They rather realized that retaining a singles pole becomes inadequate for $\alpha < 1$, and resorted to the numerics. Our results Eqs. (3.16), (3.20) and Eqs. (3.24), (3.30) for the crossover domains are fully analytical. Obtaining these results was facilitated by exploiting the small parameter $b_0\tau_0 \ll 1$ for $\alpha > 1$ and by solving Eq. (3.6) using an alternative approach for $\alpha < 1$.

3.6 Appendix: Applicability of the waiting times distribution Eq. (3.8) to the multiple trapping model

In the multiple trapping model [3-9], the waiting time is determined by activation of an electron from a localized state in the tail to the conduction band. If the energy position of the localized state is $-\varepsilon$, then the activation rate is equal to $\Gamma(\varepsilon) = \Gamma_0 \exp[\varepsilon/\mathcal{T}]$, where $\mathcal{T}$ is the temperature. Actual waiting times, t_i, are random. While the average waiting time is Γ^{-1}, the distribution of the waiting times for a given ε is given by the Poisson distribution

$$f_\varepsilon(\tau) = \Gamma(\varepsilon) \exp\left[-\Gamma(\varepsilon)\tau\right]. \tag{3.51}$$

The remaining task is to average $f_\varepsilon(\tau)$ over ε with the weight determined by the density of the tail states, $g(\varepsilon)$. In the multiple trapping model the form of $g(\varepsilon)$ is a simple exponent $g(\varepsilon) \propto \exp\left[\varepsilon/\mathcal{T}_0\right]$. The final expression for the waiting times distribution reads

$$F(\tau) \propto \int\limits_{-\infty}^{0} d\varepsilon g(\varepsilon) f_\varepsilon(\tau) \propto \frac{\alpha}{\tau^{\alpha+1}} \int\limits_{0}^{\Gamma_0\tau} dx\ x^\alpha e^{-x}, \tag{3.52}$$

where $\alpha = \mathcal{T}/\mathcal{T}_0$. For large waiting times $\tau \gg \Gamma_0^{-1}$, we have $F(\tau) \propto \tau^{-(\alpha+1)}$. At $\tau \to 0$ the power-law divergence is cut off. The character of cutoff is not precisely the one given by Eq. (3.8), but they match very closely, as illustrated in the Figure 3.6. In organic semiconductors the density of the tail states is better approximated by a stretched-exponential form $g(\varepsilon) \propto \exp\left[-\left(|\varepsilon|/\mathcal{T}_0\right)^p\right]$, with p close to 2; see Refs. [16-18]. Repeating the above steps for this $g(\varepsilon)$ we found that $F(\tau)$ can still be closely approximated with Eq. (3.8); see Figure 3.6.

In conclusion, we emphasize that in the multiple trapping model, upon activation into the conduction band, the carrier completely "forgets" about the site it was activated from. Thus the hyperfine fields "seen" by the carrier are completely uncorrelated. At low temperatures, the motion of carriers between the sites is by phonon-assisted hops. This allows the carrier, after completing a hop, to hop back to the initial site, as illustrated in Fig. 3.3, right panel. Obviously, such a back-hop would lead to a correlation between the partial fields, and consequently accelerate the relaxation [18].

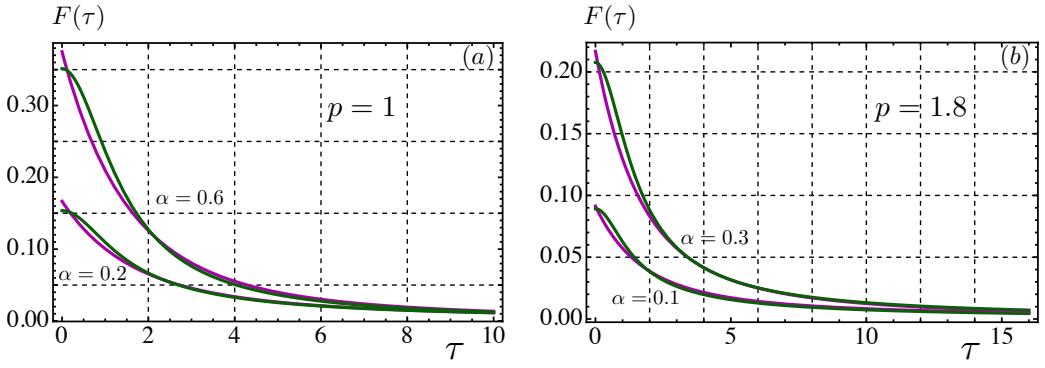

Figure 3.6: (color online). Distribution function, $F(\tau)$, of the waiting times in the multiple-trapping model is shown with purple lines for the densities of tail states of the form $g(\varepsilon) \propto \exp\left[-\left(|\varepsilon|/\mathcal{T}_0\right)^p\right]$ with $p = 1$ (a) and $p = 1.8$ (b). Green lines are the interpolations of $F(\tau)$ with the form Eq. (3.8) of the main text.

3.7 References

[1] P. W. Anderson and P. R. Weiss, Rev. Mod. Phys. **25**, 269 (1953).

[2] M. I. Dyakonov and V. I. Perel, Sov. Phys. Solid State **13**, 3023 (1971).

[3] H. Scher and E. W. Montroll, Phys. Rev. B **12**, 2455 (1975).

[4] J. Noolandi, Phys. Rev. B **16**, 4466 (1977).

[5] T. Tiedje, J. M. Cebulka, D. L. Morel, and B. Abeles, Phys. Rev. Lett. **46**, 1425 (1981).

[6] B. Hartenstein, H. Bässler, A. Jakobs, and K. W. Kehr, Phys. Rev. B **54**, 8574 (1996).

[7] N. J. Harmon and M. E. Flatte, Phys. Rev. Lett. **110**, 176602 (2013).

[8] N. J. Harmon and M. E. Flatte, Phys. Rev. B **90**, 115203 (2014).

[9] S. D. Baranovskii, Phys. Stat. Sol. (b) **251**, 487 (2014).

[10] J. R. Klauder and P. W. Anderson, Phys. Rev. **125**, 912 (1962).

[11] P. A. Bobbert, W. Wagemans, F.W. A. van Oost, B. Koopmans, and M. Wohlgenannt, Phys. Rev. Lett. **102**, 156604 (2009). T. D. Nguyen, G. Hukic-Markosian, F. Wang, L. Wojcik, X.-G. Li, E. Ehrenfreund, and Z. V. Vardeny, Nat. Mater. **9**, 345 (2010).

[12] R. Czech and K. W. Kehr, Phys. Rev. Lett. **53**, 1783 (1984); Phys. Rev. B **34**, 261 (1986).

[13] R. C. Roundy and M. E. Raikh, Phys. Rev. B **90**, 201203(R) (2014).

[14] V. V. Mkhitaryan and V. V. Dobrovitski, Phys. Rev. B **92** 054204 (2015).

[15] K. W. Kehr, G. Honig, and D. Richter, Z. Phys. B **32**, 49 (1978).

[16] S. D. Baranovskii, H. Cordes, F. Hensel, and G. Leising, Phys. Rev. **62**, 7934 (2000).

[17] J. O. Oelerich, D. Huemmer, and S. D. Baranovskii, Phys. Rev. Lett. **108**, 226403 (2012).

[18] R. C. Roundy and M. E. Raikh Phys. Rev. B **90**, 241202(R) (2014).

[19] C. P. Poole and H. A. Farach, Bull. Magn. Reson. **l**, **4**, 162 (1979).

PART II

SPIN TRANSPORT

CHAPTER 4

SPIN PUMPING FROM A FERROMAGNET INTO A HOPPING INSULATOR: THE ROLE OF RESONANT ABSORPTION OF MAGNONS

4.1 Introduction

The phenomenon of spin pumping from a ferromagnet (F) into a normal (N) layer is one of the most prominent approaches to the generation of pure spin currents. A prime manifestation that pumping indeed takes place in realistic F-N structures is the additional broadening [1] of the ferromagnetic resonance (FMR) in F, caused by a contact with the N-layer. This additional broadening was first observed experimentally in Ref. [2]. Another, more delicate, manifestation of pumping was reported shortly after. Namely, the injected spin current, entering the nonmagnetic material with spin-orbit coupling (like Pt), causes a voltage drop across the current direction. This voltage drop is due to the inverse spin-Hall effect [3] (ISHE), and has a maximum when the frequency of the microwave radiation driving the ferromagnet, ω, is equal to the FMR frequency, ω_{FMR}. In Fig. 4.1 the detection of spin current by means of ISHE is illustrated schematically together with setup for the spin pumping experiment. Fig. 4.2 demonstrates that the shape of FMR broadened due to spin pumping coincides with measured ISHE voltage signal.

Pioneering observations of pumping via ISHE in Refs. [4-6] utilized Pt as the normal layer [7-9]. They were followed by reports on similar observations of pumping into different materials [10-13], including prominent semiconductors GaAs [14], Si [15, 16], Ge [17], and, most recently, graphene [18]. Experimental results on the electric field generated due to ISHE , $\boldsymbol{E}_{ISHE}$, are analyzed using the relation $\boldsymbol{E}_{ISHE} \propto \boldsymbol{J}^{(s)} \times \boldsymbol{\sigma}$, where $\boldsymbol{J}^{(s)}$ determines the spatial direction of the spin current flow and its magnitude, while $\boldsymbol{\sigma}$ is its polarization. The magnitude of the spin current is given by

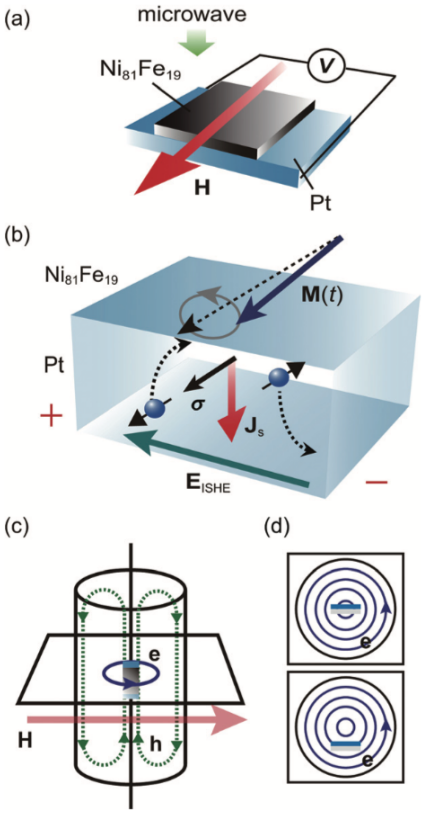

Figure 4.1: (color online). Experiment of spin pumping. (a) A schematic illustration of the $Ni_{81}Fe_{19}$/Pt film used in the present study. **H** is the external magnetic field. (b) A schematic illustration of the spin pumping and the inverse spin-Hall effect in the $Ni_{81}Fe_{19}$/Pt film. $\mathbf{M}(t)$ is the magnetization in the $Ni_{81}Fe_{19}$ layer. $\mathbf{E}_{ISHE}$, $\mathbf{J}_s$, and σ denote the electromotive force due to the inverse spin-Hall effect, the spatial direction of a spin current, and the spin-polarization vector of the spin current, respectively. (c) The sample configuration in a TE_{011} microwave cavity. At the center of the cavity, the magnetic-field component **h** of the microwave is maximized while the electric field component e is minimized. An external dc magnetic field **H** was applied perpendicular to the direction across the electrodes along the film plane. (d) Schematic illustrations of the sample placed along the longitudinal axis of the cavity at the cavity canter (top panel) and off the cavity center (bottom panel) (adapted from Ref. [9]).

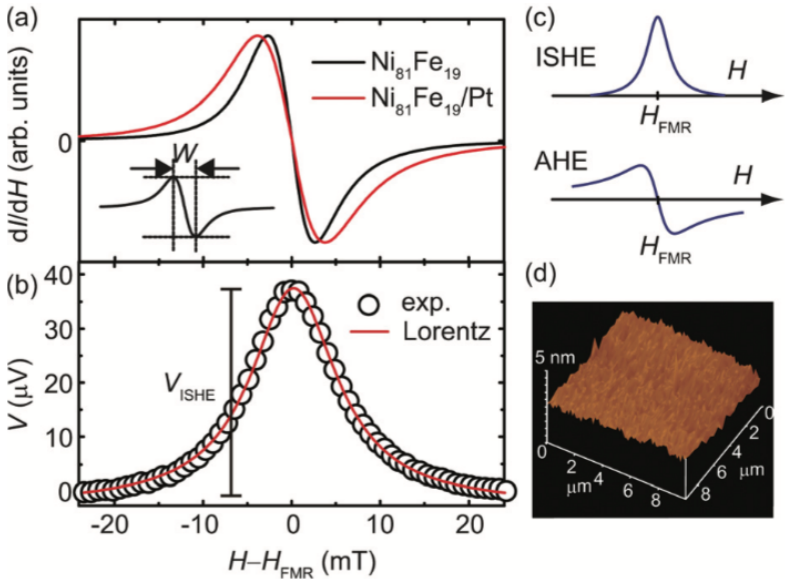

Figure 4.2: (color online). Experiment of spin pumping. (a) Field (H) dependence of the FMR signals $dI(H)/dH$ for the $Ni_{81}Fe_{19}$/Pt film and the $Ni_{81}Fe_{19}$ film. Here, I denotes the microwave absorption intensity. H_{FMR} is the resonance field. The inset shows the definition of the spectral width W in the present study. (b) Field dependence of the electric-potential difference V for the $Ni_{81}Fe_{19}$/Pt film under the 200 mW microwave excitation. The open circles are the experimental data. The curve in red shows the fitting result using a Lorentz function for the V data. (c) The spectral shape of the electromotive force due to the inverse-spin Hall effect (ISHE) and the anomalous-Hall effect (AHE). (d) An atomic force microscope image of the surface of the $Ni_{81}Fe_{19}$ layer, where the surface roughness $Ra = 1.9 \times 10^{-1}$ nm(adapted from Ref. [9]).

$$J^{(s)} = g_{\uparrow\downarrow} C \Big[\boldsymbol{m}(t) \times \frac{d\boldsymbol{m}(t)}{dt} \Big]_z , \tag{4.1}$$

where z axis is taken along the static part of the magnetization. In Eq. (4.1) the constant C characterizes the properties of the normal layer (like ratio of thickness to the spin-diffusion length) as well as the properties metal-ferromagnet interface, while $\boldsymbol{m}(t)$ describes the magnetization dynamics in the ferromagnet. The expression for $J^{(s)}$ has the same form as the damping term in the equation that governs $\boldsymbol{m}(t)$. It was a remarkable experimental finding [5] that ISHE voltage exhibits essentially the same behavior as a function of microwave power and the deviation of ω from ω_{FMR} as the additional FMR damping.

Microscopic physics of pumping is encoded in the mixing constant [1, 3, 19] $g_{\uparrow\downarrow}$ in Eq. (4.1). A fundamental process underlying the pumping is the inelastic electron-magnon scattering at the F-N interface. Microscopic treatment of this scattering [21, 22] assumes that electrons of the normal layer impinging on the interface with ferromagnet are *plane waves*. On the other hand, in a number of recent papers [19-22] spin pumping into organic materials sandwiched between ferromagnet and Pt has been reported. Strong temperature dependence of the resistance in these materials [27] suggests that the charge transport is due to hopping of polarons [20, 22], so that the description of pumping based on plane waves does not apply. This raises the question about the microscopics of spin pumping in the localized regime.

In the present paper we consider theoretically the spin pumping into a hopping insulator using the minimal model of coupling of localized states to a ferromagnet. Within this minimal model the ferromagnet is treated as a wide-gap insulator. We demonstrate that, unlike metals, the underlying process responsible for pumping is the resonant magnon absorption accompanied by transitions between localized states; see Fig. 4.3. A distinctive feature of pumping into an insulator is that that the pumping efficiency, commonly described by a constant, $g_{\uparrow\downarrow}$, depends strongly on the external dc magnetic field. This is because, in addition to causing the spin precession in a ferromagnet, this field modifies the spin structure of the localized states between which the magnon is absorbed; see Fig. 4.3. The effect of external field is most pronounced when the waiting time for a hop is longer than the period of the ac field which drives the FMR. Since the resonance frequency, ω_{FMR}, depends on the orientation of the external field [28], for certain orientations [29] this frequency coincides with the Zeeman splitting of the localized states, Fig. 4.4. Spin pumping is most efficient for such orientations, since the absorption of magnon takes place within *individual* sites. We also show that, with no charge current, the spin polarization generated at the F-N boundary

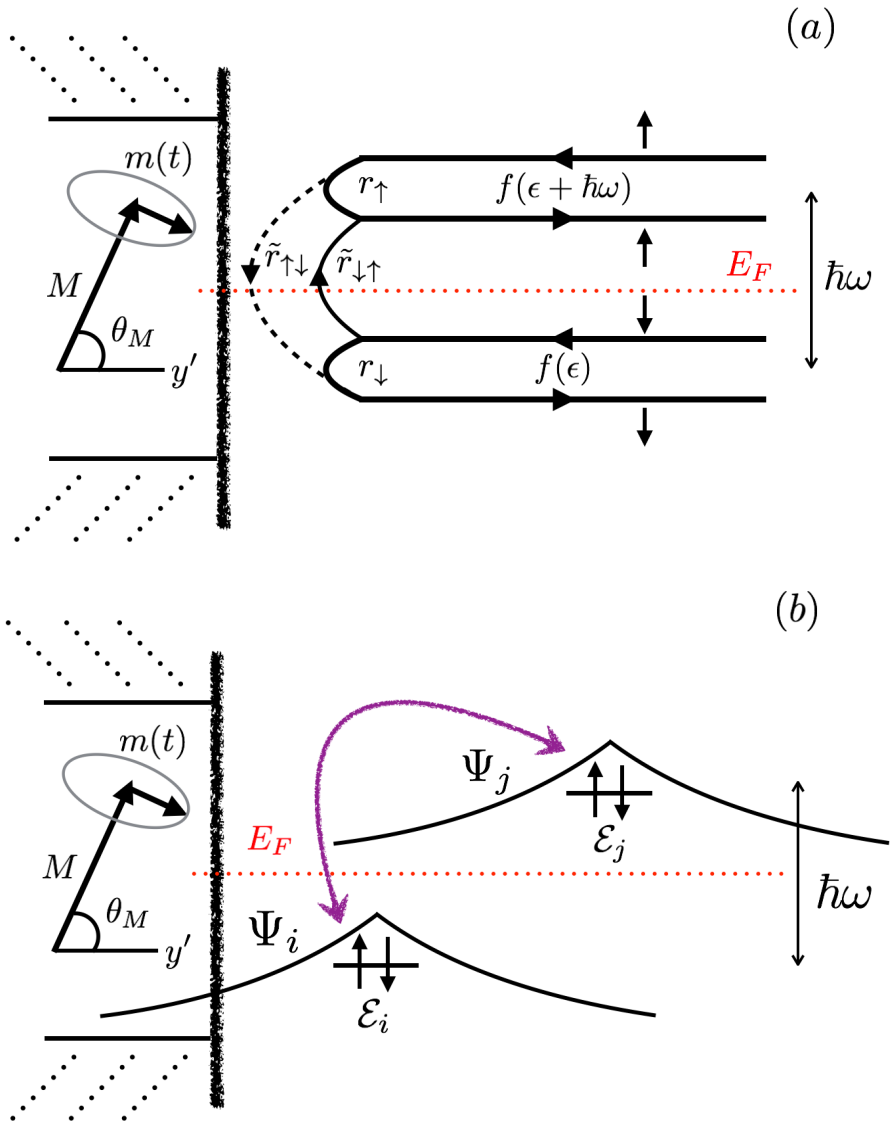

Figure 4.3: (color online). Elementary processes underlying the spin pumping into a metal (a), and into an insulator (b). In the metal, an $\uparrow$ electron, impinging on the N-F boundary, is primarily reflected elastically with amplitude $r_\uparrow$ (vertical separation of left and right arrows is a guide to an eye). Spin precession in F gives rise to inelastic reflection with amplitude $\tilde{r}_{\uparrow\downarrow}$ associated with the emission of a magnon. A $\downarrow$ electron is either reflected elastically with amplitude $r_\downarrow$, or inelastically, after absorbing of a magnon, with amplitude $\tilde{r}_{\downarrow\uparrow}$. The injected spin current is proportional to $|\tilde{r}_{\uparrow\downarrow}|^2\omega\frac{\partial f}{\partial \varepsilon}$. In the insulator, only inelastic processes are at work. Emission and absorption of magnons take place within pairs of localized states.

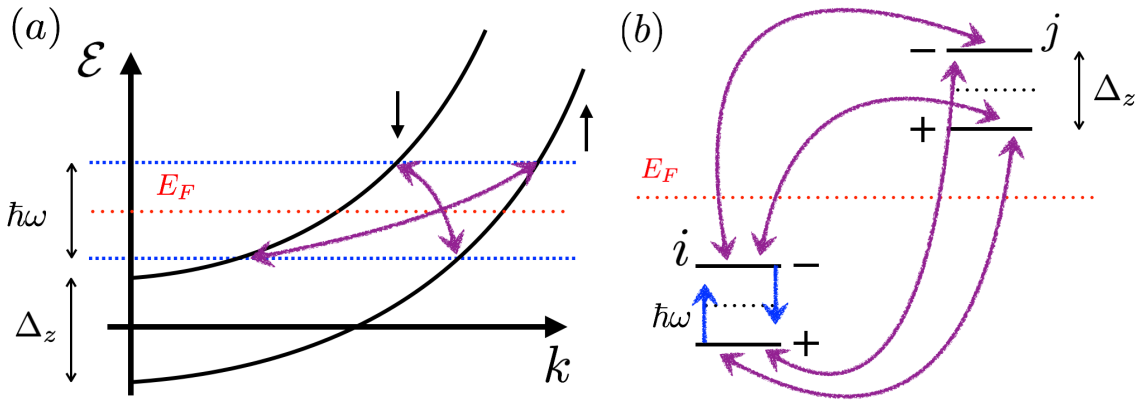

Figure 4.4: (color online). Illustration of pumping in metal (a) and in an insulator (b) in the presence of a Zeeman splitting, Δ_z. In metal, the absorption (emission) of a magnon, $\hbar\omega$, near the F-N boundary does not conserve momentum, and thus is insensitive to the ratio $\Delta_z/\hbar\omega$. By contrast, in insulator, and near the condition $\hbar\omega = \Delta_z$, the absorption (emission) of a magnon is *resonant*.

spreads in the insulator along the same percolation network [30, 31] that determines the electrical resistance.

4.2 Absorption of magnons at F-N boundary

4.2.1 General considerations

Figure 4.4 illustrates the difference between pumping into a metal, and into an insulator in an applied magnetic field, $\boldsymbol{H}$. While $\boldsymbol{H}$ is responsible for the magnetization precession in the ferromagnet, it also causes a spin splitting, Δ_z, of the spectrum in the metallic normal layer, Fig. 4.4(a). This splitting, however, does not affect the absorption of magnons. The reason is that the absorption at a boundary does not require momentum conservation, i.e., the matrix element is constant, and thus there is no dependence of the spin current, $I^{(s)}$, on the dc field in the normal layer.

The situation is different for an insulator, where the magnon absorption takes place between the discrete levels, Fig. 4.4(b). In this case, and for a general orientation of $\boldsymbol{H}$, the Zeeman levels are the linear combinations of $\uparrow$ and $\downarrow$ spin states. As a result, transitions from *each* of the initial states on site i to *both* final states on site j are allowed. This fact distinguishes absorption of magnons from the conventional absorption of an ac *electric* field [32-34] and, as we will see below, gives rise to $\boldsymbol{H}$-dependence of the spin current. Another origin of $\boldsymbol{H}$-dependence is the possibility of *intrasite* absorption of magnons at the boundary. We will see that the intrasite transitions dominate the absorption near the resonant condition $\hbar\omega = \Delta_z$. Away from this condition, the intersite transitions dominate.

4.2.2 The model

Consider a pair of localized states, i and j, Fig. 4.4(b). Assume for simplicity that the ferromagnet is an insulator, i.e., it is a barrier for electrons in N. Precession, $\boldsymbol{m}(t)$, of magnetization in a ferromagnet can be modeled as a time-dependent correction $\propto \boldsymbol{m}(t)\hat{\sigma}$ to the barrier potential. The pumping takes place since the wave function, Ψ_i, can penetrate under the barrier. As a result, the Hamiltonian of site i has a correction

$$\delta\hat{H}_i = J\Big[\hat{\sigma}_x m_x \sin\omega t + \hat{\sigma}_y m_y \cos\omega t\Big], \tag{4.2}$$

where J accounts for tunneling. Projections $m_x(t)$ and $m_y(t)$ are proportional to the magnitude of the microwave field and depend in a resonant way on the proximity of ω to ω_{FMR}. Analytical expressions for these projections can be found, e.g., in Ref. [9].

The Hamiltonian $\delta\hat{H}_i$ of Eq. (4.2) causes transitions of electrons between the sites i and j. Absorption of energy in the course of these transitions is quite similar to the absorption

of the ac *electric* field by pairs of the localized states. However, the transitions caused by $\delta\hat{H}_i$ are accompanied by spin flips, both from $\uparrow$ to $\downarrow$, and from $\downarrow$ to $\uparrow$. With regard to absorption of energy, one should add up the contributions of both types of transitions, i.e.,

$$I^{(e)} = I_{\downarrow\to\uparrow} + I_{\uparrow\to\downarrow} \tag{4.3}$$

However, the spin current results from the fact that these contributions are not equal to each other, so that

$$I^{(s)} = I_{\downarrow\to\uparrow} - I_{\uparrow\to\downarrow}. \tag{4.4}$$

Thus, for calculation of the spin current into the hopping insulator, one can use the standard "resonant" phononless absorption theory [32] and substitute the corresponding rates into Eq. (4.4).

4.2.3 Resonant absorption at $\boldsymbol{H} = 0$

We first neglect the Zeeman splitting in the normal layer. In this case resonant transitions happen within pairs of localized states, Fig. 4.3b. The correction $\delta\hat{H}_i$ causes such transitions between the sites i and j because the corresponding wave functions $|i\rangle$ and $|j\rangle$ have a finite overlap integral, t_{ij} [33]. Due to this overlap, the eigenfunctions of the pair get modified as

$$\begin{aligned} |\mathbf{i}\rangle &= \sqrt{\frac{\Gamma+\delta\varepsilon}{2\Gamma}}|i\rangle + \sqrt{\frac{\Gamma-\delta\varepsilon}{2\Gamma}}|j\rangle, \\ |\mathbf{j}\rangle &= -\sqrt{\frac{\Gamma-\delta\varepsilon}{2\Gamma}}|i\rangle + \sqrt{\frac{\Gamma+\delta\varepsilon}{2\Gamma}}|j\rangle, \end{aligned} \tag{4.5}$$

for $\delta\varepsilon = \varepsilon_j - \varepsilon_i > 0$. The corresponding energies are

$$\tilde{\varepsilon}_{i,j} = \frac{\varepsilon_i + \varepsilon_j}{2} \mp \frac{\Gamma}{2}, \qquad \Gamma = \left[\delta\varepsilon^2 + 4t_{ij}^2\right]^{1/2}. \tag{4.6}$$

Since both modified eigenfunctions contain $|i\rangle$, the matrix element of $\delta\hat{H}_i$ between them is finite, and the Golden-rule expression for the spin-flip part of the $i \to j$ transition rate for $\varepsilon_j > \varepsilon_i$ reads

$$I^{(s)}_{i\to j} = -m_x m_y J^2 \mathrm{F}(\tilde{\varepsilon}_i, \tilde{\varepsilon}_j, \omega), \tag{4.7}$$

where the function F is defined as

$$\mathrm{F}(\tilde{\varepsilon}_i, \tilde{\varepsilon}_j, \omega) = \frac{2t_{ij}^2}{(\tilde{\varepsilon}_j - \tilde{\varepsilon}_i)^2} \frac{\frac{1}{\tau}[f(\tilde{\varepsilon}_i) - f(\tilde{\varepsilon}_j)]}{(\tilde{\varepsilon}_j - \tilde{\varepsilon}_i - \hbar\omega)^2 + \left(\frac{\hbar}{\tau}\right)^2} = \frac{2t_{ij}^2}{\Gamma^2} \frac{\frac{1}{\tau}[f(\tilde{\varepsilon}_i) - f(\tilde{\varepsilon}_j)]}{(\Gamma - \hbar\omega)^2 + \left(\frac{\hbar}{\tau}\right)^2}. \tag{4.8}$$

Here we have introduced the phonon broadening of the levels, τ^{-1}.

It is easy to see that the transition rate to states with $\varepsilon_j < \varepsilon_i$ is given by Eq. (4.7) with function F from Eq. (4.8), but with $f(\tilde{\varepsilon}_i) \leftrightarrow f(\tilde{\varepsilon}_j)$, and thus the rate has the same sign as Eq. (4.7). Physically, this can be seen from the following argument: Consider the simple case of $m_x = m_y$. The Hamiltonian of Eq. (4.2) implies that for a given site at the interface, spins $\uparrow$ are transferred to states of higher energy (and there is a backflow of spins $\uparrow$ converted from $\downarrow$ from those states), while spins $\downarrow$ are pushed to states with lower energy (and there is a backflow of spins $\downarrow$ converted from $\uparrow$). Since the occupation of the state at the interface is larger than of those at higher energy, there is a negative $\downarrow\!\!\rightarrow\!\!\uparrow$ conversion rate because of transitions up the energy. This is exactly what Eq. (4.7) suggests. Further, since the occupation of the state at the interface is lower than of those at lower energy, there is a positive $\uparrow\!\!\rightarrow\!\!\downarrow$ conversion rate, or, again, negative $\downarrow\!\!\rightarrow\!\!\uparrow$ one. Hence a simple permutation $f(\tilde{\varepsilon}_i) \leftrightarrow f(\tilde{\varepsilon}_j)$ suffices to describe transitions to states with $\varepsilon_j < \varepsilon_i$.

The product $m_x m_y$ in Eq. (4.7) is specific for spin pumping, see Eq. (4.1). The expression for the net absorption rate contains $\frac{1}{2}(m_x^2 + m_y^2)$ instead. Another difference from the conventional resonance absorption [31, 32] is the structure of the matrix element in Eq. (4.7). This, however, modifies the result of averaging over the sites, j, only by a numerical factor. A crucial observation in the averaging procedure [32] is that the relevant sites, j, are located within a narrow spherical layer with a radius r_ω which is found from the condition $2|t_{ij}(r_\omega)| = \hbar\omega$. Assuming the exponential decay of the overlap integral with distance, $|t_{ij}(r)| = t_0 \exp(-r_{ij}/a)$, we have

$$r_\omega = a \ln \frac{2t_0}{\hbar\omega}. \tag{4.9}$$

The result of averaging and summing over sites far away from the boundary reads

$$I^{(s)}(\omega) = 2\pi^2 m_x m_y J^2 \left(g\omega a r_\omega^2\right) \frac{\partial f}{\partial \varepsilon}, \tag{4.10}$$

where g is the density of states. The transition rate of Eq. (4.10) should be interpreted as the spin current generated per a localized state coupled to the ferromagnet.

4.2.4 Resonant absorption at finite $\boldsymbol{H}$

To generalize Eq. (4.7) to a finite magnetic field in the normal layer, one must take into account the modification of the spin eigenstates, as well as the Zeeman splitting in energies of the latter. The spin structure of the spin-split levels depends on the orientation of $\boldsymbol{H}$ as follows

$$|\chi_{\mathbf{H}+}\rangle = \cos\Big(\frac{\theta_H - \theta_M}{2}\Big)|\chi_{\mathbf{M}+}\rangle + i \sin\Big(\frac{\theta_H - \theta_M}{2}\Big)|\chi_{\mathbf{M}-}\rangle, \tag{4.11}$$

$$|\chi_{\mathbf{H}-}\rangle = \cos\Big(\frac{\theta_H - \theta_M}{2}\Big)|\chi_{\mathbf{M}-}\rangle + i\sin\Big(\frac{\theta_H - \theta_M}{2}\Big)|\chi_{\mathbf{M}+}\rangle. \tag{4.12}$$

Here the quantization axes for $|\chi_{\mathbf{M}\pm}\rangle$ and $|\chi_{\mathbf{H}\pm}\rangle$ spinors are chosen along the static part of the magnetization, and the external magnetic field, respectively, see Fig. 4.5(a). The states $|\chi_{\mathbf{M}\pm}\rangle$ at sites i and j are split by Δ_z.

All four transitions between states with $|\chi_{\mathbf{M}\pm}\rangle$ spin wave functions, Fig. 4.4(b), are allowed for a general orientation of the magnetic field. For spin-conserving transitions ($+ \to +$ and $- \to -$), the frequency dependence of $I^{(s)}$ remains ωr_ω^2, i.e., the same as in Eq. (4.10). Orientation of $\boldsymbol{H}$ enters into the prefactor: The product $m_x m_y$ should be replaced with $\frac{1}{4}\sin^2(\theta_H - \theta_M)m_x^2$ for both transitions.

While the spin-conserving transitions do affect the spin current density distribution in the sample, they are nonresonant, and it is the spin-flipping ones ($+ \leftrightarrow -$) that are responsible for the spin current generation at the interface. In other words, no spin current is possible in a stationary state without the latter processes. Therefore, in what follows we concentrate on the frequency and magnetic field dependence of the corresponding rates.

As far as $+ \to -$ and $- \to +$ transitions are concerned, only the $+ \to -$ with absorption of a magnon, and $- \to +$ with emission of a magnon become important in the vicinity of the resonance $\hbar\omega = \Delta_z$. The other two transitions are nonresonant, and therefore disregarded here. For the $+ \leftrightarrow -$ transitions, the prefactor ω in the spin current remains intact, since it comes from the difference in the populations of levels involved. However, despite the upper and lower Zeeman levels being separated in energy, the overlap of the spatial wave functions is determined by ε_i, ε_j in *zero* magnetic field. Thus, the $+ \to -$ transitions take place between pairs with $(\varepsilon_j - \varepsilon_i) \sim |\hbar\omega - \Delta_z|$. These pairs have the "shoulder"

$$r_{\hbar\omega-\Delta_z} = a\ln\frac{2t_0}{|\hbar\omega - \Delta_z|}. \tag{4.13}$$

Logarithmic divergence of Eq. (4.13), which is cut off at $|\hbar\omega - \Delta_z| \sim \hbar/\tau$, ensures the resonant character of spin-flipping transitions that we took into account.

In addition to the replacement of r_ω by $r_{\omega-\Delta_z}$ in the spin current, the prefactor $m_x m_y$ should be modified as $m_x m_y \to \mathrm{G}(m_x, m_y)$, where the function G is defined as

$$\mathrm{G}(m_x, m_y) = \ \tfrac{1}{4}(m_x + m_y\cos(\theta_H - \theta_M))^2, \tag{4.14}$$

so that the absorption, and thus the FMR damping, do not have the usual form $\propto m_x m_y$.

The most spectacular manifestation of the resonance $\hbar\omega = \Delta_z$ is that the *intrasite* transitions become possible, as illustrated in Fig. 4.4(b). For these transitions the overlap of the spatial parts of the on-site wave functions is equal to 1, and the magnetic-field

dependence of absorption is a pure Lorentzian. Orientation-dependent prefactor, which is the matrix element of $\delta\hat{\mathcal{H}}_i$ between the spinors $|\chi_{\mathbf{H}+}\rangle$ and $|\chi_{\mathbf{H}-}\rangle$, is the same as in Eq. (4.14). Summarizing, we present the expression for spin current close to the resonance $\hbar\omega = \Delta_z$ in the form

$$I^{(s)}(\omega) = 2\mathrm{G}(m_x, m_y)J^2\omega\frac{\partial f}{\partial\varepsilon} \times \Big[\frac{\frac{\hbar}{\tau}}{(\Delta_z - \hbar\omega)^2 + \left(\frac{\hbar}{\tau}\right)^2} + \pi^2 g a^3 \ln^2\frac{2t_0}{|\hbar\omega - \Delta_z|}\Big], \qquad (4.15)$$

where the first term comes from intrasite and the second term from intersite transitions. Directly at the resonance, the first term dominates. This is ensured by the condition $ga^3\hbar/\tau \ll 1$. Since the combination $1/ga^3$ is the minimal energy spacing between two sites in the insulator located within $\sim a$ from each other, the above condition implies that this spacing is much bigger than the phonon broadening of individual levels, which is the definition of the Anderson insulator. As the deviation from the resonance increases, the behavior of $I^{(s)}(\omega)$ is dominated by the second term. Neglecting the logarithm, the crossover takes place at $|\Delta_z - \hbar\omega|\tau/\hbar \gtrsim \left(\tau/\hbar g a^3\right)^{1/2} \gg 1$. The behavior of spin current near the resonance is shown in Fig. 4.6(b), where the logarithm was cut off at $|\hbar\omega - \Delta_z| = t_0/15$.

4.3 Resonant orientations of external field

Equation (4.15) is our main result. To make connection to the experimental papers [19-22], below we calculate the magnitude and orientation of the dc field where the anomalous behavior of ISHE voltage takes place. Such behavior takes place when two conditions are met: The Zeeman splitting of the localized states is equal to $\hbar\omega$, and $\omega = \omega_{FMR}$.

We specify the orientation of $\boldsymbol{H}$ and magnetization, $\boldsymbol{M}$, using the notations common in the literature; see, e.g., Refs. [9, 15, 20], and Fig. 4.5. We will also introduce dimensionless variables $\tilde{H}$, $\tilde{M}$ and $\tilde{\omega}$, which stand for H, M and ω_{FMR} in the units of $4\pi M_s$, where M_s is the saturation magnetization. Then the angle θ_M, corresponding to the equilibrium orientation of $\boldsymbol{M}$, is found from the condition that $\boldsymbol{M}$ is parallel to the effective magnetic field, with the demagnetizing term taken into account [9]

$$2\tilde{H}\sin(\theta_H - \theta_M) + \sin 2\theta_M = 0, \qquad (4.16)$$

while the expression for the resonant frequency, $\tilde{\omega}$, reads[28]

$$\left(\frac{\tilde{\omega}}{\gamma}\right)^2 = \Big[\tilde{H}\cos(\theta_H - \theta_M) - \cos 2\theta_M\Big] \times \Big[\tilde{H}\cos(\theta_H - \theta_M) - \cos^2\theta_M\Big]. \qquad (4.17)$$

From these two equations we exclude θ_M and plot the dimensionless field $\tilde{H}$ versus θ_H, for a *given* FMR frequency $\tilde{\omega}$. Examples of these curves are shown in Fig. 4.5. Resonant

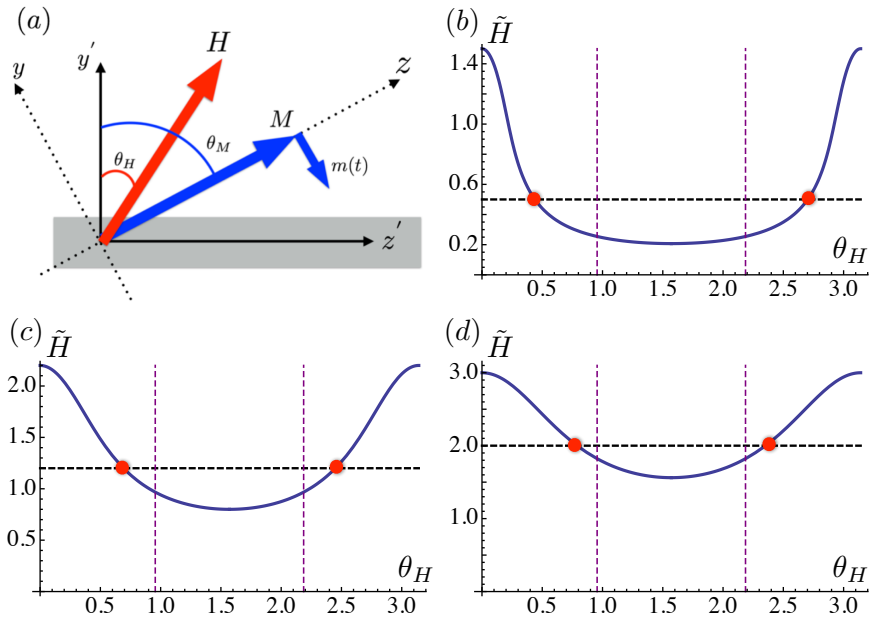

Figure 4.5: (color online). Ferromagnetic resonance. (a) The geometry of FMR; For a fixed dimensionless frequency, $\tilde{\omega} = \omega_{FMR}/4\pi M_s$, the dimensionless magnitude, $\tilde{H} = H/4\pi M_s$, and orientation, θ_H, of dc magnetic field are related via Eq. (4.17). This dependencies are shown for the values of $\tilde{\omega}/\gamma$: (b) 0.5, (c) 1.2, and (d) 2. Red dots indicate the values of H, for which the condition $\gamma H = \omega_{FMR}$ is satisfied.

orientation is obtained by crossing a curve $\tilde{H}(\theta_H)$ by the line $\tilde{\omega} = \gamma\tilde{H}$. Two intersections determine the orientations for which ω_{FMR} is equal to the Zeeman splitting of the localized states. Upon changing ω_{FMR}, we get two lines of resonances, Fig. 4.6(a). They occupy two domains: $0 < \theta_H < \cos^{-1}\frac{1}{\sqrt{3}}$ and $(\pi - \cos^{-1}\frac{1}{\sqrt{3}}) < \theta_H < \pi$. At the boundaries of the domains $\tilde{H}$ goes to infinity. Then it follows from Eqs. (4.16) and (4.17) that at these boundaries $\sin(\theta_M - \theta_H) = 0$, and θ_H satisfies the equation $\cos(2\theta_H) + \cos^2\theta_H = 0$, yielding $\theta_H = \cos^{-1}\left(\frac{1}{\sqrt{3}}\right) \approx 55°$.

In Refs. [19, 20] on pumping into organics the microwave frequency driving the resonance was 9.45 Ghz, while the values of $4\pi M_s$ were very different, namely, $4\pi M_s = 0.175$ T in Ref. [19] and $4\pi M_s = 0.805$ T in Ref. [20]. Then from Fig. 4.6(a) we find that the resonant angle θ_H should be close to 45° for Ref. [19] and 23° for Ref. [20].

4.4 Spin-resistor network

After the spin polarization is generated at the boundary, it should spread into the bulk of the insulator to avoid the backflow [35]. In a metal, where $\boldsymbol{P}$ is a continuous function of coordinates, this spreading is by spin diffusion accompanied by the Larmor precession. In a hopping insulator $\boldsymbol{P}$ takes discrete values, $\boldsymbol{P}_i$, which are the polarizations on the sites, i. The Larmor precession is accounted for by the on-site Zeeman splitting, Δ_z, of the levels; see Fig. 4.4. The frequencies of electron hops between two sites, i and j, depend strongly on their energies, ε_i, ε_j, and their spatial separation, r_{ij}. Then the issue of spreading of the spin polarization reduces to the question: what is the spin current $\boldsymbol{I}^{(s)}_{i\to j}$ between the sites with polarizations $\boldsymbol{P}_i$ and $\boldsymbol{P}_j$, provided that, on average, there is no charge current between these sites?

If bias were applied between the two sites, then the average charge current, proportional to this bias, could be found by ascribing an effective resistance, R_{ij}, to the pair of sites [30, 31]. It is easy to see that the same R_{ij} determines the proportionality coefficient between $\boldsymbol{I}^{(s)}_{i\to j}$ and $\boldsymbol{P}_i - \boldsymbol{P}_j$, namely

$$\boldsymbol{I}^{(s)}_{i\to j} = 2\frac{\boldsymbol{P}_i - \boldsymbol{P}_j}{R_{ij}\frac{\partial f}{\partial \varepsilon}}. \tag{4.18}$$

In Eq. (4.18) we have assumed that the difference $(\varepsilon_i - \varepsilon_j)$ is much smaller than the temperature, so that $\frac{\partial f}{\partial \varepsilon}$ is the same for both sites. Equation (4.18) follows from the fact that the on-site chemical potentials of the local majority and minority electrons are shifted by $\mp|\boldsymbol{P}_i|/\frac{\partial f}{\partial \varepsilon}$, respectively. The spinors that correspond to these local spin eigenstates are defined by the directions of $\boldsymbol{P}_i$, $\boldsymbol{P}_j$. Importantly, the fact that the chemical potential

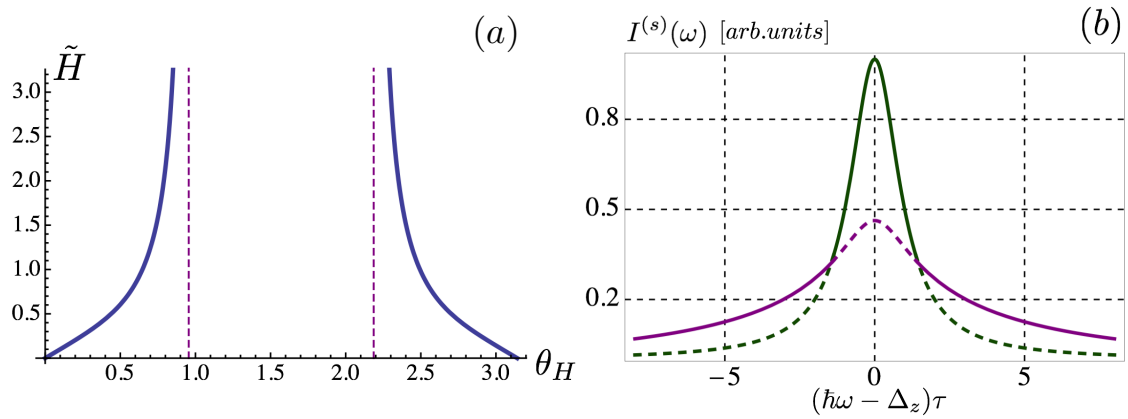

Figure 4.6: (color online). Resonant condition and spin current. (a) the resonant condition $\gamma H = \omega_{FMR}$ is satisfied along the solid lines on the $\left(\frac{H}{4\pi M_s}\right) - \theta_H$ plane. The cutoff values of θ_H are $\cos^{-1}\left(\frac{1}{\sqrt{3}}\right) \approx 55^\circ$ and $\pi - \cos^{-1}\left(\frac{1}{\sqrt{3}}\right)$. (b) the behavior of the spin current calculated from Eq. (4.15) for $ga^3\hbar/\tau = 4 \cdot 10^{-3}$ and $t_0\tau/\hbar = 15$.

splitting is symmetric around the chemical potential of the unpolarized system ensures the absence of the charge current, i.e., the net current flow $i \to j$ is compensated by the net current flow $j \to i$. With different spin polarizations of the sites, the compensation of the charge flows leads to the imbalance of the spin flows, and thus to Eq. (4.18). Note that Eq. (4.18) remains valid in the external magnetic field, which enters only via the magnitudes of polarizations. Overall, Eq. (4.18) suggests that polarization built up at the F-N boundary spreads along the current-carrying resistor network, as illustrated in Fig. 4.7.

4.5 Concluding remarks

Our result Eq. (4.15) applies when the phonon-induced broadening of the levels is smaller than ω. In the opposite case, $\omega\tau \ll 1$, the mechanism of absorption is the Pollak-Geballe relaxation mechanism, Ref. [36]; no sharp dependence of pumping near the resonance is expected in this regime. Unlike pumping into metals, the pumping rate Eq. (4.15) is not simply proportional to $\boldsymbol{m} \times \frac{d\boldsymbol{m}}{dt}$. The prefactor in Eq. (4.14) depends on the relative orientation of $\boldsymbol{m}$ and the external magnetic field, $\boldsymbol{H}$.

Suppose that we are at resonance $\hbar\omega = \Delta_z$. The microwave field acts both by driving the FMR but also directly, by causing transitions between the Zeeman levels. If the amplitude of the field in frequency units (Rabi frequency) exceeds the inverse spin relaxation time, these transitions will be saturated in the bulk. Then the pumping becomes inefficient.

In conventional theory of hopping transport the applied voltage drops not on all the resistors constituting the network, but on the highest, critical, resistors representing the "hardest" hops [31]. The spin relaxation rate will be dominated by hyperfine or spin-orbit environment [37, 29] of this hop.

We did not consider effects of electron-electron interaction, and did not describe in detail how finite resistance of the spin-current network, Section 4.4, affects the measured value of the spin current. In brief, Coulomb correlations enhance the absorption of magnons by increasing the number of singly occupied pairs [33], while the measured spin current is given by Eq. (4.15) only in the limit of vanishingly small bulk resistance. These considerations are, however, completely standard, and do not change the qualitative picture of spin current generation by resonant magnon absorption in hopping insulators, developed in this paper.

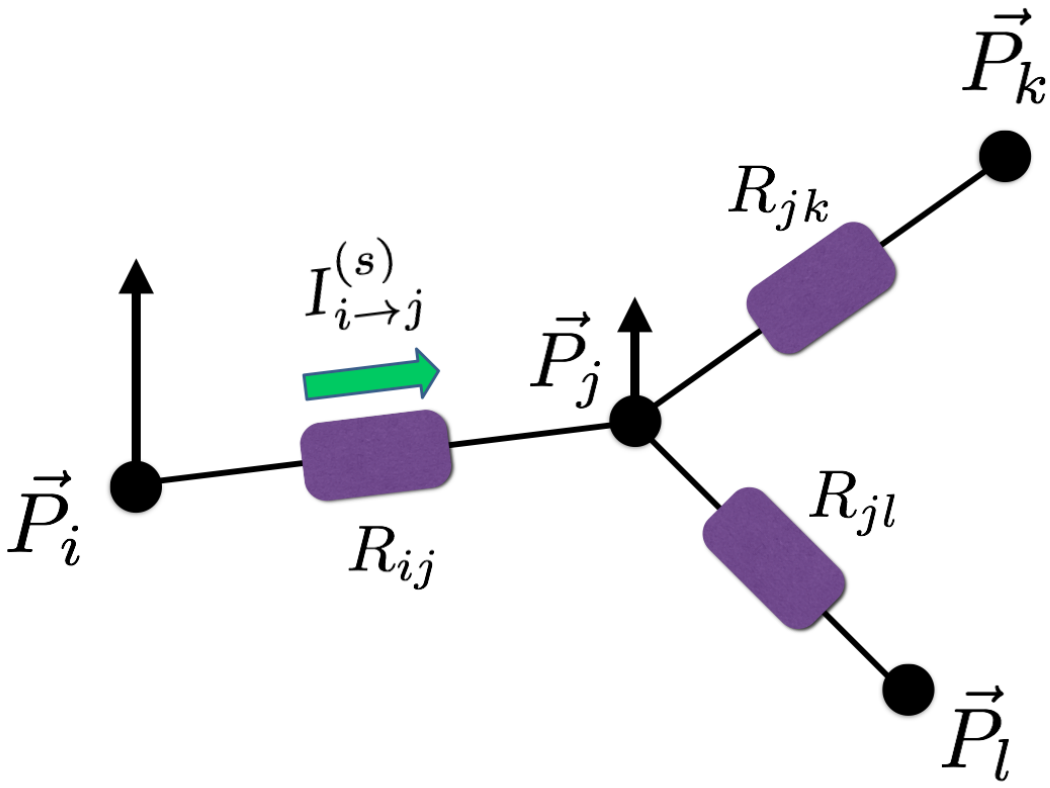

Figure 4.7: (color online). "Spin-resistor" network. Polarizations $\boldsymbol{P}_i$ and $\boldsymbol{P}_j$ on the sites i, j determine the spin current between these sites. The coefficients, R_{ij}, are proportional to the electric hopping resistances.

4.6 References

[1] Y. Tserkovnyak, A. Brataas, and G. E. W. Bauer, Phys. Rev. Lett. **88**, 117601 (2002).

[2] S. Mizukami, Y. Ando, and T. Miyazaki, Phys. Rev. B **66**, 104413 (2002).

[3] M. I. Dyakonov and A. V. Khaetskii, in *Spin Physics in Semiconductors*, ed. by M. I. Dyakonov, Chapter 8 (Springer, Berlin, 2008).

[4] E. Saitoh, M. Ueda, H. Miyajima, and G. Tatara, Appl. Phys. Lett. **88**, 182509 (2006).

[5] H. Y. Inoue, K. Harii, K. Ando, K. Sasage, and E. Saitoh, J. Appl. Phys. **102**, 083915 (2007).

[6] K. Ando, S. Takahashi, K. Harii, K. Sasage, J. Ieda, S. Maekawa, and E. Saitoh, Phys. Rev. Lett. **101**, 036601 (2008).

[7] K. Ando, T. Yoshino, and E. Saitoh, Appl. Phys. Lett. **94**, 152509 (2009).

[8] J.-C. Rojas-Sánchez, N. Reyren, P. Laczkowski, W. Savero, J.-P. Attané, C. Deranlot, M. Jamet, J.-M. George, L. Vila, and H. Jaffrès, Phys. Rev. Lett. **112**, 106602 (2014).

[9] K. Ando, S. Takahashi, J. Ieda, Y. Kajiwara, H. Nakayama, T. Yoshino, K. Harii, Y. Fujikawa, M. Matsuo, S. Maekawa, and E. Saitoh, J. Appl. Phys. **109**, 103913 (2011).

[10] O. Mosendz, J. E. Pearson, F. Y. Fradin, G. E. W. Bauer, S. D. Bader, and A. Hoffmann, Phys. Rev. Lett. **104**, 046601 (2010).

[11] B. Heinrich, C. Burrowes, E. Montoya, B. Kardasz, E. Girt, Y.-Y. Song, Y. Sun, and M. Wu, Phys. Rev. Lett. **107**, 066604 (2011).

[12] J.-C. Lee, L.-W. Huang, D.-S. Hung, T.-H. Chiang, J. C. A. Huang, J.-Z. Liang, and S.-F. Lee, Appl. Phys. Lett. **104**, 052401 (2014).

[13] J. E. Gómez, B. Z. Tedlla, N. R. Álvarez, G. Alejandro, E. Goovaerts, and A. Butera, Phys. Rev. B **90**, 184401 (2014).

[14] A. Yamamoto, Y. Ando, T. Shinjo, T. Uemura, and M. Shiraishi, Phys. Rev. B **91**, 024417 (2015).

[15] K. Ando and E. Saitoh, Nat. Commun. **3**, 629 (2012).

[16] E. Shikoh, K. Ando, K. Kubo, E. Saitoh, T. Shinjo, and M. Shiraishi, Phys. Rev. Lett. **110**, 127201 (2013).

[17] S. Dushenko, M. Koike, Y. Ando, T. Shinjo, M. Myronov, and M. Shiraishi, arXiv:1501.06691.

[18] S. Singh, A. Ahmadi, C. T. Cherian, E. R. Mucciolo, E. del Barco, and B. Özyilmaz, Appl. Phys. Lett. **106**, 032411 (2015).

[19] A. Brataas, Yu. V. Nazarov, and G. E. W. Bauer, Phys. Rev. Lett. **84**, 2481 (2000).

[20] Y. Tserkovnyak, A. Brataas, G. E. W. Bauer, and B. I. Halperin Rev. Mod. Phys. **77**, 1375 (2005).

[21] M. D. Styles and A. Zangwill, Phys. Rev. B **66**, 014407 (2002).

[22] S. A. Bender and Y. Tserkovnyak, arXiv:1409.7128.

[23] K. Ando, S. Watanabe, S. Mooser, E. Saitoh, and H. Sirringhaus, Nat. Mater. **12**, 622 (2013).

[24] S. Watanabe, K. Ando, K. Kang, S. Mooser, Y. Vaynzof, H. Kurebayashi, E. Saitoh, and H. Sirringhaus, Nat. Phys. **10**, 308 (2014).

[25] Z. Qiu, M. Uruichi, D. Hou, K. Uchida, H. M. Yamamoto, E. Saitoh, arXiv:1502.05244.

[26] M. Kimata, D. Nozaki, Y. Niimi, H. Tajima, and Y. Otani, arXiv:1411.2740.

[27] For example, the bulk resistance, $\rho(T)$, in Ref. [22] increased by two orders of magnitude between the room temperature and 20 K following the Mott's law $\ln \rho \propto T^{-1/4}$. The localization length inferred by the authors from the transport measurements is quite small: $a \approx 11$ nm.

[28] C. Kittel, Phys. Rev. **73**, 155 (1948).

[29] R. H. Silsbee, A. Janossy, and P. Monod, Phys. Rev. B **19**, 4382 (1979). The authors demonstrate theoretically and experimentally that paramagnetic resonance in copper foil is greatly enhanced when the Zeeman frequency coincides with the frequency of FMR in ferromagnet coupled to the foil.

[30] V. Ambegaokar, B. I. Halperin, and J. S. Langer, Phys. Rev. B **4**, 2612 (1971).

[31] B. I. Shklovskii and A. L. Efros, *"Electronic Properties of Doped Semiconductors"* (Springer-Verlag, Berlin, 1984).

[32] N. F. Mott, Philos. Mag. **22**, 7 (1970).

[33] A. L. Efros and B. I. Shklovskii, in *Electron-Electron Interactions in Disordered Systems*, edited by A. L. Efros and M. Pollak North-Holland, Amsterdam, 1985.

[34] B. I. Shklovskii and A. L. Efros, Zh. Eksp. Teor. Fiz. **81**, 406 (1981) [Sov. Phys. JETP **54**, 218 (1981)].

[35] A. Brataas, Y. Tserkovnyak, G. E. W. Bauer, and B. I. Halperin, Phys. Rev. B **66**, 060404(R) (2002).

[36] M. Pollak and T. H. Geballe, Phys. Rev. **122**, 1742 (1961).

[37] N. J. Harmon and M. E. Flatté Phys. Rev. Lett. **110**, 176602 (2013).

[38] R. C. Roundy and M. E. Raikh Phys. Rev. B **88**, 205206 (2013).

CHAPTER 5

EFFECTIVE SPIN HALL PROPERTIES OF A MIXTURE OF MATERIALS WITH AND WITHOUT SPIN-ORBIT COUPLING: TAILORING THE EFFECTIVE SPIN-DIFFUSION LENGTH

5.1 Introduction.

The spin Hall effect [1-3](SHE), predicted theoretically more than four decades ago [1, 2], is nowadays routinely observed in many materials [4-17], which include traditional and exotic metals, prominent semiconductors, and graphene. Moreover, the inverse spin Hall effect (ISHE), i.e., generation of voltage drop normal to the spin current, was recently "put to work". It serves as a tool to detect whether or not the spin current is injected into a nonmagnetic material from an ac-driven ferromagnet in the course of spin pumping.

Original scenario [1-3] of the SHE involves the current driven through a sample resulting in the spin-density accumulation at the boundaries. This accumulation is the result of the generation of the spin current in the direction normal to the charge current. Spin current is generated due to the spin-orbit coupling of the charge carriers in the sample. In experiments [4-17] the charge current did not flow. Instead, the spin current was injected into a nonmagnetic material through the boundary with a ferromagnet, and ISHE signal was registered. A nontrivial scheme to generate spin current was realized in Ref. [18]. The main idea of this scheme is that the sample was not a part of the electric circuit, but rather the charge current was created due to the photogalvanic effect accompanying the interband electron absorption of light beams with frequencies ω and 2ω. The photogalvanic effect originates from interference of different absorption pathways. As illustrated in Fig. 5.1, the SHE resulting from this interference when the linear polarizations in the beams are mutually orthogonal.

Most recently [19-22] the pumped spin currents in certain polymers were registered via

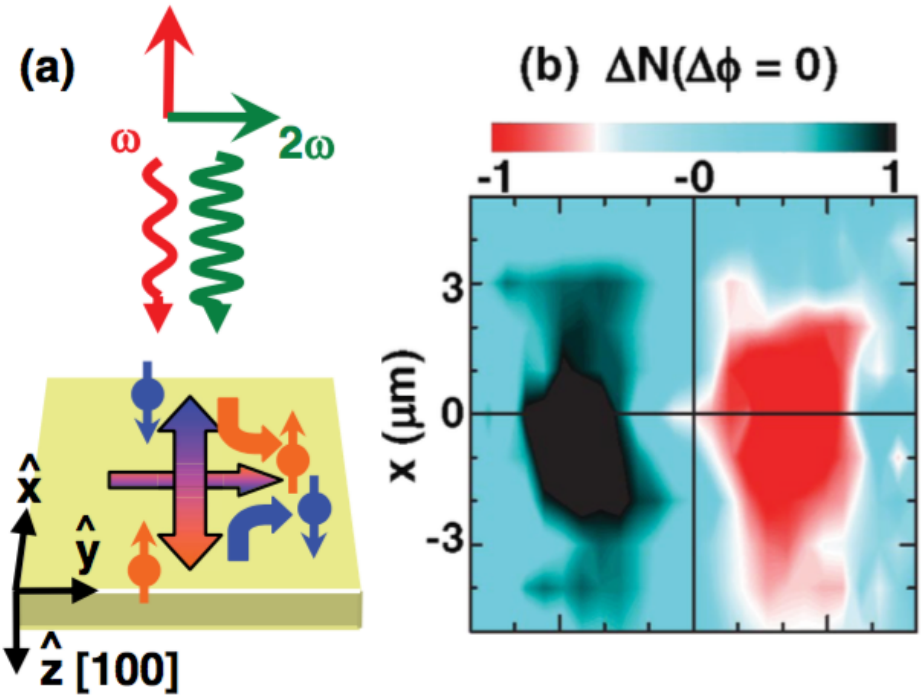

Figure 5.1: (color online). Observation of the ISHE using the two-color optical pump-and-probe technique. (a) Illustration of orthogonally polarized ω and 2ω pulses producing a pure spin current (double headed straight arrow) along the ω beam polarization direction ($\hat{x}$). The charge current due to the ISHE (curved arrows) along $\hat{y}$ leads to electron accumulation near one edge of the illuminated region. (b) Measured charge accumulation due to the ISHE (adapted from Ref. [18]).

inverse spin Hall voltage which they induced in Pt electrode located at some distance from the interface with ferromagnet.

The latest focus [23-25] of the research on the spin physics in organics is the study of the properties of platinum-containing π-conjugated polymers. In these materials Pt atoms are embedded in the polymer backbone chains. While the SO coupling, which is the origin of the SHE, is very weak in polymers, adding Pt creates the elements of the backbone; see Fig. 5.2, where it is locally strong. These elements can be separated either by one or by three π-conjugated spacer unit lengths. Experimenally [25], the ISHE signal measured on Pt-rich polymer samples looks very much the same as the signal measured on pure Pt, as can be seen in Fig. 5.2.

In this regard, a general question arises: how the spin Hall effect is realized in composite materials where the strong SO and low SO domains are intermixed? Note that, by now, all theoretical studies of SO-related transport assumed that the SO coupling is homogeneous.

The goal of the present paper is to develop an elementary theory which addresses the question formulated above. Unlike Refs. [26, 27], we will not specify a mechanism of SO on the microscopic level, but rather focus on purely "geometrical" aspects. Namely, we will consider the following minimal model: a system of SO grains is dissolved in a matrix with no SO. The question we will be interested in is: what are the effective spin Hall characteristics of the mixture.

Firstly, we address a mechanism of the formation of the inverse spin Hall voltage between the edges of the sample in the geometry of the mixture. Unlike the case of homogeneous SO, this formation happens as follows. The spin current turns each SO grain into an electric dipole. All dipole moments are oriented normal to the spin current. Thus the potentials they create at the upper and the lower boundaries of the sample add up. The difference of these potentials is the effective ISH voltage, $V_{\rm eff}^{\rm SH}$, of the mixture, which can be related to the effective spin Hall angle, $\theta_{\rm eff}^{\rm SH}$.

Naively, one would expect that, in a mixture of grains of density, n, and radius, a, the relation $\theta_{\rm eff}^{\rm SH} = (na^3)\theta^{\rm SH}$ holds within a numerical factor. Here $\theta^{\rm SH}$ is the spin Hall angle of the bulk SO material. This is simply because na^3 is the volume fraction of the SO material. Equally, one would expect that the effective spin relaxation time of the mixture is $1/(na^3)$ times longer than in the SO material, so that spin diffusion length, $\lambda_{\rm eff}$ is related to the spin diffusion length, λ, of the SO material as $\lambda_{\rm eff} = (na^3)^{-1/2}\lambda$.

The above expectations are correct only in the limit when the grains are small enough, namely, $a \ll \lambda$, so that the portion of spin polarization, which is lost within a single grain, is small. The opposite case of large grains, $a \gg \lambda$, is much less trivial. As we show below,

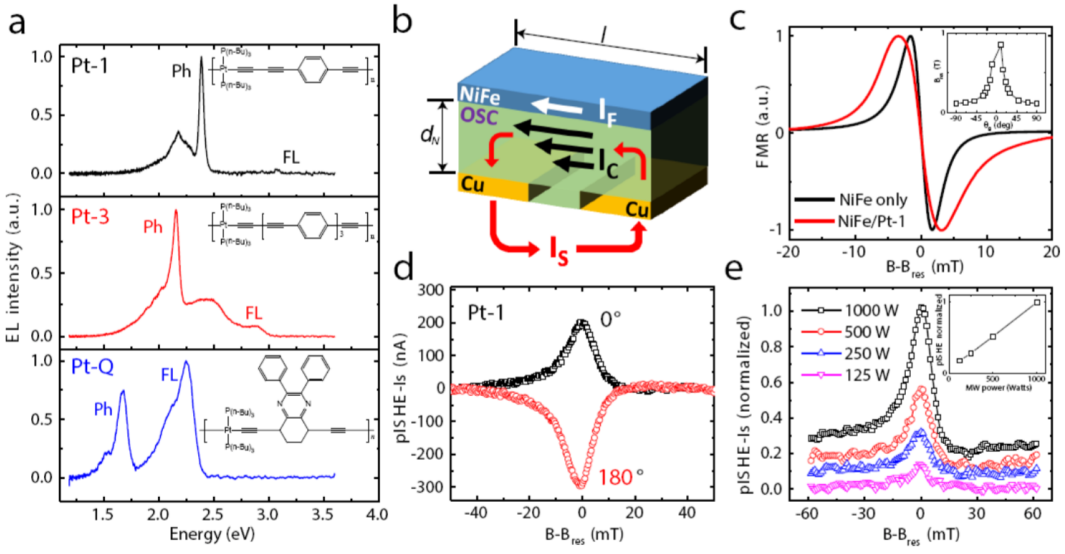

Figure 5.2: The electroluminescence spectra of the Pt-polymer series studied here, and observation of p-ISHE response in Pt-1 polymer. a, Normalized electroluminescence spectra for Pt-1 (black), Pt-3 (red), and Pt-Q (blue) polymers, respectively. The SOC strengths can be estimated from the electro-phosphorescence (Ph)/fluorescence (FL) intensity ratios. The insets show the building blocks of the studied Pt-polymers. The spacer in Pt-1 has a single phenyl ring, whereas that of Pt-3 has three phenyl rings. b, schematic illustration for the p-ISHE-I$_s$ current response in OSEC-based devices. I_C, I_F, and I_S are respectively the electric current source generated by the ISHE in the organic layer, AHE in the NiFe thin film (suppressed by capacitor geometry), and detected current response by the preamplifier. c, FMR spectra of the Cu/Pt-1 polymer/NiFe/SiO_2/Cu device measured by MW transmission without (black) and with (red) the spin coated Pt-1 polymer. The inset shows the FMR resonance field, $\mathbf{B}_{res}$ vs. the external field angle, θ_B. d, typical p-ISHE(B) response (in terms of current, I_S) in Pt-1 polymer device (ISHE/AHE ratio $\sim$ 9). The black squares and red circles lines in (d) are the data with the in-plane magnetic field $\mathbf{B}$ (at 0°) and $\mathbf{B}$ (at 180°), respectively. e, p-ISHE(B) response vs. the MW power as denoted. The inset shows the obtained linear IS vs. MW power dependence (adapted from Ref. [24]) .

in this limit $V_{\rm eff}^{\rm SH} \sim \lambda n a^2 V^{\rm SH}$, while $\lambda_{\rm eff} \sim \frac{1}{(na)^{1/2}}$. In other words, at small λ, the effective spin-diffusion length *saturates*. This finding can be loosely interpreted from the perspective of diffusion in the presence of the absorbing traps. The stronger the absorption, the smaller the concentration of particles at the position of the trap.

Finally, we will demonstrate that $V_{\rm eff}^{\rm SH}$ is sensitive to a very weak magnetic field. In a homogeneous material, the spin Hall effect gets suppressed in the field with Larmour frequency $\Omega \sim \tau_s^{-1}$, where τ_s is the spin-relaxation time. For the mixture, the characteristic field is $\sim T^{-1}$, where T is the diffusion time *between the sample edges*. This is because spin precession takes place mostly outside the grains. The paper is organized as follows. In Sect. 2 we solve an auxiliary problem of electric the polarization of a grain with a given radius, a, by the spin current. The solution is then employed to calculate the effective inverse spin Hall voltage in the mixture of grains with concentration, n. Sensitivity of this voltage to a weak longitudinal magnetic field is studied in Sect. 3. In Sect. 4 the effective diffusion length, $\lambda_{\rm eff}$, of the mixture is expressed via λ, a, and the parameter na^3. The physics of elongation of $\lambda_{\rm eff}$ for small $\lambda \ll a$ is discussed in Sect. 5. Concluding remarks are presented in Sect. 6.

5.2 Calculation of effective characteristics of the mixture

5.2.1 Single grain

The simplest way to incorporate the spin Hall effect on a quantitative level [28] is to add to the current density, $\boldsymbol{j} = \sigma \boldsymbol{E}$, the term $\gamma D \operatorname{curl} \boldsymbol{P}$, where σ and D are the conductivity and the diffusion coefficient, respectively, $\boldsymbol{P}(\boldsymbol{r})$ is the coordinate-dependent spin polarization. The strength of the SO coupling is quantified by a dimensionless parameter γ. The system of coupled equations for the spatial distribution of $\boldsymbol{P}(\boldsymbol{r})$ and $\boldsymbol{j}(\boldsymbol{r})$ reads [28]

$$\boldsymbol{j} = \sigma \boldsymbol{E} + e\gamma D \operatorname{curl} \boldsymbol{P}. \tag{5.1}$$

$$q_{ij} = -D \frac{\partial P_j}{\partial x_i} + \frac{\gamma}{e} \sigma \varepsilon_{ijk} E_k. \tag{5.2}$$

The second equation defines the component i of the flux of the j-projection of spin polarization. The system becomes closed [28] when it is complemented by the continuity equation

$$\frac{\partial q_{ij}}{\partial x_i} + \frac{P_j}{\tau_s} = 0. \tag{5.3}$$

Consider an isolated spherical grain with radius, a, and with the strength of SO-coupling, γ, embedded into an infinite medium with $\gamma = 0$ and with no spin relaxation, $\tau_s = \infty$, Fig.

5.3. Assume that the flux of spins, oriented along the x-axis and flowing along the y-axis, is incident on the grain. In application to the geometry, Fig. 5.3, the essence of the inverse spin Hall effect is that the incident spin current, i_s, induces an effective electric dipole on the sphere. The induced dipole moment is perpendicular to both, the current direction and polarization direction in the incident flux, i.e., it is directed along the z-axis.

To calculate the magnitude, $\mathcal{P}_c$, of the dipole moment it is natural to switch to spherical coordinates in which the incident polarization, $P_x = -\frac{i_s}{D_{\rm out}} y$, and the spin-current density, $i_y = i_s$, have the form

$$\boldsymbol{P} = -\frac{i_s}{D_{\rm out}} r \sin\theta\, \boldsymbol{e}_\phi, \qquad \boldsymbol{i}_s = i_s(\sin\theta\, \boldsymbol{e}_r + \cos\theta\, \boldsymbol{e}_\theta), \tag{5.4}$$

where $\boldsymbol{e}_r$, $\boldsymbol{e}_\theta$, and $\boldsymbol{e}_\phi$ are the unit vectors along radial, polar, and azimuthal axes, respectively; see Fig. 5.4.

Induced dipole moment along z creates an electrostatic potential,

$$\varphi_{\rm out} = \frac{\mathcal{P}_c \cos\theta}{r^2}, \tag{5.5}$$

outside the sphere.

From the form of $\varphi_{\rm out}$ we conclude that the θ-dependence of φ inside the sphere is also proportional to $\cos\theta$. This, together with Poisson's equation $\Delta\varphi = 0$, suggests that the induced electric field, $\boldsymbol{E}_{\rm in}$, inside the sphere is homogeneous, so that

$$\varphi_{\rm in} = -E_{\rm in} r \cos\theta. \tag{5.6}$$

Substituting Eq. (5.2) into Eq.(5.3), and taking into account that $\partial \boldsymbol{E}_{\rm in}/\partial x_i = 0$, we conclude that all the components of polarization inside the sphere satisfy the diffusion equation

$$D_{\rm in} \Delta P_j + \frac{P_j}{\tau_s} = 0, \tag{5.7}$$

where $D_{\rm in}$ is the diffusion coefficient inside the sphere.

As we will see below, the polarization, $\boldsymbol{P}(\boldsymbol{r})$, has only ϕ-component inside the sphere and at all distances outside the sphere. As in the incident flux, Eq. (5.4), the angular dependence of P_ϕ is $\propto \sin\theta$. Outside the sphere, where $\Delta \boldsymbol{P} = 0$, the general form of P_ϕ is

$$\boldsymbol{P}_{\rm out} = -\frac{i_s}{D_{\rm out}} \left(r + \frac{\chi_s}{r^2}\right) \sin\theta\, \boldsymbol{e}_\phi, \tag{5.8}$$

where the constant χ_s is the "spin polarizability". Inside the sphere, the solution of Eq. (5.7), proportional to $\sin\theta$, has the form

$$\boldsymbol{P}_{\rm in} = \tilde{P}\; i_1(r/\lambda) \sin\theta\, \boldsymbol{e}_\phi, \tag{5.9}$$

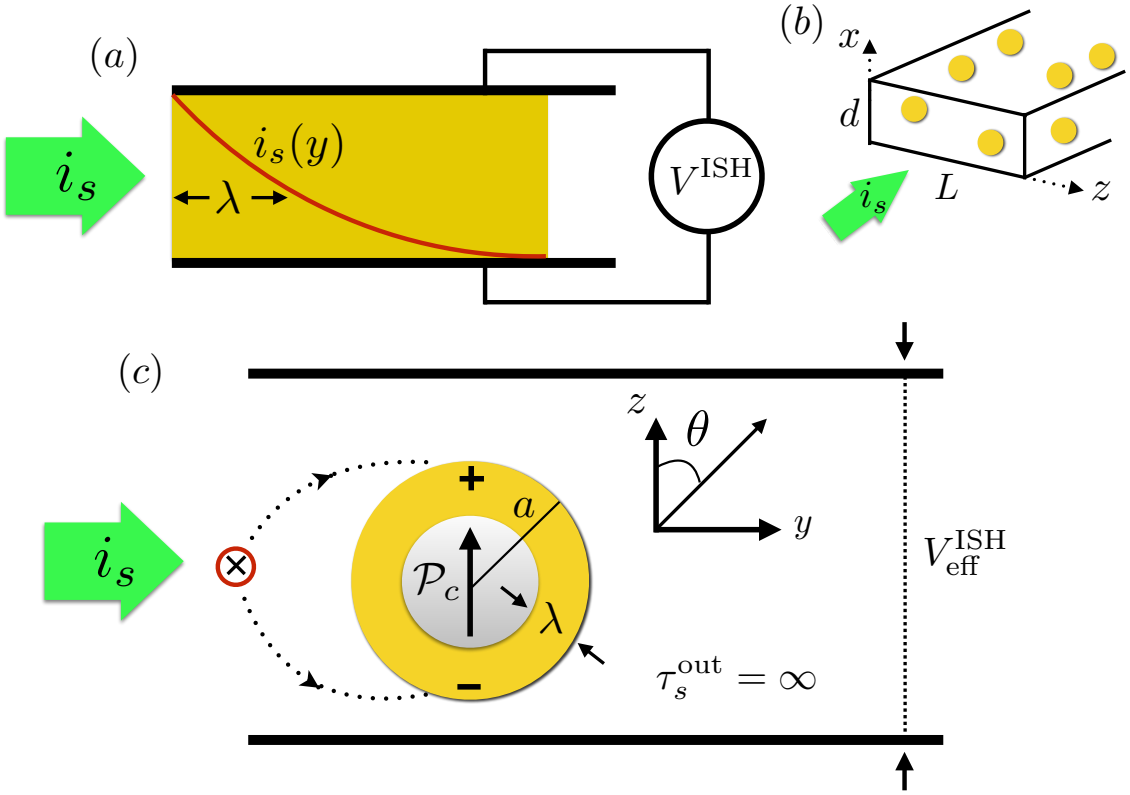

Figure 5.3: (color online). Conventional geometry for the inverse spin Hall effect. (a) Spin current flowing along y causes a buildup of the voltage, $V^{\rm ISH}$, between the edges $z = \pm L/2$. The buildup takes place as long as y is smaller than the spin diffusion length, λ. (b) Schematic illustration of a "granular" geometry, where the SO-coupled material is dissolved in the matrix with no SO coupling. (c) microscopic scenario of ISHE on a single spherical granule of a radius, a. Spin current with polarization along x turns the sphere into an electrical dipole directed normally to the current. The magnitude of a dipole moment, $\mathcal{P}_c$, depends on the ratio between a and λ, while the electric field inside the granule is homogeneous.

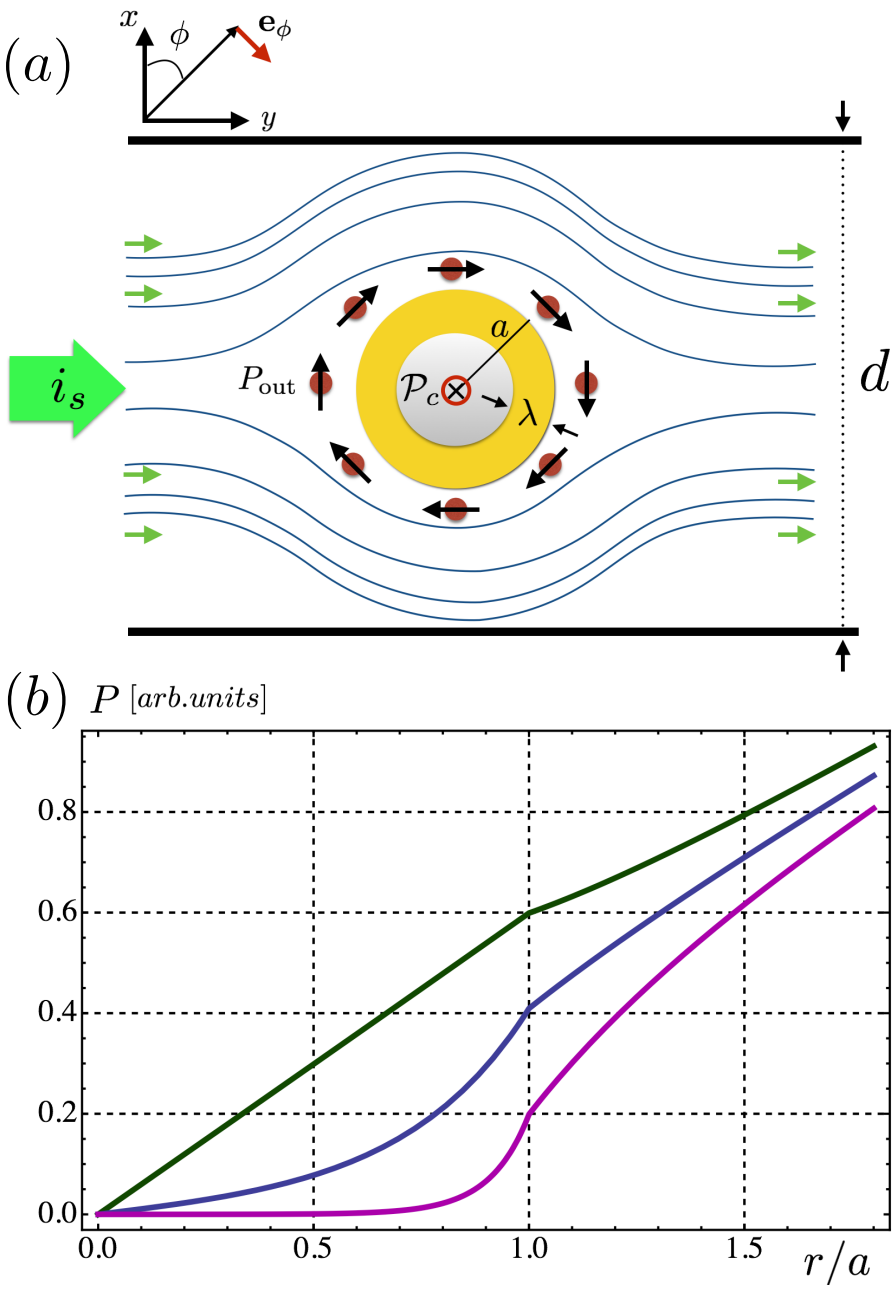

Figure 5.4: (color online). The cross section $z = 0$. (a) Distribution of the spin current in the (x, y)-plane in the presence of a spherical grain, Eq. (5.38), is illustrated schematically for $r > a$. Inside the grain, $r < a$, this distribution is determined by Eq. (5.29). (b) Distribution of the spin polarization along the radius, r, is plotted for $D_{\rm out}/D_{\rm in} = 2$ and three values of λ: $a/\lambda = 0.2$ (green), $a/\lambda = 4$ (blue), and $a/\lambda = 12$ (purple). Enhancement of the effective spin diffusion length for small λ/a is a result of a strong suppression of polarization near the boundary $r = a$.

where $\tilde{P}$ is a constant, and

$$\lambda = (D_{\rm in}\tau_s)^{1/2}\,, \tag{5.10}$$

is the diffusion length. The function $i_1(x)$ is a modified spherical Bessel function. We chose the function i_1 because it is finite at $x = 0$.

While the polarization has only ϕ-component, the spin current, defined as a flow of the ϕ-component of spin, can be presented in the vector form

$$\boldsymbol{i}_\phi = i_s\Big[(1 - \frac{2\chi_s}{r^3})\sin\theta\boldsymbol{e}_r + (1 + \frac{\chi_s}{r^3})\cos\theta\boldsymbol{e}_\theta\Big], \tag{5.11}$$

where the first term is $\partial P^\phi_{\rm out}/\partial r$, while the second term is $\left(\frac{1}{r}\right)\partial P^\phi_{\rm out}/\partial\theta$. At large distances the current Eq. (5.11) reproduces Eq. (5.4).

There are two unknown constants, $\mathcal{P}_c$ and χ_s, in the expressions for electric field and spin polarization inside the sphere, and two unknown constants, E_{in} and $\tilde{P}$, in the corresponding expressions outside the sphere. These constants are determined from the four boundary conditions at $r = a$:

(i) Continuity of the tangent component of electric field

$$E_{\rm in} = -\frac{\mathcal{P}_c}{a^3}. \tag{5.12}$$

(ii) Continuity of the normal component of the charge current

$$\sigma_{\rm in}E_{\rm in} + \frac{2e\gamma D_{\rm in}\tilde{P}}{a}i_1(a/\lambda) = \frac{2\sigma_{\rm out}\mathcal{P}_c}{a^3}. \tag{5.13}$$

(iii) Continuity of the spin polarization

$$-\frac{i_s}{D_{\rm out}}\Big(a + \frac{\chi_s}{a^2}\Big) = \tilde{P}i_1(a/\lambda). \tag{5.14}$$

(iiii) Continuity of the spin flux though the boundary

$$\frac{D_{\rm in}\tilde{P}}{\lambda}i_1'(a/\lambda) + \frac{\gamma}{e}\sigma_{\rm in}E_{\rm in} = i_s\Big(\frac{2\chi_s}{a^3} - 1\Big). \tag{5.15}$$

The system Eqs. (5.12)-(5.15) yields the sought expression for the spin-current-induced dipole moment

$$\mathcal{P}_c = -\frac{6ea^3\gamma}{(\sigma_{\rm in} + 2\sigma_{\rm out})\mathcal{M}}i_s, \tag{5.16}$$

where $\mathcal{M}$ in the denominator is the dimensionless combination

$$\mathcal{M} = \frac{2D_{\rm out}}{D_{\rm in}} - \frac{2\gamma^2\sigma_{\rm in}}{\sigma_{\rm in} + 2\sigma_{\rm out}} + \frac{ai_1'(\frac{a}{\lambda})}{\lambda i_1(\frac{a}{\lambda})} \tag{5.17}$$

Naturally, the proportionality coefficient between $\mathcal{P}_c$ and the spin current contains the first power of the SO coupling strength, γ.

The second term in Eq. (5.17) contains γ^2, and can be safely neglected. The ratio $D_{\rm out}/D_{\rm in}$ can be replaced by $\sigma_{\rm out}/\sigma_{\rm in}$. It is seen from Eq. (5.17) that the factor $\mathcal{M}$ depends strongly on the relation between the radius of the sphere and the spin-diffusion length. For $a \ll \lambda$ the last term in Eq. (5.17) is 1, while for $\lambda \ll a$ it is big and equal to a/λ. In the latter case Eq. (5.16) yields $\mathcal{P}_c \propto \lambda a^2$. This dependence has a simple interpretation. Namely, for $\lambda \ll a$ the induced dipole is generated only inside a spherical layer of a thickness $\sim \lambda$ near the surface of the sphere; see Fig. 5.4.

Description of a direct spin Hall effect for a sphere is completely similar to the case of the inverse spin Hall effect considered above. A charge current, i_c, along the y direction generates a spin dipole moment, $\mathcal{P}_s$, in the z-direction. Analytical expression for $\mathcal{P}_s$ is similar to Eq. (5.16)

$$\mathcal{P}_s = \frac{3\sigma_{\rm in} a^3 \gamma}{e(\sigma_{\rm in} + 2\sigma_{\rm out}) D_{\rm in} \mathcal{M}} i_c. \tag{5.18}$$

5.2.2 Finite density of grains

Consider a sample of a rectangular shape with a width, L, and thickness, d, ($L \gg d$). As the injected spin current flows through the cross section, the voltage builds up between the edges $z = \pm L/2$. The easiest way to calculate this voltage is to sum the contributions of individual dipoles. If a grain is located at a point with coordinates (x_i, y_i, z_i), see Fig. 5.5, then the potential difference between the edges, created by an induced dipole reads

$$V(x_i, y_i, z_i) = \frac{(\frac{L}{2} - z_i)\mathcal{P}_c}{[x_i^2 + y_i^2 + (\frac{L}{2} - z_i)^2]^{\frac{3}{2}}} - \Big(- \frac{(\frac{L}{2} + z_i)\mathcal{P}_c}{[x_i^2 + y_i^2 + (\frac{L}{2} + z_i)^2]^{\frac{3}{2}}} \Big), \tag{5.19}$$

where $\mathcal{P}_c$ is given by Eq. (5.16). In calculating the effective inverse spin Hall voltage the summation over dipoles is replaced by integration

$$V_{\rm eff}^{\rm SH}(y_0) = n \int_{-\frac{d}{2}}^{\frac{d}{2}} dx \int_{-y_0}^{\infty} dy \int_{-\frac{L}{2}}^{\frac{L}{2}} dz V(x, y, z), \tag{5.20}$$

where y_0 is the distance from the point at which voltage is measured to the point of spin-current injection. Naturally, the replacement of the sum by integral is justified when $nL^2 d \gg 1$. The integration over y is straightforward. Subsequent integral over z diverges logarithmically at $z = L/2$ and $z = -L/2$. This divergence should be cut off at $(z \pm L/2) \sim d$. Then the integration over x reduces to multiplication by d. The final result reads

$$V_{\rm eff}^{\rm SH}(y_0) = 2nd\mathcal{P}_c \times \left[\ln\Big(\frac{L}{d}\Big) + \ln\Big(\frac{2y_0}{d}\Big) - \ln\left(\frac{\sqrt{\frac{L^2}{y_0^2} + 1} + \frac{L}{y_0} + 1}{\sqrt{\frac{L^2}{y_0^2} + 1} + \frac{L}{y_0} - 1} \right) \right]. \tag{5.21}$$

At small distances from the injection point, $d \ll y_0 \ll L$, the first two terms in Eq. (5.21) dominate. The second logarithm describes a gradual increase of $V_{\rm eff}^{\rm SH}$ with y_0. At large

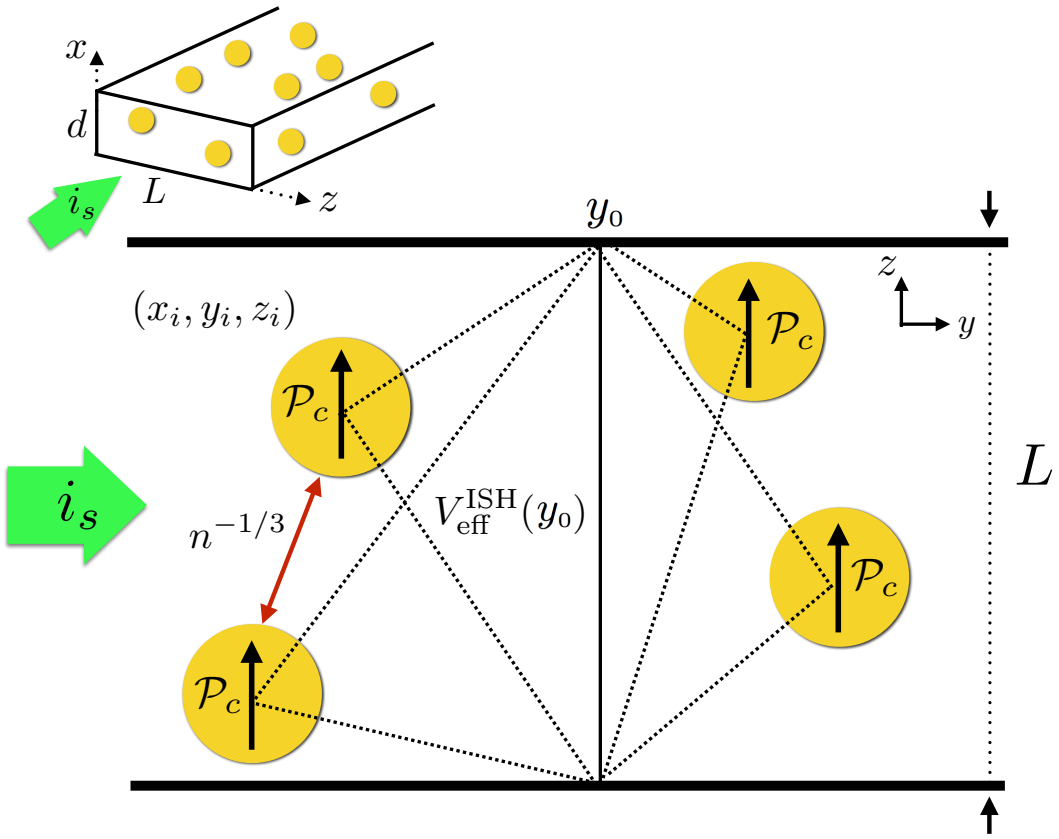

Figure 5.5: (color online). The effective spin Hall voltage is the sum of contributions from individual SO-induced dipoles. With density of granules, n, the typical distance between the neighbors is $n^{-1/3}$. It is much bigger than the radius, a, but much smaller than the sample width, L, which allows us to replace the sum by the integral Eq. (5.20).

distances, $y_0 \gg L$, the second and the third logarithms combine into $\ln(L/d)$, leading to the result

$$V_{\rm eff}^{\rm SH}(\infty) = 4nd\mathcal{P}_c \ln\left(\frac{L}{d}\right) = -\frac{24e(na^3)d\ln(\frac{L}{d})\gamma}{(\sigma_{\rm in}+2\sigma_{\rm out})\left[\frac{2D_{\rm out}}{D_{\rm in}}+\frac{ai_1'(\frac{a}{\lambda})}{\lambda i_1(\frac{a}{\lambda})}\right]} i_s. \tag{5.22}$$

Note that for highly conducting grain, both factors in the denominator do not depend on the characteristics, $\sigma_{\rm out}$ and $D_{\rm out}$, of the matrix. In this domain $V_{\rm eff}^{\rm SH}$ depends strongly on the relation between λ and a. Overall, Eq. (5.21) describes the growth and subsequent saturation of the inverse spin Hall voltage.

5.3 Magnetic-field dependence

The behavior of $V_{\rm eff}^{\rm SH}$ with position y_0 becomes nontrivial in the presence of magnetic field directed along the y-axis, a somewhat similar effect was pointed out in Ref. [28]. If the magnetic field is weak, so that the Larmour frequency, ω_L, is much smaller that τ_s^{-1} and much smaller than $D_{\rm out}/a^2$, which is the inverse diffusion time through the grain, then the effect of the magnetic field on the generation of an electric dipole can be neglected. Instead, the field affects only the polarization in the spin current incident on the grain. This allows one to use the result Eq. (5.16) in calculating the ω_L-dependence of $V_{\rm eff}^{\rm SH}$.

Outside the grains, the polarization components, P_x and P_z, satisfy the system of equations: $D_{\rm out}\frac{d^2P_x}{dy^2}+\omega_L P_z = 0$ and $D_{\rm out}\frac{d^2P_z}{dy^2}-\omega_L P_x = 0$. Assuming that at the point of injection the polarization was along x, we find

$$\begin{aligned} P_x(y) =& P_x(0)\cos\left[\left(\frac{\omega_L}{2D_{\rm out}}\right)^{\frac{1}{2}}y\right]\exp\left[-\left(\frac{\omega_L}{2D_{\rm out}}\right)^{\frac{1}{2}}y\right], \\ P_z(y) =& P_x(0)\sin\left[\left(\frac{\omega_L}{2D_{\rm out}}\right)^{\frac{1}{2}}y\right]\exp\left[-\left(\frac{\omega_L}{2D_{\rm out}}\right)^{\frac{1}{2}}y\right]. \end{aligned} \tag{5.23}$$

Suppose that a grain is positioned at $y = y_0$. Then the induced dipole moment will be a vector orthogonal to polarization with components

$$\mathcal{P}_z(y_0) = \left(\frac{P_x(y_0)}{P_x(0)}\right)\mathcal{P}_c, \quad \mathcal{P}_x(y_0) = -\left(\frac{P_z(y_0)}{P_x(0)}\right)\mathcal{P}_c, \tag{5.24}$$

where $\mathcal{P}_c$, given by Eq. (5.16), is proportional to the magnitude of the spin current, i_s, which does not change in the presence of a magnetic field. To proceed further, we notice that only the $\mathcal{P}_z$-component of the induced dipole moment contributes to the buildup of $V_{\rm eff}^{\rm SH}$ and should be substituted into Eq. (5.19) instead of $\mathcal{P}_c$. We first perform integration over z and x. The remaining integral over y takes the form

$$V_{\rm eff}^{\rm SH}(y_0,\omega_L) = 2nd\mathcal{P}_c\int_0^\infty dy\left[\frac{1}{\sqrt{(y-y_0)^2+d^2}}-\frac{1}{\sqrt{(y-y_0)^2+L^2}}\right]$$

$$\times \cos\Big[\Big(\frac{\omega_L}{2D_{\rm out}}\Big)^{\frac{1}{2}} y\Big] \exp\Big[-\Big(\frac{\omega_L}{2D_{\rm out}}\Big)^{\frac{1}{2}} y\Big]. \tag{5.25}$$

For $\omega_L = 0$ Eq. (5.25) reproduces the limiting cases of Eq. (5.21). With characteristic distance y_0, being $\sim L$, we conclude that the characteristic magnetic field is

$$\tilde{\omega}_L = \frac{1}{T} = \frac{D_{\rm out}}{L^2}, \tag{5.26}$$

which is a natural scale at which the diffusion time through a square with a side L is equal to the Larmour period. Simple asymptotic expressions for $V_{\rm eff}^{\rm SH}$ can be obtained in the domain $\omega_L \gg \tilde{\omega}_L$, when the second term in the integrand can be neglected:

(i) $d \ll y_0 \ll \Big(D_{\rm out}/\omega_L\Big)^{1/2}$. In this limit, the log-divergence at large y is cut off at $y \sim (D_{\rm out}/\omega_L)^{1/2}$, and we get

$$V_{\rm eff}^{\rm SH}(y_0, \omega_L) = 2nd\mathcal{P}_c \ln\Big(\sqrt{\frac{D_{\rm out}}{\omega_L}}\frac{y_0}{d^2}\Big) \tag{5.27}$$

(ii) $y_0 \gg \Big(D_{\rm out}/\omega_L\Big)^{1/2}$. We can now neglect y compared to y_0 in the square brackets. Then the integration can be easily performed, yielding

$$V_{\rm eff}^{\rm SH}(y_0, \omega_L) = nd\mathcal{P}_c\Big(\frac{D_{\rm out}}{\omega_L y_0^2}\Big)^{\frac{1}{2}}. \tag{5.28}$$

The asymptotes Eq. (5.27), (5.28) do not cover the entire domain of ω_L. At the crossover field $\omega_L \sim D_{\rm out}/y_0^2$. Eq. (5.27) exceeds Eq. (5.28) by a large factor $\sim \ln(y_0/d)$. As the magnetic-field dependence of voltage is plotted numerically, see Fig. 5.6, it appears that in the intermediated domain the ISHE voltage exhibits two sign reversals. This means that the oscillations in Eq. (5.23) do not average out completely after integration over the positions of the spheres.

5.4 Effective spin diffusion length

There are two reasons why the effective spin-diffusion length of the mixture exceeds λ. The first reason is obvious: the grains are sparse and there is no spin relaxation in between the grains. The second reason is much more subtle and becomes important when λ is much smaller than the grain radius. Namely, the rate of the spin relaxation at the grain surface is suppressed. Formally, this suppression, illustrated in Fig. 5.4, follows from the behavior of polarization inside the grain

$$\boldsymbol{P}_{\rm in}(\boldsymbol{r}) = -\frac{3a}{D_{\rm in}\mathcal{M}}\Big(\frac{i_1(\frac{r}{\lambda})}{i_1(\frac{a}{\lambda})}\Big) i_s \sin\theta\, \boldsymbol{e}_\phi = -\frac{3a i_1(\frac{r}{\lambda})}{2D_{\rm out} i_1(\frac{a}{\lambda}) + D_{\rm in}\frac{a}{\lambda} i_1'(\frac{a}{\lambda})} i_s \sin\theta\, \boldsymbol{e}_\phi. \tag{5.29}$$

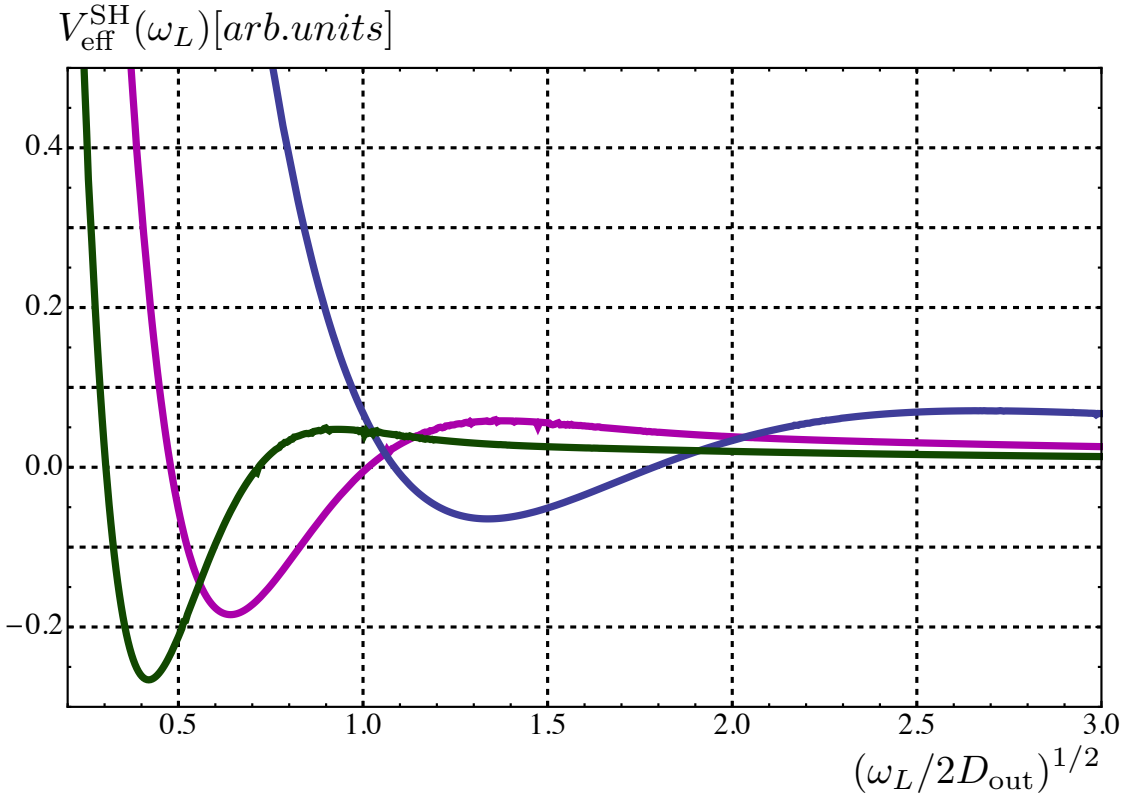

Figure 5.6: (color online). Dependence of the effective ISHE voltage on a longitudinal magnetic field, ω_L, is plotted from Eq. (5.25) for three different positions. y_0, in the units of $(dL)^{1/2}$, along the sample. Blue, violet, and green curves correspond to $y_0 = 2$, $y_0 = 4$, and $y_0 = 6$, respectively.

It is seen from Fig. 5.4 that, for $\lambda = a/12$, the radial distribution of $\boldsymbol{P}_{\rm in}(\boldsymbol{r})$ not only falls off rapidly from the surface towards the center, but its value at the surface is small. The physical origin of this smallness is elucidated in the Appendix.

While our goal is to find $\lambda_{\rm eff}$, in order not to deal with boundaries we first calculate the effective spin relaxation time of the mixture. Spin relaxation takes place only inside the spheres. If at time $t = 0$ the polarization inside the sphere is distributed according to Eq. (5.29), then the rate of decay of this polarization is given by the integral over the volume of the sphere

$$R = \frac{1}{\tau_s}\int d\Omega\Big[\boldsymbol{P}_{\rm in}(\boldsymbol{r})\Big]_\phi. \tag{5.30}$$

Using the explicit form, $i_1(x) = \left(x\cosh(x) - \sinh(x)\right)/x^2$, of the modified spherical Bessel function, the integral can be evaluated, and the result can be cast in the form

$$R = \frac{3\pi^2 a^4 i_s}{D_{\rm in}\tau_s}{\rm F}\Big(\frac{a}{\lambda}\Big), \tag{5.31}$$

where the dimensionless function ${\rm F}(x)$ is defined as

$${\rm F}(x) = \frac{x\sinh(x) - 2\cosh(x) + 2}{2(\frac{D_{\rm out}}{D_{\rm in}} - 1)[x\cosh(x) - \sinh(x)]x + x^3\sinh(x)}. \tag{5.32}$$

The result, Eq. (5.31), can also be expressed through the polarization outside the sphere by replacing i_s by $P_{\rm out}D_{\rm out}/a$, see Eq. (5.8). One has

$$R = \frac{3\pi^2 a^3 P_{\rm out}D_{\rm out}}{D_{\rm in}\tau_s}{\rm F}\Big(\frac{a}{\lambda}\Big). \tag{5.33}$$

In the absence of spin current, the spin relaxation inside the spheres causes the time decay of the spin polarization in the medium between the spheres. This is because diffusing carriers eventually "hit" a sphere. Consider an interval $(y_0 - \frac{\delta y}{2}, y_0 + \frac{\delta y}{2})$, and assume that there are hard walls at the ends, so electrons do not flow in or out. Then the initial net polarization, $P_{\rm out}(y_0)\delta y$, inside the interval will decay with some effective rate $\tau_{\rm eff}^{-1}$. To find this rate, we substitute the the two-dimensional density of spheres in the interval, $n\delta y$, into the balance equation

$$\frac{P_{\rm out}(y_0)\delta y}{\tau_{\rm eff}} = n\delta y R. \tag{5.34}$$

Substituting Eq. (5.33) into Eq. (5.34), we readily find

$$\tau_{\rm eff} = \frac{D_{\rm in}\tau_s}{3\pi^2 n a^3 D_{\rm out}{\rm F}(\frac{a}{\lambda})}. \tag{5.35}$$

Note that the product in the numerator is equal to λ^2. We can now use the expression for the effective relaxation time to find the effective spin-diffusion length

$$\lambda_{\text{eff}} = \sqrt{D_{\text{out}}\tau_{\text{eff}}} = \frac{\lambda}{\left[3\pi^2 n a^3 \mathrm{F}(\frac{a}{\lambda})\right]^{1/2}}. \tag{5.36}$$

Let us trace the decrease of λ_{eff} as the spin-diffusion rate inside the sphere gradually decreases. For $\lambda \gg a$, the function $\mathrm{F}(x)$ can be replaced by $\mathrm{F}(0) = \frac{D_{\text{in}}}{4(2D_{\text{out}}+D_{\text{in}})}$. Thus the enhancement of the spin-diffusion length due to patterning the SO material into granules is $\sim (na^3)^{-1/2}$. In the opposite limit $\lambda \ll a$ we have $\mathrm{F}(x) \approx 1/x^2$. This leads to the unexpected conclusion that in this limit λ_{eff} *saturates* at the value $\sim \frac{1}{(na)^{1/2}}$. The origin of this saturation is suppression of polarization at the surface, the effect discussed above and further elaborated on in the Appendix.

5.5 Discussion

The two main results of the present paper are Eqs. (5.21), (5.22), and Eq. (5.36) for the effective inverse spin Hall voltage and the effective spin diffusion length of the mixture. It is convenient to cast Eq. (5.22) in the form of the relation between the effective spin-Hall angle, $\theta^{\text{SH}}_{\text{eff}}$, of the mixture and the spin-Hall angle, θ^{SH}, of the material of the grain. The spin Hall angle is defined as the proportionality coefficient between the charge and spin current densities, more precisely, $j_c = \theta^{\text{SH}}(2e/\hbar)j_s$. Then Eq. (5.22) takes the form

$$\theta^{\text{SH}}_{\text{eff}} = \frac{12(na^3)\ln\left(\frac{L}{d}\right)}{\frac{2D_{\text{out}}}{D_{\text{in}}} + \frac{ai_1'(\frac{a}{\lambda})}{\lambda i_1(\frac{a}{\lambda})}}\theta^{\text{SH}}, \tag{5.37}$$

where we assumed $\sigma_{\text{in}} \gg \sigma_{\text{out}}$. Essentially, the proportionality between $\theta^{\text{SH}}_{\text{eff}}$ and θ^{SH} is determined by a "volume factor", na^3. Note, however, that θ^{SH} is the characteristics of a homogeneous SO-film, only as long as the film thickness, w, is much smaller than λ. For $w \gg \lambda$, θ^{SH} falls off as λ/w. At the same time, the decay of $\theta^{\text{SH}}_{\text{eff}}$ with y_0 sets in only when y_0 exceeds the *effective* spin diffusion length of the mixture. This length is much bigger than λ, as it was shown in Section IV.

Note that, strictly speaking, Eq. (5.36) describes λ_{eff} only within a numerical factor. This factor was lost as we replaced i_s by $P_{\text{out}}D_{\text{out}}/a$, assuming that the first term in Eq. (5.8) dominates. In fact, precisely at $r = a$, the two terms almost cancel each other. Indeed, substituting the expression for χ_s into Eq. (5.8), we can cast it in the form

$$\boldsymbol{P}_{\text{out}} = -\frac{i_s}{D_{\text{out}}}\left(r - \frac{a^3}{r^2} + \frac{3a^3}{\left[2 + \frac{aD_{\text{in}}i_1'(\frac{a}{\lambda})}{\lambda D_{\text{out}} i_1(\frac{a}{\lambda})}\right]r^2}\right)\sin\theta\,\boldsymbol{e}_\phi. \tag{5.38}$$

In the limit $\lambda \ll a$ and $r = a$, the expression in the brackets is equal to $3\lambda D_{\rm out}/D_{\rm in}$, and thus is much smaller than a. However, for bigger $r \sim a$ the compensation of the first two terms does not take place, and the relation $i_s \sim P_{\rm out} D_{\rm out}/a$ holds.

The suppression of $P_{\rm out}$ near the surface of the sphere, expressed by Eq. (5.38), is the reason why $\lambda_{\rm eff}$ saturates when $\lambda \to 0$; see Fig. 5.7. Loosely speaking, strong relaxation "repels" the spins from the boundary, which, in turn, slows down the effective relaxation. The above physics is quite general. To illustrate it, in the Appendix we consider a model example of diffusion of particles in the presence of an absorbing trap and demonstrate that, with increasing absorption rate, the concentration of particles vanishes at the position of the trap.

It is instructive to compare our result Eq. (5.22) with the expression for the perturbation of spin current flowing in a normal metal around a ferromagnetic sphere [29]. Rather that the SO coupling in our case, the difference of spin-up and spin-down carriers in Ref. [29] is caused by the difference of their conductivities inside the ferromagnet. As a result, the induced dipole moment in our case is normal to the spin current, while the induced "spin dipole moment"[29] is along the spin current. Other than that, the two expressions resemble each other. There is, however, an important difference. If the conductivity of the ferromagnetic sphere [29] is much higher than the conductivity of the surrounding normal medium, then the perturbation of the spin current is suppressed (resistance mismatch). On the contrary, for the inverse spin Hall effect, the bigger the ratio $D_{\rm in}/D_{\rm out}$, the stronger the modification of the spin current outside the sphere.

For a quantitative example of the effect of granularity on the effective parameters of the mixture, assume that the density of the SO granules is $na^3 = 10^{-2}$, while the spin diffusion length in the material of the granule is $\lambda = 0.2a$. Compared to the geometry in Fig. 5.3 with no granularity we "lose" 100 times in the inverse spin Hall voltage. At the same time, we gain in $\lambda_{\rm eff}$. Substituting $\lambda = 0.2a$ into Eq. (5.36), and assuming $D_{\rm in} \gg D_{\rm out}$, we find $\lambda_{\rm eff} = 10\lambda$.

5.6 Concluding remarks

For experimentally verifying our theoretical results, composites of SO and no SO materials can be prepared using a variety of widely available fabrication techniques. For example, in Ref. [30], authors used a pulsed laser deposition technique to prepare a composite composed of gold nanoclusters embedded in the ZnO matrix. In Ref. [31], a self-assembly approach was used to fabricate a composite composed of nickel nanoclusters embedded in amorphous Al_2O_3 matix. In Ref. [32], a nanofabrication approach was employed to prepare

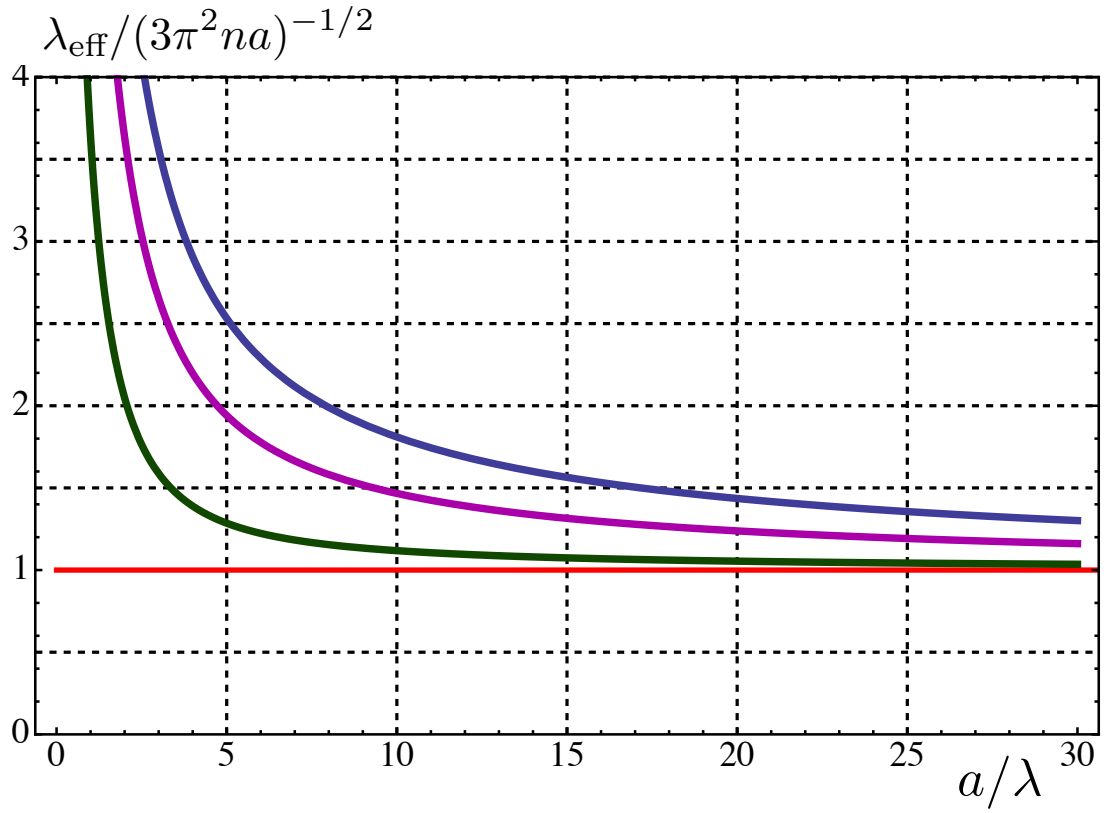

Figure 5.7: (color online). The effective spin diffusion length in the units $(3\pi^2 na)^{-1/2}$ is plotted from Eq. (5.36) for ratios $D_{\rm out}/D_{\rm in}$: $D_{\rm out}/D_{\rm in} = 1$ (green), $D_{\rm out}/D_{\rm in} = 5$ (purple), and $D_{\rm out}/D_{\rm in} = 10$ (blue). Note the saturation of $\lambda_{\rm eff}$ at small λ .

a magnonic crystal composed of cobalt nanodots embedded in a permalloy film. Similar approaches can be used to prepare the desired composite structures of SO and non-SO materials, say Pt or Au nanodots (with large $\theta^{\rm SH}$) embedded in films of low $\theta^{\rm SH}$ materials (such as copper, molybdenum or even semiconductors like silicon).

From the device point-of-view, an obvious way to enhance the spin diffusion length would be by creating a 1D structure of alternating SO and no SO layers To achieve this, however, the thickness of the SO-layer should be smaller than λ. Conversely, in a granular system the enhancement takes place when $\lambda \ll a$. This is because the spin current can flow *around* the spheres.

In numerous spin-pumping experiments, see e.g. Refs. [4-17], the measured quantity, $V^{\rm SH}$, is proportional either to $\theta^{\rm SH}\lambda$, when the thickness of nonmagnetic material is much bigger than λ, or simply to $\theta^{\rm SH}$ in the opposite limit. A comprehensive list of experimental values of $\theta^{\rm SH}$ and λ for a number of heavy metals can be found in Ref. [33]. This list indicates that, while, *separately*, $\theta^{\rm SH}$, and λ vary within wide ranges, the range of change of their product is much narrower, see also Ref. [34].

Overall, there is still experimental ambiguity in extracting the intrinsic SO parameters of materials from the experiment. In this regard, granularity can offer help by bringing a new spatial scale, the radius of the grain, a. As shown in Fig. 5.7, the value $\lambda_{\rm eff}$ depends very strongly on the relation between λ and a.

In a specific case of a semiconductor ZnO the inverse spin Hall effect was studied both in pumping experiment [35] and directly by measuring the nonlocal voltage [36]. In both measurements the value $\theta^{\rm SH}$ was found to be anomalously big, compared, e.g., to Si [14, 15]. It has recently been shown that the value $\theta^{\rm SH}$ in ZnO can be tuned very sensitively by changing the oxygen ambient under which it is grown [37]. Films prepared under a high oxygen-rich environment showed a large value for $\theta^{\rm SH}$ (~ 0.1), while the films prepared under a low oxygen ambient showed an order of magnitude lower value of $\theta^{\rm SH}$.

5.7 Appendix

Consider a diffusion in one dimension. If at time $t = 0$ the distribution of particles is a δ-peak, i.e., $n(x, 0) = \delta(x)$, then it spreads with time as

$$n(x,t) = \frac{1}{2\sqrt{\pi D t}} \exp\Big(-\frac{x^2}{4Dt}\Big) \tag{5.39}$$

where D is the diffusion coefficient.

Suppose now that an absorbing trap is placed at the coordinate origin. Then the spreading is governed by the equation

$$-\frac{\partial n}{\partial t} = -D\frac{\partial^2 n}{\partial x^2} + \frac{a\delta(x)n}{\tau_s} \tag{5.40}$$

where a is the size of the trap, and τ_s is the absorption rate. Then the time-dependent concentration, $n(x,t)$, can be expressed through the Green function of Eq. (5.40)

$$n(x,t) = \int dx' G(x,x',t) n(x',0) \tag{5.41}$$

It is convenient to present the Green function in terms of eigenfunctions, ψ_k of Eq. (5.40), which satisfy the Schödinger-like equation

$$-D\frac{\partial^2 \psi_k}{\partial x^2} + \frac{a\delta(x)}{\tau_s}\psi_k = k^2\psi_k. \tag{5.42}$$

Then the expression for G(x,x',t) reads

$$G(x,x',t) = \sum_k \psi_k(x)\psi_k(x')\exp(-Dk^2 t). \tag{5.43}$$

The second term in Eq. (5.42) plays the role of delta-potential barrier, and causes the discontinuity of the derivative of ψ_k

$$\frac{\partial \psi_k}{\partial x}\Big|_{x=0^+} - \frac{\partial \psi_k}{\partial x}\Big|_{x=0^-} = \frac{a}{D\tau_s}\psi_k(0). \tag{5.44}$$

The normalized solutions, $\psi_k(x)$, which satisfy Eq. (5.42), have the form

$$\psi_k(x) = \frac{1}{\pi^{1/2}}\cos(k|x| + \varphi_k), \tag{5.45}$$

where the phase φ_k is found from the condition

$$\tan\varphi_k = -\frac{a}{2D\tau_s k}, \tag{5.46}$$

imposed by Eq. (5.44).

Upon substituting Eq. (5.43) into Eq. (5.41) and using the initial condition, we arrive at the final result

$$n(x,t) = \frac{1}{\pi}\int_0^\infty dk \frac{\cos k|x| + \frac{a}{2D\tau_s k}\sin k|x|}{1 + (\frac{a}{2D\tau_s k})^2} e^{-Dk^2 t}. \tag{5.47}$$

It is now convenient to introduce a dimensionless coordinate $\tilde{x} = x/(Dt)^{1/2}$ and the dimensionless time-dependent parameter $\tilde{t} = a^2 t/4D\tau_s^2$. In new variables Eq. (5.47) assumes the form

$$n(x,t) = \frac{a}{2\pi D\tau_s\sqrt{\tilde{t}}}\int_0^\infty dq \frac{q^2\cos|\tilde{x}|q + \sqrt{\tilde{t}}q\sin|\tilde{x}|q}{q^2+\tilde{t}} e^{-q^2}. \tag{5.48}$$

We see that the characteristics of the trap, a and τ_s, enter only into rescaling of time. In Fig. 5.8 we plot Eq. (5.48) for four different $\tilde{t}$. It is seen from Fig. 5.8 that, with time,

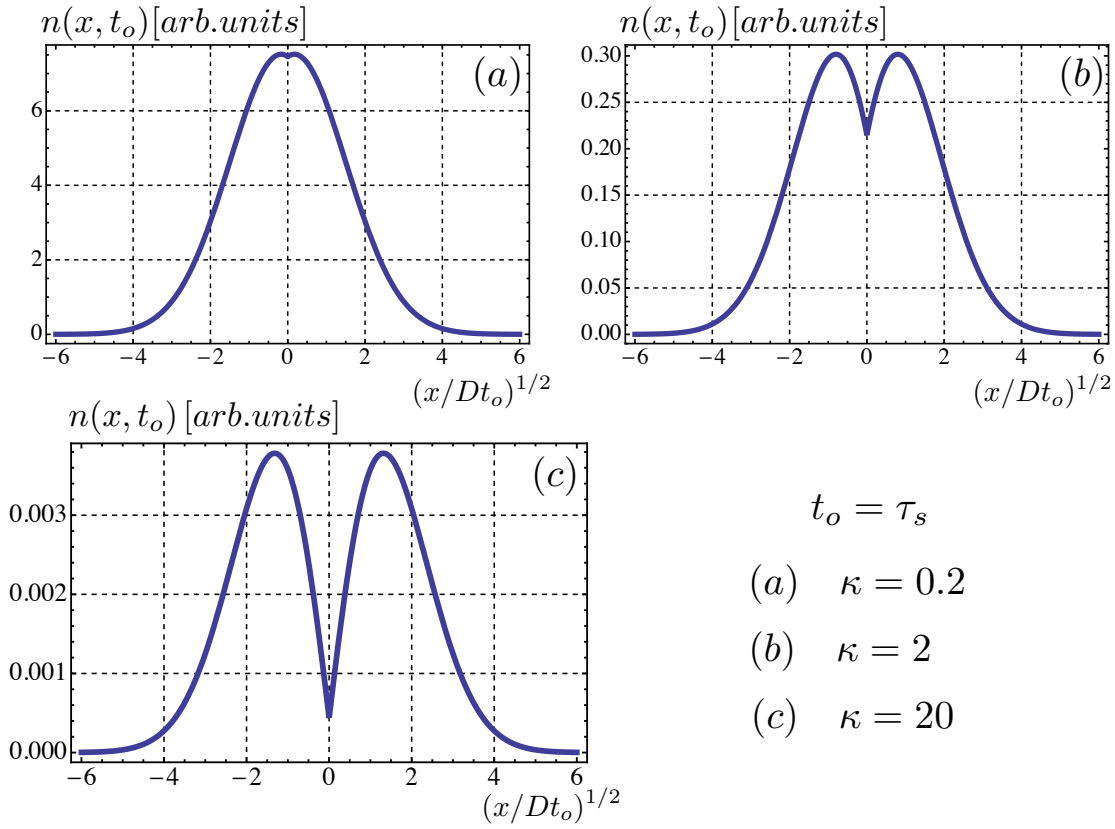

Figure 5.8: Diffusive spreading of the initial particle distribution $n(x,0) = \delta(x)$ in the presence of an absorbing trap located at $x = 0$ is described by Eq. (5.48). Shown is $n(x,t)$ at a fixed time, t_0, for different absorption efficiencies, κ, Eq. (5.51). The more absorbing the trap is, the deeper is the dip at the origin, and the slower is the decay of the net number of particles at long times, as follows from Eq. (5.50).

the density $n(0,t)$ at the origin develops a dip. The smaller τ_s, i.e., the more absorbing the trap, the sharper the dip. This conclusion also follows from the long-time asymptote of $n(x,t)$, when we neglect q^2 in denominator compared to $\tilde{t}$. Then the integration yields

$$n(x,t)\Big|_{\tilde{t}\gg 1} = \frac{a}{8\sqrt{\pi}D\tau_s\tilde{t}^{\frac{3}{2}}}\Big(\sqrt{\tilde{t}}|\tilde{x}|+1\Big)e^{-\frac{\tilde{x}^2}{4}} = \frac{\sqrt{D}\tau_s^2}{\sqrt{\pi}a^2t^{\frac{3}{2}}}\Big(\frac{a|x|}{2D\tau_s}+1\Big)e^{-\frac{x^2}{4Dt}}. \tag{5.49}$$

This asymptote indicates that the ratio of concentrations at half-width, $x \approx (Dt)^{1/2}$, and at the origin is $\sim \tilde{t}^{1/2}$, i.e., the dip is deep.

The next question we ask ourselves is how the total number of particles $\int dx\ n(x,t)$ decreases with time. Upon integration of Eq. (5.48), we get

$$N(t) = \int_{-\infty}^{\infty} dx\ n(x,t) = \mathrm{Erfc}(\tilde{t}^{\frac{1}{2}})\exp(\tilde{t}) = \begin{cases} 1-\frac{a}{\tau_s}\Big(\frac{t}{\pi D}\Big)^{\frac{1}{2}}, & \tilde{t}\ll 1, \\ \frac{2\tau_s}{a}\Big(\frac{\pi D}{t}\Big)^{\frac{1}{2}}, & \tilde{t}\gg 1, \end{cases} \tag{5.50}$$

where $\mathrm{Erfc}(s)$ is the complementary error function. It is seen from Eq. (5.50) that the change of the decay rate $\partial N/\partial t$ takes place at $\tilde{t}\sim 1$. This change is caused by the development of the dip. Indeed, for $\tilde{t}\gg 1$ the decay rate falls off with time as $t^{-3/2}$.

Overall, we conclude that the spreading of the particle density in the presence of a trap is governed by a dimensionless parameter

$$\kappa = \frac{a}{(D\tau_s)^{1/2}}, \tag{5.51}$$

which is the dimensionless efficiency of absorption by the trap. If this efficiency is small, the spreading will proceed as in the absence of the trap for most of the time, until the concentration at $x=0$ becomes really small. Only then, $n(x,t)$ will a dip develop at $x=0$, and the decay of the net number of particles will proceed even slower. For large efficiency, the dip will developed early, namely at $t\sim \tau_s/\kappa^2 \ll \tau_s$, after which time the decay of $N(t)$ will be governed by the value of $n(0,t)$ of the concentration at the dip.

Formation of a dip in our model problem puts into a general perspective the behavior of the effective spin diffusion length in the system of the SO grains. In the limit $\lambda \ll a$, see Eq. (5.36), the value λ_{eff} saturates because the polarization near the boundary gets suppressed as a result of the development of a local minimum.

5.8 References

[1] M. I. Dyakonov and V. I. Perel, Pis'ma Zh. Eksp. Teor. Fiz. **13**, 657 (1971) [Sov. Phys. JETP Lett. **13**, 467 (1971)].

[2] M. I. Dyakonov and V. I. Perel, Phys. Lett. A **35**, 459 (1971).

[3] J. E. Hirsch, Phys. Rev. Lett. **83**, 1834 (1999).

[4] E. Saitoh, M. Ueda, H. Miyajima, and G. Tatara, Appl. Phys. Lett. **88**, 182509 (2006).

[5] H. Y. Inoue, K. Harii, K. Ando, K. Sasage, and E. Saitoh, J. Appl. Phys. **102**, 083915 (2007).

[6] K. Ando, S. Takahashi, K. Harii, K. Sasage, J. Ieda, S. Maekawa, and E. Saitoh, Phys. Rev. Lett. **101**, 036601 (2008).

[7] K. Ando, T. Yoshino, and E. Saitoh, Appl. Phys. Lett. **94**, 152509 (2009).

[8] J.-C. Rojas-Sánchez, N. Reyren, P. Laczkowski, W. Savero, J.-P. Attané, C. Deranlot, M. Jamet, J.-M. George, L. Vila, and H. Jaffrès, Phys. Rev. Lett. **112**, 106602 (2014).

[9] K. Ando, S. Takahashi, J. Ieda, Y. Kajiwara, H. Nakayama, T. Yoshino, K. Harii, Y. Fujikawa, M. Matsuo, S. Maekawa, and E. Saitoh, J. Appl. Phys. **109**, 103913 (2011).

[10] O. Mosendz, J. E. Pearson, F. Y. Fradin, G. E. W. Bauer, S. D. Bader, and A. Hoffmann, Phys. Rev. Lett. **104**, 046601 (2010).

[11] B. Heinrich, C. Burrowes, E. Montoya, B. Kardasz, E. Girt, Y.-Y. Song, Y. Sun, and M. Wu, Phys. Rev. Lett. **107**, 066604 (2011).

[12] J. E. Gómez, B. Z. Tedlla, N. R. Álvarez, G. Alejandro, E. Goovaerts, and A. Butera, Phys. Rev. B **90**, 184401 (2014).

[13] A. Yamamoto, Y. Ando, T. Shinjo, T. Uemura, and M. Shiraishi, Phys. Rev. B **91**, 024417 (2015).

[14] K. Ando and E. Saitoh, Nat. Commun. **3**, 629 (2012).

[15] E. Shikoh, K. Ando, K. Kubo, E. Saitoh, T. Shinjo, and M. Shiraishi, Phys. Rev. Lett. **110**, 127201 (2013).

[16] S. Dushenko, M. Koike, Y. Ando, T. Shinjo, M. Myronov, and M. Shiraishi, Phys. Rev. Lett. **114**, 196602 (2015).

[17] S. Singh, A. Ahmadi, C. T. Cherian, E. R. Mucciolo, E. del Barco, and B. Özyilmaz, Appl. Phys. Lett. **106**, 032411 (2015).

[18] H. Zhao, E. J. Loren, H. M. van Driel, and A. L. Smirl, Phys. Rev. Lett. **96**, 246601 (2006).

[19] K. Ando, S. Watanabe, S. Mooser, E. Saitoh, and H. Sirringhaus, Nat. Mater. **12**, 622 (2013).

[20] S. Watanabe, K. Ando, K. Kang, S. Mooser, Y. Vaynzof, H. Kurebayashi, E. Saitoh, and H. Sirringhaus, Nat. Phys. **10**, 308 (2014).

[21] Z. Qiu, M. Uruichi, D. Hou, K. Uchida, H. M. Yamamoto, E. Saitoh, AIP Advances **5**, 057167 (2015).

[22] M. Kimata, D. Nozaki, Y. Niimi, H. Tajima, and Y. Otani, Phys. Rev. B **91**, 224422 (2015).

[23] B. Khachatryan, T. D. Nguyen, Z. V. Vardeny, and E. Ehrenfreund Phys. Rev. B **86**, 195203 (2012).

[24] C.-X. Sheng, S. Singh, A. Gambetta, T. Drori, M. Tong, S. Tretiak, and Z. V. Vardeny Sci. Rep. **3** (2013).

[25] D. Sun, K. J. van Schooten, H. Malissa, M. Kavand, C. Zhang, C. Boehme, and Z. V. Vardeny, arXiv:1511.07848.

[26] Z. G. Yu, Phys. Rev. Lett. **106**, 106602 (2011).

[27] Z. G. Yu, Phys. Rev. B **85**, 115201 (2012).

[28] M. I. Dyakonov, Phys. Rev. Lett. **99**, 126601 (2007).

[29] R. C. Roundy and M. E. Raikh Phys. Rev. B **91**, 045202 (2015).

[30] A. Tiwari, A. Chugh, C. Jin, and J. Narayan, J. Nanosci. Nanotechnol. **3**, 368 (2003).

[31] J. Narayan and A. Tiwari, J. Nanosci. Nanotechnol. **4**, 726 (2004).

[32] see e.g. S. Tacchi, G. Duerr, J. W. Klos, M. Madami, S. Neusser, G. Gubbiotti, G. Carlotti, M. Krawczyk, and D. Grundler Phys. Rev. Lett. **109**, 137202 (2012), and references therein.

[33] H. L. Wang, C. H. Du, Y. Pu, R. Adur, P. C. Hammel, and F. Y. Yang, Phys. Rev. Lett. **112**, 197201 (2014).

[34] P. Laczkowski, J.-C. Rojas-Sánchez, W. Savero-Torres, H. Jaffrès, N. Reyren, C. Deranlot, L. Notin, C. Beignè, A. Marty, J.-P. Attanè, L. Vila, J.-M. George, and A. Fert, Appl. Phys. Lett. **104**, 142403 (2014).

[35] J.-C. Lee, L.-W. Huang, D.-S. Hung, T.-H. Chiang, J. C. A. Huang, J.-Z. Liang, and S.-F. Lee, Appl. Phys. Lett. **104**, 052401 (2014).

[36] M. C. Prestgard and A. Tiwari, Appl. Phys. Lett. **104**, 122402 (2014).

[37] M. C. Prestgard, Ph.D thesis, University of Utah, 2015.

CHAPTER 6

RESONANT MAGNETO-TUNNELING BETWEEN NORMAL AND FERROMAGNETIC ELECTRODES IN RELATION TO THE THREE-TERMINAL SPIN TRANSPORT

6.1 Introduction

In the past decade there was remarkable progress in the fabrication of lateral structures which combine ferromagnetic and normal layers and exhibit spin transport. The first experimental evidence of spin injection from a ferromagnet into a nonmagnetic material was obtained with the help of four-terminal (4T) technique. This technique was developed in the pioneering papers Refs. [1,2]. It utilizes two ferromagnetic electrodes, injector and detector, coupled to a normal channel; see Fig. 6.1. With the detector circuit being open, the charge current does not flow between the electrodes. Instead, the current circulating in the injector circuit leads to the voltage buildup between the detector and the normal channel. This voltage buildup, or, in other words, the nonlocal voltage, is denoted with V_d in Fig. 6.1. The nonlocal voltage is suppressed by a weak magnetic field normal to the direction of magnetizations of the electrodes. Such a suppression, called the Hanle effect, reflects the precession of the spin of carriers in the course of diffusion between the electrodes. Thus, the characteristic width of the Hanle curve is the inverse spin relaxation time. This estimate is valid if the distance between the injector and detector is smaller than the spin-diffusion length. In the opposite limit, a typical spin experiences a full rotation before arriving to the detector. As a result, the shape of the Hanle curve acquires an oscillatory character. This is illustrated in Fig. 6.2, where the Hanle curves for two strongly different sample lengths are presented. Additional information about the spin transport can be inferred by measuring the Hanle curve as a function of tilt of the external field, as illustrated in Fig. 6.1.

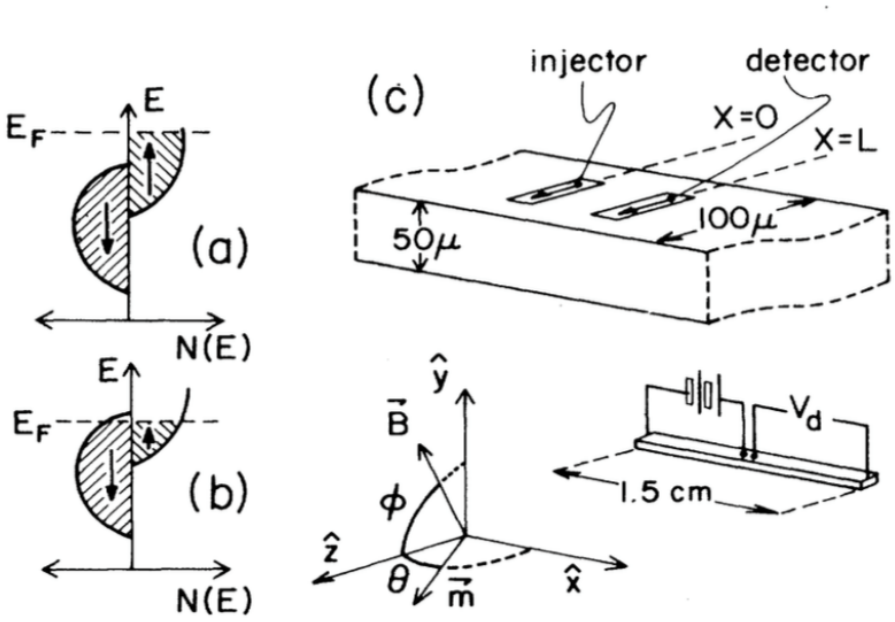

Figure 6.1: Overidealized Stoner ferromagnet with (a) a full subband and (b) inequivalent subbands. (c) The geometry of the experiment (adapted from Ref. [1]).

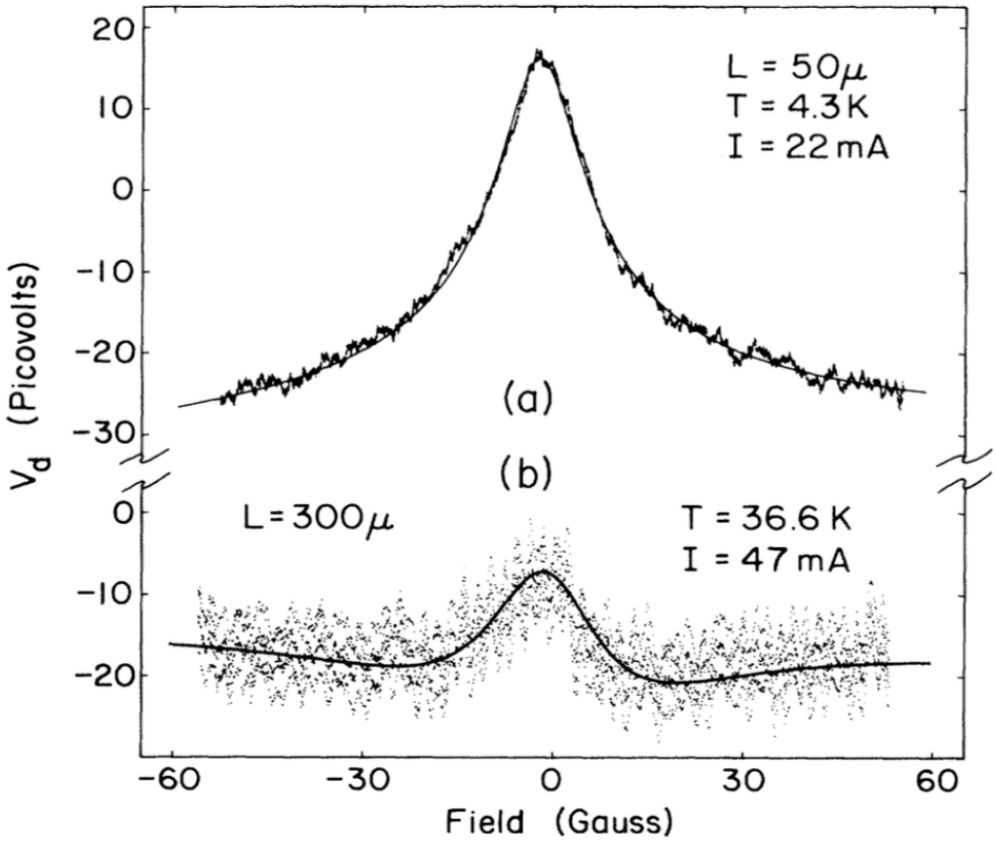

Figure 6.2: Hanle curve. (a) Sample Walrus7, $\hat{x}$ sweep and fit, in the thin limit. $\delta_s = 450\mu m \gg 50\mu m = L$. (b) Sample Walrus6, average of three $\hat{y}$ sweeps and fit, in the thick limit. $\delta_s = 170\mu m < 300\mu m = L$. (adapted from Ref. [1]).

More recently, experimental studies of spin injection were carried out using the three-terminal [3-13] (3T) technique. Unlike the 4T technique, in this technique the injector and detector electrodes are combined. The signal measured is the contact voltage between the ferromagnet and the normal channel. Thus, the sensitivity of this signal to the applied magnetic field can be viewed as simply the magnetoresistance of the junction containing ferromagnetic and normal electrodes. In particular, in the setup shown in Fig. 6.3 the Hanle measurement reveals the spin accumulation under the left ferromagnetic electrode. This accumulation results from the injection from the ferromagnet. Two other electrodes serve for passage of the current and measuring the voltage. Unlike 4T setup, spin transport in the channel is not involved. Another schematic illustration of the 3T technique is shown in Fig. 6.4. Depending on what voltage is measured, V_{NL} or V, the device acts as 4T or 3T, respectively.

In a number of papers, see e.g., Refs. [4], [9], [12], the sensitivity of the 3T signal to a weak magnetic field is, by analogy to the 4T signal, identified with the spin precession. Namely, it is maintained that the measured signal in the 3T geometry is the sum of two components, one coming from the resistance of the FM contact and the second resulting from the local accumulation of the spins beneath the ferromagnetic contact.

Experimental results reported in Refs. [3-13] consistently reveal two puzzling features of the 3T magnetoresistance. Unlike the normal Hanle curves, the magnetic field response of the 3T signal shows up for orientations of the external *both* parallel as well as perpendicular to the magnetization of the injector. Moreover, the signs of magnetoresistance are *opposite* for the two field orientations; see Fig. 6.4. In addition, the 3T magnetoresistance curves are much broader than the inverse spin-relaxation times measured independently. In general, the basic underlying physics of magnetoresistance in transport between ferromagnetic and normal electrodes constitutes a puzzle. Indeed, even if the portion of a channel under the ferromagnetic electrode accumulates the spin, the normal electrode, acting as a detector, does not "discriminate" between different spin orientations, and, thus, the current should not be sensitive to the spin precession.

Possible resolution of these puzzles was proposed very recently in the theoretical paper Ref. [14] and received some experimental support in the subsequent publications Refs. [15-17]. The main idea of Ref. [14] is that the passage of current between the ferromagnet and the normal electrode can be modeled as resonant tunneling via an impurity; see Fig. 6.5. On the qualitative level, the physics uncovered in Ref. [14] can be explained as follows. When the current flows from normal into ferromagnetic electrodes, the spins of electrons

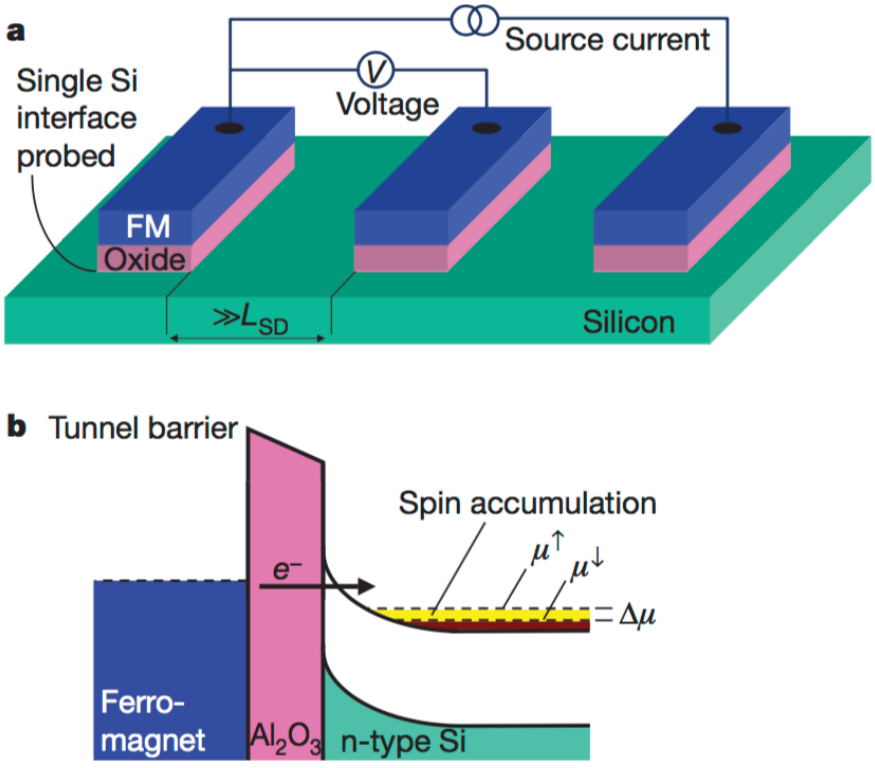

Figure 6.3: Device geometry and energy diagram of magnetic contact with n-Si. a, Three-terminal device for injection and detection of spin polarization in Si under a single contact (left) consisting of an oxide insulator and a ferromagnetic-metal electrode (FM; blue). Contacts used to source current (right) and detect the voltage (middle) are placed away from the active interface by more than several spin diffusion lengths (L_{SD}). Each contact has an area of $100 \times 200 \mu m^2$. b, Energy band profile of the junction, depicting the ferromagnet, the Al_2O_3 barrier and the n-type Si conduction and valence bands bending up towards the oxide, forming a depletion region in the Si that acts as a second part of the tunnel barrier (adapted from Ref. [3]).

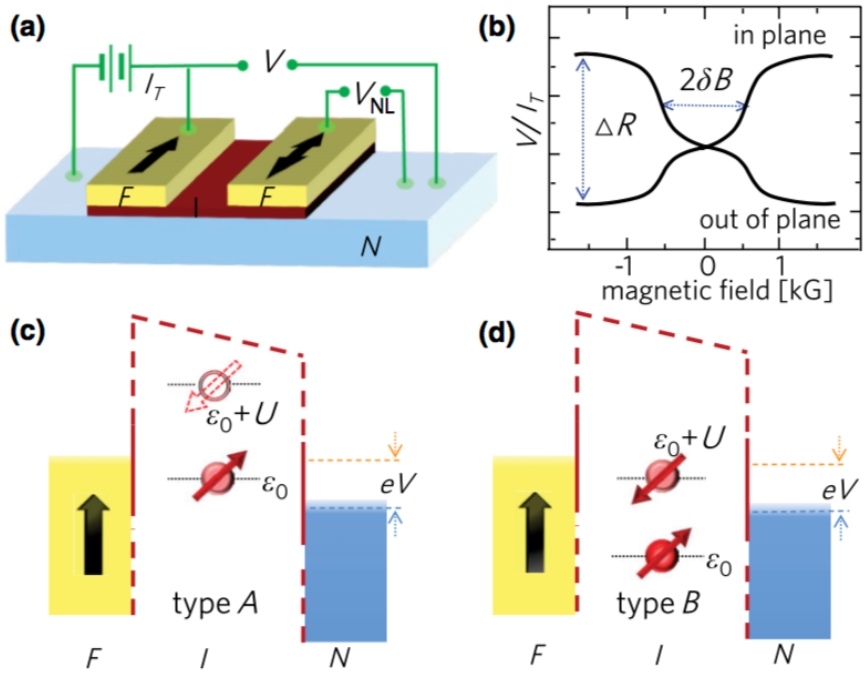

Figure 6.4: (color online). Three-terminal transport. (a) Nonlocal and local electrical setups for detecting spin accumulation. (b) The measured signal $\delta R(B) = [V(B) - V(0)]/I_T$ is a change in junction resistance when applying in-plane or out-of-plane magnetic fields. The Lorentzian due to the in-plane field is typically observed only in the local setup. Resonant tunneling via (c) type A or (d) type B impurities for spin injection (electrons flow from F to N) (adapted from Ref. [14]).

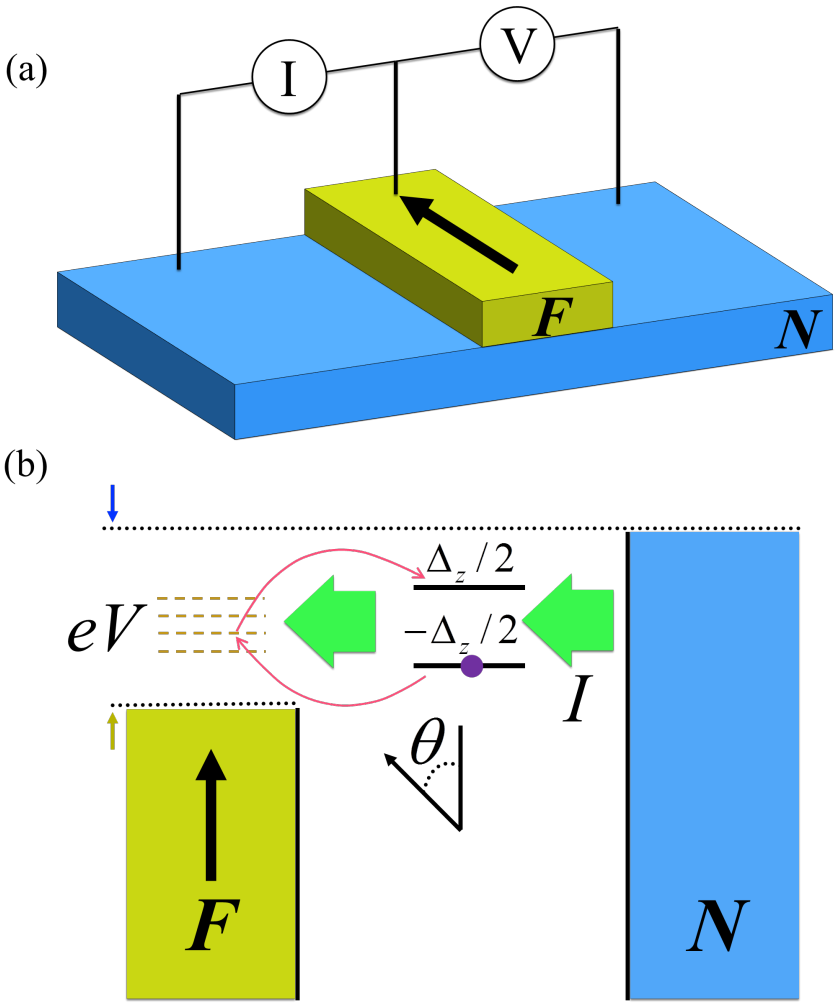

Figure 6.5: (color online). Three-terminal transport. (a) Electrical setup for measuring the spin accumulation within the 3T technique. (b) Energy diagram illustrating the passage of current in (a). The transport is by resonant magnetotunneling between a normal electrode and a ferromagnet. External field, tilted by an angle θ from the direction of magnetization, causes a splitting, Δ_z, of the the impurity level. For nonzero θ two Zeeman levels get coupled via a continuum of the states in a ferromagnet.

arriving on the impurity do not have a preferential direction. Suppose that the ferromagnet is fully polarized in $\uparrow$ direction. Then electrons arriving with spin $\downarrow$ will never tunnel into the ferromagnet. External magnetic field induces precession of spins of the arriving electrons. Then the electrons, which were "trapped" on the impurity without a magnetic field, get a chance to tunnel, unless the field is not parallel to the magnetization. As a result, the current, which did not flow in a zero field, becomes finite. The characteristic value of a magnetic field can be estimated by equating the period of precession to the waiting time for tunneling. The mechanism is efficient if the spin relaxation rate is smaller than the tunneling rate. Obviously, for the reverse bias, when electrons flow from the ferromagnet this mechanism does not apply.

The key ingredient of the above scenario is a strong repulsion, U, of $\uparrow$ and $\downarrow$ electrons on the impurity. Indeed, if the tunneling of the $\downarrow$ electron is forbidden, then, without the repulsion, the current will be carried by $\uparrow$ electrons, so that there will be no "blockade".

In the present paper we address a question: whether large U is indeed necessary to induce magnetoresistance. The question is delicate, since, for $U = 0$, the current does not depend on the polarity of bias. Thus, if magnetoresistance is finite for tunneling into a ferromagnet, it should be the same for tunneling into a normal electrode, which is highly non-obvious. On the other hand, for $U = 0$ the current can be calculated exactly. Indeed, resonant tunneling in external field can be viewed as a two-channel resonant tunneling [18] via the Zeeman-split levels. Our main analytical result is that magnetoresistance is finite for $U = 0$, and its magnitude is about 50%. The physical origin of the magnetoresistance is the interference of the two transport channels, or, in other words, the coupling of Zeeman levels via a continuum of states in the ferromagnet. We also trace how this coupling affects the current in the regime of correlated transport [14].

The paper is organized as follows. In Sect. 2 we derive and analyze the expression for noninteracting resonant conductance via two Zeeman levels and, subsequently, for the net resonant current. In Sect. 3 we study how the coupling of the Zeeman levels via a ferromagnet affects the current in the presence of correlations. Concluding remarks are presented in Sect. 4.

6.2 Magnetoresistance in the absence of Coulomb correlations

6.2.1 General expression

Within a noninteracting picture we can view the tunneling through a single impurity in a magnetic field as tunneling via two Zeeman-split levels. The noninteracting current-voltage

characteristics can be calculated from the tunnel conductance, $G(\mathcal{E})$, as follows

$$I = \int d\mathcal{E} \left[f\Big(\mathcal{E} - \frac{V}{2}\Big) - f\Big(\mathcal{E} + \frac{V}{2}\Big) \right] G(\mathcal{E}), \tag{6.1}$$

where V is the bias, and $f(\mathcal{E})$ is the Fermi distribution.

If the electrodes are normal, the tunneling via each Zeeman level, $\pm\Delta_z/2$, proceeds independently, and $G(\mathcal{E})$ is given by the Breit-Wigner formula

$$G_{\pm}(\mathcal{E}) = \frac{e^2}{\pi\hbar} \Big[\frac{\Gamma_L \Gamma_R}{(\mathcal{E} \pm \frac{1}{2}\Delta_z)^2 + \frac{1}{4}(\Gamma_L + \Gamma_R)^2} \Big], \tag{6.2}$$

where Γ_L and Γ_R are the widths with respect to tunneling into the left and right electrodes, respectively.

Two tunneling channels are independent because the normal electrodes do not couple the Zeeman levels, since the corresponding spinors are orthogonal to each other. By contrast, a ferromagnetic electrode *does* introduce the coupling between the levels for any orientation of magnetic field except for the field parallel to the magnetization. Indeed, if the angle between the magnetic field and magnetization is θ, the spinors corresponding to the Zeeman levels are

$$\chi_+ = \cos\frac{\theta}{2} \uparrow + \sin\frac{\theta}{2} \downarrow, \quad \chi_- = \sin\frac{\theta}{2} \uparrow - \cos\frac{\theta}{2} \downarrow, \tag{6.3}$$

where $\uparrow$ and $\downarrow$ are the spin states in the ferromagnet, and the azimuthal angle is set to zero. Denote with $\Gamma_L^{\uparrow}$ and $\Gamma_L^{\downarrow}$ the widths of the Zeeman levels with respect to tunneling into the ferromagnet for $\theta = 0$. At finite θ, an electron in the state χ_+ can virtually tunnel into the $\uparrow$-state of the ferromagnet. The amplitude of this tunneling is $\cos\frac{\theta}{2}$. From the $\uparrow$-state it can then virtually tunnel into χ_- with amplitude $\sin\frac{\theta}{2}$. The electron can also proceed from χ_+ to χ_- via the $\downarrow$ state of the ferromagnet. The corresponding amplitude is $-\sin\frac{\theta}{2}\cos\frac{\theta}{2}$, i.e., it has the opposite sign. As a result, the coupling matrix element between χ_+ and χ_- is equal to $(\Gamma_L^{\uparrow} - \Gamma_L^{\downarrow})\sin\frac{\theta}{2}\cos\frac{\theta}{2}$. It is finite due to the difference in the densities of the intermediate states.

With two Zeeman levels coupled, the tunneling into the ferromagnet is described by a matrix

$$\hat{\Gamma}^L = \begin{pmatrix} \Gamma_L^{\uparrow}\cos^2\frac{\theta}{2} + \Gamma_L^{\downarrow}\sin^2\frac{\theta}{2} & (\Gamma_L^{\uparrow} - \Gamma_L^{\downarrow})\cos\frac{\theta}{2}\sin\frac{\theta}{2} \\ (\Gamma_L^{\uparrow} - \Gamma_L^{\downarrow})\cos\frac{\theta}{2}\sin\frac{\theta}{2} & \Gamma_L^{\uparrow}\sin^2\frac{\theta}{2} + \Gamma_L^{\downarrow}\cos^2\frac{\theta}{2} \end{pmatrix}. \tag{6.4}$$

This matrix enters into the calculation of the differential conductance, which is given by the matrix generalization of the Landauer formula

$$G(\mathcal{E}) = \frac{e^2}{\pi\hbar} \mathrm{Tr}(\hat{\Gamma}^L \hat{S} \hat{\Gamma}^R \hat{S}^{\dagger}), \tag{6.5}$$

where the matrix $\hat{\Gamma}^R$, describing the tunneling into the normal electrode, is diagonal

$$\hat{\Gamma}^R = \Gamma_R \begin{pmatrix} 1 & 0 \\ 0 & 1 \end{pmatrix}. \tag{6.6}$$

The matrix $\hat{S}$, which is the Green function in the matrix form, is given by

$$\hat{S} = \left[\mathcal{E} - \hat{E} + \frac{i}{2}(\hat{\Gamma}^L + \hat{\Gamma}^R)\right]^{-1}. \tag{6.7}$$

The matrix $\hat{E}$ in Eq. (6.7) encodes the energy level positions

$$\hat{E} = \begin{pmatrix} -\frac{1}{2}\Delta_z & 0 \\ 0 & \frac{1}{2}\Delta_z \end{pmatrix}. \tag{6.8}$$

We will present the result of the evaluating of the matrix product Eq. (6.5) in the notations of Ref. [14], by denoting with Γ_N (instead of Γ_R) the tunnel width for the normal electrode and introducing the polarization, p, of the ferromagnetic electrode

$$p = \frac{\Gamma_L^{\uparrow} - \Gamma_L^{\downarrow}}{2\Gamma_F}, \tag{6.9}$$

where $\Gamma_F = \frac{1}{2}(\Gamma_L^{\uparrow} + \Gamma_L^{\downarrow})$ is the effective tunneling width for the ferromagnetic electrode, so that

$$\Gamma_L^{\uparrow} = \Gamma_F(1+p), \qquad \Gamma_L^{\downarrow} = \Gamma_F(1-p). \tag{6.10}$$

With the new notations, the matrix Eq. (6.4) assumes a compact form

$$\hat{\Gamma}^L = \Gamma_F \begin{pmatrix} 1 + p\cos\theta & p\sin\theta \\ p\sin\theta & 1 - p\cos\theta \end{pmatrix}. \tag{6.11}$$

The resulting expression for conductance, $G(\mathcal{E})$, reads

$$G(\mathcal{E}) = \frac{2e^2}{\pi\hbar}\Gamma_N\Gamma_F \frac{\mathcal{E}^2 + \frac{1}{4}(\Delta_z^2 + \Gamma_N^2) - \mathcal{E}\Delta_z p\cos\theta + \frac{1}{4}(1-p^2)\Gamma_F(2\Gamma_N + \Gamma_F)}{\left[\mathcal{E}^2 - \frac{1}{4}(\Delta_z^2 + \Gamma_N^2 + 2\Gamma_F\Gamma_N + (1-p^2)\Gamma_F^2)\right]^2 + \left[\mathcal{E}(\Gamma_N + \Gamma_F) - \frac{1}{2}\Gamma_F\Delta_z p\cos\theta\right]^2}. \tag{6.12}$$

6.2.2 Analysis

Naturally, the dependence $G(\mathcal{E})$ is an even function of $\mathcal{E}$ only for the perpendicular orientation of the magnetic field, $\theta = \pi/2$. The asymmetry of $G(\mathcal{E})$ is maximal for the parallel orientation. The asymmetry becomes progressively pronounced with increasing magnetic field, as illustrated in Fig. 6.6.

The specifics of tunneling from the ferromagnet, as compared to the normal electrode, is that Eq. (6.12) depends on the orientation of magnetic field. In Ref. [17] the tunneling

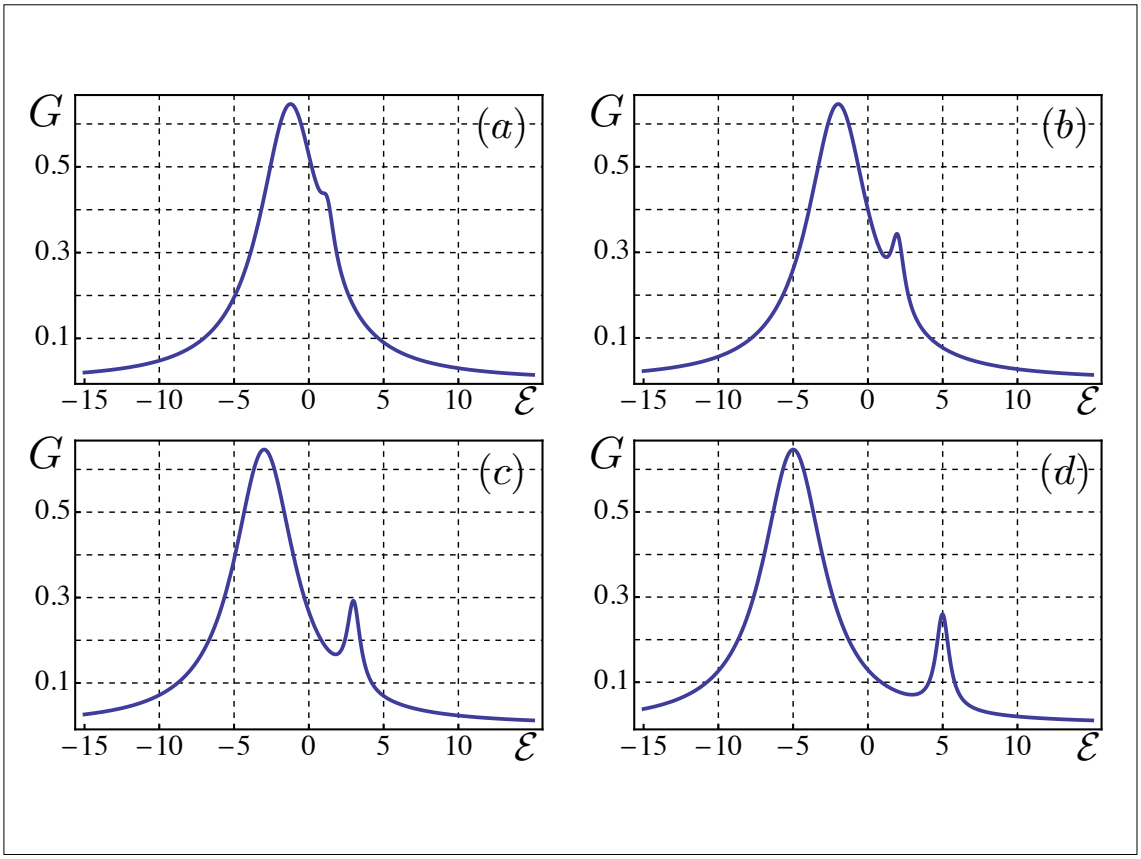

Figure 6.6: Differential conductance, $G(\mathcal{E})$, in the units of $e^2/\pi\hbar$ is plotted from Eq. (6.12) for different dimensionless magnetic fields, in the units Δ_z/Γ_N. (a)-(d) correspond to $\Delta_z/\Gamma_N = 2.5, 4, 6$, and 10, respectively. All curves are plotted for $\Gamma_F = 2\Gamma_N$ and the orientation of the magnetic field, $\theta = 15°$.

from cobalt-iron electrode into silicon via an oxide was studied using the inelastic electron tunneling spectroscopy. The curves $\frac{\partial^2 I}{\partial V^2}$ exhibited different behavior for parallel and perpendicular orientations of magnetic field. Motivated by these findings, in Fig. 6.7 we plot the $\frac{\partial^2 I}{\partial V^2}$ calculated from Eq. (6.12) for $\theta = \pi/2$ as a function of bias and magnetic field together with the difference of $\frac{\partial^2 I}{\partial V^2}$ for $\theta = \pi/2$ and $\theta = 0$. The value at $\theta = 0$ is finite due to finite polarization $p = 1/3$ of the ferromagnet. All the plots correspond to high-temperature $T = 10\Gamma_N$, so that only the magnitude, not the shape, of the curves is T-dependent. It is seen from Fig. 6.7 that the relative difference of second derivatives is $\sim 10\%$ and exhibits additional structure at small Δ_z and at small bias. Still Fig. 6.7 cannot account for the results of Ref. [17], where the observed anisotropy was really strong.

An interesting situation unfolds when the bias and temperature are of the same order and are much bigger than the level width. Then the Δ_z-dependence of current, calculated numerically from Eq. (6.1), exhibits a growth for perpendicular orientation and a minimum for parallel orientation as it is seen in Fig. 6.8.

6.2.3 The net current at large bias

In 3T experiments [3-13] the net current showed the dependence on the magnitude and orientation of magnetic field. It is not obvious whether this dependence is captured by Eqs. (6.1), (6.12). For tunneling between normal electrodes, $p = 0$, there should be no magnetoresistance. Indeed, the expression Eq. (6.12) can be presented as a sum of two Lorentzians

$$G(\mathcal{E}) = \frac{e^2}{\pi\hbar}\Gamma_N\Gamma_F \times \Big[\frac{1}{(\mathcal{E} - \frac{1}{2}\Delta_z)^2 + \frac{(\Gamma_F+\Gamma_N)^2}{4}} + \frac{1}{(\mathcal{E} + \frac{1}{2}\Delta_z)^2 + \frac{(\Gamma_F+\Gamma_N)^2}{4}}\Big], \tag{6.13}$$

so that the Δ_z-dependence disappears upon integration over $\mathcal{E}$. It turns out that magnetoresistance is nonzero for a finite p. We will present the result for the net current assuming that ferromagnetic electrode is fully polarized, $p = 1$. Then the integration over $\mathcal{E}$ yields

$$I(\Delta_z) = \frac{4e}{\hbar}\Gamma_F\Gamma_N \times \frac{(\Delta_z^2 + \Gamma_N^2 + \Gamma_N\Gamma_F)(\Gamma_N + \Gamma_F) - \Gamma_F\Delta_z^2\cos^2\theta}{(\Delta_z^2 + \Gamma_N^2 + 2\Gamma_N\Gamma_F)(\Gamma_N + \Gamma_F)^2 - \Gamma_F\Delta_z^2\cos^2\theta}. \tag{6.14}$$

Eq. (6.14) is our central result. Sensitivity of the net current to Δ_z originates from the coupling of Zeeman levels via the ferromagnetic electrode [nondiagonal element in matrix Eq. (6.11)] and, thus, it is most pronounced for $\Gamma_F \gg \Gamma_N$. In this limit Eq. (6.14) can be simplified to

$$I(\Delta_z) = \frac{4e}{\hbar}\Gamma_N\left(1 - \frac{\Gamma_N\Gamma_F}{\Delta_z^2\sin^2\theta + 2\Gamma_N\Gamma_F}\right). \tag{6.15}$$

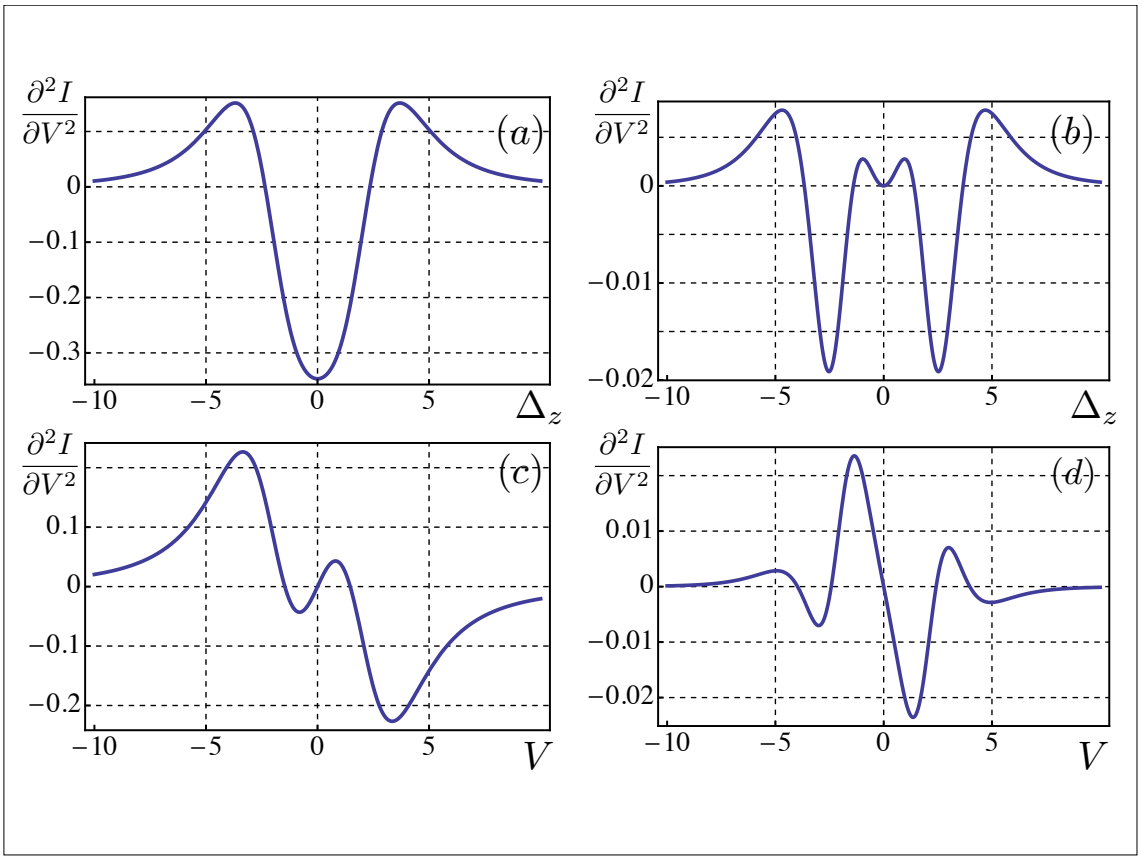

Figure 6.7: The second derivative, $\frac{\partial^2 I}{\partial V^2}|_{\theta=\pi/2}$ ((a),(c)) and the difference, $\frac{\partial^2 I}{\partial V^2}|_{\theta=\pi/2} - \frac{\partial^2 I}{\partial V^2}|_{\theta=0}$ ((b),(d)) are plotted from Eqs. (6.1), (6.12) versus dimensionless magnetic field, Δ_z/Γ_N, (a) and (b), and versus dimensionless bias, V/Γ_N, (c) and (d). Note that the unites on the vertical axis are $e^3/\pi\hbar\Gamma_N$. In (a) and (b) the bias is $V = 2\Gamma_N$, while in (c) and (d) the magnetic field is $\Delta_z = 2\Gamma_N$. In all plots $\Gamma_F = 1.5\Gamma_N$, polarization is $p = 1/3$, and temperature is $T = 10\Gamma_N$.

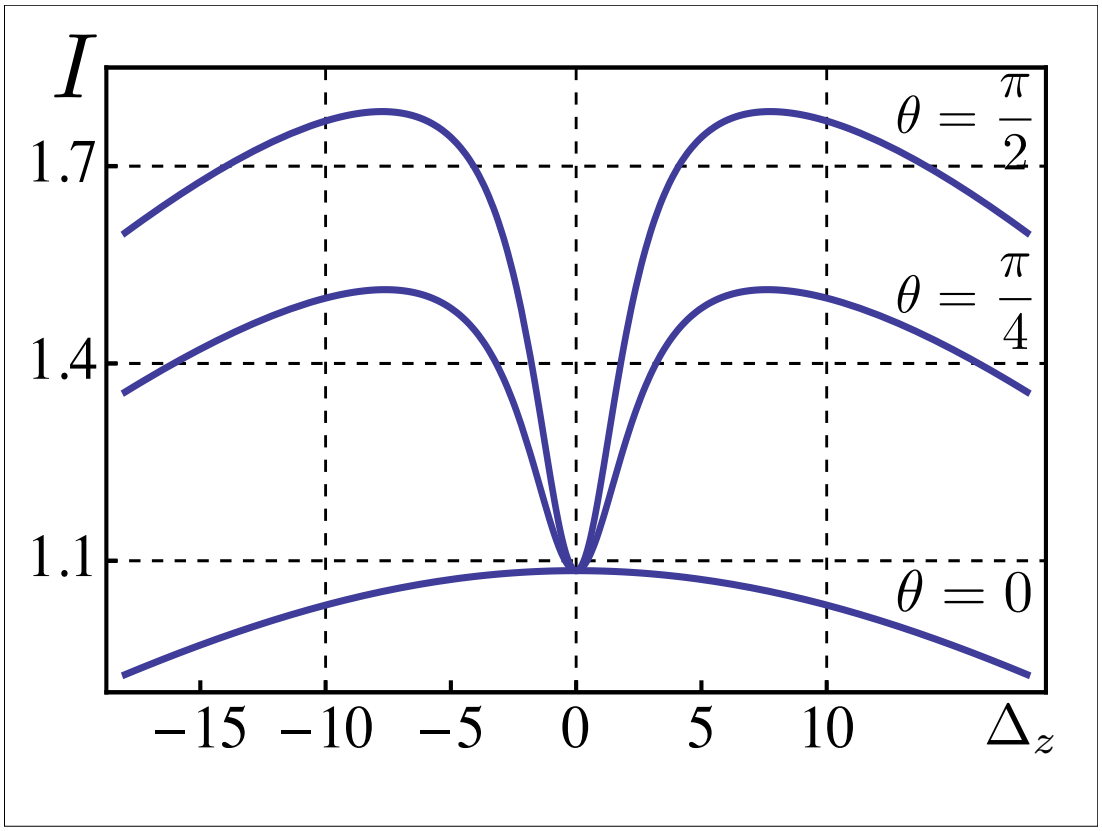

Figure 6.8: Resonant-tunneling current (in the units $e\Gamma_N/\pi\hbar$) calculated numerically from Eqs. (6.1), (6.12) is plotted versus the dimensionless magnetic field, Δ_z/Γ_N, for different field orientations. In all curves $\Gamma_F = 2\Gamma_N$, the bias is $V = 10\Gamma_N$ and the temperature is $T = 10\Gamma_N$.

The current Eq. (6.14) is a growing function of magnetic field for all orientations, θ; see Fig. 6.9. At large Δ_z the current saturates at the value

$$I_\infty = \frac{4e}{\hbar}\Gamma_F\Gamma_N\frac{\Gamma_F\sin^2\theta+\Gamma_N}{\Gamma_N^2+2\Gamma_F\Gamma_N+\Gamma_F^2\sin^2\theta}. \tag{6.16}$$

This saturation value can be understood from the following argument. At large Δ_z the tunneling via upper and lower Zeeman levels gets decoupled. The tunnel width of the upper level is $\Gamma_F\cos^2\frac{\theta}{2}+\frac{1}{2}\Gamma_N$, while the tunnel width of the lower level is $\Gamma_F\sin^2\frac{\theta}{2}+\frac{1}{2}\Gamma_N$. The sum of the currents corresponding to these widths yields Eq. (6.16). The same saturation value can be obtained from purely classical consideration, by introducing the probabilities of all four variants of the occupation of the two Zeeman levels and solving the system of master equations for these probabilities.

It is quite nontrivial that in Eq. (6.15) the characteristic scale of magnetic field, $\Delta_z \sim (\Gamma_F\Gamma_N)^{1/2}$, is much smaller than the level width $\Gamma_F/2$. This suggests that, while the tunneling times for each of the Zeeman levels is Γ_F^{-1}, i.e., short, coupling of these levels via a ferromagnet modifies them in such a way that one of the resulting levels possesses a long lifetime. Similarly to Refs. [18], [21], the origin of this long lifetime can be traced to the complex poles of $G(\mathcal{E})$ in Eq. (6.12). These poles correspond to the condition: $\det\hat{S}^{-1}=0$, where the matrix $\hat{S}$ is defined by Eq. (6.7). The secular equation reads

$$\Big[\mathcal{E}-\frac{1}{2}\Delta_z+\frac{i}{2}\left(\Gamma_N+(1-\cos\theta)\Gamma_F\right)\Big]\times\Big[\mathcal{E}+\frac{1}{2}\Delta_z+\frac{i}{2}\left(\Gamma_N+(1+\cos\theta)\Gamma_F\right)\Big]=\Big(\frac{i}{2}\Gamma_F\sin\theta\Big)^2. \tag{6.17}$$

The roots of Eq. (6.17) are

$$\mathcal{E}_\pm=\frac{1}{2}\Big[i(\Gamma_N+\Gamma_F)\pm\sqrt{\Delta_z^2-\Gamma_F^2-2i\Delta_z\Gamma_F\cos\theta}\,\Big]. \tag{6.18}$$

For $\Gamma_N \ll \Gamma_F$ and $\Delta_z \ll \Gamma_F$ the imaginary parts of the roots are

$$\mathrm{Im}\ \mathcal{E}_1=\frac{1}{2}\Gamma_F, \qquad \mathrm{Im}\ \mathcal{E}_2=\frac{\Gamma_N}{2}+\frac{\Delta_z^2\sin^2\theta}{4\Gamma_F}. \tag{6.19}$$

We see that the time $(\mathrm{Im}\ \mathcal{E}_2)^{-1}$ is long, and defines the scale $\Delta_z \sim (\Gamma_F\Gamma_N)^{1/2}$ of magnetic field.

6.3 Correlated tunneling

With strong on-site repulsion, U, and the bias, V, exceeding the Kondo temperature, the mechanism of transport is sequential tunneling. The scenario of this sequential tunneling is most simple for $U \gg V$, when the double occupancy of the impurity is forbidden. Then the passage of current, say, from the ferromagnet (F) into normal electrode (N) via impurity

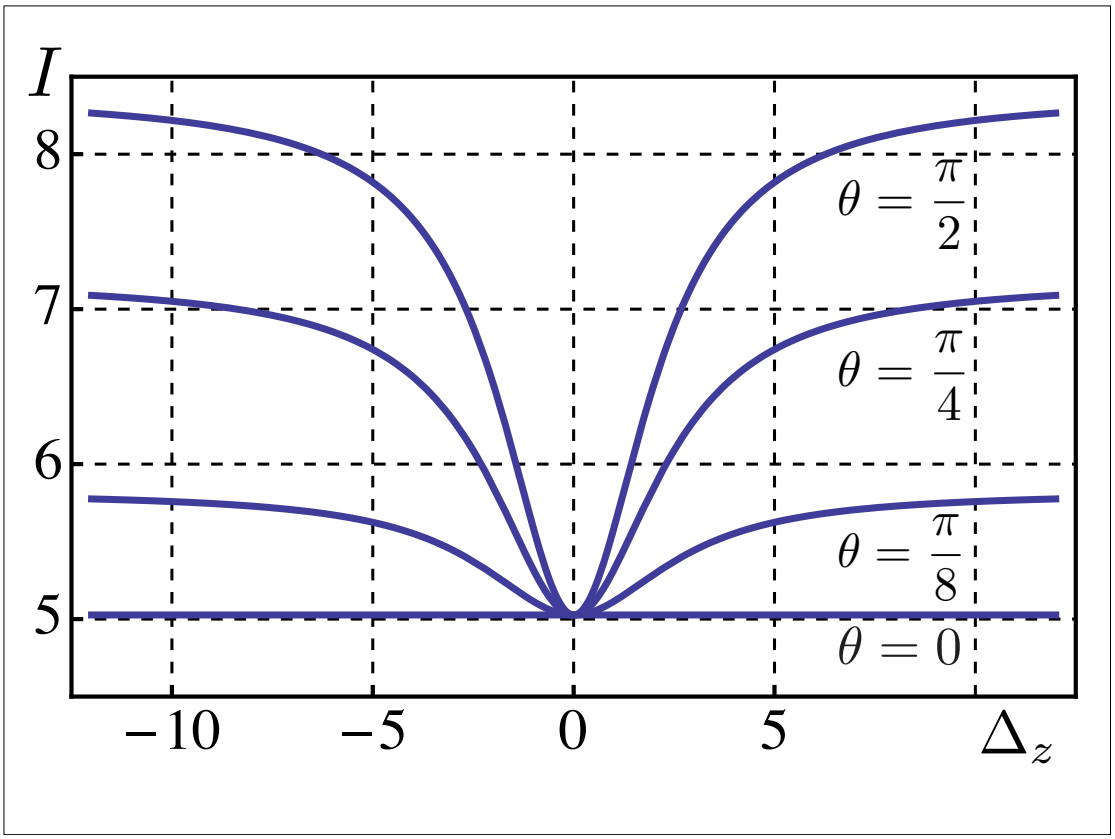

Figure 6.9: Resonant current (in the units $e\Gamma_N/\pi\hbar$) in the absence of correlations is plotted from Eq. (6.14) versus the dimensionless magnetic field, Δ_z/Γ_N, for different field orientations. In all curves $\Gamma_F = 2\Gamma_N$.

(j) proceeds in simple cycles. At the first step, the electron tunnels from F to j, and at the second step, from j to N. The current is inversely proportional to the average duration of the cycle, i.e.,

$$I^{F\to N} = \frac{e}{\tau^{F\to j} + \tau^{j\to N}}, \tag{6.20}$$

where $\tau^{F\to j}$ and $\tau^{j\to N}$ are the *average* waiting times for the corresponding tunneling processes. Similarly, the current from N to F is given by

$$I^{N\to F} = \frac{e}{\tau^{N\to j} + \tau^{j\to F}}. \tag{6.21}$$

For a normal electrode, the time $\tau^{j\to N}$ is related to $\tau^{N\to j}$ as [23]

$$\tau^{j\to N} = 2\tau^{N\to j}, \tag{6.22}$$

reflecting the fact that tunneling from the electrode onto an empty impurity is possible for both spin directions, while the electron on impurity can tunnel only into the states in the electrode having the same spin direction. If the electrode F was unpolarized, the currents Eqs. (6.20) and (6.21) would be given by[23]

$$I^{F\to N} = \frac{e}{2\tau^{j\to F} + \tau^{j\to N}}, \tag{6.23}$$

$$I^{N\to F} = \frac{e}{\tau^{j\to F} + 2\tau^{j\to N}}. \tag{6.24}$$

For a polarized electrode F the relation $\tau^{j\to F} = 2\tau^{F\to j}$ is not valid. In calculating $\tau^{j\to F}$ one should keep in mind that an electron can tunnel into F *from* both Zeeman levels described by spinors χ_+, χ_-, Eq. (6.3), so that

$$\tau^{j\to F} = \frac{\tau_+^{j\to F} + \tau_-^{j\to F}}{2}. \tag{6.25}$$

In the same way, in calculating $\tau^{F\to j}$, it should be taken into account that the electron from F can tunnel *into* both Zeeman levels. The net rate of tunneling is given by

$$(\tau^{F\to j})^{-1} = (\tau_+^{F\to j})^{-1} + (\tau_-^{F\to j})^{-1}. \tag{6.26}$$

Upon these modifications, the times $\tau^{j\to F}$ and $\tau^{F\to j}$ can be very different. Suppose that the polarization is full, $p = 1$, and that the magnetic field is directed along the direction of magnetization. Then for $\tau_+^{j\to F}$ we have $\tau_+^{j\to F} = (2\Gamma_F)^{-1}$, while $\tau_-^{j\to F} = \infty$, reflecting the fact [14] that the electron with spin $\downarrow$ cannot tunnel into F, where all spins are $\uparrow$. For a finite angle, θ, between magnetization and magnetic field this blockade is lifted.

In calculating the tunneling times, it is very important that the electron tunnels into F not from *pure* Zeeman levels, but from the levels coupled via F. This coupling is described

by the nondiagonal element of the matrix Eq. (6.11). Then the corresponding partial times are given by [18]

$$\tau_+^{j\to F} = \tau_+^{F\to j} = \frac{\hbar}{2\mathrm{Im}\ \mathcal{E}_+}, \tag{6.27}$$

$$\tau_-^{j\to F} = \tau_-^{F\to j} = \frac{\hbar}{2\mathrm{Im}\ \mathcal{E}_-}, \tag{6.28}$$

where $\mathcal{E}_+$ and $\mathcal{E}_-$ are given by Eq. (6.18) with $\Gamma_N = 0$.

It can be easily seen from Eq. (6.18) that the relation

$$\tau_+^{F\to j} + \tau_-^{F\to j} = \frac{\hbar}{2\Gamma_F} \tag{6.29}$$

holds. This, in turn, means that the current $I^{F\to N}$ is simply equal to $\frac{2e}{\hbar}\Gamma_F\Gamma_N/(2\Gamma_F+\Gamma_N)$, i.e., it does not exhibit any magnetic-field dependence [14]. On the other hand, with times given by Eq. (6.27), the current $I^{N\to F}$ acquires a nontrivial Δ_z-dependence. Taking into account that

$$\mathrm{Im}\mathcal{E}_\pm = \frac{\Gamma_F}{2} \pm \frac{1}{2}\Big[-\frac{1}{2}(\Delta_z^2-\Gamma_F^2) + \frac{1}{2}\sqrt{(\Delta_z^2-\Gamma_F^2)^2 + 4\Gamma_F^2\Delta_z^2\cos^2\theta}\ \Big]^{\frac{1}{2}}, \tag{6.30}$$

we get

$$I^{N\to F} = \Big(\frac{2e}{\hbar}\Big) \times \frac{\Gamma_N\big(\Delta_z^2+\Gamma_F^2 - \sqrt{(\Delta_z^2-\Gamma_F^2)^2 + 4\Gamma_F^2\Delta_z^2\cos^2\theta}\ \big)}{4\Gamma_N\Gamma_F + \Delta_z^2 + \Gamma_F^2 - \sqrt{(\Delta_z^2-\Gamma_F^2)^2 + 4\Gamma_F^2\Delta_z^2\cos^2\theta}}. \tag{6.31}$$

It is instructive to compare the result Eq. (6.31) with the corresponding expression from Ref. [14] for $p = 1$, which reads

$$I^{N\to F} = \Big(\frac{2e}{\hbar}\Big)\frac{\Gamma_F\Gamma_N\Delta_z^2\sin^2\theta}{\big[(2\Gamma_N+\Gamma_F)\Delta_z^2 + 2\Gamma_F^2\Gamma_N\big] - \Gamma_F\Delta_z^2\cos^2\theta}. \tag{6.32}$$

At small θ we can expand the square root in Eq. (6.31) as

$$\sqrt{(\Delta_z^2-\Gamma_F^2)^2 + 4\Gamma_F^2\Delta_z^2\cos^2\theta} \approx \Delta_z^2 + \Gamma_F^2 + \frac{2\Delta_z^2\Gamma_F^2\theta^2}{\Delta_z^2+\Gamma_F^2}. \tag{6.33}$$

It follows from Eq. (6.33) that the two results coincide at small θ. Otherwise, they are different; see Fig. 6.10. The difference is most pronounced for $\Gamma_F \ll \Gamma_N$, when the tunneling into F dominates the current. For example, for particular values $\Delta_z = \Gamma_F$ and $\theta = \pi/2$, the current Eq. (6.31) is two times bigger than $I^{N\to F}$ given by Eq. (6.32). The origin of the discrepancy is the form of the Hamiltonian, adopted in Ref. [14], where strong Coulomb

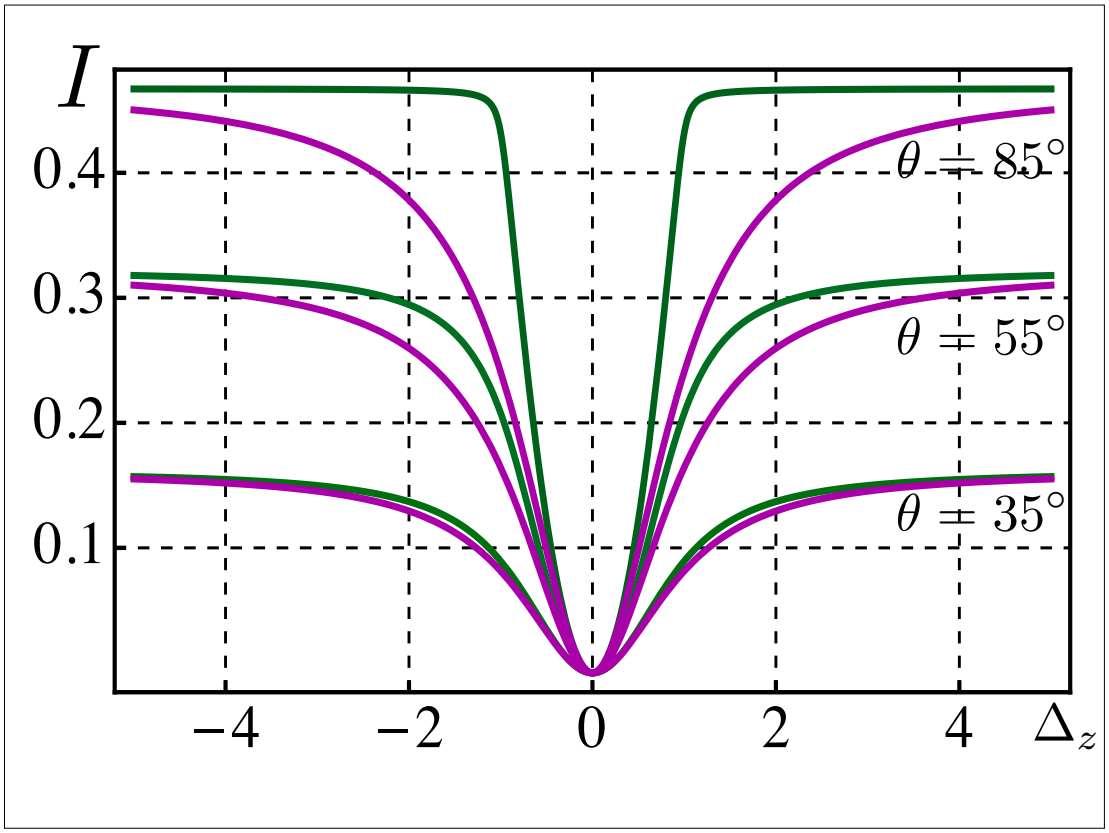

Figure 6.10: (color online). The current from normal into ferromagnetic electrode (in the units $2e\Gamma_F/\hbar$) in the correlated regime is plotted versus dimensionless magnetic field, Δ_z/Γ_F, for different orientations, θ and $\Gamma_N = 8\Gamma_F$. Green curves are plotted from Eq. (6.31), while the purple curves are plotted from Eq. (6.32), Ref. [14].

repulsion is ascribed to electrons in the states $\uparrow$ and $\downarrow$. This is permissible only for $\theta = 0$. For nonzero θ, the repulsion takes place between the electrons occupying the eigenstates χ_+ and χ_-, see Eq. (6.3). Thus, the occupation numbers of χ_+, χ_- states should enter into on-site repulsion Hamiltonian. In this way the repulsion was incorporated in Refs. [19], [20]. Comparison of Eqs. (6.31) and (6.32) is presented in Fig. 6.10.

At large Δ_z the current Eq. (6.31) saturates at the value

$$I_\infty^{N\to F} = \frac{2e}{\hbar}\frac{\Gamma_F\Gamma_N \sin^2\theta}{\Gamma_F \sin^2\theta + 2\Gamma_N}. \tag{6.34}$$

In this limit, the coupling between the Zeeman levels is negligible, so that the value $I_\infty^{N\to F}$ follows from Eq. (6.23), with $\tau^{N\to j} = 1/2\Gamma_N$ and $\tau^{j\to F} = 1/\Gamma_F \sin^2\theta$. Naturally, the large-$\Delta_z$ limit of Eq. (6.32), in which the coupling of the Zeeman levels is completely neglected, coincides with Eq. (6.34).

In closing of this Section we present the expression for the current which generalizes Eq. (6.31) to the case of a finite polarization of the ferromagnetic electrode

$$I^{N\to F} = \Big(\frac{2e}{\hbar}\Big)\frac{\Gamma_N\big(\Delta_z^2 + (2-p^2)\Gamma_F^2 - \sqrt{(\Delta_z^2 - p^2\Gamma_F^2)^2 + 4p^2\Gamma_F^2\Delta_z^2\cos^2\theta}\ \big)}{4\Gamma_N\Gamma_F + \Delta_z^2 + (2-p^2)\Gamma_F^2 - \sqrt{(\Delta_z^2 - p^2\Gamma_F^2)^2 + 4p^2\Gamma_F^2\Delta_z^2\cos^2\theta}}. \tag{6.35}$$

6.4 Concluding remarks

Our main physical message is that in resonant magneto-tunneling between the normal electrode and the ferromagnet, the effect of coupling of Zeeman levels via a ferromagnetic electrode affects the current both in correlated and noncorrelated regimes. At this point we would like to draw a link to the earlier studies, Refs. [21], [22], where the correlated resonant transport between the *normal* electrodes via a *two-level* system, e.g., two quantum dots in parallel [22], was addressed. The authors realized that the current is strongly affected by the coupling between the levels via continuum of the states in the electrodes, and that the rate-equations-based description is invalid due to this coupling. They demonstrated that this coupling gives rise to a strong dependence of current on the energy separation of the levels. In our situation, this separation is simply the Zeeman splitting, Δ_z. In Refs. [21,22], the ferromagnet was mimicked by the asymmetry of coupling of the components of the two-level system to the electrodes. In our situation, the source of asymmetry is the angle, θ, between the magnetic field and the magnetization. The effect analogous to "magnetoresistance" was captured in Refs. [21,22] by numerically solving the master equations. Our situation, when only one electrode is ferromagnetic, is simpler, which allowed us to get the analytical result Eq. (6.31) for the correlated current.

In the correlated regime, the magnetoresistance is present only for one current direction $N \to F$. Our result Eq. (6.14) suggests that outside the blockaded regime $V > U$, when the current is the same for both voltage polarities, the magnetoresistance is still finite and strong. Probably, by this prediction, equal mangetoresistances for both bias polarities for high enough bias, can be tested in 3T spin-transport experiments.

Except for the papers Refs. [19,20,25,27], the bulk of theoretical studies [24-32] of resonant transport between two ferromagnetic electrodes was focused on the low-temperature Kondo regime. As it was pointed in Ref. [25], outside the Kondo regime, in addition to blocking, there is another prominent many-body effect, which results from the polarization of the electrodes and might affect the transport. Namely, the on-site repulsion gives rise to a pseudomagnetic field

$$\Delta_0 = \frac{\Gamma_F}{\pi} \int_{-V/2}^{V/2} d\varepsilon \Big(\frac{1}{\varepsilon - U} - \frac{1}{\varepsilon} \Big) \tag{6.36}$$

directed along the magnetization. The structure of Eq. (6.36) suggests that the underlying mechanism is similar to cotunneling. Incorporating this field into Eq. (6.31) is performed by replacing $\Delta_z \cos\theta$ with $\Delta_z \cos\theta + \Delta_0$ and Δ_z^2 with $\Delta_z^2 + \Delta_0^2 + 2\Delta_z \Delta_0 \cos\theta$. The effect of the pseudomagnetic field on the shape of magnetoresistance curves is illustrated in Fig. 6.11. We see that for large enough $\Delta_0 \sim 10\Gamma_F$ the shapes can undergo a dramatic transformation becoming asymmetric and even non-monotonic. Still these shapes do not explain the experimental observation that the current grows with Δ_z at $\theta = \pi/2$ and drops with Δ_z at $\theta = 0$. To account for this observation it was assumed in Ref. [14] that, in addition to external field, a strong in-plane hyperfine field is present.

Throughout the paper we assumed that the impurity level position, $\mathcal{E}_0$, is zero. In fact, we required that $\mathcal{E}_0$ lies within the interval $(-\frac{V}{2}, \frac{V}{2})$; see Fig. 6.5. For $\mathcal{E}_0$ lower than $-\frac{V}{2}$ the resonant tunneling is forbidden. It will be allowed again [23] when $\mathcal{E}_0$ falls into the interval $(-\frac{V}{2} - U, \frac{V}{2} - U)$ (impurity of the "type B" in the language of Ref. [14]); see Fig. 6.4 for illustration. Then the intermediate state for the passage of current will be doubly occupied, and magnetoresistance will be present [14] for $I^{F\to N}$, but absent for $I^{N\to F}$. If $\mathcal{E}_0$ is lower than $-\frac{V}{2}$ but above $\frac{V}{2} - U$, the mechanism of passage of current is cotunneling, i.e., an elastic two-electron process in course of which one electron leaves the impurity to N and another arrives from F. The cotunneling rate, τ_c^{-1}, is given by $\tau_c^{-1} \sim \Gamma_F \Gamma_N / \mathcal{E}_0$, so that the magnitude of current is $I_c = e/\tau_c$. There is a question whether or not the cotunneling current, $I^{F\to N}$, exhibits the magnetic field dependence. In our opinion it does. Indeed, without the magnetic field and for fully polarized F electrode, the state of the impurity after a single cotunneling act is $\uparrow$. This forbids the next cotunneling act, so that $I_c = 0$. Finite

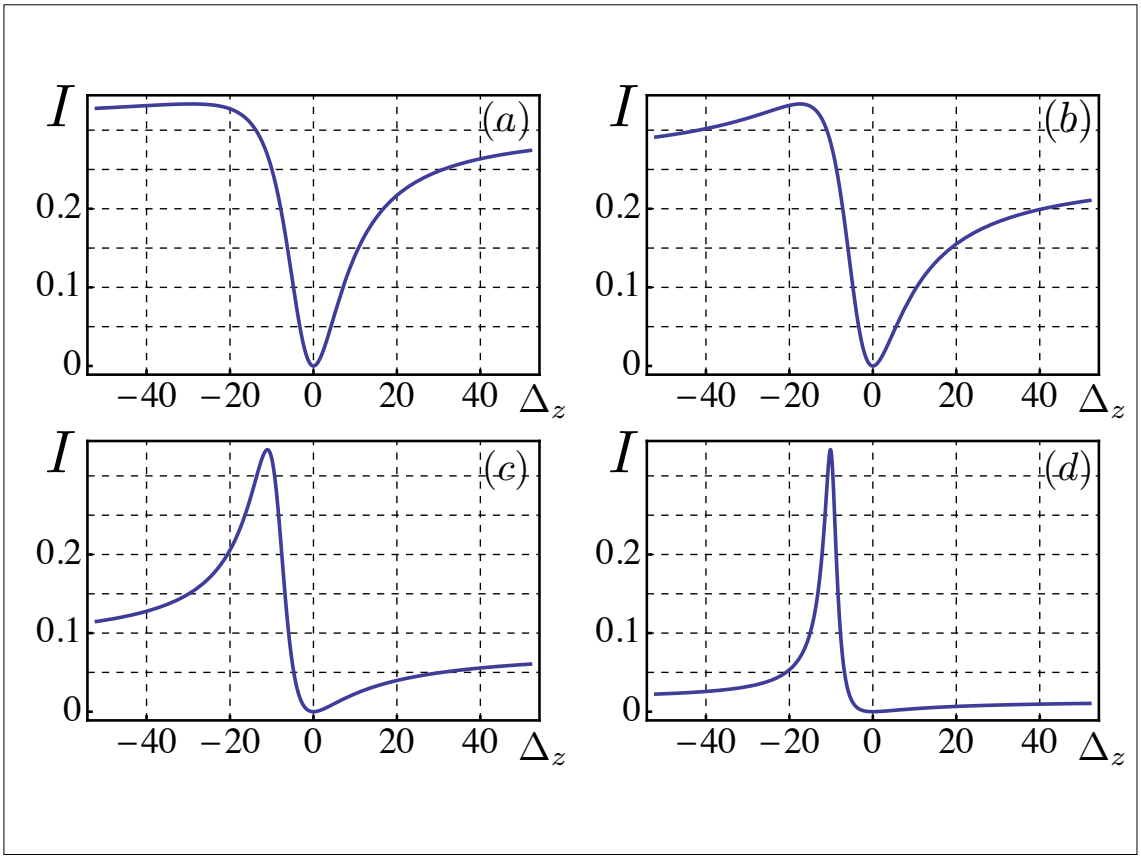

Figure 6.11: The effect of the pseudomagnetic field on magnetotunneling. The current (in the units $2e\Gamma_F/\hbar$) in the correlated regime is plotted versus dimensionless magnetic field, Δ_z/Γ_F, for orientations $\theta = 70^\circ$ (a), $\theta = 55^\circ$ (b), $\theta = 25^\circ$ (c), and $\theta = 10^\circ$ (d). The plots correspond to $\Gamma_N = \Gamma_F$ and pseudomagnetic field $\Delta_0 = 10\Gamma_F$.

magnetic field lifts this blockade in the same way as it does for a direct resonant current. We thus expect the mangetoresistance of the form $I^{F\to N}(\Delta_z) = e\Big[\Delta_z^2\tau_c \sin^2\theta/\left(1+\Delta_z^2\tau_c^2\right)\Big]$.

The presence of resonant magneto-tunneling can be confirmed via experimental investigations. The deliberate introduction of atomic-level defects into the tunneling layer can be used to modulate the magneto-tunneling through variations in the defect states present. These variations can be achieved by using defects with different on-site repulsion and investigating the impact the defect concentration has on the magnetoresistance.

6.5 References

[1] M. Johnson and R. H. Silsbee, Phys. Lett. **55**, 1790 (1985).

[2] F. J. Jedema, A. T. Filip, and B. J. van Wees, Nature (London) **410**, 345 (2001).

[3] S. P. Dash, S. Sharma, R. S. Patel, M. P. de Jong, and R. Jansen, Nature **426**, 491 (2009).

[4] M. Tran, H. Jaffrés, C. Deranlot, J.-M. George, A. Fert, A. Miard, and A. Lemaître, Phys. Rev. Lett. **102**, 036601 (2009).

[5] K.-R. Jeon, B.-C. Min, I.-J. Shin, C.-Y. Park, H.-S. Lee, Y.-H. Jo, and S.- C. Shin, Appl. Phys. Lett. **98**, 262102 (2011).

[6] H. Saito, S. Watanabea, Y. Minenoa, S. Sharmaa, R. Jansen, S. Yuasa, and K. Ando, Solid State Commun. **151**, 1159 (2011).

[7] N. W. Gray and A. Tiwari, Appl. Phys. Lett. **98**, 102112 (2011).

[8] R. Jansen, A. M. Deac, H. Saito, and S. Yuasa, Phys. Rev. B **85**, 134420 (2012).

[9] Y. Aoki, M. Kameno, Y. Ando, E. Shikoh, Y. Suzuki, T. Shinjo, M. Shiraishi, T. Sasaki, T. Oikawa, and T. Suzuki, Phys. Rev. B **86**, 081201(R) (2012).

[10] N. Reyren, M. Bibes, E. Lesne, J. M. George, C. Deranlot, S. Collin, A. Barthèlèmy, and H. Jaffrés, Phys. Rev. Lett. **108**, 186802 (2012).

[11] A. Jain, J. C. Rojas-Sanchez, M. Cubukcu, J. Peiro, J. C. LeBreton, E. Prestat, C. Vergnaud, L. Louahadj, C. Portemont, C. Ducruet, V. Baltz, A. Barski, P. Bayle-Guillemaud, L. Vila, J. P. Attanè, E. Augendre, G. Desfonds, S. Gambarelli, H. Jaffrés, J. M. George, and M. Jamet, Phys. Rev. Lett. **109**, 106603 (2012).

[12] K. Kasahara, Y. Baba, K. Yamane, Y. Ando, S. Yamada, Y. Hoshi, K. Sawano, M. Miyao, and K. Hamaya, J. Appl. Phys. **111**, 07C503 (2012).

[13] Y. Pu, J. Beardsley, P. M. Odenthal, A. G. Swartz, R. K. Kawakami, P. C. Hammel, E. Johnston-Halperin, J. Sinova, and J. P. Pelz, Appl. Phys. Lett. **103**, 012402 (2013).

[14] Y. Song and H. Dery, Phys. Rev. Lett. **113**, 047205 (2014).

[15] A. G. Swartz, S. Harashima, Y. Xie, D. Lu, B. Kim, C. Bell, Y. Hikita, and H. Y. Hwang, Appl. Phys. Lett. **105**, 032406 (2014).

[16] O. Txoperena, Y. Song, L. Qing, M. Gobbi, L. E. Hueso, H. Dery, and F. Casanova, Phys. Rev. Lett. **113**, 146601 (2014).

[17] H. N. Tinkey, P. Li, and I. Appelbaum, Appl. Phys. Lett. **104**, 232410 (2014).

[18] T. V. Shahbazyan and M. E. Raikh, Phys. Rev. B **49**, 17123 (1994).

[19] J. N. Pedersen, J. Q. Thomassen, and K. Flensberg, Phys. Rev. B **72**, 045341 (2005).

[20] J. N. Pedersen, D. Bohr, A. Wacker, T. Novotný, P. Schmitteckert, and K. Flensberg, Phys. Rev. B **79**, 125403 (2009).

[21] M. G. Schultz and F. von Oppen, Phys. Rev. B **80**, 033302 (2009).

[22] G. Schaller, G. Kießlich, and T. Brandes, Phys. Rev. B **80**, 245107 (2009).

[23] L. I. Glazman and K. A. Matveev, Pisma Zh. Eksp. Teor. Fiz. **48**, 403 (1988) [L. I. Glazman and K. A. Matveev, JETP Lett. **48**, 445 (1988)].

[24] J. König and J. Martinek, Phys. Rev. Lett. **90**, 166602 (2003);

[25] J. Martinek, Y. Utsumi, H. Imamura, J. Barnaś, S. Maekawa, J. König, and G. Schø"n, Phys. Rev. Lett. **91**, 127203 (2003).

[26] M. Braun, J. König, and J. Martinek, Phys. Rev. B **70**, 195345 (2004).

[27] S. Braig and P. W. Brouwer, Phys. Rev. B **71**, 195324 (2005).

[28] J. Martinek, M. Sindel, L. Borda, J. Barnaś, J. König, G. Schön, and J. von Delft, Phys. Rev. Lett. **91**, 247202 (2003).

[29] M.-S. Choi, D. Sánchez, and R. López, **92**, 056601 (2004).

[30] P. Simon, P. S. Cornaglia, D. Feinberg, and C. A. Balseiro, Phys. Rev. B **75**, 045310 (2007).

[31] S. Lindebaum and J. König, Phys. Rev. B **84**, 235409 (2011).

[32] S. Hoffman and Y. Tserkovnyak, arXiv:1412.4663.

CHAPTER 7

SPIN TRANSPORT IN N-TYPE SINGLE-LAYER TRANSITION METAL DICHALCOGENIDES

7.1 Introduction

Transition-metal dichalcogenides (TMDs) in a two-dimensional domain are single-layer semiconductors with lattice similar to graphene. Unlike graphene, they possess a bandgap, which makes them attractive for optoelectronic applications, such as field-effect transistor [1, 2], see, e.g., Ref. [3] for review. Unlike graphene, the electron states in K and K' valleys are not equivalent. This inequivalence is owed to the spin-orbit coupling. The K and K' wave functions corresponding to the same momenta and energies differ by the spin direction. Spin-orbit splitting of the conduction band is much smaller than that of the valence band [4-10]. As a result of the band splitting, there are two excitons in a given valley. Correspondingly, in undoped samples, the spectra of the exciton absorption, reflection, and luminescence exhibit a two-peak structure, as was demonstrated experimentally by many groups [11-20]. The bandstructure of monolayer TMDs is illustrated schematically in Fig. 7.1 left panel. Characteristic parameters for MoS_2, a representative of TMDs, are the following: the bandgap is ≈ 1.5eV, while the splitting of the valence band is ≈ 150meV. This splitting manifests itself in the reflection spectrum shown in Fig. 7.2 together with a photoluminescence spectrum. Two minima in the reflection and two peaks in luminescence correspond to two excitons, A and B, related to upper and lower valence bands, respectively. Differences in their spectral positions reflect the valence band splitting. Circularly polarized light creates one exciton, say A, in the valley K, and the exciton B in the valley K'. Upon reversal of polarization, exciton B is created in the valley K, and the exciton A in the valley K'. As long as the valleys K and K' are symmetric, optical properties of TMDs are polarization-insensitive.

Upon photoexcitation of n-type samples, generated holes rapidly recombine with resident electrons, while generated electrons preserve spin memory for rather long times ~ 1ns. This

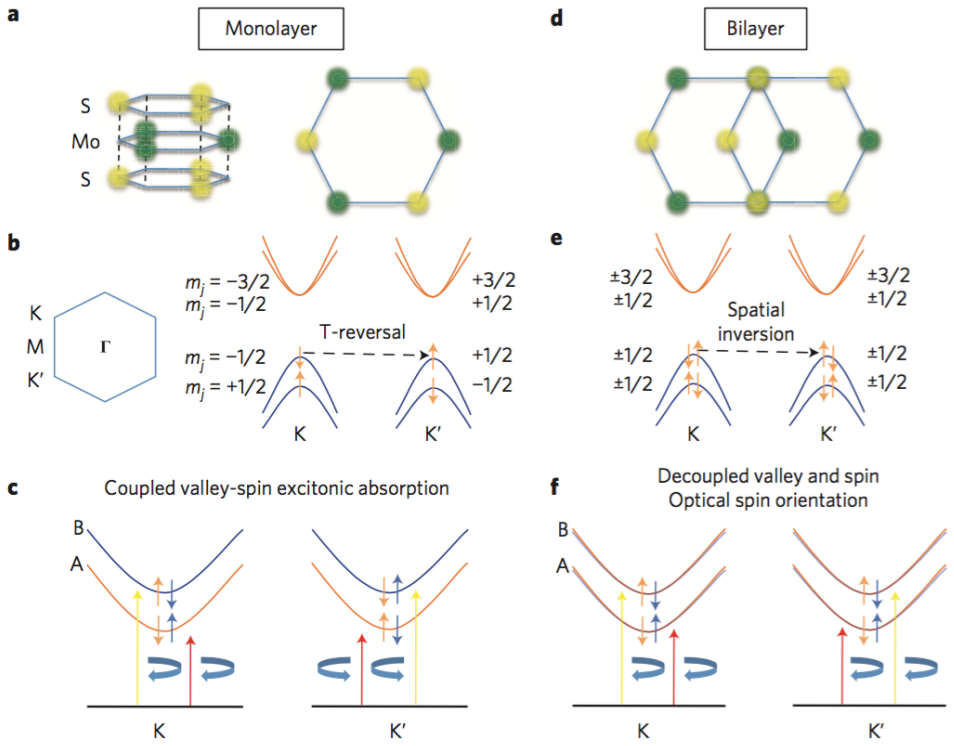

Figure 7.1: Atomic structure and electronic structure at the K and K' valleys of monolayer (a-c) and bilayer (d-f) MoS_2. a, The honeycomb lattice structure of monolayer MoS_2 with two sublattice sites occupied by one molybdenum and two sulphur atoms. Spatial inversion symmetry is explicitly broken. b, The lowest-energy conduction bands and the highest-energy valence bands labelled by the z-component of their total angular momentum. The spin degeneracy at the valence-band edges is lifted by the spin-orbit interactions. The valley and spin degrees of freedom are coupled. c, Optical selection rules for the A and B exciton states at two valleys for circularly polarized light. d, Bilayer MoS_2 with Bernal stacking. e, Spin degeneracy of the valence bands is restored by spatial inversion and time-reversal symmetries. Valley and spin are decoupled. f, Optical absorption in bilayer MoS_2. Under circularly polarized excitation (shown for σ_-) both valleys are equally populated and only a net spin orientation is produced (adapted from Ref. [16]).

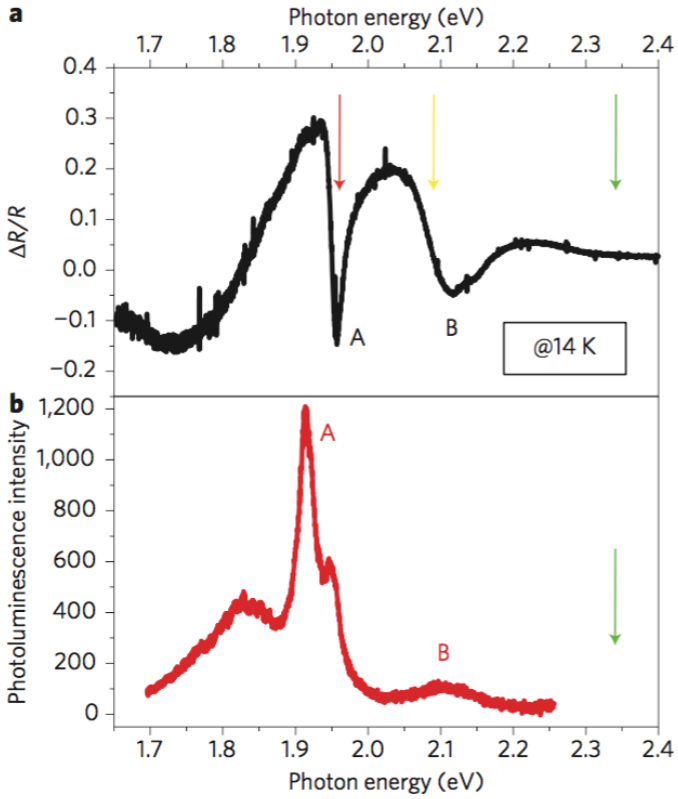

Figure 7.2: Optical absorption and photoluminescence spectra of monolayer MoS_2. a, Differential reflectance spectrum showing the narrow A exciton and the broader B exciton features. Red, yellow and green arrows represent the three different photon energies used to excite the samples in the photoluminescence measurements. b, Photoluminescence spectrum (not polarization resolved) for 2.33 eV (532 nm) excitation. The spectrum consists of B exciton hot luminescence and A exciton luminescence (including the neutral exciton emission and the charged exciton emission, redshifted by 40 meV). The lower energy feature is attributed to trapped excitons (adapted from Ref. [16]).

was established in Refs. [21, 22] on the basis of the analysis of the Hanle-Kerr data is magnetic field parallel to the layer. The fact that the optical response is sensitive to a magnetic field of $\sim$ 50mT which is much smaller than the effective spin-orbit (SO) field seems rather unusual. The explanation for that suggested in Ref. [21] is based on the fact that an electron, created by light, undergoes fast intervalley scattering, which effectively averages out the SO field. This scattering is facilitated by disorder, unlike the intervalley scattering of excitons [23, 24] which is facilitated by the exchange interaction. The latter mechanism is similar to the nonradiative Förster energy transfer. Optical response to a magnetic field perpendicular to the layer emerges only when the field is very strong [25] $\sim$ 50T.

Gate voltages [26] can control the type and the concentration of carriers in TMDs. However, the transport measurements reported to date are scarce compared to the optical studies. The highest mobility reported to date [27] in n-type MoS_2 is $\sim 10^3 cm^2/Vs$. For most samples the mobility is lower [28] $\sim 10^2 cm^2/Vs$. The fact that it depends on temperature [27, 28] suggests that the electron states are not far from the metal-insulator transition. Hopping transport has also been reported in disordered MoS_2 samples [29].

Spin transport has never been studied in TMDs [24]. On the other hand, relatively low mobility does not prevent such studies, see e.g., Ref. [31]. Note that the spin transport and the Kerr rotation signals are both limited by the spin-memory loss of carriers. In this regard, the most interesting question is how the spin dynamics of electrons reflected in the spin transport in n-type TMDs is related to the spin dynamics of excitons inferred from the Hanle-Kerr measurements [21, 22]. This issue is studied theoretically in the present paper. One cannot expect an observable spin transport in p-type TMDs. The separation of $\sim$ 150meV between the tops of $\uparrow$ and $\downarrow$ bands in each valley suggests that "intrinsic" spin precession is too fast. Intervalley scattering is also strictly forbidden unless phonons are involved [32, 33].

There are apparent differences between the spin-transport studies and polarization-of-luminescence techniques. Firstly, the optical experiments reveal the dynamics of the z-component of spin, $S_z(t)$, while conventional spin transport measures $S_x(t)$, $S_y(t)$, as illustrated in the Fig. 7.3. Secondly, the magnitude of the SO field in the metallic regime depends strongly on the electron density and is much smaller than for the excitons. It is also nontrivial that the electron inter-valley scattering rate, γ_v, depends on the concentration of the short-range impurities (defects[34]) allowing the large momentum transfer between the valleys. Finally, the Förster-like mechanism, which is at work for excitons, does not apply

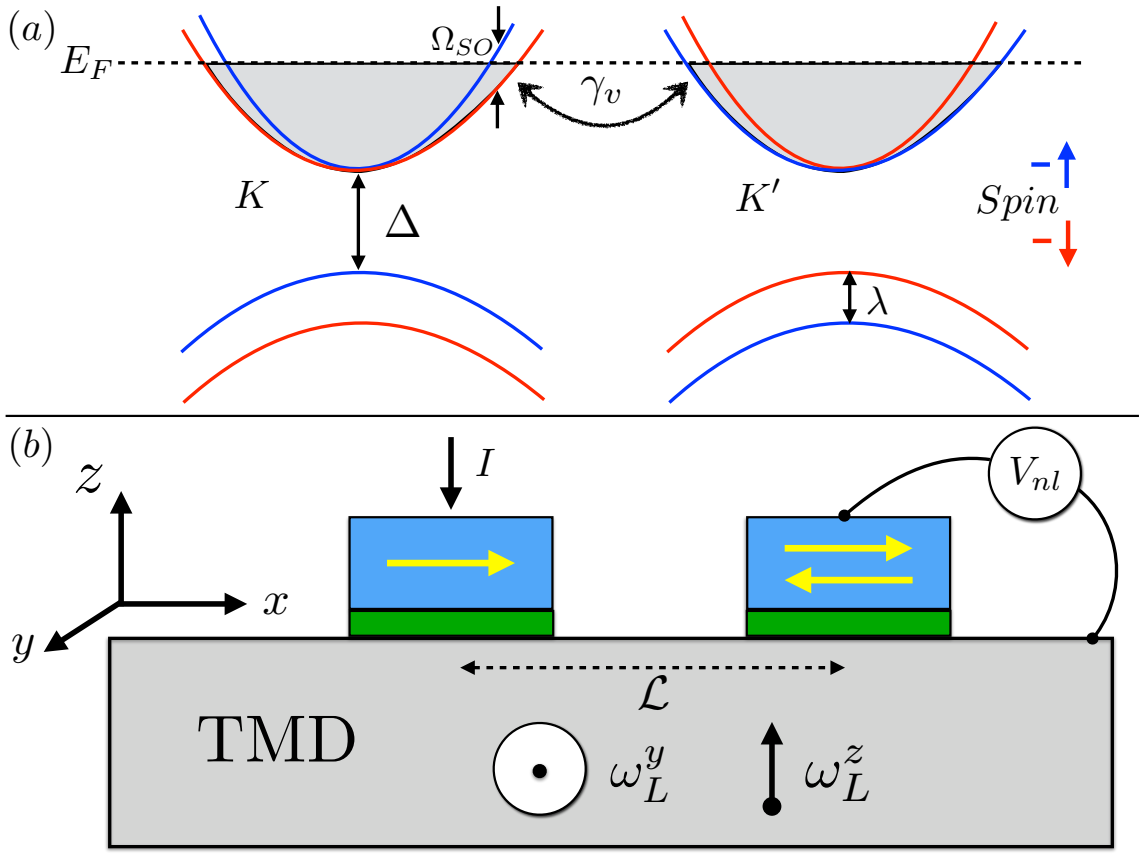

Figure 7.3: (color online). Band structure and experimental setup. (a) The energy spectrum of TMD at K and K' valleys is shown schematically. In n-type material the states with energies below E_F are occupied. The splitting between the $\uparrow$ and $\downarrow$ branches at the Fermi level is $\Omega_{SO} = \left(\frac{\lambda}{\Delta}\right)E_F$ and is much smaller than E_F. Short-range impurities are responsible for intervalley scattering with a rate γ_v. (b) Schematic illustration of the spin-transport experiment in TMD. The measure of the nonlocal resistance is a voltage between the channel and the right ferromagnet detector generated upon injecting the current through the left ferromagnetic electrode. Injector and detector shown in blue are separated from the channel by a tunnel barrier shown in green. While the injected polarized electrons travel either in the valley K or in the valley K', their spin precesses in the effective field $\boldsymbol{\omega}_L + \hat{z}\Omega_{SO}$ or $\boldsymbol{\omega}_L - \hat{z}\Omega_{SO}$. As a result of intervalley scattering, the spin dynamics is described by a system of the coupled equations Eq. (7.7). We study the limit of a small, compared to the diffusion length, distance $\mathcal{L}$ between injector and detector. The specifics of TMDs is that for external field, $\boldsymbol{\omega}_L$, oriented along z and y the shapes of the Hanle curves $V_{nl}(\omega_L)$ are completely different.

for two Fermi seas at K and K' valleys. As for the relation between the spin transport and the Kerr rotation techniques, the latter also studies $S_z(t)$. Besides, the Kerr rotation signal is pronounced for probe frequencies near the A-exciton resonance [21, 22] not at the Fermi level.

We will demonstrate that the shapes of the transport Hanle curves in TMDs depend dramatically on the ratio of γ_v to the SO splitting of the electron spectrum, Ω_{SO}, and that these shapes are different from the conventional transport Hanle curves. In this regard, we emphasize that the shapes of the Hanle curves reported for a wide variety of materials are very robust [7]. Specifics of the Hanle curves in TMDs is due to the valley asymmetry.

We show that, unlike conventional materials, the shape of the transport Hanle curve in TMDs depends on the orientation of the external field. If the spin polarization of electrons injected from a ferromagnet is along the x-axis, see Fig. 7.3, the dynamics of the injected spin is different for the external field parallel to the layer (along y) or normal to the layer (along z). For normal orientation and $\gamma_v \ll \Omega_{SO}$ this dynamics is different for different valleys. As a result, of this the Hanle curve has a two-peak structure. A distinct Hanle shape also persists for the normal orientation when $\gamma_v \gg \Omega_{SO}$. It represents the difference of two conventional Hanle profiles with very different widths: the wider reflecting the valley-symmetric mode of the overdamped spin dynamics, and the narrower reflecting the valley-antisymmetric mode.

When the external field is parallel to the layer, the Hanle curve has a singularity at a zero field. This singularity is due to the valley-asymmetric mode describing the slow time decay of the spin density. The decay is slow as a result of fast alternation of valleys; external field is responsible for coupling of the initial spin distribution to this mode. Characteristic width of the Hanle curve for the parallel orientation of external field is much smaller than for normal orientation. This is in accord with results from experimental findings [21, 22, 25] for magnetic-field response of photoexcited carriers, and is not surprising, since the spin dynamics for electrons and excitons are qualitatively similar.

7.2 Density dependence of the SO splitting of the electron spectrum

The $\boldsymbol{k}\cdot\boldsymbol{p}$ Hamiltonian of a TMD, established in Ref. [36], see also Refs. [4-10], contains three energies, namely, the gap, Δ; the hopping integral, t; and the SO-induced spin splitting of the valence band top, 2λ. With two valleys coupled to two spin projections, it represents a 4×4 matrix. In the presence of an external field having y and z components, this matrix has the form

$$H=\begin{pmatrix} \frac{\Delta}{2}+\omega_L^z & at\tau k e^{-i\theta\tau} & -i\omega_L^y & 0 \\ at\tau k e^{i\theta\tau} & -\frac{\Delta}{2}+\omega_L^z+\lambda\tau & 0 & -i\omega_L^y \\ i\omega_L^y & 0 & \frac{\Delta}{2}-\omega_L^z & at\tau k e^{-i\theta\tau} \\ 0 & i\omega_L^y & at\tau k e^{i\theta\tau} & -\frac{\Delta}{2}-\omega_L^z-\lambda\tau \end{pmatrix}, \tag{7.1}$$

where a is the lattice constant, ω_L^y and ω_L^z are the corresponding Zeeman energies, k and θ are the magnitude and the orientation of the wave vector. The valley index τ takes the values ± 1.

The spectrum, $\varepsilon(k)$, originating from the Hamiltonian Eq. (6.1) is the solution of the fourth-order equation

$$\Big[\big(\varepsilon+\frac{\Delta}{2}+\omega_L^z+\lambda\tau\big)\big(\varepsilon-\frac{\Delta}{2}+\omega_L^z\big)-(atk)^2\Big]\Big[\big(\varepsilon+\frac{\Delta}{2}-\omega_L^z-\lambda\tau\big)\big(\varepsilon-\frac{\Delta}{2}-\omega_L^z\big)-(atk)^2\Big]$$
$$=\Big[2\varepsilon^2+2\big(\frac{\Delta}{2}\big)^2+2(atk)^2-(\omega_L^z)^2-(\omega_L^z+\lambda\tau)^2\Big](\omega_L^y)^2. \tag{7.2}$$

In the absence of magnetic field the right-hand side is zero, and each bracket in the left-hand side determines the corresponding branch of the spectrum. With magnetic field, we can find the spectrum of the conduction band perturbatively in the small parameter ω_L^y/Δ. The result reads

$$\varepsilon(k)=\frac{\Delta}{2}+\frac{\hbar k^2}{2m_c}\pm\sqrt{\Big[\omega_L^z+\Big(\frac{\lambda\tau}{\Delta}\Big)\frac{\hbar k^2}{2m_c}\Big]^2+(\omega_L^y)^2}. \tag{7.3}$$

Here $m_c=\Delta\hbar/2a^2t^2$ is the effective mass of the conduction-band electron. Relative splitting of $\uparrow$ and $\downarrow$ branches is always small by virtue of the parameter λ/Δ, which is ≈ 0.1 for MoS_2. The above result has a simple interpretation. Namely, Ω_{SO} acts as an effective field directed along z which assumes opposite values for two the valleys.

In n-type TMDs the electron states with $k<k_F$, where k_F is the Fermi momentum, are occupied. The parameter crucial for spin transport is the ratio, γ_v/Ω_{SO}, of the intervalley scattering rate and the band splitting,[37] $\Omega_{SO}=\big(\frac{\lambda}{\Delta}\big)E_F$, at the Fermi level $E_F=\hbar k_F^2/2m_c$. We can perform a numerical estimate of this ratio assuming that the mobility is limited by the same short-range impurities that are responsible for intervalley scattering. The fact that point-like defects are the leading source of scattering in TMDs is commonly accepted, see, e.g., Ref. [34]. With mobility given by $\mu=\frac{e}{m_c\gamma_v}$ and $k_F^2=4\pi n$, where n is the electron density, we find

$$\Gamma=\frac{\gamma_v}{\Omega_{SO}}=\left(\frac{\Delta}{\lambda}\right)\frac{e}{2\pi\hbar\mu n}. \tag{7.4}$$

For a numerical estimate we choose a typical value, $n=10^{13}cm^{-2}$. Then for the highest reported mobility [27] for electrons in MoS_2, $\mu=10^3cm^2/Vs$, the ratio Eq. (7.4) is equal to 0.2, while for typical mobility [28] $\mu=10^2cm^2/Vs$ it is 10 times bigger. Thus, we conclude that both regimes $\Gamma\ll 1$ and $\Gamma\gg 1$ are viable for spin transport.

7.3 Nonlocal resistance

Once the spectrum Eq. (7.3) in the magnetic field is known and the intervalley scattering rate is introduced, the procedure of calculation of nonlocal resistance is straightforward [38]. First the splitting of the spectrum is incorporated into the equation of the dynamics for the spin density $\boldsymbol{S}(t)$, which is solved with an initial condition $\boldsymbol{S}(0) = \hat{x}$. Then the solution for $S_x(t)$ is multiplied by the diffusion propagator

$$P_{\mathcal{L}}(t) = \frac{1}{(4\pi Dt)^{1/2}} \exp\left(-\frac{\mathcal{L}^2}{4Dt}\right), \tag{7.5}$$

where $\mathcal{L}$ is the distance between the injector and detector and D is the diffusion coefficient related to mobility via the Einstein relation. Finally, the nonlocal resistance is obtained by integration over time

$$R(\omega_L) = \mathcal{R}_0 \int_0^\infty dt S_x(t) P_{\mathcal{L}}(t), \tag{7.6}$$

where $\mathcal{R}_0$ is the prefactor. The specifics of TMDs is that $S_x(t)$ is the sum $S_x(t) = S_x^K(t) + S_x^{K'}(t)$ of contributions of the two inequivalent valleys, so that the spin dynamics is governed by the system of the coupled equations [21, 39]

$$\begin{aligned}
\frac{d\boldsymbol{S}^K}{dt} &= \omega_L^y \hat{y} \times \boldsymbol{S}^K + (\Omega_{SO} + \omega_L^z)\hat{z} \times \boldsymbol{S}^K - \gamma_v \left(\boldsymbol{S}^K - \boldsymbol{S}^{K'}\right), \\
\frac{d\boldsymbol{S}^{K'}}{dt} &= \omega_L^y \hat{y} \times \boldsymbol{S}^{K'} - (\Omega_{SO} - \omega_L^z)\hat{z} \times \boldsymbol{S}^{K'} + \gamma_v \left(\boldsymbol{S}^K - \boldsymbol{S}^{K'}\right).
\end{aligned} \tag{7.7}$$

We will consider the cases of the normal, $\omega_L \parallel z$, and tangential, $\omega_L \parallel y$, orientations of the external field separately.

7.4 Normal orientation of the external field

For normal orientation, the z-component of the spin drops out from the system Eq. (7.7). To analyze this system, it is convenient, following Ref. [21], to introduce, in addition to the net spin projections $S_x(t)$ and $S_y(t)$, the valley imbalances

$$S_x^- = S_x^K - S_x^{K'}, \quad S_y^- = S_y^K - S_y^{K'}. \tag{7.8}$$

Upon the Laplace transform, the system of four equations for S_x, S_y, S_x^-, and S_y^- assumes the form

$$\begin{aligned}
p\tilde{S}_x - 1 &= -\Omega_{SO}\tilde{S}_y^- - \omega_L^z \tilde{S}_y \\
p\tilde{S}_y &= \Omega_{SO}\tilde{S}_x^- + \omega_L^z \tilde{S}_x \\
p_1\tilde{S}_x^- &= -\Omega_{SO}\tilde{S}_y - \omega_L^z \tilde{S}_y^-
\end{aligned}$$

$$p_1\tilde{S}_y^- = \Omega_{SO}\tilde{S}_x + \omega_L^z\tilde{S}_x^-, \tag{7.9}$$

where $\tilde{S}(p)$ stands for the Laplace-transformed $S(t)$, and p_1 is defined as

$$p_1 = p + 2\gamma_v. \tag{7.10}$$

The solution of the system for $\tilde{S}_x$ reads

$$\tilde{S}_x = \frac{pp_1^2 + p(\omega_L^z)^2 + p_1\Omega_{SO}^2}{(pp_1)^2 + 2pp_1\Omega_{SO}^2 + (p^2+p_1^2)(\omega_L^z)^2 + [\Omega_{SO}^2 - (\omega_L^z)^2]^2}. \tag{7.11}$$

Four frequencies of the modes describing the spin dynamics are determined by the zeros of the denominator. They are given by

$$p = \Omega_{SO}\Big[-\Gamma \pm i\Big(\frac{\omega_L^z}{\Omega_{SO}} \pm \sqrt{1-\Gamma^2}\Big)\Big], \tag{7.12}$$

where the parameter Γ is the dimensionless intervalley scattering rate defined by Eq. (7.4).

It is seen from Eq. (7.12) that the spin dynamics depends dramatically on the value of Γ. For $\Gamma \ll 1$ there are two different oscillation frequencies, $\Omega_{SO} \pm \omega_L^z$, which decay with the same rate, γ_v. On the contrary, for $\Gamma \gg 1$ both frequencies are equal to ω_L^z, but the decay rates are very different. For the valley-symmetric mode it is equal to $2\gamma_v$, while the valley-antisymmetric mode decays *very slowly* with the Dyakonov-Perel [40] rate $\approx \Omega_{SO}^2/2\gamma_v$. The time evolution of $S_x(t)$ has different forms for $\Gamma < 1$ and $\Gamma > 1$. Namely, for $\Gamma < 1$ this evolution is given by

$$\begin{aligned} S_x(t) =& \frac{1}{2}\Bigg\{\frac{\Gamma}{\sqrt{1-\Gamma^2}}\Bigg[\sin\Bigg(\Big(\frac{\omega_L^z}{\Omega_{SO}} + \sqrt{1-\Gamma^2}\Big)\Omega_{SO}t\Bigg) - \sin\Bigg(\Big(\frac{\omega_L^z}{\Omega_{SO}} - \sqrt{1-\Gamma^2}\Big)\Omega_{SO}t\Bigg)\Bigg] \\ &+ \Bigg[\cos\Bigg(\Big(\frac{\omega_L^z}{\Omega_{SO}} + \sqrt{1-\Gamma^2}\Big)\Omega_{SO}t\Bigg) + \cos\Bigg(\Big(\frac{\omega_L^z}{\Omega_{SO}} - \sqrt{1-\Gamma^2}\Big)\Omega_{SO}t\Bigg)\Bigg]\Bigg\}\exp\Big[-\Gamma\Omega_{SO}t\Big], \end{aligned} \tag{7.13}$$

while for $\Gamma > 1$ we have

$$\begin{aligned} S_x(t) =& \frac{1}{2}\Bigg\{\Big(1 + \frac{\Gamma}{\sqrt{\Gamma^2-1}}\Big)\exp\Big[-\Big(\Gamma - \sqrt{\Gamma^2-1}\Big)\Omega_{SO}t\Big] \\ &+ \Big(1 - \frac{\Gamma}{\sqrt{\Gamma^2-1}}\Big)\exp\Big[-\Big(\Gamma + \sqrt{\Gamma^2-1}\Big)\Omega_{SO}t\Big]\Bigg\}\cos\omega_L^z t. \end{aligned} \tag{7.14}$$

7.5 External field along $\hat{y}$

For a parallel magnetic field, there are, in general, six modes of the spin dynamics. Although the spin dynamics in this geometry was considered in Ref. [21], only the time evolution of S_z was studied, while we are interested in $S_x(t)$, $S_y(t)$. It turns out that the

frequencies for $S_x(t)$ are the same as for $S_z(t)$, while for $S_y(t)$ they are completely different. This is certainly the specifics of TMDs.

The field along $\hat{y}$ couples $S_x(t)$ and $S_z(t)$ via the conventional Larmor precession. In addition, the valley-asymmetric field $\pm\hat{z}\Omega_{SO}$ couples $S_x(t)$ to the spin *imbalance*, S_y^-. As a result, the system 6×6 decouples into two systems 3×3. The Laplace-transformed system involving $\tilde{S}_x$ reads

$$\begin{aligned} p\tilde{S}_x - 1 &= -\Omega_{SO}\tilde{S}_y^- + \omega_L^y \tilde{S}_z \\ p\tilde{S}_z &= -\omega_L^y \tilde{S}_x \\ p_1\tilde{S}_y^- &= \Omega_{SO}\tilde{S}_x, \end{aligned} \tag{7.15}$$

By contrast to the normal orientation, the solution

$$\tilde{S}_x = \frac{pp_1}{p^2p_1 + p_1(\omega_L^y)^2 + p\Omega_{SO}^2} \tag{7.16}$$

contains a third-order polynomial in the denominator. With regard to sensitivity of the spin dynamics to the external field, the most interesting case is $\Gamma \gg 1$, when the intervalley scattering is fast. In this limit, the expressions for the two poles have a simple form,

$$p = \Omega_{SO}\left[-\frac{1}{4\Gamma} \pm \sqrt{\left(\frac{1}{4\Gamma}\right)^2 - \left(\frac{\omega_L^y}{\Omega_{SO}}\right)^2}\right], \tag{7.17}$$

and reproduce the corresponding frequencies obtained in Ref. [21]. Expression Eq. (7.17) defines a small characteristic magnetic field, $\omega_L^y \sim \Omega_{SO}/\Gamma$, which is the inverse Dyakonov-Perel relaxation time. In the same limit, $\Gamma \gg 1$, the third frequency is given by

$$p = \Omega_{SO}\left[-2\Gamma + \frac{2\Gamma}{4\Gamma^2 + \left(\frac{\omega_L^y}{\Omega_{SO}}\right)^2}\right]. \tag{7.18}$$

It corresponds to the decay with the rate $2\gamma_v$ and is insensitive to weak magnetic fields.

As magnetic field increases, the argument of the square root in Eq. (7.17) changes sign. This is reflected in the spin dynamics, which is different for ω_L^y bigger and smaller than $\Omega_{SO}/4\Gamma$. At low fields we have

$$\begin{aligned} S_x(t) =& \frac{1}{2}\left[\left(1 + \frac{1}{\sqrt{1-\left(\frac{4\omega_L^y\Gamma}{\Omega_{SO}}\right)^2}}\right)\exp\left[-\left(\frac{1}{4\Gamma} + \sqrt{\left(\frac{1}{4\Gamma}\right)^2 - \left(\frac{\omega_L^y}{\Omega_{SO}}\right)^2}\right)\Omega_{SO}t\right]\right. \\ &\left. + \left(1 - \frac{1}{\sqrt{1-\left(\frac{4\omega_L^y\Gamma}{\Omega_{SO}}\right)^2}}\right)\exp\left[-\left(\frac{1}{4\Gamma} - \sqrt{\left(\frac{1}{4\Gamma}\right)^2 - \left(\frac{\omega_L^y}{\Omega_{SO}}\right)^2}\right)\Omega_{SO}t\right], \end{aligned} \tag{7.19}$$

i.e., the dynamics is overdamped. It becomes oscillatory for $\omega_L^y > \Omega_{SO}/4\Gamma$. In this domain we find

$$S_x(t) = \exp\Big[-\frac{\Omega_{SO}}{4\Gamma}t\Big]\Bigg[\cos\left(\sqrt{\Big(\frac{\omega_L^y}{\Omega_{SO}}\Big)^2-\Big(\frac{1}{4\Gamma}\Big)^2}\,\Omega_{SO}t\right) - \frac{1}{\sqrt{\big(\frac{4\omega_L^y\Gamma}{\Omega_{SO}}\big)^2-1}}\sin\left(\sqrt{\Big(\frac{\omega_L^y}{\Omega_{SO}}\Big)^2-\Big(\frac{1}{4\Gamma}\Big)^2}\,\Omega_{SO}t\right)\Bigg]. \tag{7.20}$$

Compared to Ref. [21], where $S_z(t)$ was calculated, the amplitudes of the harmonics in Eq. (7.20) are different.

7.6 Shapes of the Hanle curves

To find the Hanle profiles for normal orientation of magnetic field one should substitute Eqs. (7.13) and (7.14) into Eq. (7.6) and perform the integration over time. The structure of $S_x(t)$, sinusoidal function times exponential decay, suggests that the integration can be carried out analytically [41, 42] for arbitrary $\mathcal{L}$. However, in samples with low mobility, the regime of small distance, $\mathcal{L}$, between injector and detector is most relevant. This is because the diffusion time, $\mathcal{L}^2/D$, should not exceed the spin relaxation time much. Upon setting $\mathcal{L} = 0$ in $P_{\mathcal{L}}(t)$ Eq. (7.5), the integration is easily performed with the help of the relations

$$\int_0^\infty \frac{dt\ e^{-vt}}{\sqrt{t}}\sin(ut) = \mathrm{sign}(u)\sqrt{\frac{\pi}{2v}}\mathrm{F}\Big(\frac{u}{v}\Big),$$
$$\int_0^\infty \frac{dt\ e^{-vt}}{\sqrt{t}}\cos(ut) = \sqrt{\frac{\pi}{2v}}\mathrm{G}\Big(\frac{u}{v}\Big), \tag{7.21}$$

where the functions $\mathrm{F}(z)$ and $\mathrm{G}(z)$ are defined as

$$\mathrm{F}\big(z\big) = \frac{\sqrt{\sqrt{1+z^2}-1}}{\sqrt{1+z^2}}, \qquad \mathrm{G}\big(z\big) = \frac{\sqrt{\sqrt{1+z^2}+1}}{\sqrt{1+z^2}}. \tag{7.22}$$

The expressions for nonlocal resistance in the $\perp$ geometry can be now expressed via the functions F and G. For $\Gamma < 1$ we have

$$R(\omega_L^z) = \frac{\mathcal{R}_0}{4\sqrt{2D\Omega_{SO}\Gamma}}\Bigg\{\mathrm{G}\Big(\frac{\omega_L^z}{\Omega_{SO}\Gamma}+\sqrt{\frac{1}{\Gamma^2}-1}\Big)+\mathrm{G}\Big(\frac{\omega_L^z}{\Omega_{SO}\Gamma}-\sqrt{\frac{1}{\Gamma^2}-1}\Big) + \frac{\Gamma}{\sqrt{1-\Gamma^2}}\Bigg[\mathrm{sign}\Big[\big(\frac{\omega_L^z}{\Omega_{SO}}+\sqrt{1-\Gamma^2}\big)\Omega_{SO}\Big]\mathrm{F}\Big(\frac{\omega_L^z}{\Omega_{SO}\Gamma}+\sqrt{\frac{1}{\Gamma^2}-1}\Big) - \mathrm{sign}\Big[\big(\frac{\omega_L^z}{\Omega_{SO}}-\sqrt{1-\Gamma^2}\big)\Omega_{SO}\Big]\mathrm{F}\Big(\frac{\omega_L^z}{\Omega_{SO}\Gamma}-\sqrt{\frac{1}{\Gamma^2}-1}\Big)\Bigg]\Bigg\}. \tag{7.23}$$

The corresponding expression for $\Gamma > 1$ reads

$$R(\omega_L^z) = \frac{\mathcal{R}_0}{4\sqrt{2D\Omega_{SO}(\Gamma^2-1)}}\left[\frac{1}{\left(\Gamma-\sqrt{\Gamma^2-1}\right)^{3/2}}\mathrm{G}\left(\frac{\omega_L^z}{\Omega_{SO}}\left(\Gamma+\sqrt{\Gamma^2-1}\right)\right)\right.$$
$$\left. - \frac{1}{\left(\Gamma+\sqrt{\Gamma^2-1}\right)^{3/2}}\mathrm{G}\left(\frac{\omega_L^z}{\Omega_{SO}}\left(\Gamma-\sqrt{\Gamma^2-1}\right)\right)\right]. \tag{7.24}$$

Evolution of the shape of the Hanle curves with Γ described by Eqs. (7.23), (7.23) is the following. For slow intervalley scattering $R(\omega_L^z)$ exhibits a two-peak structure with maxima at $\omega_L^z \approx \pm\Omega_{SO}$. Each peak corresponds to the "compensation" of the SO-splitting in a given valley by the external field. The widths of the peaks are $\sim \gamma_v$. For $\Gamma \approx 0.7$ the peaks merge, and, upon further increase of Γ, transform into the *difference* of the two peaks with small, $\sim \Omega_{SO}/\Gamma$, and big, $\sim \Omega_{SO}\Gamma$, widths centered at $\Omega_L^z = 0$. The broad peak, however, has a much smaller magnitude. So the shape for $\Gamma \gg 1$ is, essentially, the conventional Hanle shape with width determined by the inverse Dyakonov-Perel relaxation time. The evolution of $R(\omega_L^z)$ with Γ is illustrated in Fig. 7.4.

Turning to the geometry with external field along $\hat{y}$, we first observe that $S_x(t)$ given by Eqs. (7.19), (7.20) contains only one scale of ω_L^y, namely, $\omega_L^y = \Omega_{SO}/\Gamma$. Since we assumed fast intervalley scattering, this characteristic field is much smaller than the splitting Ω_{SO}. Naturally, the Hanle curve is a function of a single parameter $\omega_L^y\Gamma/\Omega_{SO}$. The form of this function can be found using the identities Eq. (7.21). While the integrands in Eq. (7.6) are different for $\omega_L^y < \Omega_{SO}/4\Gamma$ and $\omega_L^y > \Omega_{SO}/4\Gamma$, the resulting shape is given by a single concise expression

$$R(\omega_L^y) = \frac{\mathcal{R}_0}{\sqrt{2D\Omega_{SO}}}\frac{\Gamma}{\sqrt{1+\left|\frac{4\omega_L^z\Gamma}{\Omega_{SO}}\right|}}. \tag{7.25}$$

The Hanle curve in the form of Eq. (7.25) falls off with magnetic field as $1/\sqrt{\omega_L^y}$, i.e., in the same way as a regular Hanle curve. However, it exhibits a unique feature at small field, where the slope has an abrupt cusp; see Fig. 7.5. The origin of the cusp can be traced to the second term in Eq. (7.19). Rather than spin precession, this term describes the slow decay, as $\exp(-|\omega_L^y|t)$, of the spin density. This slow decay reveals the specifics of the two-valley spin dynamics Eq. (7.15), for which the valley-asymmetric mode decays anomalously slow.

7.7 Concluding remarks

In optics experiments the valleys were "addressed" separately, in the sense that, for a given frequency, different polarizations of light generated excitons in different valleys.

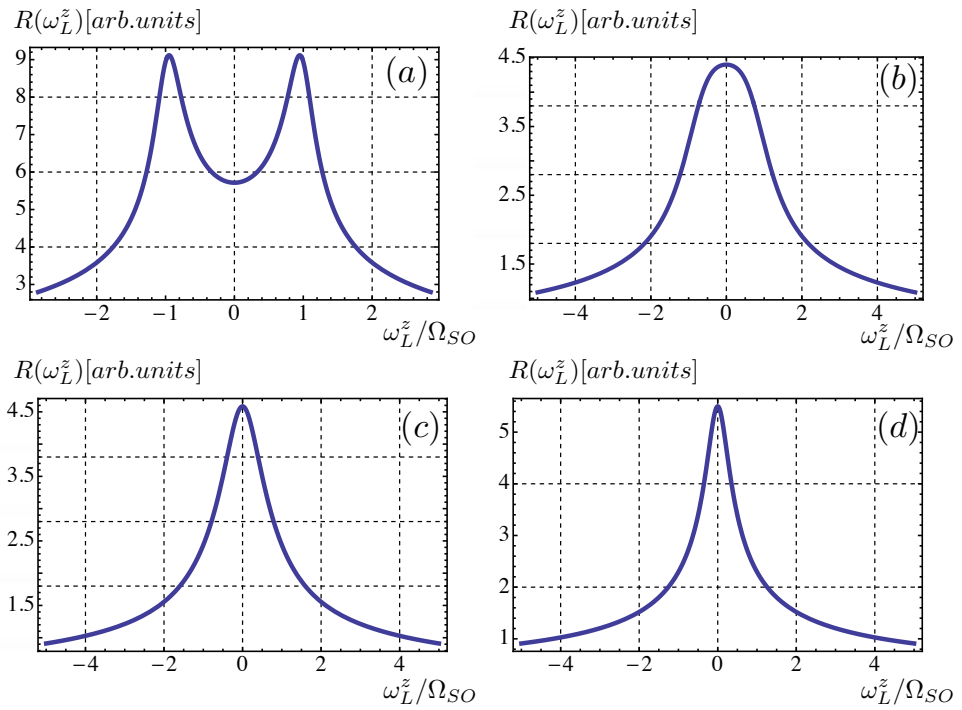

Figure 7.4: (color online). Nonlocal resistance calculated from Eqs. (7.23), (7.24) is plotted versus the dimensionless magnetic field normal to the plane for different intervalley scattering rates (in the units of Ω_{SO}): $\Gamma = 0.2$ (a), $\Gamma = 0.7$ (b), $\Gamma = 1.2$ (c), and $\Gamma = 1.8$ (d). Two-peak structure of the Hanle curves centered at $\omega_L^z = \pm\Omega_{SO}$ evolves with increasing Γ to a conventional Hanle shape.

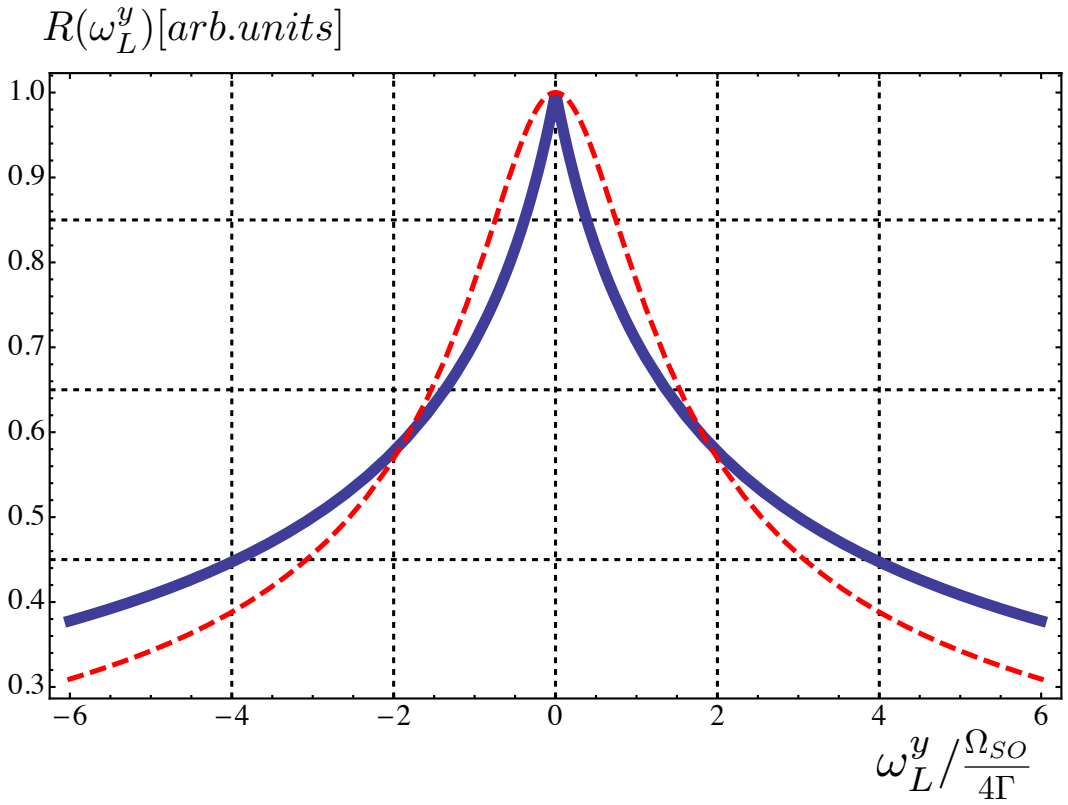

Figure 7.5: (color online). Universal shape of the Hanle curve, $R(4\omega_L^y\Gamma/\Omega_{SO})$, for the parallel orientation of the magnetic field is plotted from Eq. (7.25). A cusp at zero field reflects the slow-decaying valley-asymmetric mode of the spin dynamics. For comparison, the conventional Hanle curve Eq. (7.22) is plotted with dashed line.

Conventional spin transport is valley-insensitive. On the other hand, the spin-pumping setup [43] can serve as an analog of optical selective valley excitation. Assume that the ferromagnetic resonance is excited in the ferromagnet that injects spin into a TMD layer. The pumped spin current would flow in one of the valleys depending on the polarization of the microwave field exciting the resonance. The analogy between the selective valley excitation in optics and by the spin pumping is straightforward. While in optical experiments an absorbed photon generates an electron in the conduction band and a hole in the valence band, in spin pumping it is a magnon that creates an electron-hole pair in the Fermi sea of the conduction band.

For fast intervalley scattering, the slow-decaying modes of the spin dynamics are present for both orientations of the external field. These modes are valley-asymmetric and originate from almost complete compensation of the SO field, Ω_{SO}, in the valley K and $-\Omega_{SO}$ in the valley K'. However, the decay rates of these modes are drastically different in a weak external field. This is because, for $\perp$ orientation, the result of compensation is simply the external field $\hat{z}\omega_L^z$, while, for $\parallel$ orientation, the result of compensation of $\hat{y}\omega_L^y + \hat{z}\Omega_{SO}$ and $\hat{y}\omega_L^y - \hat{z}\Omega_{SO}$ is only quadratic in the external field. Then the prime effect of the external field on the spin-dynamics is the field-dependent decay.

Measuring the Hanle curves in both $\parallel$ and $\perp$ orientations allows, in principle, to determine the values of both relevant parameters, Ω_{SO} and γ_v.

Our main results Eqs. (7.23), Eq. (7.24), and Eq. (7.25) were derived in the limit of small distance $\mathcal{L}$ between injector and detector. Now we can quantify the corresponding condition. Characteristic magnetic field in Eq. (7.25) is $\omega_L^y \sim \Omega_{SO}/\Gamma$. Thus, the diffusion time, $\mathcal{L}^2/D$ should be smaller than the precession time, i.e., $\mathcal{L} \ll \Big(D\Gamma/\Omega_{SO}\Big)^{1/2}$. In the opposite limit the Hanle curve exhibits sensitivity to even weaker fields. The corresponding expression for nonlocal resistance in this limit can be cast in the form

$$\frac{R(\omega_L^y) - R(0)}{R(0)} = -\frac{2|\omega_L^y|\Gamma}{\Omega_{SO}} \exp\Big[-2|\omega_L^y|\Big(\frac{\mathcal{L}^2\Gamma}{D\Omega_{SO}}\Big)^{\frac{1}{2}}\Big]. \tag{7.26}$$

This result suggests that the Hanle curve has a minimum at zero field and two maxima at $\omega_L^y = \pm\Big(D\Omega_{SO}/4\mathcal{L}^2\Gamma\Big)^{1/2}$ much smaller than Ω_{SO}/Γ.

In the experimental paper Ref. [25] the sensitivity of the optical response to the normal magnetic field was not registered until ω_L^z was as high as 65T. We, on the other hand, predict the sensitivity of the spin transport to much weaker fields. The reason is that z-projection of spin, $S_z(t)$, registered in optical experiments, drops out from the equations

Eq. (7.9) for the spin dynamics in $\perp$ orientation, whereas the dynamics, $S_x(t)$, relevant for spin transport, persists.

Hanle shapes with minima at zero external field, like Fig. 7.4 for $\perp$ orientation and Eq. (7.26) for $\parallel$ orientation are unique and constitute our main verifiable prediction. More experimental studies of nonlocal Hanle measurements with non-optical spin injection techniques (preferably electrical spin injection) are needed to fully understand the peculiar spin transport characteristics of TMD films.

7.8 References

[1] B. Radisavljevic, A. Radenovic, J. Brivio, V. Giacometti, and A. Kis, Nature Nanotechnology **6**, 147 (2011).

[2] S. Kim, A. Konar, W.-S. Hwang, J. H. Lee, J. Lee, J. Yang, C. Jung, H. Kim, J.-B. Yoo, J.-Y. Choi, Y. W. Jin, S. Y. Lee, D. Jena, W. Choi, and K. Kim, Nature Communications **3**, 1011 (2012).

[3] Y. P. V. Subbaiah, K. J. Saji, and A. Tiwari, Adv. Funct. Mater. (2016); DOI: 10.1002/adfm.201504202.

[4] D. Mastrogiuseppe, N. Sandler, and S. E. Ulloa, Phys. Rev. B **90**, 161403 (2014).

[5] K. Kechedzhi and D. S. L. Abergel, Phys. Rev. B **89**, 235420 (2014).

[6] H. Wang, C. Zhang, W. Chan, C. Manolatou, S. Tiwari, and F. Rana, Phys. Rev. B **93**, 045407 (2016).

[7] A. Kormányos, G. Burkard, M. Gmitra, J. Fabian, V. Zólyomi, N. D. Drummond, and V. Fal'ko, 2D Mater. **2**, 022001 (2015).

[8] A. Kormányos, P. Rakyta, and G. Burkard, New J. Phys. **17**, 103006 (2015).

[9] H. Hatami, T. Kernreiter, and U. Zülicke, Phys. Rev. B **90**, 045412 (2014).

[10] A. Kormányos, V. Zólyomi, N. D. Drummond, P. Rakyta, G. Burkard, and V. I. Fal'ko, Phys. Rev. B **88**, 045416 (2013).

[11] Y. Li, J. Ludwig, T. Low, A. Chernikov, X. Cui, G. Arefe, Y. D. Kim, A. M. van der Zande, A. Rigosi, H. M. Hill, S. H. Kim, and J. Hone, Phys. Rev. Lett. **113**, 266804 (2014).

[12] A. M. Jones, H. Yu, N. J. Ghimire, S. Wu, G. Aivazian, J. S. Ross, B. Zhao, J. Yan, D. G. Mandrus, D. Xiao, W. Yao, and X. Xu, Nature Nanotechnology **8**, 634 (2013).

[13] A. M. Jones, H. Yu, J. S. Ross, P. Klement, N. J. Ghimire, J. Yan, D. G. Mandrus, W. Yao, and X. Xu, Nat. Phys. **10**, 130 (2014).

[14] G. Aivazian, Z. Gong, A. M. Jones, R. Chu, J. Yan, D. G. Mandrus, C. Zhang, D. Cobden, W. Yao, and X. Xu, Nat. Phys. **11**, 148 (2015).

[15] K. F. Mak, C. Lee, J. Hone, J. Shan, and T. F. Heinz, Phys. Rev. Lett. **105**, 136805 (2010).

[16] K. F. Mak, K. He, J. Shan, and T. F. Heinz, Nature Nanotechnology **7**, 494 (2012).

[17] E. J. Sie, A. J. Frenzel, Y.-H. Lee, J. Kong, and N. Gedik, Phys. Rev. B **92**, 125417 (2015).

[18] S. D. Conte, F. Bottegoni, E. A. A. Pogna, D. D. Fazio, S. Ambrogio, I. Bargigia, C. D'Andrea, A. Lombardo, M. Bruna, F. Ciccacci, A. C. Ferrari, G. Cerullo, and M. Finazzi, Phys. Rev. B **92**, 235425 (2015).

[19] C. R. Zhu, K. Zhang, M. Glazov, B. Urbaszek, T. Amand, Z. W. Ji, B. L. Liu, and X. Marie, Phys. Rev. B **90**, 161302(R) (2014).

[20] G. Wang, M. M. Glazov, C. Robert, T. Amand, X. Marie, and B. Urbaszek, Phys. Rev. Lett. **115**, 117401 (2015).

[21] L. Yang, N. A. Sinitsyn, W. Chen, J. Yuan, J. Zhang, J. Lou, and S. A. Crooker, Nat. Phys. **11**, 830 (2015).

[22] L. Yang, W. Chen, K. M. McCreary, B. T. Jonker, J. Lou, and S. A. Crooker, Nano. Lett. **10**, 1271 (2010).

[23] M. M. Glazov, T. Amand, X. Marie, D. Lagarde, L. Bouet, and B. Urbaszek, Phys. Rev. B **89**, 201302 (2014).

[24] T. Yu and M. W. Wu, Phys. Rev. B **89**, 205303 (2014).

[25] A. V. Stier, K. M. McCreary, B. T. Jonker, J. Kono, and S. A. Crooker, arXiv:1510.07022.

[26] J. Wang, D. Rhodes, S. Feng, M. An T. Nguyen, K. Watanabe, T. Taniguchi, T. E. Mallouk, M. Terrones, L. Balicas, and J. Zhu, Appl. Phys. Lett. **106**, 152104 (2015).

[27] B. W. H. Baugher, H. O. H. Churchill, Y. Yang, and P. Jarillo-Herrero, Nano. Lett. **13**, 4212 (2013).

[28] K. Kang, S. Xie, L. Huang, Y. Han, P. Y. Huang, K. F. Mak, C. Kim, D. Muller, and J. Park, Nature **520**, 656 (2015).

[29] S.-T. Lo, O. Klochan, C.-H. Liu, W.-H. Wang, A. R. Hamilton, and C.-T. Liang, Nanotechnology **25**, 375201 (2014).

[30] A weak spin-valve effect in multilayer MoS_2 was reported in a recent preprint S. H. Liang, Y. Lu, B. S. Tao, S. Mc-Murtry, G. Wang, X. Marie, P. Renucci, H. Jaffres, F. Montaigne, D. Lacour, J.-M. George, S. Petit-Watelot, M. Hehn, A. Djeffal, and S. Mangin, arXiv:1512.05022.

[31] M. C. Prestgard, G. Siegel, R. Roundy, M. Raikh, and A. Tiwari, J. Appl. Phys. **117**, 083905 (2015).

[32] T. Cheiwchanchamnangij, W. R. L. Lambrecht, Y. Song, and H. Dery, Phys. Rev. B **88**, 155404 (2013).

[33] Y. Song and H. Dery, Phys. Rev. B **111**, 026601 (2013).

[34] J. Hong, Z. Hu, M. Probert, K. Li, D. Lv, X. Yang, L. Gu, N. Mao, Q. Feng, L. Xie, J. Zhang, D. Wu, Z. Zhang, C. Jin, W. Ji, X. Zhang, J. Yuan, and Z. Zhang, Nature Communications **6**, 6293 (2015).

[35] R. C. Roundy, M. C. Prestgard, A. Tiwari, and M. E. Raikh, Phys. Rev. B **90**, 205203 (2014).

[36] D. Xiao, G.-B. Liu, W. Feng, X. Xu, and W. Yao, Phys. Rev. Lett. **108**, 196802 (2012).

[37] We assume that the Fermi level is high, so that this splitting is much bigger the intrinsic splitting.[7]

[38] F. J. Jedema, A. T. Filip, and B. J. van Wees, Nature (London) **410**, 345 (2001).

[39] We neglected the intraband spin relaxation introduced phenomenologically in Ref. [21] since it does not lead to the qualitatively new effects.

[40] M. I. Dyakonov and V. I. Perel, Sov. Phys. Solid State **13**, 3023 (1971).

[41] M. Johnson and R. H. Silsbee, Phys. Rev. Lett. **55**, 1790 (1985).

[42] M. Johnson and R. H. Silsbee, Phys. Rev. B **37**, 5312 (1988).

[43] Y. Tserkovnyak, A. Brataas, G. E. W. Bauer, and B. I. Halperin, Rev. Mod. Phys. **77**, 1375 (2005).

[44] Y. P. V. Subbaiah, K. J. Saji, and A. Tiwari, Adv. Funct. Mater. **26**, 2046 (2016).

PART III

QUANTUM ANOMALOUS HALL EFFECT

CHAPTER 8

EFFECT OF EXTENDED CONFINEMENT ON THE STRUCTURE OF EDGE CHANNELS IN THE QUANTUM ANOMALOUS HALL EFFECT

8.1 Introduction

Quantum anomalous Hall effect is achieved by doping the films possessing nontrivial band structure with magnetic impurities [1-15]. This doping gives rise to a spontaneous magnetization caused by exchange between the impurities. The most exciting consequence of this magnetization is that the associated spin splitting results in the band inversion. Magnetization-induced band inversion was predicted theoretically in Refs. [16], [17]; see Fig. 8.1. First experiments [1-3] indicated that there is a jump in nondiagonal component, σ_{xy}, of the conductivity at ferromagnetic transition, confirming the theoretical prediction. Very recently [11, 12], upon improving the quality of the samples, a very accurate quantization of σ_{xy} was demonstrated.

In experiments [1-15], the ferromagnetism is switched on and off by application of a weak external field. The observed quantized steps in nondiagonal resistance look similar to the steps observed in conventional quantum Hall effect only in much weaker external fields. One of the conclusions which can be drawn from these experimental studies is that the structure of the edge states plays a crucial role in achieving an almost zero longitudinal resistance, ρ_{xx}.

On the theoretical side, it was demonstrated numerically in Ref. [18] that the dispersion law of the edge states in realistic multilayer QAH structure contains nonchiral edge modes along with a chiral one. It was also demonstrated in Ref. [18] that coexistence of chiral and nonchiral edge modes leads to a finite longitudinal resistance. In order to suppress the contribution of nonchiral channels to ρ_{xx}, in experiment Ref. [11] it was proposed to localize them by disorder, see Fig. 8.2 and Fig. 8.3, which shows the precise quantization at low

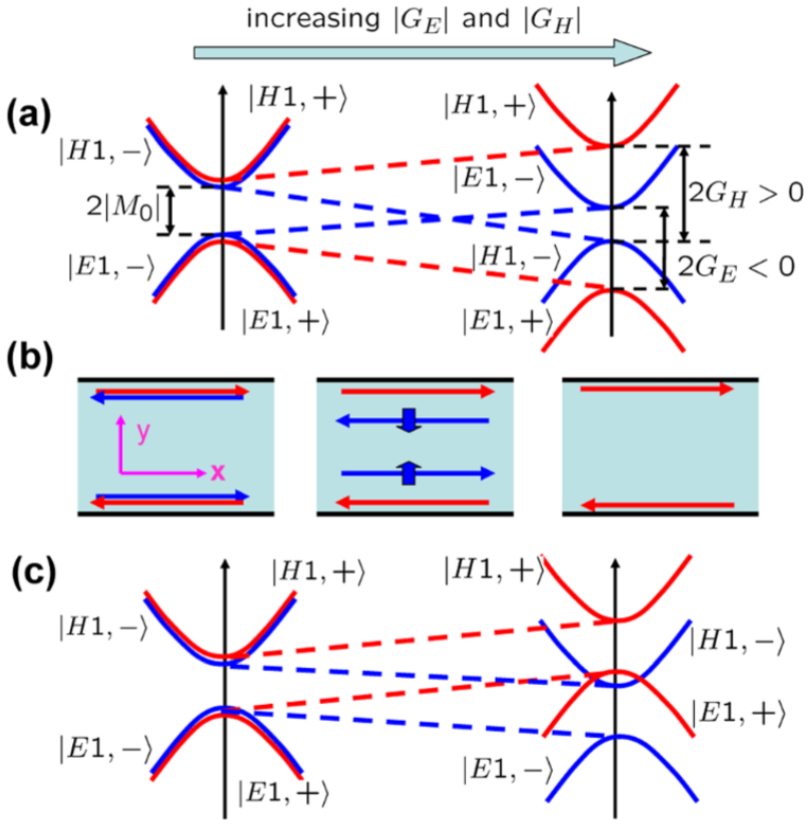

Figure 8.1: (color online). Evolution of band structure and edge states upon increasing the spin splitting. For (a) $G_E < 0$ and $G_H > 0$, the spin-down states $|E1,-\rangle$ and $|H1,-\rangle$ in the same block of the Hamiltonian (7.1) touch each other and then enter the normal regime. But for (c) $G_E > 0$ and $G_H > 0$, gap closing occurs between $|E1,+\rangle$ and $H1,-\rangle$ bands, which belong to different blocks of the Hamiltonian, and thus will cross each other without opening a gap. In (b) we show the behavior of the edge states during the level crossing in the case of (a)(adapted from Ref. [17]).

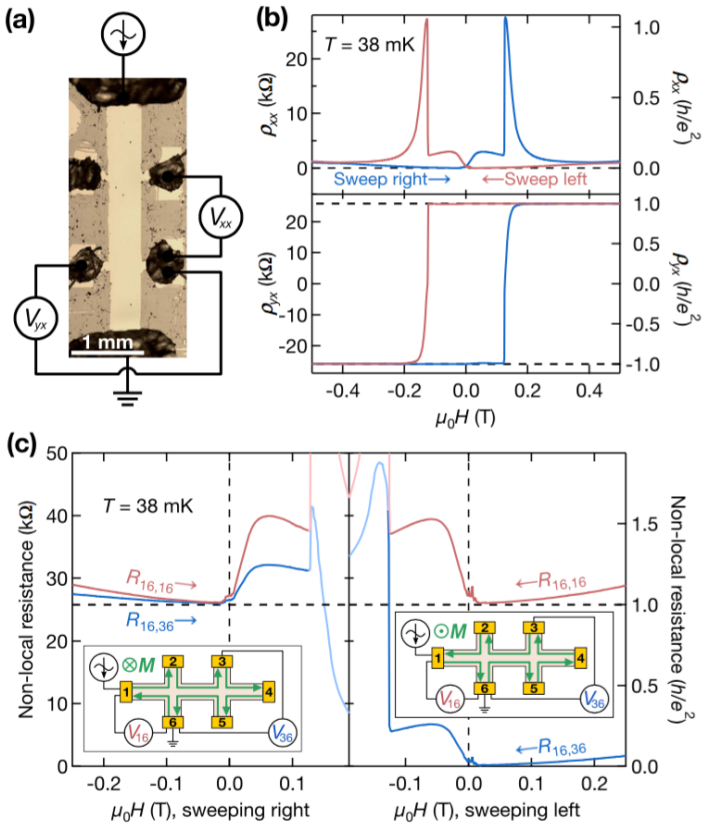

Figure 8.2: (color online). Device demonstrating quantum anomalous Hall effect. (a) Photograph of 10-nm-thick film of $(Cr_{0.12}Bi_{0.26}Sb_{0.62})_2Te_3$ on a GaAs substrate, scratched by hand into a Hall bar shape, with indium metal Ohmic contacts. Schematic measurement setup included. (b) Longitudinal resistivity ρ_{xx} and transverse resistivity ρ_{yx} of the device at base temperature as a function of the applied magnetic field $\mu_0 H$ in each sweep direction, forming a ferromagnetic hysteresis loop. As the field approaches zero from either starting point, ρ_{yx} reaches its quantized value h/e^2 and ρ_{xx} approaches zero. (c) Nonlocal and two-terminal measurements verifying edge-dominated transport. The insets show the measurements performed and chirality at each magnetization (adapted from Ref. [11]).

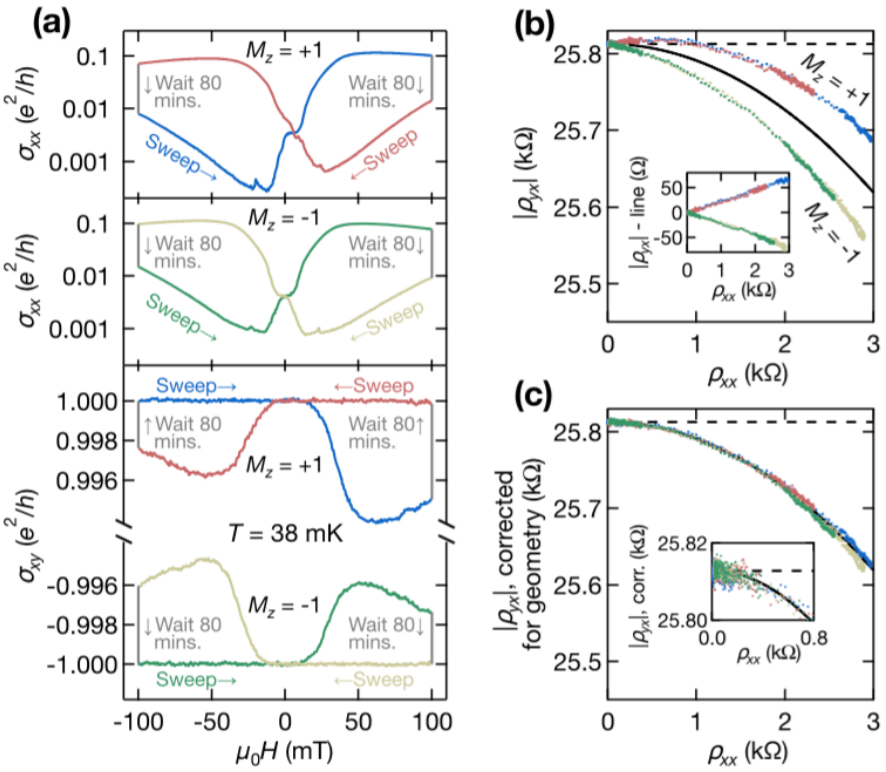

Figure 8.3: (color online). Precise quantization near zero applied field. (a) Longitudinal and transverse conductivities in hysteresis loops over field ranges smaller than the coercive field so as to maintain the starting magnetization M_z. When approaching zero field from either starting point, $\sigma_{xy} = e^2/h$ to 0.01% precision while σ_{xx} reaches as low as $0.0002e^2/h$. (b),(c) Resistivities measured during the hysteresis loops, plotted parametrically, both before (b) and after (c), performing a correction for geometry. The inset of (b) shows the linear deviation of the two magnetization branches from a parabolic line, resulting from uneven spacing of the leads. The inset of (c) shows a close-up of the corrected resistivity data, with ρ_{yx} quantized to h/e^2 within 3Ω whenever $\rho_{xx} < 200\Omega$ (adapted from Ref. [11]).

temperature. Indeed, for nonchiral edge modes, the backscattering and, consequently, the interference is allowed. This interference, on the other hand, is the origin of the quantum localization.

In theory, the question whether or not a given band structure allows a chiral edge state is decided by calculating the Chern number. Naturally, this calculation does not answer a question whether or not this band structure supports nonchiral in-gap edge modes. An alternative microscopic approach [19-22] to the issue of edge states confirms the prediction about their presence or absence made on the basis of Chern number calculation. This microscopic approach also allows us to calculate analytically the modification of the wave function of the chiral edge state due to the orbital action of the magnetic field, and even to trace how this edge state transforms into the quantum Hall edge state upon increasing the field. However, the microscopic approach [19-22] equally does not reproduce the nonchiral modes within the envelop-function description.

The Hamiltonian describing the gapped edge spectrum in QAH has a 2×2 matrix form [16]. This is in contrast to the conventional spin-orbit 4×4 Hamiltonian [23] describing the states in HgTe-based quantum wells. The reason is that the transition between inverted and trivial band structures due to magnetization takes place only for one spin projection. As a consequence of the matrix form of the Hamiltonian, the in-gap eigenstates are characterized by two decay lengths. Edge state is allowed if the two corresponding eigenvectors can be combined to satisfy the hard-wall boundary condition [26]. It appears that only "nontrivial" band structure allows such combination.

In the present paper we demonstrate that nonchiral edge modes emerge naturally upon generalization of the microscopic approach [19-22] to the case of the extended confinement. In fact, we employ the simplest model of the extended confinement in the form of a step next to the hard wall. We demonstrate that both chiral and nonchiral modes emerge as solutions of the same characteristic equation. The wave functions of nonchiral modes oscillate within the step before decaying into the bulk. Within the simplest model considered, we compare, for the same confinement, nonchiral edge modes for inverted band structure, supporting the chiral mode, and for "trivial" band structure. Our main finding is that, for "trivial" band structure, the nonchiral modes have a lower threshold with respect to, e.g., the step height. Nonchiral modes with inverted band structure are more extended. Disorder-induced scattering into these states extends the localization length of the chiral edge mode.

8.2 Edge modes in the presence of a step

8.2.1 Hard wall

To introduce notations, we briefly review the structure of the bulk QAH Hamiltonian [17]. It emerges from the conventional 4×4 Hamiltonian [23]

$$\hat{H}_{\text{eff}} = \begin{pmatrix} \hat{h}(\mathbf{k}) & 0 \\ 0 & \hat{h}^*(-\mathbf{k}) \end{pmatrix} \tag{8.1}$$

where $\hat{h}(\mathbf{k})$ is a 2×2 matrix defined as $\hat{h}(\mathbf{k}) = A(k_x\sigma_x + k_y\sigma_y) + (m + Bk^2)\sigma_z$, while σ_y, σ_z are the Pauli matrices acting in the pseudospin (electron-heavy hole) subspace. Upon adding the exchange [24]

$$\hat{h}_{\text{exch}} = \begin{pmatrix} \Delta & 0 & 0 & 0 \\ 0 & -\Delta & 0 & 0 \\ 0 & 0 & -\Delta & 0 \\ 0 & 0 & 0 & \Delta \end{pmatrix} \tag{8.2}$$

the two blocks become inequivalent

$$\hat{h}(\mathbf{k}) \to \begin{pmatrix} m + \Delta + Bk^2 & -A(k_x - ik_y) \\ -A(k_x + ik_y) & -m - \Delta - Bk^2 \end{pmatrix} \tag{8.3}$$

$$\hat{h}^*(-\mathbf{k}) \to \begin{pmatrix} m - \Delta + Bk^2 & A(k_x + ik_y) \\ A(k_x - ik_y) & -m + \Delta - Bk^2 \end{pmatrix}. \tag{8.4}$$

Near $m = \Delta$ the band inversion takes place only in the second block. Thus the transition can be swept through by applying a weak magnetic field, since the field controls the parameter, Δ.

It follows from Eq. (8.4) that at the transition $m = \Delta$ the Hamiltonian possesses only a single spatial scale,

$$l_0 = \frac{B}{A}. \tag{8.5}$$

Away from the transition, a new spatial scale,

$$l_\Delta = \frac{A}{m - \Delta}, \tag{8.6}$$

appears. The theory is greatly simplified by the fact that the first scale is much smaller than the second one [25]. In terms of the edge states, for a given, say positive, sign of B, the edge state is present for $m < \Delta$ and is absent for $m > \Delta$. To see this, consider the two eigenvectors of $\hat{h}^*(-\mathbf{k})$ propagating, as $\exp(ik_x x)$, along the boundary $y = 0$ and decaying, as $\exp(-qy)$, into the bulk, $y > 0$. For these eigenvectors, the elements of corresponding pseudospinors are related as

$$[m - \Delta + B(k_x^2 - q^2) - E]\alpha + A(k_x - q)\beta = 0,$$

$$[m-\Delta+B(k_x^2-q^2)+E]\beta-A(k_x+q)\alpha=0. \tag{8.7}$$

With $l_0 \ll |l_\Delta|$, the q-values for the two eigenvectors differ strongly, and the expressions for them have a simple form

$$q_0=\frac{1}{l_0}, \quad q_\Delta=\frac{1}{|l_\Delta|}\sqrt{1+(l_\Delta k_x)^2-\left(\frac{El_\Delta}{A}\right)^2}. \tag{8.8}$$

Note that, by virtue of the condition $l_0 \ll |l_\Delta|$, the nonparabolicity parameter B does not enter into q_Δ. Substituting Eq. (8.8) into Eq. (8.7), we find the form of the corresponding eigenvectors

$$\Psi_0=\begin{pmatrix}-1\\1\end{pmatrix}\exp\Big[ik_x x-q_0 y\Big], \tag{8.9}$$

$$\Psi_\Delta=\begin{pmatrix}1\\ \frac{A(k_x+q_\Delta)}{m-\Delta+E}\end{pmatrix}\exp\Big[ik_x x-q_\Delta y\Big]. \tag{8.10}$$

To satisfy the hard-wall boundary condition, both components of the linear combination of the eigenvectors Eqs. (8.9), (8.10) should turn to zero at $y=0$. This amounts to the requirement

$$1+\frac{A(k_x+q_\Delta)}{m-\Delta+E}=\frac{2(Ak_x+E)}{m-\Delta+E+A(k_x-q_\Delta)}=0. \tag{8.11}$$

One immediately concludes from Eq. (8.11) that the dispersion law of the chiral edge mode is linear

$$E=-Ak_x. \tag{8.12}$$

However, this conclusion applies only on one side of the transition, namely, for $(m-\Delta)<0$. Indeed, as it follows from Eq. (8.8), for $E=-Ak_x$, we have $q_\Delta=A/|m-\Delta|$. Therefore, for positive $m-\Delta$, the denominator in Eq. (8.11) turns to zero together with the numerator, so that the boundary condition cannot be satisfied.

8.2.2 Chiral edge mode in the presence of a step

Consider a boundary with a potential step next to it depicted in Fig. 8.4. In the domain $0<y<d$ the potential is equal to U_0. It creates the energy shift, so that the value q_Δ gets modified

$$q_\Delta \to \kappa=\frac{1}{|l_\Delta|}\sqrt{1+(l_\Delta k_x)^2-\left[\frac{(E-U_0)l_\Delta}{A}\right]^2}. \tag{8.13}$$

A general solution within the domain $0<y<d$ contains two growing and two decaying exponents

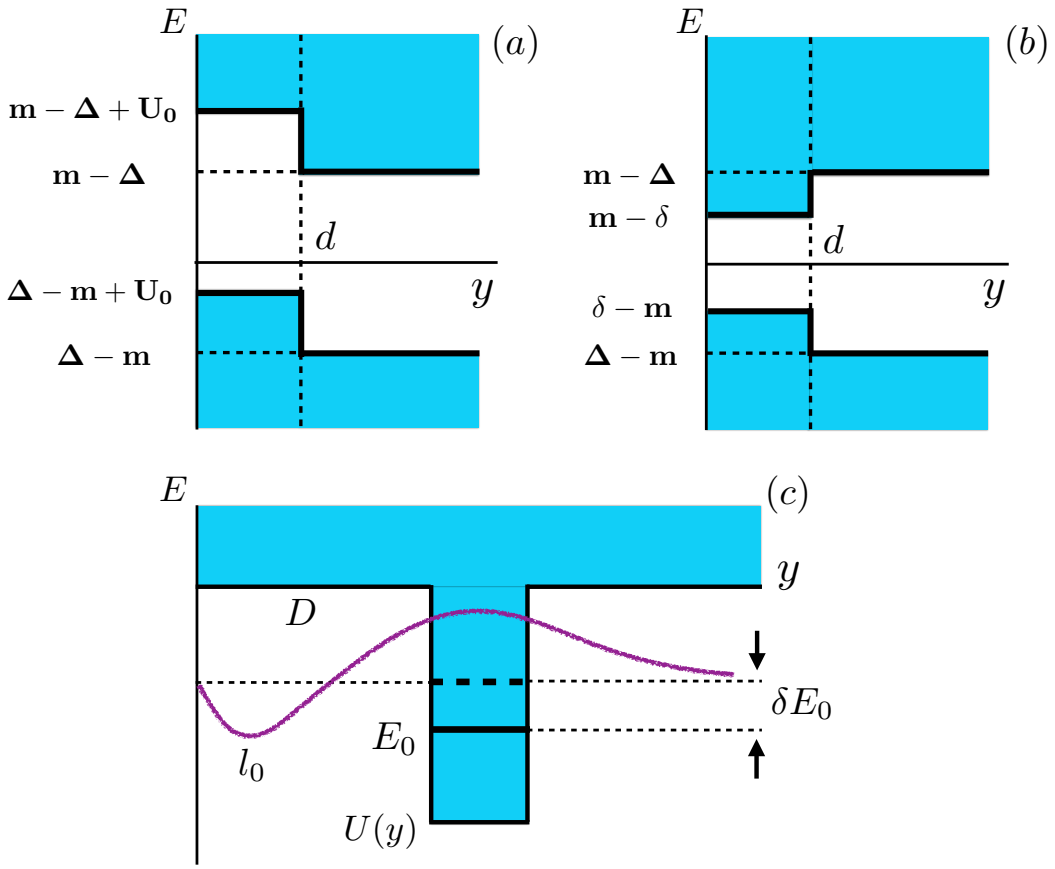

Figure 8.4: Two variants of the extended confinement: (a) potential step next to the hard wall, and (b) step in the gapwidth next to the hard wall.

$$\Psi_{y<d} = C_0 \begin{pmatrix} -1 \\ 1 \end{pmatrix} \exp\Big[ik_x x - q_0 y\Big] + C_\Delta \begin{pmatrix} 1 \\ \frac{A(k_x+\kappa)}{m-\Delta+E-U_0} \end{pmatrix} \exp\Big[ik_x x - \kappa y\Big] + D_0 \begin{pmatrix} 1 \\ 1 \end{pmatrix} \exp\Big[ik_x x + q_0(y-d)\Big] + D_\Delta \begin{pmatrix} 1 \\ \frac{A(k_x-\kappa)}{m-\Delta+E-U_0} \end{pmatrix} \exp\Big[ik_x x + \kappa y\Big]. \tag{8.14}$$

On the other hand, the solution for $y > d$ is still a linear combination of Ψ_0 and Ψ_Δ, namely

$$\Psi_{y>d} = C_0^- \begin{pmatrix} -1 \\ 1 \end{pmatrix} \exp\Big[ik_x x - q_0(y-d)\Big] + C_\Delta^- \begin{pmatrix} 1 \\ \frac{A(k_x+q_\Delta)}{m-\Delta+E} \end{pmatrix} \exp\Big[ik_x x - q_\Delta(y-d)\Big]. \tag{8.15}$$

Overall, there are 6 unknown amplitudes in Eqs. (8.14), (8.15). The 6 boundary conditions to be satisfied is the vanishing of both components of the wave function at $y = 0$ and the continuity of both components together with their derivatives at $y = d$. At this point we note that the step affects the dispersion law of the edge state only for $d \gtrsim l_\Delta \gg l_0$. This observation allows for two fundamental simplifications. Firstly, the term with amplitude C_0 in Eq. (8.14) decays rapidly with y from $y = 0$, so that its magnitude at the boundary $y = d$ is $\sim \exp(-d/l_0)$. Thus, this term should be taken into account only at the boundary $y = 0$. Similarly, the term with coefficient D_0 should be taken into account only at $y = d$. Next, the solutions with coefficients D_0 and C_0^- have big derivatives, $1/l_0$. Then, the matching with the derivatives of a slow decaying solutions renders their amplitude small, $\sim l_0/l_\Delta \ll 1$. Neglecting the terms D_0 and C_0^- leaves us with the system for 4 unknowns with 4 boundary conditions to satisfy. The form of this system is the following

$$\begin{aligned} &-C_0 + C_\Delta + D_\Delta = 0, \\ &C_0 + C_\Delta \frac{A(k_x+\kappa)}{m-\Delta+E-U_0} + D_\Delta \frac{A(k_x-\kappa)}{m-\Delta+E-U_0} = 0, \\ &C_\Delta e^{-\kappa d} + D_\Delta e^{\kappa d} = C_\Delta^-, \\ &\frac{C_\Delta(k_x+\kappa)e^{-\kappa d} + D_\Delta(k_x-\kappa)e^{\kappa d}}{m-\Delta+E-U_0} = C_\Delta^- \frac{(k_x+q_\Delta)}{m-\Delta+E}. \end{aligned} \tag{8.16}$$

The first two equations ensure that the wave function Eq. (8.14) turns to zero at $y = 0$, while the second two equations express the continuity of the wave function at $y = d$.

The consistency condition for the system Eq. (8.16) yields the following transcendental equation for the dispersion, $E(k_x)$, of the edge modes

$$\frac{\frac{m-\Delta+E-U_0}{A(k_x-\kappa)}+1}{\frac{m-\Delta+E-U_0}{A(k_x+\kappa)}+1} e^{-2\kappa d} = \frac{\frac{(k_x+q_\Delta)(m-\Delta+E-U_0)}{(k_x-\kappa)(m-\Delta+E)}-1}{\frac{(k_x+q_\Delta)(m-\Delta+E-U_0)}{(k_x+\kappa)(m-\Delta+E)}-1}. \tag{8.17}$$

To analyze this equation we first rewrite it in a dimensionless form

$$\frac{\frac{1+\mathcal{E}-\tilde{U}_0}{\mathcal{K}_x-\mathrm{sign}(m-\Delta)\mathcal{P}}+1}{\frac{1+\mathcal{E}-\tilde{U}_0}{\mathcal{K}_x+\mathrm{sign}(m-\Delta)\mathcal{P}}+1}e^{-2\mathcal{P}\tilde{d}}=\frac{\frac{[\mathcal{K}_x+\mathrm{sign}(m-\Delta)\mathcal{Q}_\Delta](1+\mathcal{E}-\tilde{U}_0)}{[\mathcal{K}_x-\mathrm{sign}(m-\Delta)\mathcal{P}](1+\mathcal{E})}-1}{\frac{[\mathcal{K}_x+\mathrm{sign}(m-\Delta)\mathcal{Q}_\Delta](1+\mathcal{E}-\tilde{U}_0)}{[\mathcal{K}_x+\mathrm{sign}(m-\Delta)\mathcal{P}](1+\mathcal{E})}-1}, \tag{8.18}$$

where we have introduced the dimensionless energy, momentum, and the decay constant

$$\begin{aligned}\mathcal{E}&=\frac{E}{m-\Delta},\quad \mathcal{K}_x=\frac{Ak_x}{m-\Delta},\\ \mathcal{P}&=\frac{A\kappa}{|m-\Delta|}=\sqrt{1+\mathcal{K}_x^2-(\mathcal{E}-\tilde{U}_0)^2},\\ \mathcal{Q}_\Delta&=\frac{Aq_\Delta}{|m-\Delta|}=\sqrt{1+\mathcal{K}_x^2-\mathcal{E}^2},\end{aligned} \tag{8.19}$$

while the dimensionless size and the depth of the step are defined as

$$\tilde{U}_0=\frac{U_0}{m-\Delta},\quad \tilde{d}=\frac{|m-\Delta|d}{A}. \tag{8.20}$$

Note that the sign of $(m-\Delta)$ appears in Eq. (8.18) to ensure that the decay constant is positive for any sign of $(m-\Delta)$.

The dispersion law Eq. (8.12) for the chiral edge state follows from Eq. (8.18) in the limit $\tilde{d}\to 0$. Indeed, in dimensionless units, Eq. (8.12) reads $\mathcal{E}=-\mathcal{K}_x$. This suggests that $\mathcal{Q}_\Delta=1$. For $(m-\Delta)<0$, the ratio $(1+\mathcal{E})/(\mathcal{K}_x+\mathrm{sign}(m-\Delta)\mathcal{Q}_\Delta)$ is equal to -1, the fractions in the left-hand side and in the right-hand side are equal to each other, so that Eq. (8.18) is satisfied. It is even easier to see that in the limit $\tilde{d}\to\infty$ Eq. (8.18) yields the dispersion law $\mathcal{E}=-\mathcal{K}_x+\tilde{U}_0$. In this limit the denominator in the left-hand side turns to zero for negative $(m-\Delta)$.

For general parameters of the step the dispersion law of the chiral mode is illustrated in Figs. 8.5, 8.6. Naturally, presence of the step does not violate the fact that the chiral mode exists only for negative $(m-\Delta)$. For a "weak" step the edge mode is present for both positive and negative momenta, while for a "strong" step only at positive momenta. Although it is not a rigorous statement, the dispersion is linear, with very high accuracy. Numerically, the relative change of the slope with $\mathcal{K}_x$ is $\approx 10^{-3}$.

Figs. 8.5, 8.6 also suggest that the dispersion of a chiral edge mode has an endpoint. This is also the consequence of a finite accuracy of the numerical procedure. The true behavior of the slope, as the edge mode merges with continuum at certain point $\mathcal{K}_x=\mathcal{K}_x^c$, $\mathcal{E}=\mathcal{E}^c=\left[1+(\mathcal{K}_x^c)^2\right]^{1/2}$ is $\left[\frac{\partial\mathcal{E}}{\partial\mathcal{K}_x}-\frac{\mathcal{K}_x^c}{\mathcal{E}^c}\right]\propto(\mathcal{K}_x-\mathcal{K}_x^c)$. To see this, one can view the transcendental equation Eq. (8.18) as a relation between the variables $\mathcal{K}_x$ and $\mathcal{Q}_\Delta$. Since it contains the terms linear in $\mathcal{K}_x$ and $\mathcal{Q}_\Delta$, its variation yields $\delta\mathcal{K}_x=\eta\delta\mathcal{Q}_\Delta$, where η is some

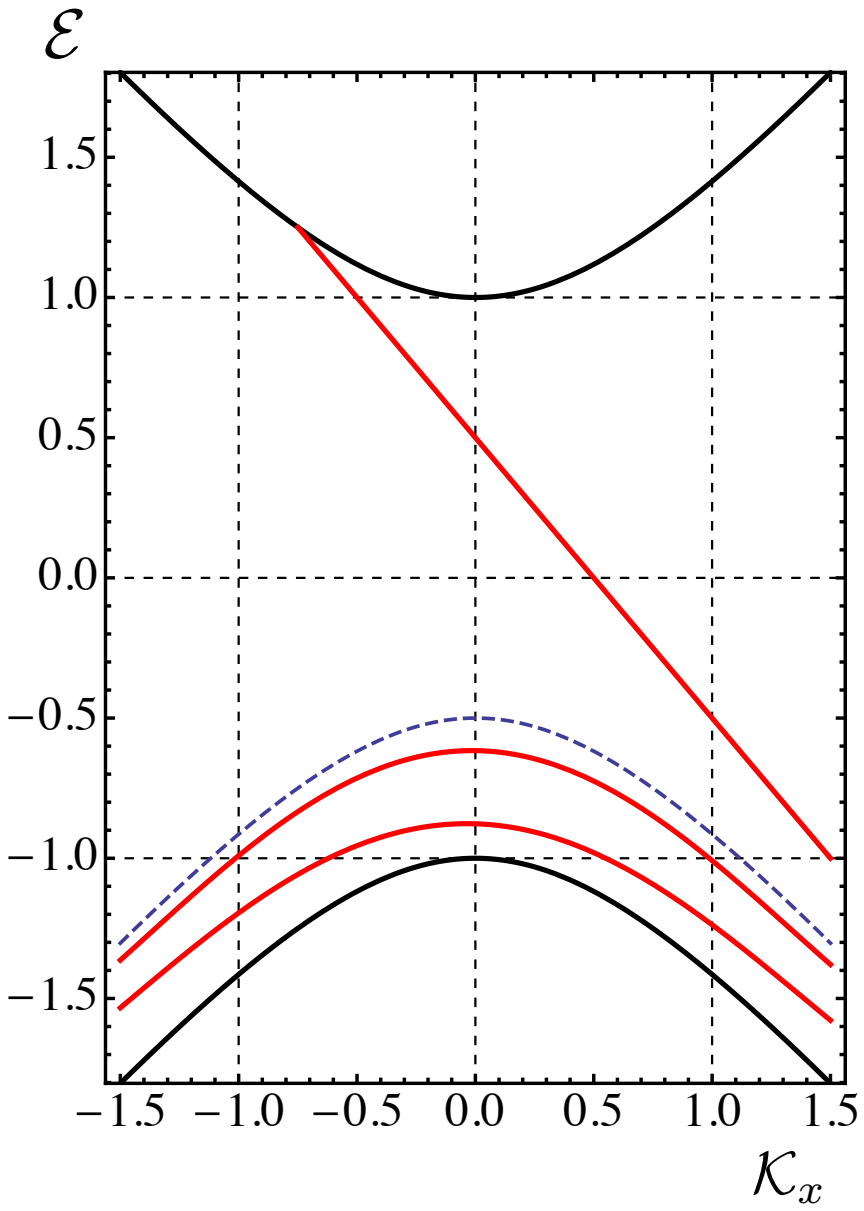

Figure 8.5: (color online). The dispersions of the modes propagating along the boundary $y = 0$ is plotted from Eqs. (8.18) and (8.22) for dimensionless step height $\tilde{U}_0 = 0.5$ and dimensionless step width $\tilde{d} = 6$. The spectrum of the edge mode and of two nonchiral modes is shown with red lines. Bulk spectrum (black) and the spectrum in the step region, $0 < y < d$, (dashed) are also shown.

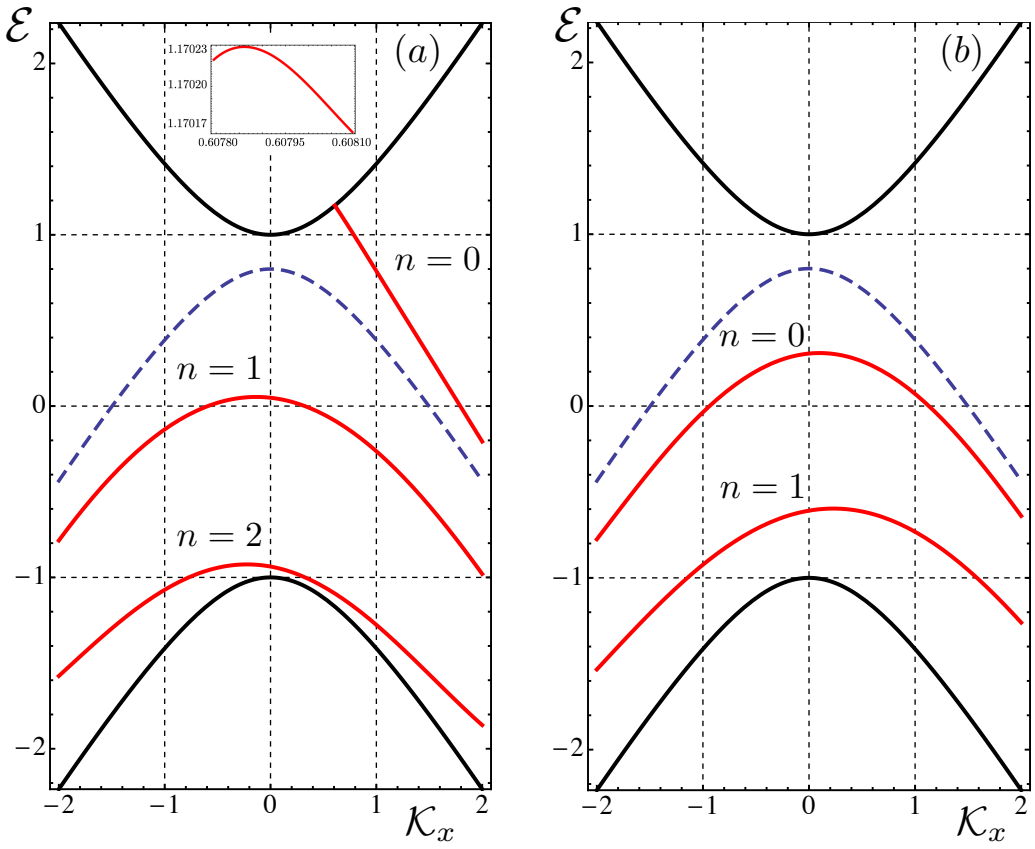

Figure 8.6: (color online). Comparison of the dispersions of edge modes, shown with red, for "topological" (a) and "trivial" (b) boundaries. Parameters of the step are $\tilde{U}_0 = 1.8$ and $\tilde{d} = 2.2$. Bulk spectrum (black) and the spectrum in the step region, $0 < y < d$, (dashed) are also shown. The inset detalizes how the dispersion of the chiral mode merges with the bulk spectrum.

constant. On the other hand, from definition of $\mathcal{Q}_\Delta$ it follows that $\mathcal{Q}_\Delta \delta \mathcal{Q}_\Delta = \mathcal{K}_x \delta \mathcal{K}_x - \mathcal{E}\delta\mathcal{E}$. Thus, one has

$$\frac{\mathcal{Q}_\Delta}{\mathcal{E}} = \eta\Big(\frac{\mathcal{K}_x}{\mathcal{E}} - \frac{\partial \mathcal{E}}{\partial \mathcal{K}_x}\Big). \tag{8.21}$$

As the dispersion law approaches the continuum, the variable $\mathcal{Q}_\Delta$ turns to zero. Then it follows from Eq. (8.21) that the velocity of the edge mode approaches $\frac{\mathcal{K}_x^c}{\mathcal{E}^c}$, which is the velocity of the bulk mode. Numerically, the merging of the chiral edge mode dispersion with the bulk spectrum is illustrated in Fig. 8.6, inset. It is seen that the change of sign of the slope takes place within a very narrow domain of momenta $\sim 10^{-4}$.

8.2.3 Nonchiral edge modes

Our main finding in the present paper is that the transcendental equation Eq. (8.18) captures, along with the chiral mode, a set of nonchiral edge modes. For these modes the decay rate, κ, within the step and, thus, the dimensionless $\mathcal{P}$ are purely imaginary. For such $\mathcal{P}$ it is convenient to cast Eq. (8.18) in the form

$$|\mathcal{P}|\tilde{d} + \Phi_1 + \Phi_2 = \pi n, \tag{8.22}$$

where n is integer and the phases Φ_1, Φ_2 are defined as

$$\begin{aligned}
\Phi_1 &= \arctan\left(\frac{\mathrm{sign}(m-\Delta)|\mathcal{P}|}{1+\mathcal{E}-\tilde{U}_0+\mathcal{K}_x}\right),\\
\Phi_2 &= \arctan\left(\frac{\mathrm{sign}(m-\Delta)|\mathcal{P}|}{\frac{1+\mathcal{E}-\tilde{U}_0}{1+\mathcal{E}}(\mathcal{K}_x+\mathrm{sign}(m-\Delta)\mathcal{Q}_\Delta)-\mathcal{K}_x}\right).
\end{aligned} \tag{8.23}$$

The meaning of $|\mathcal{P}|\tilde{d}$ is the phase accumulated by the components of the pseudospinor on the interval $0 < y < d$, where they oscillate. The meaning of Φ_1 and Φ_2 is the phase shift at the boundary $y = 0$ and $y = d$, respectively.

The maximal value of n, i.e., the number of modes with dispersion law having its origin in the bulk gap, is finite and is determined by the thickness, d.

Note that both phase shifts depend on sign of $(m - \Delta)$. Thus, the dispersion laws of nonchiral modes "know" whether or not the band structure is inverted. These dispersion laws, obtained from Eq. (8.22), are shown in Fig. 8.6 for a given step and with opposite signs of $(m - \Delta)$. It is seen that for $(m - \Delta) > 0$ the nonchiral branches lie *deeper in the gap* than nonchiral branches for negative $(m - \Delta)$. The sign of $(m - \Delta)$ also determines the classification of the branches. For $(m - \Delta) > 0$ the values of n start from $n = 0$, while $(m - \Delta) > 0$ they start from $n = 1$. Qualitatively, this suggests that a chiral mode "complicates" the formation of nonchiral modes. Different dispersions for positive and

negative $(m-\Delta)$ imply that the behavior of $|\Psi(y)|^2$ is different. This is illustrated in Fig. 8.7. We see that nonchiral mode for $(m-\Delta)<0$ is significantly more extended than for $(m-\Delta)>0$.

It is instructive to compare the above results for the step potential with dispersion of nonchiral modes emerging from a jump of the gap magnitude next to the boundary in the domain $0<y<d$; see Fig. 8.4b. Modifications of Eq. (8.18) to this case are straightforward. Firstly, the decay constant $\mathcal{P}$ should be redefined

$$\mathcal{P}\to\sqrt{\tilde{\delta}^2+\mathcal{K}_x^2-\mathcal{E}^2}, \tag{8.24}$$

where $\tilde{\delta}=(m-\delta)/(m-\Delta)$ is the relative reduction of the gap in the domain $0<y<d$. The second modification is the replacement of the combination $1-\tilde{U}_0$ in Eq. (8.18) by $\tilde{\delta}$. The solutions of Eq. (8.18) for a particular set of parameters are shown in Fig. 8.8a. Naturally, nonchiral modes are symmetric with respect to $E=0$. Unlike the case of the potential step, they never reach the midgap. With regard to the density profile, Fig. 8.8b, the nonchiral mode is repelled from the boundary even further than in the case of the potential step.

8.3 "Topological" shift of the dispersion of the mode localized far away from the boundary

8.3.1 Formulation of the problem

In the present Section we consider the following problem. Suppose that a potential well, $U(y)$, is located far away from the boundary; see Fig. 8.4c. Quantitatively, this implies that the distance, D, is much bigger than l_Δ. Even in the limit $D\to\infty$ the potential $U(y)$ supports a nonchiral mode with dispersion, $E_0(k_x)$. This dispersion does not depend on whether the underlying band structure is trivial or inverted. Finite D causes a small correction, $\delta E_0(k_x)$, to the dispersion of the mode guided by $U(y)$. We will demonstrate that this correction has a "topological" character: it shifts $E_0(k_x)$ towards the center of the gap for $(m-\Delta)>0$ and away from the midgap for $(m-\Delta)<0$. Moreover, we will see that the "topological" character of the correction manifests itself in the fact that it depends on the *sign* of k_x, while the bare dispersion, $E_0(k_x)$, is obviously an even function of k_x. Qualitatively, this effect can be understood as follows. Consider the situation $(m-\Delta)<0$. The guided mode "senses" the boundary via the far tail of the wavefunction; see Fig. 8.4c. For $(m-\Delta)<0$ there is a chiral mode propagation along the boundary. The coupling of the tail to this mode is either strong or weak depending on weather the guided mode co-propagates ($k_x<0$) or counterpropagates ($k_x>0$) with the chiral mode. In the next subsection we trace analytically the resonance between the guided mode in potential

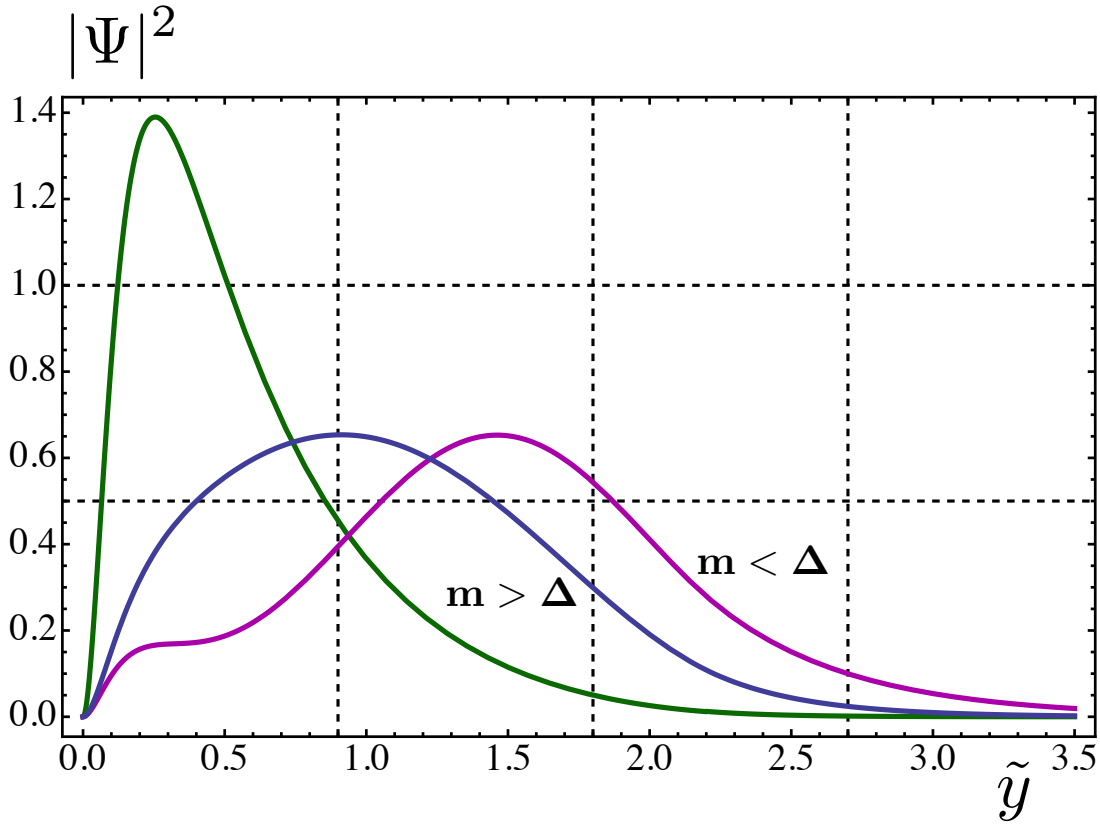

Figure 8.7: (color online). Comparison of the probability density profiles for different edge modes. For "topological" boundary the profiles of chiral edge mode and lowest nonchiral mode are shown with green and purple, respectively. The profile for the nonchiral mode at the "trivial" boundary is shown with blue. All three profiles are calculated for energy in the center of the gap.

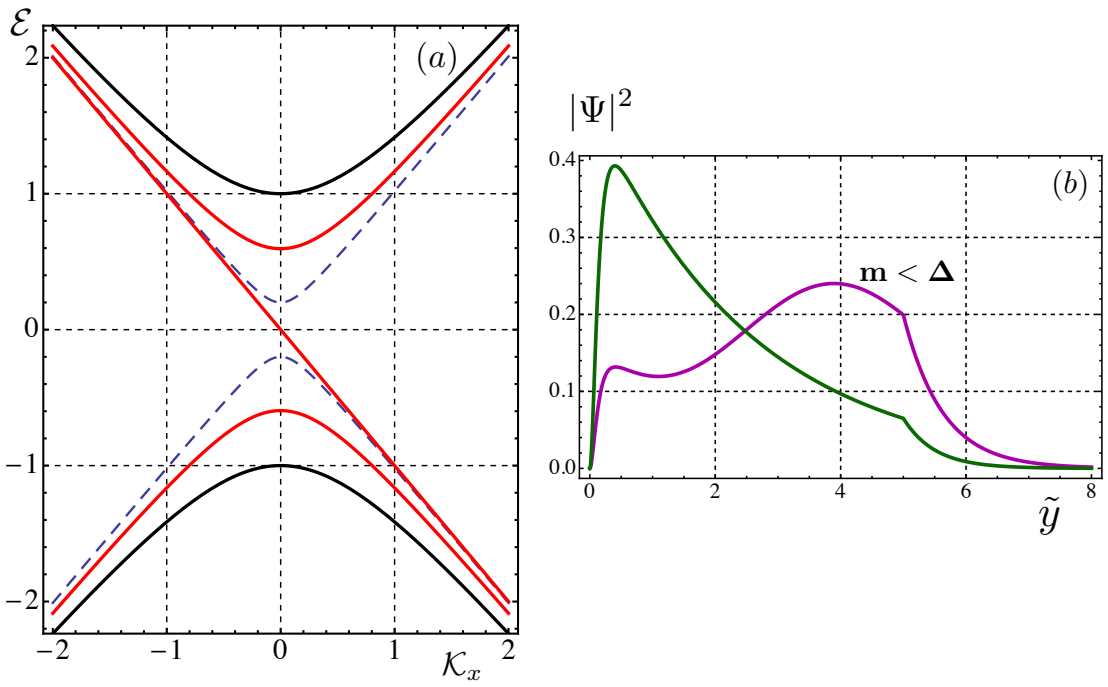

Figure 8.8: (color online). Dispersions (a) and the density profiles (b) of a chiral and nonchiral modes are shown for the extended confinement Fig. 1b. The magnitude of the gap reduction near the edge is $\delta = 0.2\Delta$, while the dimensionless width is $\tilde{d} = 5$. Density profile of both modes is calculated for dimensionless energy $\mathcal{E} = 0.6$. Bulk spectrum (black) and the spectrum in the step region (dashed) are also shown.

$U(y)$ and the chiral edge mode. Calculation can be performed explicitly due to the small parameter l_Δ/D.

8.3.2 Calculation of the shift

Denote with $\psi_e(y)$ and $\psi_h(y)$ the components of a pseudospinor describing the wave function of a nonchiral mode

$$\Big(\hat{h}^*(-\hat{\mathbf{k}})+U(y)\Big)\Psi=\Big(\hat{h}^*(-\hat{\mathbf{k}})+U(y)\Big)\begin{pmatrix}\psi_e\\ \psi_h\end{pmatrix}=E(k_x)\begin{pmatrix}\psi_e\\ \psi_h\end{pmatrix}. \tag{8.25}$$

For $l_0 \ll l_\Delta$ presence of the boundary is taken into account by imposing a boundary condition

$$\Psi(0)=\begin{pmatrix}1\\ -1\end{pmatrix}. \tag{8.26}$$

We emphasize that, as in the case of a step, the meaning of $y=0$ in this condition is, in fact, $l_0 \ll y \ll l_\Delta$, see Eqs. (8.9), (8.10). Denote now with $\psi_e^{(0)}(y)$, $\psi_h^{(0)}(y)$ the component of the pseudospinor for the case when the boundary is absent (moved to $y=-\infty$). One has

$$\Big(\hat{h}^*(-\hat{\mathbf{k}})+U(y)\Big)\Psi^{(0)}=\Big(\hat{h}^*(-\hat{\mathbf{k}})+U(y)\Big)\begin{pmatrix}\psi_e^{(0)}\\ \psi_h^{(0)}\end{pmatrix}=E_0(k_x)\begin{pmatrix}\psi_e^{(0)}\\ \psi_h^{(0)}\end{pmatrix}. \tag{8.27}$$

As a next step, we multiply Eq. (8.25) by $\Psi^{(0)}$ from the left and Eq. (8.27) by Ψ from the left and subtract them from each other. This yields

$$A\frac{d(\psi_e^{(0)}\psi_h-\psi_e\psi_h^{(0)})}{dy}=\delta E_0(k_x)\Big(\psi_e^{(0)}(y)\psi_e(y)+\psi_h(y)\psi_h^{(0)}(y)\Big). \tag{8.28}$$

Upon integrating Eq. (8.28) from $y=0$ to ∞, we find the analytical expression for $\delta E_0(k_x)$

$$\delta E_0(k_x)=-A\frac{\psi_e^{(0)}(0)\psi_h(0)-\psi_e(0)\psi_h^{(0)}(0)}{\int\limits_0^\infty dy\Big(\psi_e^{(0)}(y)\psi_e(y)+\psi_h(y)\psi_h^{(0)}(y)\Big)}. \tag{8.29}$$

The difference between the boundary values $\psi_e(0)$ and $\psi_e^{(0)}(0)$ as well as $\psi_h(0)$ and $\psi_h^{(0)}(0)$ is that the exact wave functions satisfy the boundary condition Eq. (8.26). The boundary leads to the admixture to $\Psi^{(0)}$ of the "short-range" solution decaying into the bulk as $\exp(-q_0 y)$ and of the "reflected" solution decaying as $\exp(-q_\Delta y)$. The corresponding amplitudes, C_0 and C_Δ, are found from the boundary condition

$$C_0\begin{pmatrix}-1\\ 1\end{pmatrix}+C_\Delta\begin{pmatrix}1\\ \frac{A(k_x+q_\Delta)}{m-\Delta+E_0}\end{pmatrix}+\begin{pmatrix}\psi_e^{(0)}(0)\\ \psi_h^{(0)}(0)\end{pmatrix}=0, \tag{8.30}$$

which yields

$$C_0=\frac{-\frac{A(k_x+q_\Delta)}{m-\Delta+E_0}\psi_e^{(0)}(0)+\psi_h^{(0)}(0)}{1+\frac{A(k_x+q_\Delta)}{m-\Delta+E_0}},\ C_\Delta=-\frac{\psi_e^{(0)}(0)+\psi_h^{(0)}(0)}{1+\frac{A(k_x+q_\Delta)}{m-\Delta+E_0}}. \tag{8.31}$$

At distance $y \gg l_0$ from the boundary the short-range solution vanishes. Thus, the differences $\psi_h(0)-\psi_h^{(0)}(0)$, and $\psi_e(0)-\psi_e^{(0)}(0)$ are determined only by the reflected solution

$$\begin{pmatrix}\psi_e(0)\\ \psi_h(0)\end{pmatrix} = C_\Delta \begin{pmatrix}1\\ \frac{A(k_x+q_\Delta)}{m-\Delta+E_0}\end{pmatrix} + \begin{pmatrix}\psi_e^{(0)}(0)\\ \psi_h^{(0)}(0)\end{pmatrix}. \tag{8.32}$$

Substituting Eq. (8.32) into Eq. (8.29), we express the correction $\delta E_0(k_x)$ via the components of the bare pseudospinor

$$\delta E_0(k_x) = -A\frac{\psi_e^{(0)}(0)\psi_h^{(0)}(0)\Big(1-\frac{k_x+q_\Delta}{k_x-q_\Delta}\Big)\Big(\frac{1+\frac{A(k_x-q_\Delta)}{m-\Delta+E_0}}{1+\frac{A(k_x+q_\Delta)}{m-\Delta+E_0}}\Big)}{\int\limits_{-\infty}^{\infty} dy\Big[(\psi_e^{(0)}(y))^2+(\psi_h^{(0)}(y))^2\Big]}, \tag{8.33}$$

where we took into account that $\psi_h^{(0)}(0)/\psi_e^{(0)}(0) = A(k_x-q_\Delta)/(m-\Delta+E_0)$.

We see that the correction is proportional to the product of the bare amplitudes, and thus to $\exp(-2q_\Delta D)$, which is the probability to find an electron at the edge. The result Eq. (8.33) applies when this probability is small. For this reason we replaced $\psi_e(0)$, $\psi_h(0)$ in the denominator by $\psi_e^{(0)}(0)$, $\psi_h^{(0)}(0)$ and extended the low limit of integration to $-\infty$. To analyze the dependence of the correction on the bare spectrum, $E_0(k_x)$, it is instructive to recast the last bracket into the form

$$\frac{m-\Delta+E_0+A(k_x-q_\Delta)}{m-\Delta+E_0+A(k_x+q_\Delta)} = \frac{\Big[m-\Delta+E_0+Ak_x-\sqrt{(m-\Delta)^2+A^2k_x^2-E_0^2}\Big]^2}{2(E_0+Ak_x)(m-\Delta+E_0)}. \tag{8.34}$$

The above expression illustrates the topological origin of the shift of a nonchiral mode, $E_0(k_x)$. Indeed, the correction Eq. (8.33) contains a pole corresponding to the dispersion law of the chiral edge mode. This confirms our earlier observation that presence of this mode complicates the formation of nonchiral modes. The shift Eq. (8.33) tends to reduce the binding energy. Another feature that points at the topological origin of the correction is that it depends on the sign of k_x. This is in contrast to nonperturbed behavior $E_0(k_x)$, which is an even function of k_x. As k_x increases, the parameter q_Δ, which is the characteristics of proximity of $E_0(k_x)$ to the continuous spectrum, becomes much smaller than k_x. Then the second bracket in Eq. (8.33) is close to 1, while the first bracket falls off as $1/k_x$.

The result Eq. (8.33) strongly simplifies for small k_x. Then we have

$$\delta E_0(k_x) = -A\frac{2\psi_e^{(0)}(0)\psi_h^{(0)}(0)}{\int\limits_{-\infty}^{\infty} dy\Big[(\psi_e^{(0)}(y))^2+(\psi_h^{(0)}(y))^2\Big]}\left[\frac{(m-\Delta)-\sqrt{(m-\Delta)^2-E_0^2}}{E_0}\right]. \tag{8.35}$$

It is the factor in the square brackets that carries information on whether or not the boundary supports the chiral mode. Indeed, if the level, E_0, in the potential $U(y)$ is close to midgap, then this factor diverges for $(m-\Delta)<0$, while it turns to zero for $(m-\Delta)>0$. This is because, for $(m-\Delta)<0$, there is a level $E=0$ at the boundary from which the level E_0 is repelled. When this level is absent, the behavior of the shift $\delta E_0 \propto E_0$ is natural. For $E_0 \to 0$ there are equal probabilities to be shifted up or down.

8.4 Concluding remarks

The presence or absence of chiral modes in QAH effect is decided by the relative sign of $(m-\Delta)$ and parameter B in the Hamiltonian $\hat{h}(\mathbf{k})$, although the parameter B itself does not enter into the dispersion law of the chiral mode. The situation with nonchiral modes is analogous, their dispersion relations do not contain B. Still, these relations depend on whether $(m-\Delta)$ and B have the same sign or opposite signs. Moreover, similarly to chiral mode, nonchiral modes will not exist without the term Bk^2 on the diagonal of the matrix $\hat{h}$. This is because, without the short-range solution $\propto \exp(-q_0 y)$ in Eq. (8.14), the hard-wall boundary conditions cannot be satisfied.

Within the standard picture of the QAH transition [17], it takes place as the gap closes and two chiral modes at the opposite edges merge. Disorder would facilitate this merging and, thus, smear the transition. In this regard, it is instructive to draw an analogy of QAH with conventional quantum Hall transition. This transition is broadened due to the disorder-assisted overlap between the counterpropagating chiral edge modes. This mechanism was appreciated already in the early papers on the quantum Hall effect; see, e.g., Refs. [27-30]. Quantitatively, scattering by disorder-induced in-gap states effectively enhances the localization radius of the edge modes boosting their overlap. In the present paper we found that extended confinement gives rise to in-gap nonchiral modes. This suggests that chiral edge modes can "communicate" with each other using nonchiral modes, which are less localized, as virtual intermediate states [27-30]. This is how the extended confinement may cause the smearing of the QAH transition.

Our other finding is that, while nonchiral modes are present for both signs of $(m-\Delta)$, their formation is much less likely for $(m-\Delta)<0$. This can be interpreted as follows. The pseudospinor corresponding to the nonchiral mode should be orthogonal to the chiral mode if it is present. Thus the formation of the nonchiral mode is impeded for "topological" sign of $(m-\Delta)$.

In Ref. [31] it was assumed that the boundary of the system is planar, and the generalized, compared to hard wall, version of the boundary conditions was employed.

It was demonstrated that variation of parameters in the boundary condition can lead to disappearance of the chiral mode form the gap, but nonchiral modes do not emerge upon this variation.

It is straightforward to generalize our results for the rectangular step to the arbitrary profile of the step. Essentially, the decay constant κ defined by Eq. (8.13) becomes the function of the coordinate. Qualitative conclusions do not change.

The probable microscopic origin of the extended confinement is a conventional band bending at the interface. For the material Bi_2Se_3 this bending was studied experimentally in Ref. [33]. According to this paper, the extension of the bending region is about $200\mathring{A}$, while bending magnitude is about 0.2eV. These quantities should be viewed as estimates for our d and U_0.

8.5 References

[1] J. G. Checkelsky, J. Ye, Y. Onose, Y. Iwasa, and Y. Tokura, Nat. Phys. **8**, 729 (2012).

[2] C.-Z. Chang, J. Zhang, M. Liu, Z. Zhang, X. Feng, K. Li, L.-L. Wang, X. Chen, X. Dai, Z. Fang, X.-L. Qi, S.-C. Zhang, Y. Wang, K. He, X.-C. Ma, and Q.-K. Xue, Adv. Mater. **25**, 1065 (2013).

[3] X. Kou, M. Lang, Y. Fan, Y. Jiang, T. Nie, J. Zhang, W. Jiang, Y. Wang, Y. Yao, L. He, and K. L. Wang, ACS Nano **7**, 9205 (2013).

[4] C.-Z. Chang, J. Zhang, X. Feng, J. Shen, Z. Zhang, M. Guo, K. Li, Y. Ou, P. Wei, L.-L. Wang, Z.-Q. Ji, Y. Feng, S. Ji, X. Chen, J. Jia, X. Dai, Z. Fang, S.-C. Zhang, K. He, Y. Wang, L. Lu, X.-C. Ma, and Q.-K. Xue, Science **340**, 167 (2013).

[5] J. G. Checkelsky, R. Yoshimi, A. Tsukazaki, K. S. Takahashi, Y. Kozuka, J. Falson, M. Kawasaki, and Y. Tokura, Nat. Phys. **10**, 731 (2014).

[6] X. Kou, S.-T. Guo, Y. Fan, L. Pan, M. Lang, Y. Jiang, Q. Shao, T. Nie, K. Murata, J. Tang, Y. Wang, L. He, T.-K. Lee, W.-L. Lee, and K. L. Wang, Phys. Rev. Lett. **113**, 137201 (2014).

[7] C.-Z. Chang, W. Zhao, D. Y. Kim, H. Zhang, B. A. Assaf, D. Heiman, S.-C. Zhang, C. Liu, M. H. W. Chan. and J. S. Moodera, Nat. Mater. **14**, 473 (2015).

[8] A. Kandala, A. Richardella, S. Kempinger, C.-X. Liu, N. Samarth, Nat. Commun. **6**, 7434 (2015).

[9] M. Mogi, R. Yoshimi, A. Tsukazaki, K. Yasuda, Y. Kozuka, K. S. Takahashi, M. Kawasaki, and Y. Tokura, Appl. Phys. Lett. **107**, 182401 (2015).

[10] X. Kou, L. Pan, J. Wang, Y. Fan, E. S. Choi, W.-L. Lee, T. Nie, K. Murata, Q. Shao, S.-C. Zhang, and K. L. Wang, Nat. Commun. **6**, 8474 (2015).

[11] A. J. Bestwick, E. J. Fox, X. Kou, L. Pan, K. L. Wang, and D. Goldhaber-Gordon, Phys. Rev. Lett. **114**, 187201 (2015).

[12] C.-Z. Chang, W. Zhao, D. Y. Kim, H. Zhang, B. A. Assaf, D. Heiman, S.-C. Zhang, C. Liu, M. H. W. Chan, and J. S. Moodera, Nat. Mater. **14**, 473 (2015).

[13] C.-Z. Chang, W. Zhao, D. Y. Kim, P. Wei, J. K. Jain, C. Liu, M. H. W. Chan, and J. S. Moodera, Phys. Rev. Lett. **115**, 057206 (2015).

[14] S. Grauer, S. Schreyeck, M. Winnerlein, K. Brunner, C. Gould, and L. W. Molenkamp, Phys. Rev. B **92**, 201304(R) (2015).

[15] E. O. Lachman, A. F. Young, A. Richardella, J. Cuppens, H. R. Naren, Y. Anahory, A. Y. Meltzer, A. Kandala, S. Kempinger, Y. Myasoedov, M. E. Huber, N. Samarth, and E. Zeldov, Sci. Adv. **1**, e1500740 (2015).

[16] X.-L. Qi, Y.-S. Wu, and S.-C. Zhang, Phys. Rev. B **74**, 085308 (2006).

[17] C.-X. Liu , X.-L. Qi, X. Dai, Z. Fang, and S.-C. Zhang, Phys. Rev. Lett. **101**, 146802 (2008).

[18] J. Wang, B. Lian, H. Zhang, and S.-C. Zhang, Phys. Rev. Lett. **111**, 086803 (2013).

[19] E. B. Sonin, Phys. Rev. B **82**, 113307 (2010).

[20] B. Scharf, A. Matos-Abiague, and J. Fabian, Phys. Rev. B **86**, 075418 (2012).

[21] A. M. Lunde and G. Platero, Phys. Rev. B **88**, 115411 (2013).

[22] M. V. Durnev and S. A. Tarasenko, Phys. Rev. B **93**, 075434 (2016),

[23] B. A. Bernevig, T. L. Hughes, and S.-C. Zhang, Science **314**, 1757 (2006).

[24] Following C.-X. Liu, S.-C. Zhang, and X.-L. Qi, arXiv:1508.07106, we assumed that the absolute values of diagonal components of $\hat{h}_{\rm exch}$ are equal to each other. In fact, the band inversion requires only that the signs of these components within one block are opposite.[17] Still the form Eq. (8.2) is not a loss of generality. Indeed, if the sum of these components is nonzero, it causes an overall shift of the spectrum.

[25] To estimate the length l_0 we take the experimental value $B = 60\text{eV}\cdot\mathring{A}^2$ from Ref. [32] and the value $A = 3\text{eV}\cdot\mathring{A}$ from Ref. [17]. This yields $l_0 = B/A = 20\mathring{A}$, which is only 3 times bigger than the distance between the magnetic dopants in experiment as well as the thickness of the layer where the surface reconstruction[34] takes place. On the other hand, for the gap ~ 10meV the length l_Δ is $\sim 300\mathring{A}$, i.e. it is much bigger.

[26] M. I. Dyakonov and A. V. Khaetskii, JETP Lett. **33**, 110 (1981) [Pisma Zh. Eksp. Teor. Fiz. **33**, 115 (1981)].

[27] J. K. Jain and S. A. Kivelson, Phys. Rev. Lett. **60**, 1542 (1988).

[28] T. Martin and S. Feng, Phys. Rev. Lett. **64**, 1971 (1990).

[29] J. Hajdu, M. E. Raikh, and T. V. Shahbazyan, Phys. Rev. B **50**, 17625 (1994).

[30] M. M. Fogler, A. Yu. Dobin, and B. I. Shklovskii, Phys. Rev. B **57**, 4614 (1998).

[31] V. V. Enaldiev, I. V. Zagorodnev, and V. A. Volkov, Pisma Zh. Eksp. Teor. Fiz. **101**, 94 (2015) [JETP Lett. **101**, 89 (2015)].

[32] H. Zhang, C. Liu, X. Qi, X. Dai, Z. Fang, and S. Zhang, Nat. Phys. **5**, 438 (2009).

[33] C. E. ViolBarbosa, C. Shekhar, B. Yan, S. Ouardi, E. Ikenaga, G. H. Fecher, and C. Felser, Phys. Rev. B **88**, 195128 (2013).

[34] T. M. Edmonds, J. T. Hellerstedt, A. Tadich, A. Schenk, K. M. ODonnell, J. Tosado, N. P. Butch, P. Syers, J. Paglione, and M. S. Fuhrer, J. Phys. Chem. C **118**, 20413 (2014).

CHAPTER 9

SMEARING OF THE QUANTUM ANOMALOUS HALL EFFECT DUE TO STATISTICAL FLUCTUATIONS OF MAGNETIC DOPANTS

9.1 Introduction

Pairs of spin-degenerate chiral edge modes are implicit for insulators with inverted bandstructure [1, 2]. The minimal model [2] that captures these modes is a 4×4 matrix Hamiltonian acting in the basis of two spin and two orbital states.

The origin of the quantum anomalous Hall effect [4] (QAH) is breaking of the time-reversal symmetry induced by magnetic order. As a result, the symmetry between the two counterpropagating modes at the sample edges is lifted. With a single chiral mode per edge, the Hall conductance of the sample becomes nonzero, and the transport resembles the conventional quantum Hall effect. Experimental studies [5-20], on Cr-doped and V-doped layers of BiTe-based insulating compounds confirm both the quantization of the Hall resistance and the edge transport that accompany the buildup of the magnetic order.

For QAH effect to be pronounced, the bulk of the sample should be strongly insulating. On the other hand, the crossover between a trivial and "topological" bandstructure takes place as the gap passes through zero. Obviously, the smaller the gap the easier it is washed out by the disorder. More precisely, the disorder gives rise to in-gap states. However, in QAH, the disorder is of a special type: randomness in positions of magnetic ions causes the local fluctuations of the gap *width*. For such fluctuations the energies near the gap center remain unaffected. This is probably the reason why robust QAH is observed in experiments of several groups.

In the present paper we study quantitatively the smearing of the gap due to statistical, and thus unavoidable, magnetic disorder [21]. We find that the states near the gap center are due to the local reversals of the gap *sign* within narrow rings. By employing the

instanton approach [22, 23] we specify the shape of these fluctuations and the likelihood of their occurrence, which determines the density of the in-gap states. This density of states exhibits a semihard gap near zero energy. The experimental picture [14, 20] corresponding to this situation is shown in Fig. 9.1 and Fig. 9.2.

9.2 Instanton approach

Due to the composition disorder, the local value of x, which is the portion of magnetic ions, differs from the average

$$x(\mathbf{r}) = \overline{x} + \delta x(\mathbf{r}). \tag{9.1}$$

Fluctuations $\delta x(\mathbf{r})$ are gaussian with a zero correlation radius

$$\langle \delta x(\mathbf{r}) \delta x(\mathbf{r}') \rangle = \frac{\overline{x}(1-\overline{x})}{N_0} \delta(\mathbf{r}-\mathbf{r}'), \tag{9.2}$$

where N_0 is the concentration of Bi lattice sites in which the substitution magnetic ions reside. It is natural to assume that the local gap fluctuations, $\Delta(\mathbf{r})$, are proportional to δx, i.e.,

$$\Delta(\mathbf{r}) = E_g(\mathbf{r}) - \overline{E}_g = \alpha\, \delta x(\mathbf{r}), \qquad \alpha = \frac{d\overline{E}_g}{d\overline{x}}. \tag{9.3}$$

It follows from Eq. (9.3) that the probability to find the fluctuation $\Delta(\mathbf{r})$ is given by

$$\mathcal{P}\big\{\Delta(\mathbf{r})\big\} \propto \exp\Big[-\frac{1}{2\gamma}\int d\mathbf{r}\Delta^2(\mathbf{r})\Big]. \tag{9.4}$$

where $\gamma = \frac{\alpha^2}{N_0}\overline{x}(1-\overline{x})$.

According to the instanton approach [22, 23], the density of states with energy, E, corresponds to the maximum of the functional $\mathcal{P}$ among all the fluctuations that create a level with energy, E. In application to QAH effect, the wave function, $\Psi(\mathbf{r})$, corresponding to this level is a two-component spinor,

$$\Psi(\mathbf{r}) = \begin{pmatrix} \psi_e(\mathbf{r}) \\ \psi_h(\mathbf{r}) \end{pmatrix}, \tag{9.5}$$

which satisfies the Schrödinger equation

$$\hat{h}_{\Delta(\mathbf{r})}\Psi = E\Psi. \tag{9.6}$$

The Hamiltonian $\hat{h}_{\Delta(\mathbf{r})}$ is a standard Hamiltonian of the minimal model Ref. [2] in which only one spin component is retained. In the conventional notations [2] it has the form

$$\hat{h}_{\Delta(\mathbf{r})} = A(\hat{k}_x\sigma_x + \hat{k}_y\sigma_y) + \Big(B\hat{k}^2 + \overline{E}_g + \Delta(\mathbf{r})\Big)\sigma_z, \tag{9.7}$$

where σ_x, σ_y, and σ_z are the Pauli matrices acting in the pseudospin space [24]. Relative sign of $\overline{E}_g$ and parameter B determines whether or not the chiral modes are the eigenstates of this Hamiltonian in the presence of an edge [4].

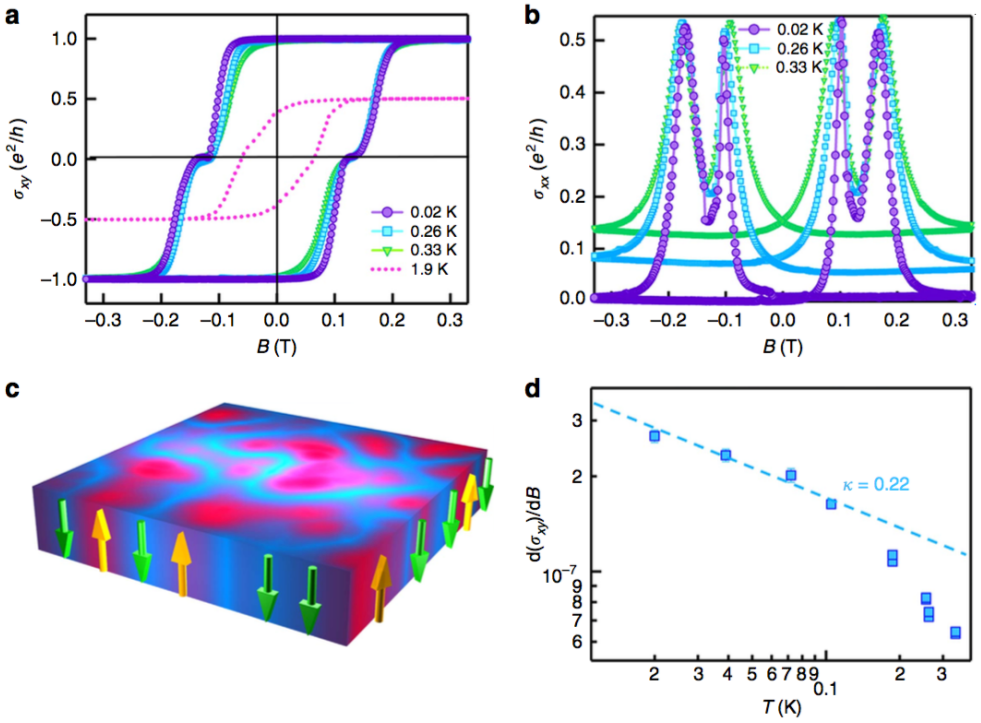

Figure 9.1: (color online). Quantum phase transition of quantum anomalous Hall effect. (a) Magnetic field-dependent σ_{xy} at different temperatures. Zero Hall plateaus at $\pm H_C$ are developed between the two QAHE states up to 0.33 K. (b) Magnetic field-dependent σ_{xx} at different temperatures. Even when the film already deviates from the perfect QAHE state at $T = 0.33$ K, both the zero σ_{xy} plateaus and double-peaked σ_{xx} still persist. (c) Schematic representation of the multidomain network formed during the magnetization reversal process. The upward yellow arrows and downward green arrows denote the up ($\Delta_M > |m_0|$) and down ($\Delta_M < -|m_0|$) magnetic domains, respectively. (d) Temperature-dependent transition slope $S = (\partial\sigma_{xy}/\partial H)_{max}$ extracted from a. When $T < 0.1$K, $S \propto T^{-\kappa}$ follows the power low scaling behavior with $\kappa = 0.22$ (adapted from Ref. [14]).

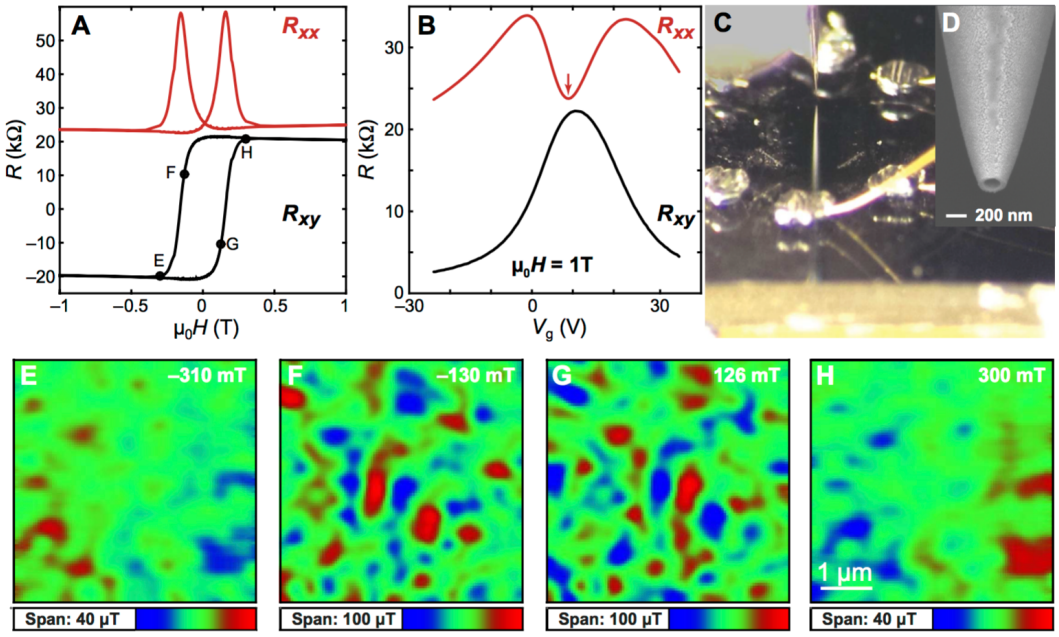

Figure 9.2: (color online). Electrical transport and scanning magnetic imaging of 7-QL-thick $Cr_{0.1}(Bi_{0.5}Sb_{0.5})_{1.9}Te_3$ sample at $T = 250$mK. (A and B) Transport measurements showing magnetic field dependence of R_{xx} (red) and R_{xy} (black) at $V_g = 6$V (A) and the V_g dependence at 1T (B). The dip in R_{xx} marked by the arrow shows the incipient QAH state. (C) Optical image of the sample and SOT showing the electrical contacts and the SOT reflection from the sample surface. (D) Electron micrograph of the SOT used for the magnetic imaging. (E to H) Scanning SOT images (5×5 μ^2) of the out-of-plane magnetic field $B_z(x, y)$ at 300 nm above the sample surface at four antisymmetric locations along the magnetization loop marked in (A). Note the strong anticorrelation between (E) and (H), and (F) and (G). Pixel size, 50 nm; pixel integration time, 10 ms (adapted from Ref. [20]).

The procedure of minimization of the functional Eq. (9.4) with restriction Eq. (9.6) is conventionally carried out [22, 23] by introducing the Lagrange multiplier, λ, and searching for a minimum of the auxiliary functional

$$\lambda\langle\Psi|\hat{h}_{\Delta(\mathbf{r})}|\Psi\rangle + \frac{1}{2\gamma}\int d\mathbf{r}\Delta^2(\mathbf{r}). \tag{9.8}$$

with respect to $\Delta(\mathbf{r})$. The minimization yields

$$\Delta(\mathbf{r}) = -\lambda\gamma\Big(|\psi_e(\mathbf{r})|^2 - |\psi_h(\mathbf{r})|^2\Big). \tag{9.9}$$

The remaining task is to substitute Eq. (9.9) into the Schrödinger equation, find $\psi_e(\mathbf{r})$, $\psi_h(\mathbf{r})$, substitute them into Eq. (9.9), and evaluate $\mathcal{P}$ with extremal $\Delta(\mathbf{r})$ defined by Eq. (9.9).

9.3 Asymptotic solution of the instanton equation

Assuming the azimuthal symmetry of $\Delta(\mathbf{r})$, the solutions of Eq. (9.6) can be classified according to the angular momentum: $\psi_e(\mathbf{r}) = i\psi_e^m(\rho)\exp(im\phi)$, $\psi_h(\mathbf{r}) = \psi_h^m(\rho)\exp[i(m+1)\phi]$, where ρ and ϕ are the radius and the azimuthal angle, respectively. Then the system of equations for $\psi_e^m(\rho)$ and $\psi_h^m(\rho)$ reads

$$\begin{aligned}
\Big[\overline{E}_g - E - \lambda\gamma\Big(|\psi_e^m(\rho)|^2 - |\psi_h^m(\rho)|^2\Big)\Big]\psi_e^m(\rho) &= A\Big(\frac{\partial}{\partial\rho} + \frac{m+1}{\rho}\Big)\psi_h^m(\rho),\\
\Big[\overline{E}_g + E - \lambda\gamma\Big(|\psi_e^m(\rho)|^2 - |\psi_h^m(\rho)|^2\Big)\Big]\psi_h^m(\rho) &= A\Big(\frac{\partial}{\partial\rho} - \frac{m}{\rho}\Big)\psi_e^m(\rho).
\end{aligned} \tag{9.10}$$

Here we dropped the term $B\hat{k}^2$ in the Hamiltonian $\hat{h}_{\Delta(\mathbf{r})}$ and will incorporate it later [25].

The solution of the system is straightforward when the energy, E, is close to the band-edge, $(\overline{E}_g - E) \ll \overline{E}_g$. Then we have $\psi_h^m \ll \psi_e^m$, so that the system Eq. (9.10) reduces to a single equation

$$\frac{A^2}{2\overline{E}_g}\nabla^2\psi_e(\mathbf{r}) + \lambda\gamma\big[\psi_e(\mathbf{r})\big]^3 = (\overline{E}_g - E)\psi_e(\mathbf{r}). \tag{9.11}$$

This is a standard instanton equation for a particle moving in a white-noise random potential [22, 23, 26, 27]. The radial size of this instanton is $\sim \big[\overline{E}_g(\overline{E}_g - E)/A^2\big]^{1/2}$. Thus, the integral over $\mathbf{r}$ in Eq. (9.4) is proportional to $(\overline{E}_g - E)$. The full expression for the density of states in the tail reads

$$N(E) \propto \exp\Big[-\kappa_0\Big(\frac{A^2}{\gamma}\Big)\frac{\overline{E}_g - E}{\overline{E}_g}\Big], \tag{9.12}$$

so that the characteristic tail energy is given by $E_t = \frac{\gamma\overline{E}_g}{A^2}$. The value of the numerical factor $\kappa_0 = 5.8$ was established in Refs. [26], [27]. It originates from the solution of Eq. (9.11)

with zero angular momentum. Physically, the tail states are due to local gap reductions, as depicted in Fig. 9.3.

The result Eq. (9.12) applies when the tail energy is much smaller than the gap, i.e., for $\gamma \ll A^2$. This result cannot be used even as an order-of-magnitude estimate for the middle of the gap. This is because the shape of the fluctuation, $\Delta(\mathbf{r})$, at $|E| \ll \overline{E}_g$ is dramatically different from a simple gap reduction, $\Delta(\mathbf{r})$, captured by Eq. (9.11). Below we demonstrate that for $|E| \ll \overline{E}_g$ the expression for the density of states has the form

$$N(E) \propto \exp\left[-\kappa_1 \Big(\frac{A^2}{\gamma}\Big) \frac{\overline{E}_g}{|E|} \ln \frac{\overline{E}_g}{|E|} \right]. \tag{9.13}$$

Singular energy dependence of $|\ln N(E)|$ reflects the fact that the probability of formation of a state near the gap center is highly unlikely since the corresponding fluctuation requires a local gap reversal.

To create a state exactly at $E = 0$ the gap should be negative in the left half-space and positive in the right half-space [28] (or vice versa). Naturally, such a fluctuation has a zero probability. To have a finite probability, the fluctuation must include two gap reversals, i.e., $|\Delta(\mathbf{r})|$ should exceed $\overline{E}_g$ inside the fluctuation. To establish the shape of this fluctuation, we start from a one-dimensional case when $|\Delta(\mathbf{r})|$ changes only along the coordinate, y, Fig. 9.3.

A one-dimensional version of the system Eq. (9.10) reads

$$\begin{aligned} \Big[\overline{E}_g - E - \lambda\gamma\Big(|\psi_e(y)|^2 - |\psi_h(y)|^2\Big)\Big]\psi_e(y) &= A\frac{d\psi_h(y)}{dy}, \\ \Big[\overline{E}_g + E - \lambda\gamma\Big(|\psi_e(y)|^2 - |\psi_h(y)|^2\Big)\Big]\psi_h(y) &= A\frac{d\psi_e(y)}{dy}. \end{aligned} \tag{9.14}$$

Upon a natural rescaling

$$y = \frac{A}{\overline{E}_g}\chi, \quad \varepsilon = \frac{E}{\overline{E}_g}, \quad \psi_{e,h} = \Big(\frac{\overline{E}_g}{\lambda\gamma}\Big)^{1/2}\Phi_{e,h}, \tag{9.15}$$

it acquires a fully dimensionless form

$$\begin{aligned} \Big[1 - \varepsilon - \Big(|\Phi_e(\chi)|^2 - |\Phi_h(\chi)|^2\Big)\Big]\Phi_e(\chi) &= \frac{d\Phi_h}{d\chi}, \\ \Big[1 + \varepsilon - \Big(|\Phi_e(\chi)|^2 - |\Phi_h(\chi)|^2\Big)\Big]\Phi_h(\chi) &= \frac{d\Phi_e}{d\chi}. \end{aligned} \tag{9.16}$$

Dimensionless length in Eq. (9.16) corresponds to a physical decay length of the wave function in the middle of the gap. Local gap reversals correspond to the regions of χ where $\Big(|\Phi_e(\chi)|^2 - |\Phi_h(\chi)|^2\Big)$ exceed 1. A formal reason why there are no midgap fluctuation states

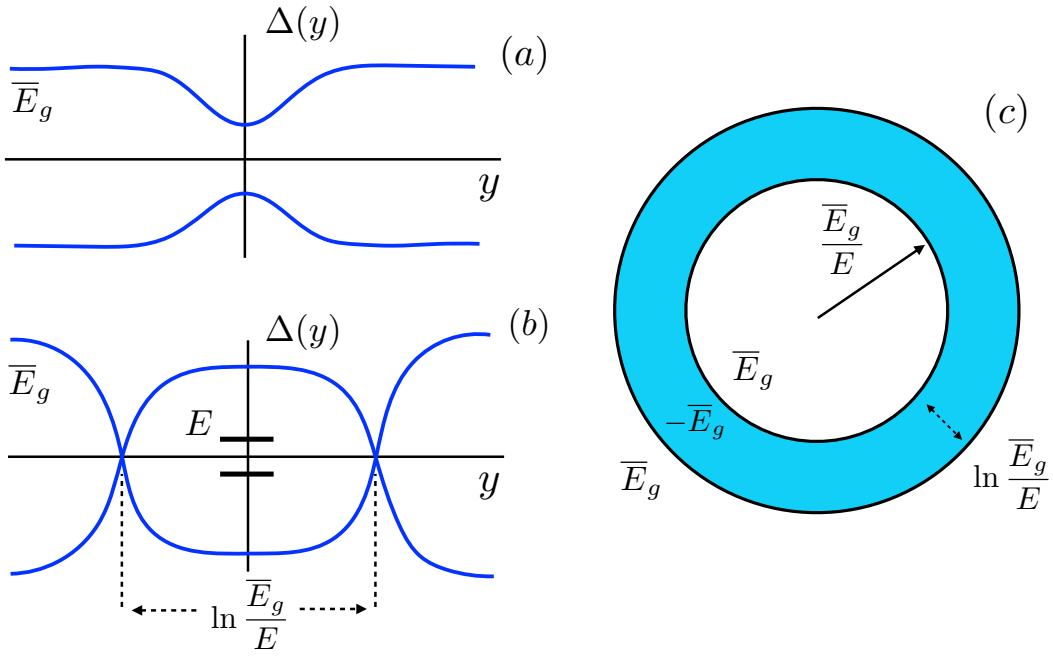

Figure 9.3: (color online). Gap fluctuation. (a) Fluctuation states near the gap edges are due to local reductions of the width of the gap caused by the the composition disorder. (b) To create an in-gap state with energy, E, much smaller than the gap width in 1d *two* local gap reversals are required. (c) In 2d, the angular motion tends to shift the fluctuation levels away from the gap center. Thus, the fluctuation, responsible for the state, E, represents a narrow ring of gap reversals with radius $\propto \overline{E}_g/E$.

is that for $\varepsilon = 0$ electron-hole symmetry requires $|\Phi_e(\chi)|^2 = |\Phi_h(\chi)|^2$, which is incompatible with decay of $\Phi_{e,h}$ at $\chi \to \pm\infty$.

To find an asymptotic solution of the system at finite energy, we make use of the smallness of parameter, ε. As a first step, instead of Φ_e and Φ_h, we introduce new functions

$$\Phi_e(\chi) = C(\chi)\cosh\varphi(\chi), \quad \Phi_h(\chi) = -C(\chi)\sinh\varphi(\chi), \tag{9.17}$$

after which the system takes the form

$$\begin{aligned} 1 - \varepsilon - C(\chi)^2 &= -\Big[\frac{d\varphi}{d\chi} + \tanh\varphi(\chi)\Big(\frac{dC}{Cd\chi}\Big)\Big], \\ 1 + \varepsilon - C(\chi)^2 &= -\Big[\frac{d\varphi}{d\chi} + \frac{1}{\tanh\varphi(\chi)}\Big(\frac{dC}{Cd\chi}\Big)\Big]. \end{aligned} \tag{9.18}$$

Upon subtracting the two equations, we can express the function $C(\chi)$ in terms of $\varphi(\chi)$ as follows

$$C(\chi) = C_0 \exp\Big[-\varepsilon\int\limits_0^\chi d\chi' \sinh 2\varphi(\chi')\Big], \tag{9.19}$$

where C_0 is a constant. Substituting this expression back into the system, we arrive to a closed differential-integral equation for $\varphi(\chi)$

$$1 - C_0^2 \exp\Big[-2\varepsilon\int\limits_0^\chi d\chi' \sinh 2\varphi(\chi')\Big] = -\frac{d\varphi}{d\chi} + \varepsilon\cosh 2\varphi. \tag{9.20}$$

In a zero order in $\varepsilon \ll 1$ the solution of Eq. (9.20) is a linear function

$$\varphi(\chi) = \frac{\chi}{b}, \qquad b = \frac{1}{C_0^2 - 1}. \tag{9.21}$$

Gap reversal, which corresponds to $C_0 > 1$, is terminated at certain distance $\chi = \chi_\varepsilon$ when $\varepsilon\cosh\varphi$ becomes big. This yields $\chi_\varepsilon = \frac{b}{2}|\ln\varepsilon|$. Importantly, the exponential term in the left-hand side of Eq. (9.20) drops abruptly from 1 to 0 at the same $\chi = \chi_\varepsilon$, or, more precisely, in the domain $|\chi - \chi_\varepsilon| \lesssim 1$.

The behavior of $C(\chi)$ at $|\chi - \chi_\varepsilon| > 1$ can be found taking into account that C_0^2-term in Eq. (9.20) is negligible in this domain. Then it follows from Eq. (9.20) that the function $\varphi(\chi)$ saturates at the value $\varphi = \varphi_\varepsilon$, such that $\varepsilon\cosh 2\varphi_\varepsilon = 1$. Smallness of ε allows us to simplify φ_ε to $\frac{1}{2}|\ln\varepsilon|$. This is exactly the same value that one obtains upon substituting χ_ε into Eq. (9.21). The fact that $\varphi(\chi)$ saturates at $\chi > \chi_\varepsilon$ suggests that the function $C(\chi)$ falls off exponentially, as $\exp\big[-(\chi - \chi_\varepsilon)\big]$ at $\chi > \chi_\varepsilon$, as follows from Eq. (9.19). The behavior of $\varphi(\chi)$ and $C(\chi)$ is depicted in Fig. 9.4.

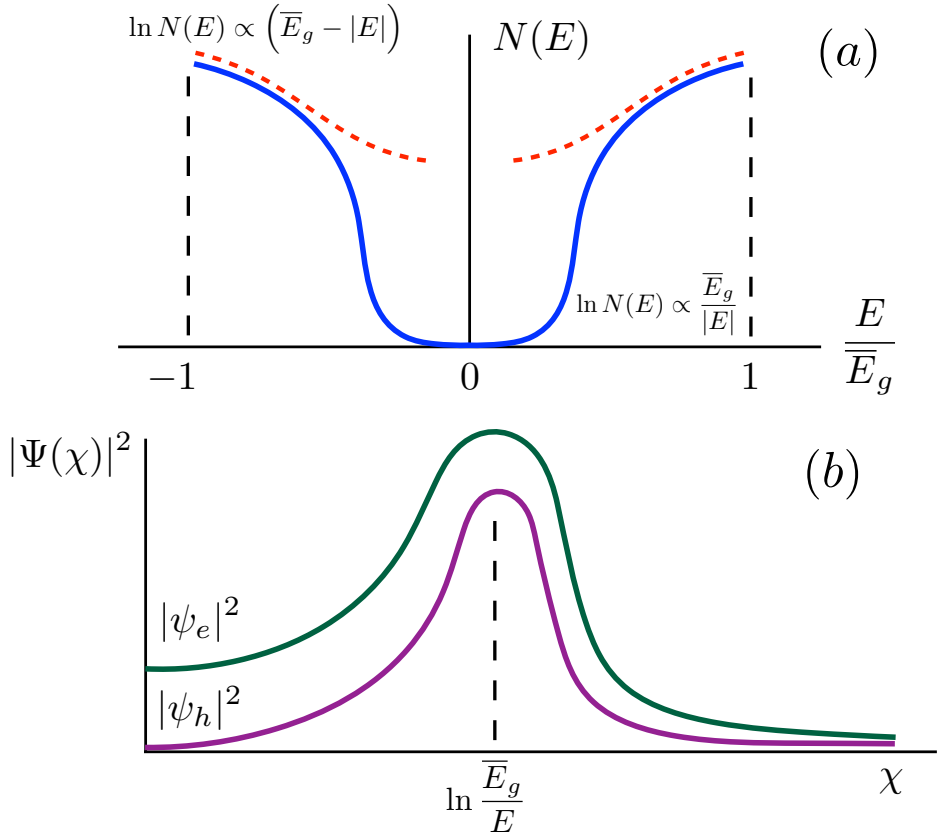

Figure 9.4: (color online). Density of the in-gap states. (a) The density of the in-gap states due to the composition disorder is shown schematically. Near the gap edges (dashed lines) it is a simple exponent, see Eq. (9.12), while near $E = 0$ it represents a semi-hard gap, Eq. (9.13). (b) The components, ψ_e and ψ_h, of the spinor corresponding to the fluctuation state, $E \ll \overline{E}_g$, are shown schematically versus the dimensionless distance from the ring center. Analytically, ψ_e is given by Eq. (9.22). The width of the ring exceeds logarithmically the in-gap decay length at $E = 0$.

Returning to dimensional units, we summarize our result

$$\Phi_e(y) = \left[\frac{\overline{E}_g}{\lambda\gamma}\Big(1+\frac{1}{b}\Big)\right]^{1/2} \times \begin{cases} \cosh\Big(\frac{\overline{E}_g y}{Ab}\Big), & y < y_E, \\ \Big(\frac{\overline{E}_g}{E}\Big)^{1/2} \exp\big[-\frac{\overline{E}_g}{A}(y-y_E)\big], & y > y_E. \end{cases} \tag{9.22}$$

where $y_E = \frac{A}{\overline{E}_g}\chi_\varepsilon = \frac{Ab}{2\overline{E}_g}\ln\frac{\overline{E}_g}{E}$. The corresponding expression for ψ_h differs by replacement of cosh by sinh. At $y = y_E$ the two expressions match within a numerical factor.

The solution Eq. (9.22) of the system of instanton equations in one-dimensional is actually, sufficient to find the two-dimensional density of states. Compared to the system Eq. (9.14), the two-dimensional instanton equations contain the extra "centrifugal" terms $\propto 1/\rho$. These terms create an energy shift $\sim A/\rho$, and thus prevent the formation of the fluctuation in-gap levels with small energies. For such levels to exist the double reversal of the gap sign should take place within a ring with radius, ρ_E, much bigger than the width; see Fig. 9.3. Then the solutions of the system Eq. (9.14) near the ring center are *one-dimensional* with $y = \rho - \rho_E$. More quantitatively [25], with angular motion taken into account, the energy levels of the ring-shape fluctuation are given by

$$E_m = \pm\left[A^2\Big(\frac{2m+1}{\rho_E}\Big)^2 + E^2\right]^{1/2}, \tag{9.23}$$

where the first term described the quantization of the angular kinetic energy. The above equation suggests that, for level E to exist, the minimal radius of the ring is $A/|E|$.

In the expression Eq. (9.4) for the density of states the integral $d\mathbf{r}$ can be replaced by the integral $2\pi\rho_E dy$ over the area of the ring

$$N(E) \propto \exp\left[-\frac{1}{2\gamma}\Big(2\pi\rho_E \int\limits_{-\infty}^{\infty} dy\Delta^2(y)\Big)\right]. \tag{9.24}$$

The expression for magnitude of the fluctuation, $\Delta(y)$, is given by Eq. (9.9). Taking into account that the dominant contribution to the integral over y comes from the domain $|y| < y_E$, we get

$$N(E) \propto \exp\left[-2\pi\lambda^2\gamma\rho_E \int\limits_0^{y_E} dy\Big(\psi_e^2(y) - \psi_h^2(y)\Big)^2\right]. \tag{9.25}$$

Substituting Eq. (9.22) into Eq. (9.24), and taking into account that the difference $\big(\psi_e^2 - \psi_h^2\big)$ is constant for $y < y_E$, we reproduce the result Eq. (9.13) in which the constant κ_1 should be identified with a combination

$$\kappa_1(b) = \pi\Big(1 + \frac{1}{b}\Big)^2 b. \tag{9.26}$$

The dependence $\kappa_1(b)$ has a minimum at $b = 1$, where it is equal to 4π. The value $b = 1$ corresponds to $C_0 = 2^{1/2}$, which, in turn, means that the most probable fluctuation corresponds to a complete gap reversal, i.e., the gap is equal to $-\overline{E}_g$ at the core of the fluctuation.

9.4 Discussion

The main outcome of our study is that, even when the spins of magnetic dopants are fully aligned, the unavoidable statistical fluctuations in their density (alloy disorder [29-31] smear the gap, $\overline{E}_g$. The degree of smearing is governed by a dimensionless material parameter

$$\nu = \frac{\gamma}{A^2} = \frac{\overline{x}(1-\overline{x})}{A^2 N_0}\Big(\frac{d\overline{E}_g}{d\overline{x}}\Big)^2. \tag{9.27}$$

For $\nu \ll 1$ only a narrow energy interval $|E - \overline{E}_g| \sim \nu\overline{E}_g$ is affected by the disorder, see Eq. (9.12). As ν exceeds 1, it might seem from Eq. (9.12) that the gap is completely washed out. However, our result Eq. (9.13), see also Fig. 9.4, suggests that, even for strong disorder, there is an almost hard gap near $E = 0$ which exists in the domain $|E| \lesssim \overline{E}_g/\nu$. Probably [25], it is this hard gap that governs the temperature dependence of the longitudinal resistance in the experiments [5-20]. The scale of temperatures for QAH effect is known to be much lower than the Curie temperature. The fact that the bulk gap in QAH is narrow follows most convincingly from Ref. [10], where the strong temperature-dependent deviations from the quantized value of nondiagonal resistance were observed in high applied external field, so that they cannot be accounted for by the domain structure in the sample. Moreover, the analysis in experimental paper Ref. [15] indicates that the low-temperature behavior of the zero-field diagonal conductivity is activational rather than the variable-range hopping, which is consistent with the scenario of a hard gap. To estimate the experimental value of parameter ν we chose $x = 0.1$, as in most experiments, $A = 3\text{eV}\mathring{A}$ (Ref. [4]), and $\alpha = 2.7$eV (Ref. [24]). With $N_0 = 5 \cdot 10^{14}\text{cm}^{-2}$, we got $\nu \approx 0.5$, suggesting that statistical disorder is relevant for QAH effect.

It is instructive to compare the magnitudes of the gap smearing originating from magnetic and nonmagnetic disorders. The strength of a nonmagnetic disorder, $U(\mathbf{r})$, can be quantified via the prefactor, Γ, in correlator $\langle U(\mathbf{r})U(\mathbf{r}')\rangle = \Gamma\delta(\mathbf{r} - \mathbf{r}')$. Calculations leading to the result Eq. (9.12) do not depend on whether the disorder is magnetic or potential. From Eq. (9.12) we conclude that the relative smearing, $\delta E/\overline{E}_g$, of the gap is Γ/A^2

within a numerical factor. Note that this ratio does not depend on $\overline{E}_g$. In the absence of magnetization the gap is large ($E_g^* \sim 0.5$eV according to tight-binding calculation in Ref. [24]). We can estimate the ratio Γ/A^2 from the mobility, $\mu = 760\text{cm}^2/\text{Vs}$, measured in Ref. [8] at temperature 80K, much higher than the Curie temperature, 15K. Mobility is related to the scattering time, $\tau = M\mu/e$, via the effective mass, $M = \hbar^2 E_g^*/A^2$. Since the energy scale related to τ is $\hbar/\tau$, the ratio Γ/A^2 can be expressed as $\hbar/(\tau E_g^*) = eA^2/(\hbar\mu E_g^{*2})$. Substituting numbers yields the estimate 10^{-2}, which is an indication that potential disorder is not strong. Still the value of E_g^* crucial for this estimate is not reliable.

In conclusion, we point out that for a really strong disorder $\nu \gg 1$, the hard gap near $E = 0$ disappears. In this limit one can neglect $\overline{E}_g$ in the Hamiltonian, so that the problem is reduced to disorder induced smearing of a linear Dirac spectrum. This problem has a long history [32-34], and was addressed in relation to, e.g., d-wave superconductivity. However, in the absence of energy scale to compare the disorder with, there is no definite answer.

9.5 Appendix

9.5.1 Quantized levels on a ring with inverted bandgap

Consider a gap-inverting fluctuation confined to a ring $\rho_1 < \rho < \rho_2$. More specifically, the gap, $\Delta(\mathbf{r})$, changes in a radial direction as follows:

$$\Delta(\mathbf{r}) = \begin{cases} \Delta_0, & 0 < \rho < \rho_1, \\ -\Delta_0, & \rho_1 < \rho < \rho_2, \\ \Delta_0, & \rho > \rho_2. \end{cases} \tag{9.28}$$

We assume for simplicity that the gap reversal is full. In the domain $\rho < \rho_1$, the in-gap solution of the system Eq. (9.10) which is finite at the origin reads

$$\begin{pmatrix} \psi_e^m(\rho) \\ \psi_h^m(\rho) \end{pmatrix} = \begin{pmatrix} \alpha I_{m+1}(s\rho) \\ \sqrt{\frac{\Delta_0 - E}{\Delta_0 + E}}\alpha I_m(s\rho) \end{pmatrix}, \tag{9.29}$$

where $I_m(z)$ is the modified Bessel function, and $s = \frac{\sqrt{\Delta_0^2 - E^2}}{A}$. Corresponding solution for $\rho > \rho_2$, which decays at $\rho \to \infty$ can expressed in terms of the Macdonald function as follows

$$\begin{pmatrix} \psi_e^m(\rho) \\ \psi_h^m(\rho) \end{pmatrix} = \begin{pmatrix} \beta K_{m+1}(s\rho) \\ -\sqrt{\frac{\Delta_0 - E}{\Delta_0 + E}}\beta K_m(s\rho) \end{pmatrix}. \tag{9.30}$$

Within the ring, the solution is a linear combination of $I_m(s\rho)$ and $K_m(s\rho)$

$$\begin{pmatrix} \psi_e^m(\rho) \\ \psi_h^m(\rho) \end{pmatrix} = \begin{pmatrix} \alpha_1 I_{m+1}(s\rho) + \beta_1 K_{m+1}(s\rho) \\ \sqrt{\frac{\Delta_0 + E}{\Delta_0 - E}}\Big(-\alpha_1 I_m(s\rho) + \beta_1 K_m(s\rho) \Big) \end{pmatrix}. \tag{9.31}$$

The gap inversion is reflected in the relative signs of the components of the spinor inside and outside the ring. Four unknown coefficients, α, β, α_1, and β_1 are related by continuity

of the components of the spinors at $\rho = \rho_1$ and $\rho = \rho_2$. Energy levels are determined from the condition of consistency of the system, which reads

$$\Big(\frac{\Delta_0 - E}{\Delta_0 + E}\Big)\frac{K_m(s\rho_2)}{K_{m+1}(s\rho_2)} = \frac{\Big(I_{m+1}(s\rho_1)K_m(s\rho_1) - \frac{\Delta_0 - E}{\Delta_0 + E} I_m(s\rho_1)K_{m+1}(s\rho_1)\Big)I_m(s\rho_2) - \frac{2\Delta_0}{\Delta_0+E} I_{m+1}(s\rho_1)I_m(s\rho_1)K_m(s\rho_2)}{\Big(I_{m+1}(s\rho_1)K_m(s\rho_1) - \frac{\Delta_0 - E}{\Delta_0 + E} I_m(s\rho_1)K_{m+1}(s\rho_1)\Big)I_{m+1}(s\rho_2) + \frac{2\Delta_0}{\Delta_0+E} I_{m+1}(s\rho_1)I_m(s\rho_1)K_{m+1}(s\rho_2)}. \tag{9.32}$$

The near-midgap levels with $|E| \ll \Delta_0$ appear only when the conditions $s\rho_1 \gg 1$ and $s(\rho_2 - \rho_1) \gg 1$ are met. Under these conditions Eq. (9.32) allows serious simplifications. Firstly, using the asymptotes of the Bessel functions, the common bracket in the numerator and denominator of the right-hand side simplifies to

$$I_{m+1}(s\rho_1)K_m(s\rho_1) - \Big(\frac{\Delta_0 - E}{\Delta_0 + E}\Big)I_m(s\rho_1)K_{m+1}(s\rho_1) \approx \frac{1}{2s\rho_1}\Big(\frac{2E}{\Delta_0} - \frac{2m+1}{s\rho_1}\Big). \tag{9.33}$$

As a next step, we divide both sides by the ratio $I_m(s\rho_2)/I_{m+1}(s\rho_2)$ and take the large-ρ asymtotes. Then the left-hand side takes the form

$$\Big(\frac{\Delta_0 - E}{\Delta_0 + E}\Big)\frac{K_m(s\rho_2)I_{m+1}(s\rho_2)}{K_{m+1}(s\rho_2)I_m(s\rho_2)} = 1 - \frac{2E}{\Delta_0} - \frac{2m+1}{s\rho_2}. \tag{9.34}$$

The expressions in the numerator and denominator of the right-hand side are equal to Eq. (9.33) $\pm$ a small correction. The asymptotic form of this correction is the following

$$\frac{2\Delta_0}{\Delta_0 + E} I_{m+1}(s\rho_1)I_m(s\rho_1)\frac{K_m(s\rho_2)}{I_m(s\rho_2)} \approx \frac{2\Delta_0}{\Delta_0 + E} I_{m+1}(s\rho_1)I_m(s\rho_1)\frac{K_{m+1}(s\rho_2)}{I_{m+1}(s\rho_2)} \approx \frac{2e^{-2s(\rho_2-\rho_1)}}{2s\rho_1}. \tag{9.35}$$

Upon combining Eqs. (9.33)-(9.35), the equation for the energy levels reduces to

$$1 - \frac{2E}{\Delta_0} - \frac{2m+1}{s\rho_2} = 1 - \frac{4\exp\big[-2s(\rho_2 - \rho_1)\big]}{\frac{2E}{\Delta_0} - \frac{2m+1}{s\rho_1}}. \tag{9.36}$$

For a narrow ring one can replace ρ_1 and ρ_2 in the denominators by $(\rho_1 + \rho_2)/2$. Also, with accuracy E^2/Δ_0^2, one can replace s by Δ_0/A. This leads to the following expression for the energy levels

$$\left(\frac{2E}{\Delta_0}\right)^2 = \left[\frac{2(2m+1)A}{\Delta_0(\rho_1 + \rho_2)}\right]^2 + 4\exp\Big[-2\frac{(\rho_2 - \rho_1)\Delta_0}{A}\Big]. \tag{9.37}$$

The right-hand side is the sum of contributions from the quantized motion along the ring and quantized motion across the ring, as in Eq. (9.23) of the main text.

9.5.2 Temperature dependence of conductivity

Neglecting the energy dependence of logarithm in Eq. (9.13), we approximate the energy-dependent density of states with

$$N(E) = N_0 \exp\Big(- \frac{\overline{E}_g}{\nu E}\Big), \tag{9.38}$$

where parameter ν is defined by Eq. (9.27). Assume that the energy responsible for the transport is E_0. The density of states can be treated as a constant within a strip $|E - E_0| < \nu E_0^2/\overline{E}_g$. A typical distance between the localized states within the strip is

$$r(E_0) = \Big(\frac{\nu E_0^2 N(E_0)}{\overline{E}_g}\Big)^{-1/2}. \tag{9.39}$$

Following the derivation of Mott's law, we minimize the log-resistance,

$$\ln R\,(E_0) = \frac{E_0}{T} + \frac{2r(E_0)}{\xi}, \tag{9.40}$$

corresponding to activation into the strip and tunneling between the neighbors, with respect to E_0. Here ξ is the localization radius. The condition of minimum reads

$$\frac{1}{T} = \frac{1}{(N_0\xi^2)^{1/2}}\Big(\frac{\overline{E}_g}{\nu E_0^2}\Big)^{3/2} \exp\left(\frac{\overline{E}_g}{2\nu E_0}\right), \tag{9.41}$$

where we have differentiated only the exponent in $r(E_0)$. Upon expressing E_0 from Eq. (9.41) and substituting it back into Eq. (9.40), we find with logarithmic accuracy

$$\ln R\,(E_0) = \frac{\overline{E}_g}{2\nu T}\left[\ln \frac{\overline{E}_g}{\nu T}\Big(\frac{N_0\xi^2\overline{E}_g}{\nu}\Big)^{1/2}\right]^{-1}. \tag{9.42}$$

The result Eq. (9.42) applies when the logarithm is big. By virtue of the same condition the activation term in Eq. (9.41) exceeds the tunneling term. Concerning the dimensionless combination, $N_0\xi^2\overline{E}_g$, under the logarithm, with localization length, $\xi = A/\overline{E}_g$, in the middle of the gap being disorder independent, this combination is some unknown power of ν. Thus, for $\nu \sim 1$, Eq. (9.42) applies for $T < \overline{E}_g$. We conclude that, due to a rapid growth of the density of states away from the gap center, the behavior of the resistance remains Arrhenius even at low temperatures. This is consistent with observation in Ref. [15].

9.5.3 The role of Bk^2 term in the Hamiltonian

In order to estimate the effect of Bk^2 term in the Hamiltonian Eq. (9.7), we compare it to the linear term and find the scale of momenta $k \sim A/B$ when this term becomes important. In other words, the term Bk^2 plays a dominant role when the spatial scales in the problem are $\sim B/A$. On the other hand, with logarithmic accuracy, the size of the fluctuation is

$\sim A/\overline{E}_g$. The ratio of the two scales yields a dimensionless parameter $B\overline{E}_g/A^2$, which becomes progressively small as the gap decreases. More quantitative information about the role of Bk^2 can be obtained upon incorporating it into Eq. (9.20). Then it takes the form

$$\frac{d\varphi}{d\chi} = C_0^2 \exp\Big[-2\varepsilon \int_0^\chi d\chi' \sinh 2\varphi(\chi')\Big] - 1 + \varepsilon \cosh 2\varphi + \frac{B\overline{E}_g}{A^2}\left[\Big(\frac{d\varphi}{d\chi}\Big)^2 - \frac{d^2\varphi}{d\chi^2}\right]. \quad (9.43)$$

Similar to the steps in the main text, we neglect small terms containing ε and substitute $\varphi(\chi) = \chi/b$. This leads to the following modified relation between the parameters b and C_0

$$C_0^2 = 1 + \frac{1}{b} - \left(\frac{B\overline{E}_g}{A^2}\right)\frac{1}{b^2}. \quad (9.44)$$

Note that for the "topological" bandstructure, when the signs of B and $\overline{E}_g$ are opposite, the last term in Eq. (9.44) causes only a slight increase of C_0, which results in a small suppression of the exponent in the density of states. On the contrary, for a "trivial" bandstructure, this last term decreases C_0, leading to the enhancement of the density of states. Moreover, Eq. (9.44) suggests that this enhancement can be parametrically big when the second and the third terms closely compensate each other. For such a compensation the width of the ring should be of the order of the minimal length B/A. This, however, violates our basic assumption that the shape of the fluctuation is dominated by the inner part.

9.6 References

[1] C. L. Kane and E. J. Mele, Phys. Rev. Lett. **95**, 226801 (2005).

[2] B. A. Bernevig, T. L. Hughes, and S.-C. Zhang, Science **314**, 1757 (2006).

[3] B. A. Bernevig and S.-C. Zhang, Phys. Rev. Lett. **96**, 106802 (2006).

[4] C.-X. Liu, X.-L. Qi, X. Dai, Z. Fang, and S.-C. Zhang, Phys. Rev. Lett. **101**, 146802 (2008).

[5] J. G. Checkelsky, J. Ye, Y. Onose, Y. Iwasa, and Y. Tokura, Nat. Phys. **8**, 729 (2012).

[6] C.-Z. Chang, J. Zhang, M. Liu, Z. Zhang, X. Feng, K. Li, L.-L. Wang, X. Chen, X. Dai, Z. Fang, X.-L. Qi, S.-C. Zhang, Y. Wang, K. He, X.-C. Ma, and Q.-K. Xue, Adv. Mater. **25**, 1065 (2013).

[7] X. Kou, M. Lang, Y. Fan, Y. Jiang, T. Nie, J. Zhang, W. Jiang, Y. Wang, Y. Yao, L. He, and K. L. Wang, ACS Nano **7**, 9205 (2013).

[8] C.-Z. Chang, J. Zhang, X. Feng, J. Shen, Z. Zhang, M. Guo, K. Li, Y. Ou, P. Wei, L.-L. Wang, Z.-Q. Ji, Y. Feng, S. Ji, X. Chen, J. Jia, X. Dai, Z. Fang, S.-C. Zhang, K. He, Y. Wang, L. Lu, X.-C. Ma, and Q.-K. Xue, Science **340**, 167 (2013).

[9] J. G. Checkelsky, R. Yoshimi, A. Tsukazaki, K. S. Takahashi, Y. Kozuka, J. Falson, M. Kawasaki, and Y. Tokura, Nat. Phys. **10**, 731 (2014).

[10] X. Kou, S.-T. Guo, Y. Fan, L. Pan, M. Lang, Y. Jiang, Q. Shao, T. Nie, K. Murata, J. Tang, Y. Wang, L. He, T.-K. Lee, W.-L. Lee, and K. L. Wang, Phys. Rev. Lett. **113**, 137201 (2014).

[11] C.-Z. Chang, W. Zhao, D. Y. Kim, H. Zhang, B. A. Assaf, D. Heiman, S.-C. Zhang, C. Liu, M. H. W. Chan. and J. S. Moodera, Nat. Mater. **14**, 473 (2015).

[12] A. Kandala, A. Richardella, S. Kempinger, C.-X. Liu, N. Samarth, Nat. Commun. **6**, 7434 (2015).

[13] M. Mogi, R. Yoshimi, A. Tsukazaki, K. Yasuda, Y. Kozuka, K. S. Takahashi, M. Kawasaki, and Y. Tokura, Appl. Phys. Lett. **107**, 182401 (2015).

[14] X. Kou, L. Pan, J. Wang, Y. Fan, E. S. Choi, W.-L. Lee, T. Nie, K. Murata, Q. Shao, S.-C. Zhang, and K. L. Wang, Nat. Commun. **6**, 8474 (2015).

[15] A. J. Bestwick, E. J. Fox, X. Kou, L. Pan, K. L. Wang, and D. Goldhaber-Gordon, Phys. Rev. Lett. **114**, 187201 (2015).

[16] C.-Z. Chang, W. Zhao, D. Y. Kim, H. Zhang, B. A. Assaf, D. Heiman, S.-C. Zhang, C. Liu, M. H. W. Chan, and J. S. Moodera, Nat. Mater. **14**, 473 (2015).

[17] C.-Z. Chang, W. Zhao, D. Y. Kim, P. Wei, J. K. Jain, C. Liu, M. H. W. Chan, and J. S. Moodera, Phys. Rev. Lett. **115**, 057206 (2015).

[18] S. Grauer, S. Schreyeck, M. Winnerlein, K. Brunner, C. Gould, and L. W. Molenkamp, Phys. Rev. B **92**, 201304(R) (2015).

[19] E. O. Lachman, A. F. Young, A. Richardella, J. Cuppens, H. R. Naren, Y. Anahory, A. Y. Meltzer, A. Kandala, S. Kempinger, Y. Myasoedov, M. E. Huber, N. Samarth, and E. Zeldov, Sci. Adv. **1**, e1500740 (2015).

[20] Y. Feng, X. Feng, Y. Ou, J. Wang, C. Liu, L. Zhang, D. Zhao, G. Jiang, S.-C. Zhang, K. He, X. Ma, Q.-K. Xue, and Y. Wang, Phys. Rev. Lett. **115**, 126801 (2015).

[21] Statistical randomness is present in a zero external field and is distictively different from the randomness in orientations of the domains. The latter is important near the coercive field and gives rise to the plateau with zero Hall conductance predicted in J. Wang, B. Lian, and S.-C. Zhang, Phys. Rev. B **98**, 085106 (2014), and recently observed in Ref. [20].

[22] B. I. Halperin and M. Lax, Phys. Rev. **148**, 722 (1966).

[23] J. Zittartz and J. S. Langer, Phys. Rev. **148**, 741 (1966).

[24] The issue whether the two-dimensional Hamiltonian Eq. (9.7) applies to realistic magnetic structures involving several layers is discussed in R. Yu, W. Zhang, H.-J. Zhang, S.-C. Zhang, X. Dai, Z. Fang, Science **329**, 61 (2010). It was concluded that it captures the low-energy excitations, and the pseudospin components should be identified with symmetric and antisymmetric combinations of the top and bottom surface states.

[25] see *Supplemental Material*.

[26] D. J. Thouless and M. E. Elzain, J. Phys. C **11**, 3425 (1978).

[27] E. Brezin and G. Parisi, J. Phys. C **13**, L307 (1980).

[28] A. W. W. Ludwig, M. P. A. Fisher, R. Shankar, and G. Grinstein, Phys. Rev. B **50**, 7526 (1994).

[29] Zh. I. Alferov, E. L. Portnoi, and A. A. Rogachev, Sov. Phys. Semicond. **2**, 1001 (1969).

[30] S. D. Baranovskii and A. L. Efros, Sov. Phys. Semicond. **12**, 1328 (1978).

[31] A. L. Efros and M. E. Raikh, in *Optical Properties of Mixed Crystals*, edited by R. J. Elliot and I. P. Ipatova (Elsevier Science, Amsterdam, 1988), p. 133.

[32] M. P. A. Fisher and E. Fradkin, Nucl. Phys. B **251**, 457 (1985).

[33] P. A. Lee, Phys. Rev. Lett. **71**, 1887 (1993).

[34] A. A. Nersesyan, A. M. Tsvelik, and F. Wenger, Phys. Rev. Lett. **72**, 2628 (1994).